Imaging and thermal characterization of materials by scanning photo-thermal radiometry

Alejandro Mateos Canseco

université de BORDEAUX

THÈSE PRÉSENTÉE

POUR OBTENIR LE GRADE DE

DOCTEUR DE L'UNIVERSITÉ DE BORDEAUX

ECOLE DOCTORALE SCIENCES PHYSIQUES ET DE L'INGENIEUR

SPÉCIALITÉ : MÉCANIQUE

Par Alejandro MATEOS CANSECO

Imagerie et caractérisation thermique des matériaux par radiométrie photo-thermique en balayage.

Sous la direction de : M. Andrzej KUSIAK

(co-directeur : M. Jean-Luc BATTAGLIA)

Soutenue le 10/02/2023

Membres du jury :

M. DUVAUT Thierry,	Professeur, ITheMM, Université de Champagne Ardenne,	Président
M. GARDAREIN Jean-Laurent,	Maitre de Conférences HDR, IUSTI, Ecole Polytechnique Marseille,	Rapporteur
M. SEMMAR Nadjib,	Professeur, GREMI, Université d'Orléans,	Rapporteur
M. HAY Bruno,	Ingénieur HDR, Laboratoire National de Essais et Métrologie,	Examinateur
M. BATTAGLIA Jean-Luc,	Professeur, Université de Bordeaux,	Co-directeur de thèse
M. KUSIAK Andrzej,	Maitre de Conférences HDR, Université de Bordeaux,	Directeur de thèse

Titre : Imagerie et caractérisation thermique des matériaux par radiométrie photo-thermique en balayage.

Résumé:

L'imagerie des propriétés thermiques permet le développement de matériaux hétérogènes nouveaux dont les propriétés sont adaptées à l'application visée. Dans les applications modernes, les matériaux sont souvent composites tant dans leur épaisseur que dans le plan. La détermination des propriétés thermiques doit donc s'adapter à l'échelle d'observation, du micron à la dimension du composant. La caractérisation aux petites échelles spatiales nécessite des métrologies adaptées, différentes de celles utilisées à l'échelle macroscopique. Les méthodes existantes d'imagerie thermique sans contact (thermoréflectométrie et thermographie dans l'IR) présentent des avantages et des inconvénients. Au regard de ces derniers, il nous a donc paru nécessaire de développer une technique de balayage à haute fréquence fiable et permettant d'être utilisée sur des surfaces très différentes.

Dans ce travail, une technique robuste permettant l'imagerie et la caractérisation des propriétés thermiques à l'échelle micrométrique est donc développée. Elle est basée sur le principe de radiométrie photo thermique modulée, implantée ici en mode balayage. Ce choix est motivé par plusieurs raisons, à savoir, l'objectif de disposer d'une mesure optique, permettant ainsi d'éviter les problématiques liées à la mesure par contact. Un deuxième objectif est de pouvoir explorer des temps caractéristiques inférieurs à ceux accessibles en thermographie infrarouge. Il est aussi possible de réaliser la caractérisation dans et hors plan. Enfin, cette approche permet d'envisager la caractérisation à haute température. Ainsi, le développement expérimental associé au modèle représentatif de l'expérience et l'inversion des mesures sont utilisés pour déterminer les propriétés thermiques d'intérêt.

Le couplage de l'image thermique obtenue par balayage avec un pas spatial inférieur à la limite de diffraction dans l'infrarouge avec les techniques de traitement de l'image constitue une perspective majeure de ce travail.

Mots clés :

Caractérisation thermique, science des matériaux, propriétés thermiques, radiométrie photo thermique.

Title: Imaging and thermal characterization of materials by scanning photo-thermal radiometry.

Abstract:

Imaging of thermal properties allows the development of new heterogeneous materials whose properties are adapted to the intended application. In modern applications, materials are often composite in both thickness and plane. Therefore, the determination of thermal properties must be adapted to the scale of observation, from micron to the component size. Small scale characterization needs the appropriate metrology, different from those used at macroscopic scale. The existing contactless methods for thermal imaging (thermoreflectance and infrared thermography) have advantages and drawbacks. In view of the latest, it therefore deemed necessary to us to develop a reliable high frequency scanning technique that can be used on different surfaces.

In this work, a robust technique allowing imaging and thermal characterization at the micrometric scale is developed. It is based on the principle of modulated thermal photo radiometry, implemented here in scanning mode. This choice is motivated by several reasons, namely, the objective of having an optical measurement, thus making it possible to avoid the problems linked to measurement by contact. A second objective is being able to explore characteristic times lower than those accessible by infrared thermography. In addition, the possibility of carrying out in-plane and out-of-plane characterization, and finally, the potential to transpose measurement to high-temperature characterization. Thus, the experimental development associated with the representative model of the experiment and the inversion of the measurements are used to determine the thermal properties of interest.

The coupling of the thermal image obtained by scanning with a spatial step lower than the diffraction limit in the infrared with image processing techniques constitutes a major perspective of this work.

Keywords:

Thermal characterization, material science, thermal properties, photothermal radiometry.

Contents

Résumé: i
Abstract: ii
Contents iii
List of figures vi
List of tables xi
Nomenclature xii
Context 1
Chapter 1: Thermal Characterization at Microscale. 5
1.1 Introduction. 5
1.2 Techniques for imaging temperature and thermal properties at the microscale. 5
1.2.1 Scanning Thermal Microscopy (SThM). 5
1.2.2 Thermoreflectance. 12
1.2.3 Photothermal radiometry. 16
1.3 Conclusions 22
Chapter 2: Scanning Photothermal Radiometry (SPR). 23
2.1 Introduction. 23
2.2 A first scanning experiment in contact mode based on the use of an optical fiber probe. 24
2.2.1 Complete experimental setup. 26
2.2.2 Expected collected radiation. 28
2.2.3 Static measurements. 30
2.2.4 Measurements across the strip. 31
2.2.5 Heat transfer model. 33
2.3 A second scanning experiment in contactless mode based on Photothermal Radiometry. 37
2.3.1 SPR experimental setup. 38
2.3.2 Heat source. 40
2.3.3 Measurement area. 44
2.3.4 Optical Alignment. 45
2.3.5 Detector calibration. 46

2.3.6 The scanning configuration. 47
2.3.7 Scanning-Measurement synchronization. 50
2.4 Conclusions 51
Chapter 3: Model describing the experimental measurement. 53
3.1 Introduction. 53
3.2 The influence of the scan velocity. 54
3.3 Heat transfer in a semi-infinite media submitted to a heat flux with Gaussian distribution. 57
3.3.1 Simplification for isotropic assumption. 60
3.3.2 Uniform disk Heat flux and punctual heat flux. 63
3.3.3 Comparison of models with: Gaussian, Uniform and Punctual heat flux excitation. 64
3.4 A comparison between the analytical solution and that from the FEM. 66
3.5 Multilayer material 67
3.6 Parameter identification. 69
3.7 Conclusions 71
Chapter 4: Applications of the SPR experiment. 73
4.1 Introduction. 73
4.2 Motionless experiments. 73
4.2.1 Assessment of the performance of the setup on bulk sample. 73
4.2.2 Application on the 3-ω sample. 84
4.3 Scanning experiments. 91
4.3.1 Scanning across contact interface perpendicular to the surface. 91
4.3.2 Scanning across the 3-ω pattern 97
4.3.3 Imaging on composite materials 101
4.4 Conclusions 107
Chapter 5: General Conclusions and perspectives. 109
5.1 Conclusions 109
5.2 Perspectives 112
Appendix. 113
I. The lock-in amplifier. 113
II. Principle and model of the 3-ω method. 117
III. Heat transfer in a semi-infinite media submitted to a heat flux with Gaussian distribution. 123

IV. Heat transfer in a layer. 127
V. Emittance calculation 131
Bibliography 133

List of figures.

Figure 1.1. Time and spatial resolution of current techniques for thermal imaging. 2
Figure 1.1: Schematic diagram of typical AFM based SThM. 6
Figure 1.2: SEM image of thermoresistive probes: (a) Wollaston wire probe [12], (b) KNT probe [13] and (c) Doped Si probe [14]. 7
Figure 1.3: Schematic representation of the probe-sample interaction. (a) Probe-Sample flux distribution. (b) Tip-sample interactions. 9
Figure 1.4: Normalized, thermal conductivity calibration curves for SThM (a) Wollaston wire, (b) KNT and (c) doped Si tips [23]. 10
Figure 1.5: Topography AFM (left); amplitude (center) and phase (right) measured at 871 Hz (SThM 3-ω) on a Sb_2Te_3 nanowire [47]. 10
Figure 1.6: Topography (AFM), amplitude and phase measured at 523 Hz (SThM 3-ω) on an In_3SbTe_2 crystalline nanowire. 11
Figure 1.7: (a) Topography (AFM mode), amplitude and phase (SThM 3-ω mode) measured at 1125 Hz on a silica fiber/pyrocarbon composite. Contact radius of 100 nm and $Rc=7.83 \times 10^{-8}$ $K \cdot m^2 \cdot W^{-1}$. (b) Effective Thermal Boundary Resistance from scan line Δ ($TBR=5 \times 10^{-8}$) [49]. 12
Figure 1.8: Typical sample configurations of thin film and bulk materials measured using the thermoreflectance technique [58]. 13
Figure 1.9: Scheme of TDTR experimental setup [60]. 14
Figure 1.10: Scheme of a) CCD image thermoreflectance setup [76] and b) Scanning thermoreflectance microscopy setup [78]. 15
Figure 1.11: $\Delta R/R$ thermoreflectance image of sample with pixel size of 150 nm [78]. 15
Figure 1.12: TDTR in point scanning configuration applied to patterned titanium-gold on a silicon substrate: a) scheme of the sample, b) phase images acquired at the six modulation frequencies [79]. 16
Figure 1.13: Results obtained from TDTR measurements presented in Figure 1.12: (a) Thermal interface conductance map. (b) Conductance across the path shown by the dashed line in (a). (c) Substrate thermal conductivity map. (d) Substrate thermal conductivity across the path shown by the dashed line in (c) [79]. 16
Figure 1.14 Scheme of MPTR setup. 17
Figure 1.15: Temperature field during the relaxation of heterogeneous anisotropic materials studied in [104]. 19
Figure 1.16: a) Measured temperature field at t = 1 s after the pulsed spot, b) logarithmic representation of the measured temperature field the same time [105]. 20
Figure 1.17: Sequence in time of thermograms from flying spot technique where the arrow indicates the position of the crack [106]. 20
Figure 1.18: Thermograms of the amplitude (a) and phase (b) from lock-in thermography on moving sample [107]. 21
Figure 1.19: Diagram of the laser-spot lock-in thermography experimental setup [108]. 21

Figure 2.1 Scheme of fiber-based probe. 24
Figure 2.2 Measured attenuation of the Ø100 μm core InF_3 fiber provided by Thorlabs from four independent runs [114]. 25
Figure 2.3 a) Scheme of fiber probe holder and the passive contact mechanism configuration in contact and contactless conditions; b) Optical image of the Cu probe tip deposited at the end of the 100 μm core diameter InF_3 optical fiber. 25
Figure 2.4 Scheme of experimental setup with fiber-based probe. 26
Figure 2.5: Output power vs. amplitude of the control wave from the waveform generator considering a Heaviside voltage. 27
Figure 2.6 Ge window transmission from Edmund optics [115]. 27
Figure 2.7: In scheme (a) the Numerical Aperture (NA) of a fiber is defined as the sine of the largest angle an incident ray can have for total internal reflectance in the core. In scheme (b) the angle of acceptance defines the cone of emitted radiation that will be transmitted by the optic fiber. 29
Figure 2.8: Amplitude and phase measured with four P%. 30
Figure 2.9: Scheme of the 3-ω sample used in the evaluation of fiber-based probe in contact mode. 31
Figure 2.10: Frequency sweep in static mode of the fiber-based probe in out of contact condition, in contact with SiO_2 layer (zone I) and in contact with Au strip (zone II). 31
Figure 2.11: Scan across 20 μm in width Au strip (line III) over SiO_2 layer on Si substrate with: a) 27 Hz; b) 185 Hz excitation frequency. 32
Figure 2.12: Scheme of the scanning process with four main positions indicated in scan plots. 32
Figure 2.13: Impedance network representation of the fiber probe in contactless mode. 33
Figure 2.14: Comparison between phase measurements obtained in contactless condition and the simulation from the model based on the lumped body assumption for the tip. 34
Figure 2.15: Thermal impedance network of the probe in contactless and in contact modes for low frequencies. 35
Figure 2.16: Phase comparison between experiment and simulation in contact with a) SiO_2 zone and b) Au zone. 36
Figure 2.17: Schematic representation of the probe-sample contact. 36
Figure 2.18: Diagram of the experimental setup. 38
Figure 2.19: In yellow, the focused laser incident on the sample with spot radius of $w0$ at sample surface and in red, the emittance from the sample collected with effective radius rm at sample surface in a lateral view (a) and top view (b). 39
Figure 2.20 (a) Gaussian beam propagation. (b) Transversal Intensity distribution of the Gaussian beam. 40
Figure 2.21: Scheme of knife-edge experiment. 41
Figure 2.22 Experimental data from one knife-edge measurement (at $z = 25$ μm) and fitting curve (equation (2.27)) with optimal parameters $w = 6.81$ μm and $y0 = 47.3$ μm. 42
Figure 2.23 Diagram of Gaussian beam propagation near to the focal plane. 43
Figure 2.24 Representation of the beam radius measurement procedure with knife-edge method for several positions in z-axis. 43

Figure 2.25 Experimental data from $w(z)$ measurements and fitting curve with equation (2.28) with optimal parameters $w0 = 3.3$ µm, $b = 5.9$ µm and $z0 = 14.14$ µm 44
Figure 2.26: Optical arrangement for measurement of the infrared radiation. 45
Figure 2.27: Scheme of the setup for calibration of the measurement chain phase lag. 46
Figure 2.28: Phase lag calibration curve for the two infrared detectors 47
Figure 2.29: Scheme of the scanning - sampling process. 48
Figure 2.30: E-517 trigger behavior. 50
Figure 3.1: Moving heat source: (a) coordinates *x, y, z* fixed on the sample and (b) moving coordinates fixed on the heat source *X , y, z*. 55
Figure 3.2: Péclet number for two scan velocities v and thermal diffusivity $a = 1 \times 10 - 7$ m²·s⁻¹ according to frequency range exploited in the SPR measurement. 56
Figure 3.3: Dimensionless ratio rm/lh with $rm = 6.25$ µm for different thermal diffusivity values: $a = 10 - 7, 10 - 6, 10 - 5, 10 - 4$ m²·s⁻¹ 57
Figure 3.4: Geometrical representation of a semi-infinite sample submitted to a Gaussian heat flux on its top surface. 57
Figure 3.5: Reduced sensitivity function $S\phi ai$ using $\rho Cp = 3$ MJ·m⁻³·K⁻¹, calculated for parameters: $w0 = 3.3$ µm, $rm = 6.25$ µm and a) $kr = 0.1$ W·m⁻¹·K⁻¹, $kz = 300$ W·m⁻¹·K⁻¹ ; b) $kr = 50$ W·m⁻¹·K⁻¹, $kz = 150$ W·m⁻¹·K⁻¹ ; c) $kr = 280$ W·m⁻¹·K⁻¹, $kz = 0.3$ W·m⁻¹·K⁻¹. 59
Figure 3.6: Reduced sensitivity function $S\Theta ai$ using $\rho Cp = 3$ MJ·m⁻³·K⁻¹, calculated for parameters: $w0 = 3.3$ µm, $rm = 6.25$ µm and a) $kr = 0.1$ W·m⁻¹·K⁻¹, $kz = 300$ W·m⁻¹·K⁻¹ ; b) $kr = 50$ W·m⁻¹·K⁻¹, $kz = 150$ W·m⁻¹·K⁻¹ ; c) $kr = 280$ W·m⁻¹·K⁻¹, $kz = 0.3$ W·m⁻¹·K⁻¹. 60
Figure 3.7: Reduced sensitivity function $S\phi g\ ai$ for isotropic material using $\rho Cp = 3$ MJm − 3K − 1, calculated for parameters: $w0 = 3.3$ µm, $rm = 6.25$ µm and a) $k = 0.1$ Wm − 1K − 1; b) $k = 50$ Wm − 1K − 1; c) $k = 280$ Wm − 1K − 1. 61
Figure 3.8: Ratio of the reduced sensitivity functions ($S\phi g(k)/S\phi g(rm)$) with three different thermal conductivities. 62
Figure 3.9: Comparison of phase (a) and amplitude (b) of orthotropic model (equation (3.14)) and isotropic model (equation (3.23)) for a semi-infinite media. 62
Figure 3.10: (a) Phase lag and (b) normalized amplitude from the three models for surface sample temperature: Gaussian (circle), Uniform (square), Point (dot). The thermal conductivities considered are: $k = 0.3,\ 30,\ 300$ Wm − 1K − 1. 64
Figure 3.11: Absolute phase difference between point heat source and Gaussian heat source model 65
Figure 3.12: Absolute phase difference between: a) point heat source and Gaussian heat source models; b) uniform heat source and Gaussian heat source models 65
Figure 3.13: a) Geometry and mesh of the domain used in the FEM simulation of the semi-infinite media moving at constant velocity and submitted to a uniform heat flux distribution on its top surface. 66
Figure 3.14: Comparison between analytical static model (equation (3.23)) and FEM model with constant velocities v = 1, 5, 20 µms − 1 for three thermal conductivities $k = 0.3, 30, 300$ Wm − 1K − 1. 67
Figure 3.15: Schematic representation of a multilayer stack over a substrate. 68
Figure 4.1: AFM images on SST sample in (a) 2D and (b) 3D view 74

Figure 4.2: Experimental setup with infrared detector IRD-1. The yellow line represents the laser beam, the red line represents the IR signal and the green line represents the visible. 75
Figure 4.3: Amplitude (a) and phase (b) measured of SST sample for diferent P%..... 76
Figure 4.4: Phase and amplitude measured for the SST sample and the results of fitted model. 77
Figure 4.5: a) Schematic representation of out of focus sample displacement. b) Estimated thermal conductivity (k) for different sample position in z, with the focal plane at z=0, $rm = 6.25$ µm and power at 47 P%. 77
Figure 4.6: Comparison of measured phase and simulated phase with fitted model for low power and high power. 78
Figure 4.7: Influence of the noise in the phase measured. At high power the variation of the phase measured is lower as consequence of better signal but the trend line is shifted..... 78
Figure 4.8: a) Estimated rm according to the power; b) Standard deviation of the estimated rm according with the power..... 79
Figure 4.9: Phase measured from SST sample for several P% in the 200 Hz to 100 kHz frequency range where the effect of the power is visible. It reduces the white noise but also add a phase shift. 79
Figure 4.10: a) Experimental phase and fitted model in 200 Hz to 100 kHz frequency range for SST sample at 30 P%. b) Phase error between the experimental phase and its fitted model for all the tested P% presented in Figure 4.9. 80
Figure 4.11: Comparison of phases calculated using FEM for the semi-infinite sample SST considering three measurement areas: a disk of radius $rc = 6.25$ µm, a square of $2b$=12.5 µm width and a second disk of radius re=7.05 µm..... 81
Figure 4.12: Comparison between modeled phase with rm=7.05 µm and experimental phase at 25 P%, 35 P% and 75 P%. 81
Figure 4.13: Phase (a) and amplitude (b) of background noise signal generated by the germanium window measured without sample. 82
Figure 4.14: Experimental setup with infrared detector IRD-2. The yellow line represents the laser beam, the red line represents the IR signal and the greed line represents the visible light. 83
Figure 4.15: (a) Experimental phase and fitted model for SST sample at 40 P%; (b) estimated rm for 40 P_2%, 50 P_2% and 60 P_2%. 84
Figure 4.16: Schema of the 3-omega pattern and stack composition..... 85
Figure 4.17: Scheme of experimental arrangement for the 3-ω measurement. 86
Figure 4.18: Measured $V3\omega$ vs current at different frequencies for samples $M1 \rightarrow eGGST = 100$ nm, $M2 \rightarrow eGGST = 200$ nm, $M3 \rightarrow eGGST = 300$ nm and $M4 \rightarrow eGGST = 400$ nm thick GGST layer. 87
Figure 4.19: Measurement of electrical resistance according to the temperature. 88
Figure 4.20: Thermal resistance vs layer thickness for the GGST material. Experimental measurements in red squares, and fitting line in black. 89
Figure 4.21 Phase measured on the 3-ω sample (400 nm GGST) for several %P. 90
Figure 4.22: a) Comparison between experimental and simulated phase; b) Sensitivity curves for TBR in the 400 nm thick GGST sample obtained with multilayer model..... 90
Figure 4.23: Sample configuration (a) and SEM image of contact interface (b). 91
Figure 4.24: Image of the scanning zone. 92

Figure 4.25: Amplitude and phase scan of the contact interface between two stainless steel parts pressed mechanically. 92
Figure 4.26: Phase and amplitude comparison between first and last scan line in Figure 4.25. 93
Figure 4.27: Comparison between scan with 20 sweeps by line (SL20 in blue) and scan with 3 sweeps by line (SL3 in magenta). 94
Figure 4.28: Model of the contact interface with the finite element method in COMSOL. 94
Figure 4.29: a) Phase vs position for $= 5 \times 10 - 8,\ 5 \times 10 - 7,\ 5 \times 10 - 6,\ 5 \times 10 - 5$ $m^2 \cdot K \cdot W^{-1}$; b) minimum phase calculated at x=10 μm vs TBR. 95
Figure 4.30: Comparison between the experimental scan and simulated scan with TBR $= 13 \times 10 - 7$ $m^2 \cdot K \cdot W^{-1}$. 95
Figure 4.31: Phase calculated at x=0 versus the thickness of the layer interface. 96
Figure 4.32: a) Comparison between experimental and calculated using numerical simulation phase according to the probe shape (circular and square) of equal area. b) Comparison between experimental and calculated using numerical simulation amplitude. 97
Figure 4.33: Scan images of amplitude and phase acquired with 99kHz excitation frequency. 98
Figure 4.34: Model of the 3-ω strip with the finite element method in COMSOL. 99
Figure 4.35: (a) Phase and (b) amplitude comparison between simulated and experimental scanning of 50 μm wide strip. 99
Figure 4.36: (a) Scan image of the 300 nm wide 3-ω strip with 400 nm thick GGST layer. (b) Amplitude and phase plot of first scan line (y=0.5 μm). 100
Figure 4.37: (a) Phase and (b) amplitude comparison between the simulated and experimental scanning of 300 nm wide strip. 101
Figure 4.38: a) SEM image of the Composite Structure; b) Scheme of the silica fiber surrounded by the lamellar PyC matrix. 102
Figure 4.39: a) Visible image of the scanned area on the PyC composite sample. Obtained images of amplitude and phase on the scanned area using different excitation frequency: b) 99 kHz; c)75 kHz; d)28.3 kHz; e) 10.7; f) 1.1 kHz. 103
Figure 4.40: Frequency comparison of scan line at y=10 μm for (a) amplitude and (b) phase. Blue shadow represents the fiber region. 104
Figure 4.41: Visible image of the CF-Al composite. The SPR scanned zone is delimited with red rectangle. 105
Figure 4.42: a) Amplitude and phase measured by SPR on the CF-Al composite at 8.5 kHz excitation frequency. b) Amplitude and phase measured at y=9 μm scanline (black dashed line on amplitude and phase image). 105
Figure 4.43: Image of CF-E sample with the scan zone is marked by a red square. 106
Figure 4.44 Amplitude and phase images obtained by SPR on CF-E composite with two scanning velocities: a) v = 6.6 μm · s − 1 and b) v = 2 μm · s − 1. 107

List of tables.

Table 1.1: Comparison of different thermal probes [18]. 8
Table 1.2 Performances of thermoreflectance techniques [78] 15
Table 1.3: Advantages and drawbacks of thermal imaging techniques 22
Table 1.4: Spatial, temporal and temperature resolution of thermal imaging techniques 22
Table 2.1: Thermal properties of the probe and sample. 34
Table 2.2: Summary of scanning parameters. 50
Table 4.1: Properties of the stainless-steel sample (SST). 74
Table 4.2: Results from area roughness measured and calculated with Nanosurf EasyScan-2 AFM tool. 74
Table 4.3: Thermal Properties (Thermal Conductivity (k), Density (ρ) and Specific Heat (Cp)) of the different materials involved in the 3-ω sample. 85
Table 4.4: Scan parameters for the image presented in Figure 4.25. 92
Table 4.5: Scan parameters for the line y=1 µm. 93
Table 4.6: Scanning parameters for strip of 50 µm in width and 400 nm in GGST thickness (results presented in Figure 4.33). 97
Table 4.7: Properties of the silica fiber and PyC present in the composite sample. 102
Table 4.8: Scanning parameters for the PyC composite imaging and presented in Figure 4.39. 102
Table 4.9: SPR scanning parameters used for the CF-Al composite imaging. 105
Table 4.10: Scanning parameters used in SPR imaging of the CF-E composite. Visible image presented in Figure 4.44. 106
Table 5.1: Parameters used in the thermal image acquisition by SPR. 111

Nomenclature

Symbols

A	Amplitude
A_{ref}	Amplitude of reference
$\boldsymbol{a}$	vector of seek parameters
a	Thermal diffusivity [$m^2 \cdot s^{-1}$]
a_s	Thermal diffusivity of sample [$m^2 \cdot s^{-1}$]
a_i	Seek parameter
C_p	Heat capacity [$J \cdot kg^{-1}K^{-1}$]
C_{pt}	Heat capacity of the fiber probe tip [$J \cdot kg^{-1}K^{-1}$]
D	Detector size [m]
E	Vector of residuals
e_i	Thickness of layer i [m]
e_s	Thickness of substrate [m]
F	Function to minimize
f	Frequency [Hz]
f_{obj}	Focal length of microscope objective [m]
f_{opm}	Focal length of off-axis parabolic mirror
f_{ft}	IR camera acquisition frequency [Hz]
f_{lk}	Lock-in frequency [Hz]
$G_{0\to\lambda}$	Fraction of the radiation emitted in the spectral band 0 to λ
$\mathcal{H}$	Hankel transform
h	Thermal impulse response [K]
h_a	Heat transfer coefficient by convection [$W \cdot m^{-2} \cdot K^{-1}$]
I_0	Modified Bessel function of first kind and order 0
i_0	Maximum current [A]
J	Jacobian
J_0	Bessel function of the first kind and order 0
J_1	Bessel function of the first kind and order 1
j	Imaginary number
K_i	Known parameters
k	Thermal conductivity [$W \cdot m^{-1} \cdot K^{-1}$]
k_f	Thermal conductivity of optical fiber [$W \cdot m^{-1} \cdot K^{-1}$]
k_s	Thermal conductivity of substrate [$W \cdot m^{-1} \cdot K^{-1}$]
L	Length [m]
$\mathcal{L}$	Laplace transform
$L_{\lambda1\to\lambda2}$	Spectral band $\lambda1$ to $\lambda2$ intensity [$W \cdot m^{-2} \cdot sr^{-1}$]
l_h	Diffusion length [m]
M	Emittance [$W \cdot m^{-2}$]
M_0	Initial, constant emittance [$W \cdot m^{-2}$]
M_λ^0	Spectral black body emittance [$W \cdot m^{-2}$]
$M_{\lambda1\to\lambda2}^0$	Spectral band $\lambda1$ to $\lambda2$ black body emittance [$W \cdot m^{-2}$]
$\overline{M}_{\lambda1\to\lambda2}$	Angular spectral band emittance [$W \cdot m^{-2}$]
M^i	Matrix of layer i
M_R^i	Matrix of TBR i
m	Optical magnification
N	Number of elements
N_C	Number of columns
N_L	Number of lines
n	Numerical
P	Total power [W]
P_e	Péclet number
P_f	Power entering into the fiber [W]
P_n	Normalized power
P_p	Power entering into the probe [W]
P_s	Power entering into the sample [W]
P_t	Power entering into the tip [W]
p	Laplace variable
Q	Quantity, Measured signal
Q_{ref}	Quantity, Signal of reference
$\boldsymbol{Q}$	Measured quantity vector
R	Electrical resistance [Ω]
R_0	Electrical resistance at the reference temperature [Ω]
R_{air}	Thermal resistance of air [$K \cdot W^{-1}$]
R_c	Thermal contact resistance [$m^2 \cdot K \cdot W^{-1}$]
R_f	Reflectivity
R_{th}	Thermal resistance [$m^2 \cdot K \cdot W^{-1}$]
R_T	Constant thermal resistance [$m^2 \cdot K \cdot W^{-1}$]
r	Radial variable [m]
r_0	Probe-sample contact radius [m]
r_f	Radius of optical fiber [m]
r_L	Radius of sample [m]
r_m	Radius of measurement area [m]

$\boldsymbol{S}_Q$	Sensitivity function of Q
S_Θ	Reduced sensitivity function of amplitude
S_ϕ	Reduced sensitivity function of phase [deg.]
T	Temperature [K]
T_0	Initial, constant temperature [K]
T_a	Ambient temperature [K]
T_C	Time constant of lock-in amplifier [s]
T_t	Temperature of probe tip [K]
T_ω	Temperature at frequency ω [K]
TBR	Thermal boundary resistance [$m^2 \cdot K \cdot W^{-1}$]
t	Time [s]
V_t	Volume of probe tip [m^3]
v	Velocity [$m \cdot s^{-1}$]
W	Width [m]
w	Laser beam radius [m]
w_0	Radius of heating area/Laser beam waist [m]
X	Moving coordinate axis [m]
$\boldsymbol{Y}$	Calculated quantity vector
Z	Thermal impedance [$K \cdot W^{-1}$]
Z_e	Identified transfer function [$K \cdot W^{-1}$]
Z_f	Thermal impedance of optical fiber [$K \cdot W^{-1}$]
Z_{ML}	Thermal impedance of multilayer material [$K \cdot W^{-1}$]
Z_p	Probe impedance [$K \cdot W^{-1}$]
Z_s	Thermal impedance of the substrate [$K \cdot W^{-1}$]
z_R	Rayleigh range [m]
x_0, y_0, z_0	Center of coordinate axis [m]
x,y,z	Coordinate axis [m]

Greek symbols

α	Hankel variable
α_R	Temperature coefficient of resistance [K^{-1}]
γ	Voltage coefficient of thermal impedance [$K \cdot W^{-1} \cdot V^{-1}$]
Δt	Sampling time interval [s]
Δx	Sampling interval in x-axis [m]
Δy	Sampling interval in y-axis [m]
ε	Emissivity coefficient
θ	Temperature in frequency domain [K]
ϑ_a	Angle of acceptance [deg.]
$\bar{\theta}$	Average temperature [K]
$\tilde{\theta}$	Hankel transform of θ [K]
λ	Wavelength [m]
ρ	Mass density [$kg \cdot m^{-3}$]
σ	Standard deviation
σ_s	Stefan-Boltzmann constant [$W \cdot m^{-2} k^{-4}$]
φ	Heat flux density [$W \cdot m^{-2}$]
φ_0	Maximum heat flux density [$W \cdot m^{-2}$]
ϕ	Temperature phase lag [deg.]
ϕ_D	Phase lag of measurement chain [deg.]
ϕ_{ref}	Phase lag of reference [deg.]
$\tilde{\phi}$	Lock-in measured phase lag [deg.]
ψ	Flux in frequency domain [$W \cdot m^{-2}$]
$\tilde{\psi}$	Hankel transform of ψ [$W \cdot m^{-2}$]
ω	Angular frequency [$rad \cdot s^{-1}$]
ω_{ref}	Angular frequency of reference [$rad \cdot s^{-1}$]

Acronyms

AFM	Atomic Force Microscopy
AOI	Angle of Incidence
A-O	Acousto-Optic Modulator
FDTR	Frequency Domain Thermoreflectance
FEM	Finite Element Method
IR	Infrared Radiation
IRD	Detector J10D-M204-R100U-60
IRD-1	Detector J15D12-M204-S500U-60
IRD-2	Detector J15D12-M204-S01M-60
KNT	Kelvin Nanotechnology
MPTR	Modulated Photothermal Radiometry
NA	Numerical Aperture
NSOM	Near-Field Scanning Optical Microscope
PPL	Phase-locked-loop
P%	Power Percentage
SEM	Scanning Electron Microscopy
SL	Sweeps per line
SPR	Scanning Photothermal Radiometry
SST	Stainless Steel
SThM	Scanning Thermal Microscopy
TBR	Thermal Boundary Resistance
TDTR	Time-Domain Thermoreflectance

Context.

Over the years, humanity has developed a variety of technologies with the aim of improving his quality of life. Along with technological progress the need for new materials that meet specific characteristics arises. In recent years, a wide range of new materials, such as, composites, advanced polymers, specialized alloys, semiconductors, optical materials, and nanomaterials, have been developed. The new generations of materials are continuously increasing their complexity and heterogeneous nature. The need of new materials with enhanced thermal properties for a wide range of applications where a key performance parameter is thermal conductivity is one of the reasons. Moreover, assessment of heat transfer at the microscale permits to understand and design the thermal behavior of different kinds of systems like microelectronic or micro-electro-mechanical devices with effective properties of composite materials.

The thermal parameters (diffusivity, thermal resistance of interfaces, and thermal conductivity) of heterogeneous materials at very small scale are difficult to measure. It is an essential and challenging task that requires suitable methods involving both high spatial resolution and sensitivity. This is at the core of the developments performed in our team at I2M.

Several contact and contactless techniques have been implemented and improved in the team such as the Scanning Thermal Microscopy (SThM) in 3-ω mode, the Modulated Photothermal Radiometry (MPTR) and the Periodic Pulsed phothermal Radiometry (PPTR). These techniques are efficient for the thermal characterization of either thin layers or nanostructured materials and devices. The SThM technique is suitable with low temperature characterization (from 4K up to 400 K) whereas the photothermal techniques are more suitable with the high temperature range investigations (from 300K up to 1300 K). All those techniques can be implemented to perform imaging.

The scan of the probe on the material surface in the SThM leads to either a temperature or a thermal conductivity mapping. The dimension of the investigated area is of some micrometers. The SThM has been widely used and developed in the laboratory using mainly the 3-ω mode. Different applications have been proposed: nanowires, composite materials, microelectronic devices. The influence of thermal resistances at interfaces can be achieved with a high spatial resolution (less than 1 µm). In fact, the SThM offers the best spatial resolution among other thermal measurement techniques. Nevertheless, there are several limitations linked to the tip-sample contact. This contact is the main factor that limits the heat flux in the instigated surface and therefore the sensitivity of the technique to the range of insulators. Another limiting factor is the significant thermal inertia of the SThM probes that limits its application only to low frequency ranges.

The thermoreflectance can also be implemented to perform imaging of the surface using a CCD camera. As well, the IR thermography can be associated to a photothermal excitation to perform a thermal imaging of the surface. In both cases, the spatial resolution is limited by the pixel size and the diffraction of light (VIS for the thermoreflectance and IR for the thermography). The sensitivity of the thermoreflectance is at least three orders of magnitude lower than that of

thermography. On the other hand, the modulated photothermal thermography is limited in frequency to some kHz.

The main objective of the present work is the design, development and validation of a new scanning setup that would give access to the thermal analysis at the microscale at high frequencies, beyond those allowed from the SThM or infrared thermography. Figure 1.1 shows the limits in time and space of the current thermal characterization techniques and the region we are aiming to cover with our new development. In next chapters the experimental setup will be described as well as its application on several samples to evaluate the capabilities of the developed technique.

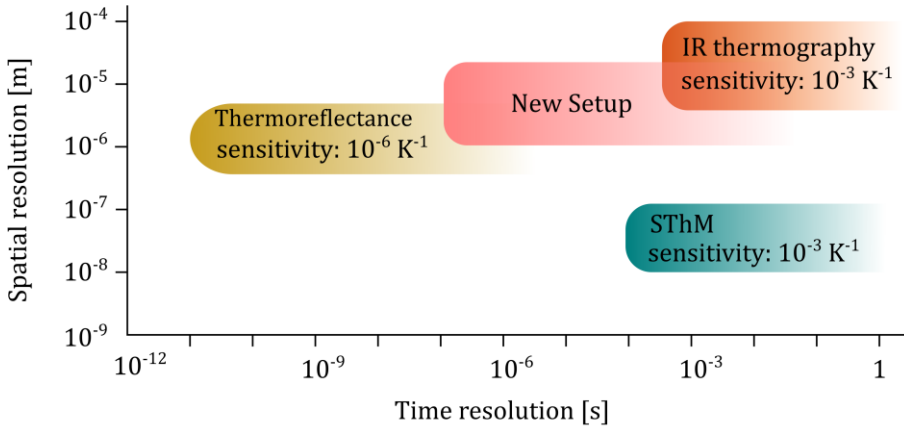

Figure 1.1. Time and spatial resolution of current techniques for thermal imaging.

In chapter 1, the state of the art of the techniques used for thermal characterization at the microscale is presented. We will review the main well-known techniques of thermal imaging as well. We will examine both the advantages and drawbacks of existing methods. The methods can be categorized in two specific well-known groups: the contact and contactless methods. In the group of contact methods, the SThM will be presented. Within the group of the contactless methods we will present the thermoreflectance and the photothermal radiometry. The imaging techniques in thermoreflectance and thermography will be particularly considered with respect to the aim of the present work that is the modulated photothermal scanning.

In chapter 2 we will present two different scanning experiments, the first one is a contact measurement whereas the second one is a contactless method. Both techniques are based on the modulated photothermal radiometry as sensing principle. The self-emission subsequent to the periodic photothermal excitation on an opaque surface is sensed with an infrared mono detector. The first part of the chapter will be dedicated to the scanning experiment in contact mode. In this experiment we use a home developed probe based on the use of an optical fiber. This fiber allows both to supply the modulated laser beam and to collect the IR emitted by a small transducer attached at the fiber extremity. The idea behind this probe is to generate and monitor the temperature change in a small volume at the end of the fiber working as heater and sensor at the same time. The full experimental setup will be presented followed by its application and model identification. In this configuration we obtained reliable results regarding the differentiation between two different materials but its application remains at low frequency. Indeed, although the basic principle is simple, its practical implementation yields major technical challenges

regarding mainly the contact conditions during the scan. Therefore, we decided to reduce the number or unknown variables involved within such an experiment and to change to a contactless technique. We think however that this contact method could be improved in the future and this is the raison why we reported the results we obtained using this technique. In the second part of the chapter, the scanning experiment in contactless mode will be detailed. In the contactless experiment of scanning photothermal radiometry (SPR) we replace the optical fiber probe by a Cassegrain microscope objective. The microscope objective allows to focus the laser beam directly over the sample and collect the IR emitted by the surface. In this configuration we will manage the formation of two concentric areas over the sample surface namely: the heating area and the measurement area; whose characterization will be presented in this section as well as the definition of the scanning parameters. Several configurations have been tested to assess the spatial resolution and the sensitivity to the thermal properties of the sample. Since the technique presents remarkable results at the high frequency regime with high spatial resolution, this experiment appears as a very efficient complementary tool to the classical IR thermography.

In chapter 3 we will focus on the mathematical model that describes the heat transfer process in the sample under investigation within the experimental conditions presented in chapter 2. The analysis of the experiments in contactless mode will be done assuming the sample is an opaque material and the photothermal excitation is absorbed on its surface. In this chapter, we will show that the velocity used in the experiment is too slow to significantly modify the heat diffusion profile in the investigated medium. Therefore, the amplitude and phase at the aimed by the IR detector area can be calculated with the model for motionless conditions. Thus, the modulated laser can be modeled as a boundary heat source at the sample surface. The simulated quantities (amplitude and phase) will be compared with the experimental results in the parameter identification process using an inverse procedure that will be described at the end of the chapter. To verify the correct operation of the SPR setup and to validate the experimental assumptions, measurements will be performed on a known stainless-steel bulk sample. The sample will behave as a semi-infinite medium submitted to a Gaussian heat flux on its surface and the analytical solution for the measured temperature will be derived. The calculated temperature produced by a Gaussian heat flux will be compared with the ones obtained considering a uniform and point heat flux. In addition, the analytical solution for the semi-infinite media in static conditions will be compared with the numerical model for the semi-infinite media that moves at constant velocity with respect to the photothermal source. This numerical solution will be obtained from the finite element method (FEM) using the Comsol Multiphysics software. Then, an analytical solution for the multilayer sample will be presented. This model is developed in order to simulate the behavior of the 3-ω sample in static condition and verify the correct operation of the SPR before the scanning. Indeed, in the high frequency regime the stack of layers cannot be treated as a thermal resistance as it is the case at the low frequency regime.

In chapter 4 we will present the SPR application to several configurations of sample to assess the performance and capabilities of the technique. Due to the type of application addressed, the chapter will be divided into two segments: motionless experiments and scanning experiments. The interest of motionless experiments is to compare the results of the new setup with the results from known measurements like the Hot Disk and the 3-ω setup in order to assess the performance of the SPR before passing to the image acquisition in the scanning mode and to validate the obtained data. Thus, the new experimental setup will be used on a steel bulk sample, previously

characterized with commercial Hot Disk in order to validate the experimental configuration and signal processing. In this configuration, we will show how the experimental parameters affect the measurements and the conditions required to obtain reliable results. Then, the motionless configuration will be applied on a multilayer thin strip typically used in the 3-ω method for thermal characterization of thin films. We will present the results obtained using the 3-ω mode and we will face them to the results obtained from the SPR in motionless configuration. The film under investigation is a chalcogenide alloy used in phase change memory devices. In the scanning experiment application, we will first present the characterization of an interface perpendicular to the surface formed by the mechanical junction of two pieces of steel. We will show that the SPR measurement allows to reach the quantitative estimation of the thermal boundary resistance at this interface. Then, we will present an application of the SPR to the 3-ω sample that was used in the static mode already. Finally, we will show an application of the SPR to the thermal surface imaging of composite samples to assess the capability of the technique in terms of spatial accuracy. Obviously, all those experiments, and mainly the ones realized in scanning, illustrate the capability of such SPR experiment to deal with configurations where the classical imaging by thermography is difficult to implement in terms of the high frequency resolution.

Finally, in chapter 5, we will present the general conclusion of this work and we will present also some arising perspectives.

Chapter 1:
Thermal Characterization at Microscale.

1.1 Introduction.

During last years, the continuous effort to improve the energy efficiency drives the development of new micro-structured materials. The miniaturization of electronic and optoelectronic devices and the increasing switching speeds involve exasperated localized heating problems. Steady-state and transient characterization of temperature distribution in devices and interconnects is important for performance and reliability analysis. Thus, being able to engineer the thermal properties, as the thermal conductivity, is an important part of the material development effort.

Furthermore, the thermal parameters (diffusivity, thermal resistance of interfaces and thermal conductivity) of inhomogeneous materials are of special importance in the application field of the composites [1], [2]. Thus, measurement of thermal properties at the microscale is an essential and challenging task that requires suitable experimental methods.

Following the miniaturization of the technology, the thermal characterization techniques of materials at micron and sub micrometric scales has been extensively studied and improved during the last years for a wide range of applications from building thermal insulation [3], [4] to microelectronic applications [5]. These techniques have different spatial, thermal, and temporal resolutions, and can be used for absolute or relative measurements.

In this chapter we give an overview of the main well-known techniques for thermal imaging. We present both the advantages and drawbacks of the existing methods. The methods are classified in two main groups: the contact and contactless methods. In the group of contact methods the SThM, is presented. Within the group of the contactless methods we present the thermoreflectance and the photothermal radiometry. The imaging techniques by thermoreflectance and thermography will be particularly considered with respect to the aim of the present work that is the modulated photothermal radiometry in scanning mode.

1.2 Techniques for imaging temperature and thermal properties at the microscale.

1.2.1 Scanning Thermal Microscopy (SThM).

The SThM is a contact technique providing measurements of either the temperature or the thermal properties at a sample surface with high spatial resolution (< 1 µm). The first application of the method was the scanning thermal profile presented in 1986 by Williams and Wickramasinghe [6]. This technique for surface profiling is based upon a near-field thermal interaction between a heated tip and the surface. A small thermocouple was embedded at the tip of the probe with dimensions about 100 nm. The temperature-dependent voltage generated by the junction was then used as the feedback mechanism to control the tip–sample distance. In this way, the surface topography was obtained. The same experimental setup was used for temperature mapping with submicron spatial resolution. However, since the feedback signal is based on maintaining a constant probe temperature, it is difficult to separate the temperature

from topographical variations. To overcome this problem, Majumdar et al. [7] built in 1993 a SThM based on AFM configuration using tip-surface force as a feedback signal and replacing the commercial AFM-cantilever by a handmade cantilever equipped with a sharp K-type thermocouple junction at the tip. Since this new cantilever is equipped with a thermal sensor, SThM provides simultaneously topographical and thermal measurements with a high spatial resolution. This, on AFM based solution, become the standard configuration for the most of actual SThM devices.

Figure 1.1 shows a schematic diagram of a typical SThM which is basically an AFM with an extra thermal module composed of a thermal sensor and the thermal control unit. An AFM uses a cantilever with small sharp probe tip at the end. The cantilever is mounted on *z*-stage to control the distance and contact force between the tip and the sample while an additional *xy*-stage is used to control the surface scanning. The tip-sample contact force is determined through the deflection of the cantilever. A laser beam is reflected by the cantilever to a sensitive photodetector and the change in the position of the reflected spot on the photodiode is related to the cantilever bending. With the cantilever deflection and the known value of the cantilever spring constant the contact force is determined. For the SThM operation mode, the probe is equipped with a thermal sensor at the tip connected to a thermal module which manages the sensor information and provides thermal image. The probe is the fundamental part of the SThM since its shape and behavior determine the quality of the measurements. The probe acts as the heater and the temperature sensor at the same time. Those measurements are based on the temperature dependence of the electrical resistance of the sensor. The electrical resistance is function of the temperature change as:

$$R = R_0(1 + \alpha_R \Delta T) \tag{1.1}$$

Where α_R is the temperature coefficient of the electrical resistance and R_0 is the electric resistance at the reference temperature.

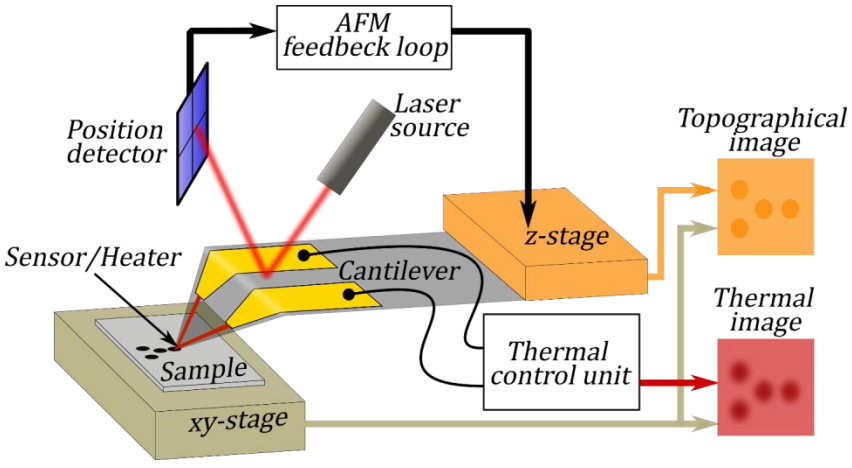

Figure 1.1: Schematic diagram of typical AFM based SThM.

The first thermal probe was presented in 1994 [8], [9]. It was made from Wollaston wire of 5µm diameter platinum-rhodium (Pt_{90}/Rh_{10}) core surrounded by 75 µm silver shell. The wire was bent into a V-shape cantilever and the tip was electrochemically etched to expose a 200 µm segment of the platinum alloy core. The cantilever is mounted on a carrier and an aluminum tape was

attached to the cantilever arms as a mirror that reflects the laser beam onto a photodetector to follow the cantilever deflection. These micrometric dimensions lead to a spatial resolution of the order of several hundreds of nanometers.

In order to improve the spatial resolution, the shrinking size thermal probes were developed. The fabrication process was originally dedicated to the thermocouple probes [10] but it was used for the resistive ones [11]. The cantilever of these micro-fabricated probes is a ~400 nm thick plate of silicon oxide (SiO_2) or silicon nitride (SiNx) with a sharp, bent tip. The sensing and heating element is made of a thin palladium (Pd) ribbon near the apex of the tip. Commercial probes with Pd as core element, produced by Kelvin Nanotechnology (KNT) achieved sub-100 nm spatial resolution and 0.1 K temperature resolution. Thermal probes based on semiconductors for SThM applications are also available. The probe is a U-shaped cantilever with high-doped silicon (Si) legs and a low-doped curved part. This part is the sensor and heater with a tip radius around 10 nm. Figure 1.2 shows three types of thermoresistive probes.

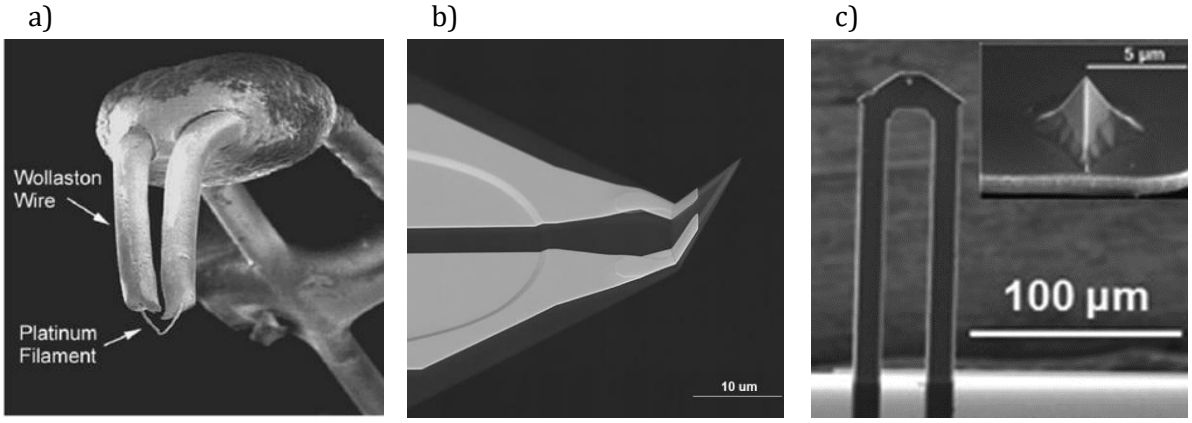

Figure 1.2: SEM image of thermoresistive probes: (a) Wollaston wire probe [12], (b) KNT probe [13] and (c) Doped Si probe [14].

In the last decades, different types of probes have been developed in order to improve the capability of the SThM technique in different fields. Additionally to the variation in electrical resistance and Seebeck thermovoltage, thermal probe sensing mechanism such as fluorescence or thermal expansion heave been tested [15]–[17].

Table 1.1 presents a comparison between common SThM probe types, and detailed analysis of the works done in SThM field and evolution from its invention until now, can be found in [18]–[22].

Probe	Thermoresistive probes			Thermovoltage-based probes	Fluorescent probes
Thermal sensor	Pt/Rh	Pd	Doped Si	Chromel-alumel Au-Cr Pt-Cr Au-Ni	Er/Yb codoped fluoride glass
Operation principle	Electrical resistance			Seebeck effect	Optical
Operation mode	Active/Passive			Active/Passive	Active/Passive
Tip radius [nm]	>1000	25-100	10-20	<100	≈200

Probe	Thermoresistive probes	Thermovoltage-based probes	Fluorescent probes	Probe	Thermoresistive probes
Lateral spatial resolution [nm]	>500	<100	<100	<100	<200
Temperature resolution [mK]	500	12	7	15	—
Thermal time constant [μs]	≈200	100-700	400	≈150	—
Thermal sensitivity	—	0.18 [K μW^{-1}]	2 [$\mu K\ Hz^{0.5}$]	1.06 [KμW^{-1}]	0.5 [K^{-1}]
Effective sample k range [$Wm^{-1}K^{-1}$]	0.1-10	0.01-10	0.01-10	—	—
Maximum operating temperature [°C]	200	160	1000	800	50
Example works		[23]–[31]		[32]–[36]	[37]–[40]

Table 1.1: Comparison of different thermal probes [18].

Although several probes with different physical principles have been studied since the first presentation of SThM, most of them have an extremely difficult fabrication process and had been produced as a prototype in specialized laboratories. Only thermoresistive probes are commercially available and are quite expensive.

The SThM with thermoresistive probe can operate in two basic modes: the passive mode, also called the temperature contrast mode and the active mode, also called the conductivity contrast mode. In the first case, the probe acts just as a thermometer. On the other hand, in the active mode the probe senses the thermal transport between the probe and the sample, therefore the probe temperature changes depending on the thermal properties of the sample. This allows the estimation of the thermal conductivity of the sample material.

The SThM technique can be implemented within DC or AC modes. The 3-ω method is a popular active mode technique that have been used in the SThM measurements [41]–[44]. It was shown that using the 3-ω method leads to more accurate results. In the experiment, a modulated current with frequency ω is sent through the metallic strip. This leads to Joule effect that generates a heat flux into the strip and leads to a temperature rise with frequency 2ω. Finally, the temperature variation change appears in the voltage at 3-ω frequency. The method takes advantage of the lock-in amplifier to measure the third harmonic component of the voltage on the strip. Furthermore, apart from the amplitude, the 3-ω method gives an insight into the phase of the alternating component of the voltage across the tip which has dependence on the thermophysical properties of the sample material [45].

The accuracy and sensitivity of SThM technique depend on the interaction between the probe tip and the sample surface. Figure 1.3(a) illustrates the probe-sample interaction and the thermal resistance network which can be associated. In this representation the total heat power generated by Joule effect, P, is introduced in the resistance network as a current source. One can identify that the heat flux generated at the probe-tip is dissipated in two main ways. The first one, P_s, is the power going from tip to the sample through thermal resistance R_c and the sample thermal

impedance Z_s. The second one, P_p, is going to the probe itself and the surroundings through the probe thermal impedance Z_p.

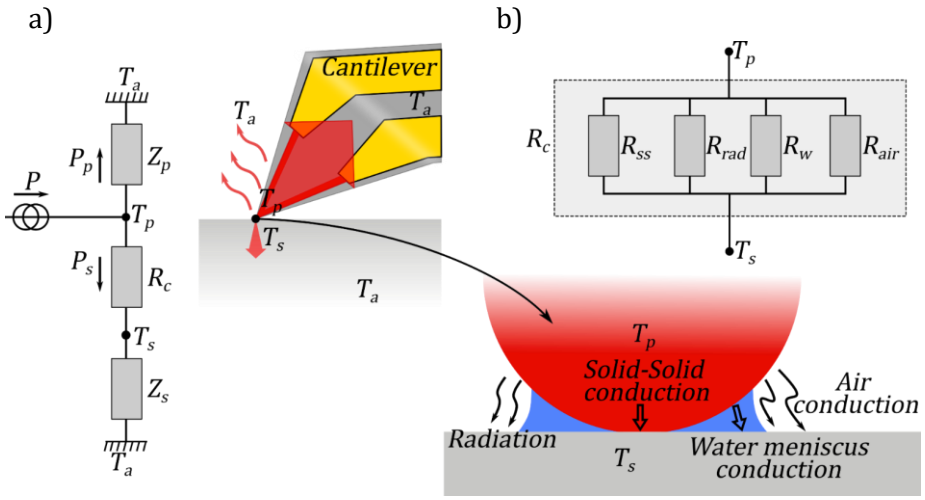

Figure 1.3: Schematic representation of the probe-sample interaction. (a) Probe-Sample flux distribution. (b) Tip-sample interactions.

If P is the total heat power applied to the probe, the flux distribution in function of the tip temperature is expressed as:

$$P = P_s + P_p = T_p \left(\frac{1}{R_c + Z_s} + \frac{1}{Z_p} \right) \tag{1.2}$$

From the previous equation one can deduce that to maximize the flux going to the sample the thermal impedance of the probe must be high. Additionally, one can remark that R_c limits the effective sensitivity of the study, because in the case where the sample impedance is lower the effective flux will be determined by the contact resistance. Therefore, the thermal design of the probes is extremely important for the SThM performances.

A Wollaston wire probes calibration study by Lefèvre [46], shows that approximately 80%-90% of the flux generated by the probe diffuses into the probe itself and is not transmitted into the sample even for those with high thermal conductivity. With the KNT probes this value increases to 90%–99% [27] and similar behavior was found for Si-doped probes [23]. The low sensitivity range to the sample thermal conductivity is shown in Figure 1.4. This low sensitivity represents the main practical drawback of the SThM measurement technique.

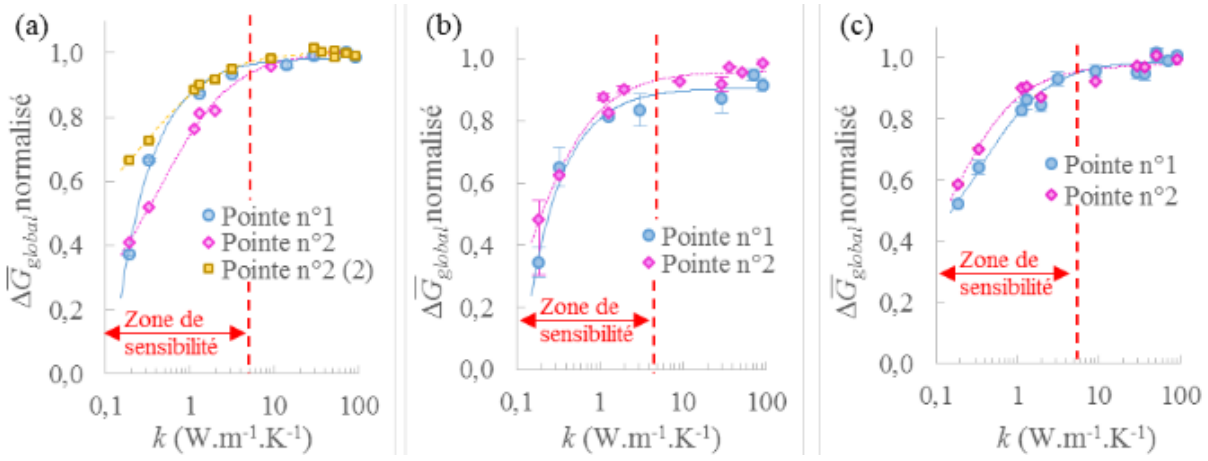

Figure 1.4: Normalized, thermal conductivity calibration curves for SThM (a) Wollaston wire, (b) KNT and (c) doped Si tips [23].

The thermal resistance R_c is a simplification of the more complex phenomena of heat transport which take place at nanoscale in the contact region (tip-sample) whose full description remains under study. However, R_c, is a well-adapted simplification in metrological applications that accounts for several contributions:

R_{ss} : The thermal solid-solid contact resistance including both the heat flux constriction resistance and the resistance related to phonon scattering at the probe-tip interface.

R_{rad} : The thermal resistance linked to the heat transfer by radiation.

R_w : The thermal resistance related to the heat transfer through the water meniscus that cannot be avoided when working under ambient atmosphere.

R_{air} : The thermal resistance linked to the heat transfer by diffusion in the surrounding air.

Because of the complexity involved in the contact resistance, it is important to perform a careful calibration of the probe in conditions as close as possible to the conditions of the final application. In addition, one must remember that the probe wears during measurements, therefore a good manner to do is comparing the results obtained for at least on the reference sample at the beginning and at the end of measurements.

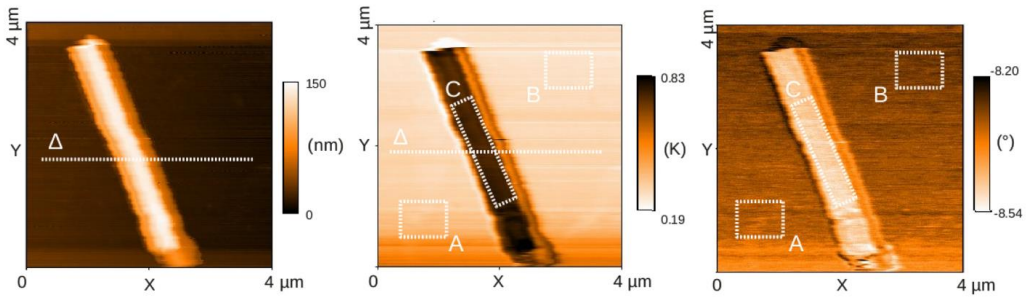

Figure 1.5: Topography AFM (left); amplitude (center) and phase (right) measured at 871 Hz (SThM 3-ω) on a Sb_2Te_3 nanowire [47].

In [47] the transverse thermal conductivity of a 150 nm thick and 850 nm in width Sb_2Te_3 nanowire is measured using SThM in the 3-ω mode (Figure 1.5). The contact parameters, in terms of contact resistance and contact area radius, were determined in a specific calibration configuration and the values found were assumed not to vary within the nanowire study. The measured thermal conductivity at room temperature was found to be in good agreement with that of the bulk, since the nanowire characteristic dimension in the diffusion direction is larger than the phonon mean free path.

In [48] the same approach was used to measure the thermal resistance along the thickness of In_3SbTe_2 crystalline nanowires on a SiO_2/Si substrate. Two nanowires of 13 nm and 23 nm thicknesses and 80 nm and 100 nm in width respectively were investigated. The topographic and thermal images are shown in Figure 1.6. The estimated thermal resistance of nanowires is 5 times higher than that obtained from the value of the bulk material. This is explained by the expected phonon confinement along the nanowires thickness. It is shown that phonon mean free path in In_3SbTe_2 is comparable to the thickness of the studied nanowires.

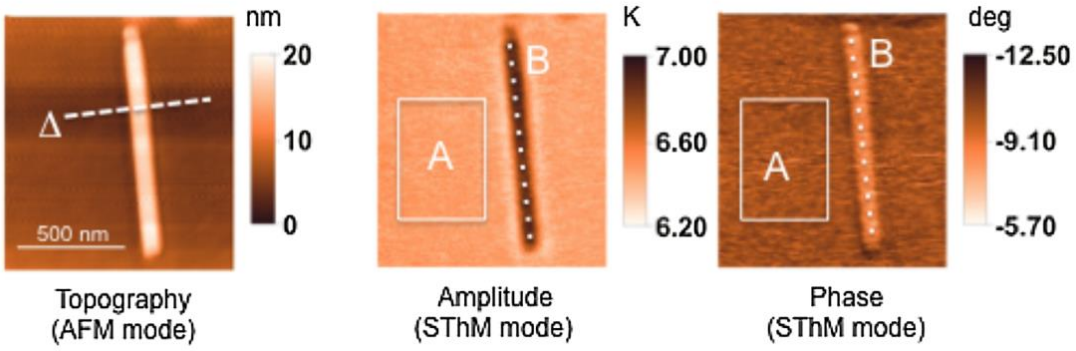

Figure 1.6: Topography (AFM), amplitude and phase measured at 523 Hz (SThM 3-ω) on an In_3SbTe_2 crystalline nanowire.

SThM in 3-ω mode was also used in [49] on a silica fiber/regenerative laminar pyrocarbon matrix composite in order to provide an insight into the effective thermal conductivity of pyrocarbon as well as the thermal boundary resistance (TBR) at the interface between the fiber and the matrix (Figure 1.7-a). The authors measured an effective thermal conductivity of the pyrocarbon matrix of 20.18 $W \cdot m^{-1} \cdot K^{-1}$. In addition, it could be observed the temperature rise due the TBR when scanning across the fiber matrix interface (Figure 1.7-b) providing a way for identification of the TBR.

a)

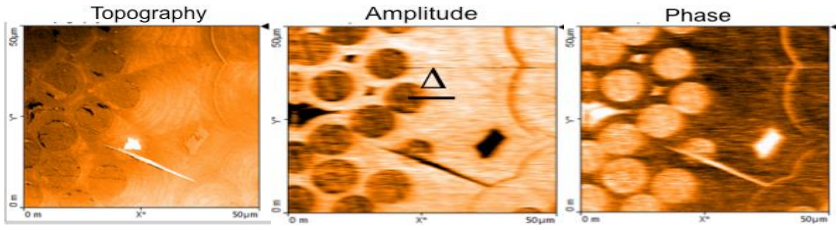

b)

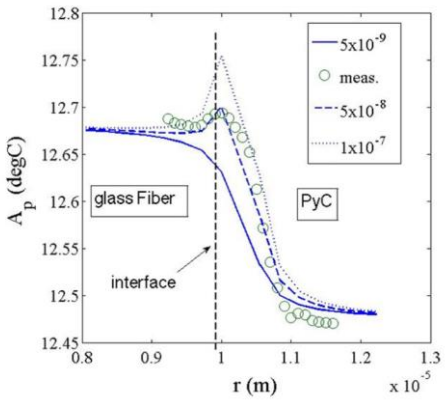

Figure 1.7: (a) Topography (AFM mode), amplitude and phase (SThM 3-ω mode) measured at 1125 Hz on a silica fiber/pyrocarbon composite. Contact radius of 100 nm and Rc=7.83 × 10^{-8} K·m^2· W^{-1}. (b) Effective Thermal Boundary Resistance from scan line Δ (TBR=5 × 10^{-8}) [49].

1.2.2 Thermoreflectance.

1.2.2.1 Principle.

The thermoreflectance is a popular contactless technique for thermal characterization of materials. It is based on the temperature dependence of the sample surface reflectivity. Originally used to measure the thermal diffusivity of thin metallic films [50], the technique has been applied to measure thermal properties of bulk samples [51] and TBR between different materials [52]–[57]. In the thermoreflectance method, a frequency modulated laser, or a pulsed laser, is used to disturb the sample temperature which is usually called pump beam. The sample temperature change is detected by monitoring the variation in the reflectance of a second laser, the called probe beam. Typically, the sample surface is covered with a thin metallic layer called transducer in order to ensure the absorption of the pump beam at the sample surface as shown in Figure 1.8. Gold or aluminum are usually used as transducer materials.

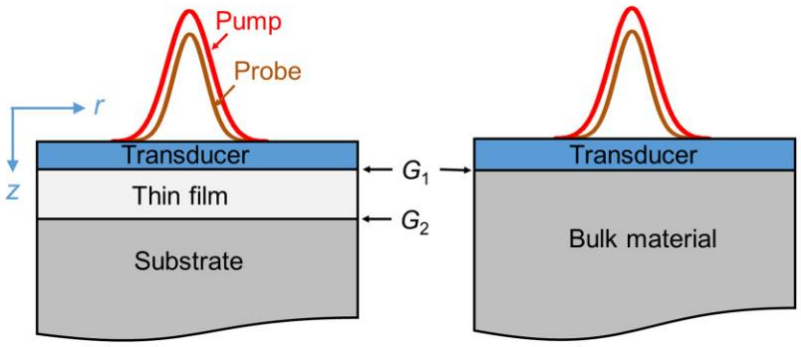

Figure 1.8: Typical sample configurations of thin film and bulk materials measured using the thermoreflectance technique [58].

The pump beam is absorbed by the transducer and this leds to the temperature rise into the sample. This induced temperature modifies the optical properties of the sample surface introducing the reflectivity variation $\Delta R_f/R_f$. For a temperature variation in the range of few degrees the transducer reflectivity change is linear and are related to the temperature change ΔT as:

$$\frac{\Delta R_f}{R_f} = \left(\frac{1}{R_f}\frac{\partial R_f}{\partial T}\right)\Delta T \tag{1.3}$$

A scheme of typical experimental setup of the time-domain thermoreflectance (TDTR) is presented in Figure 1.9. In this configuration, a high-energy picosecond or femtosecond laser produces a very short pulse with high frequency repetition rate. The laser is split into a pump beam with high energy and a probe beam with low energy. The probe is continuously delayed from the pump in nanosecond time range to measure the time evolution of the temperature variation of the sample resulting from the pump pulse. The probe is modulated at low frequency what allows the accurate extraction of the measured periodic change of the surface reflectivity using a lock-in amplifier that measure the voltage drop at the photodiode. Pump and probe beams have generally the same diameter and are superposed at the sample surface. The spatial resolution of thermoreflectance is limited by the diffraction of the probe beam, which is of order of its half wavelength. The temporal resolution is determined by the bandwidth of the detection system and the duration of the optical excitation.

An aditional configuration of thermoreflectance technique is the frequency domain thermoreflectance (FDTR). In this configuration the thermoreflectance signal is collected as a function of the modulated frequency of the pump beam instead of monitoring the signal as a function of the time delay between the pump and probe pulses. FDTR is easier to implement because it avoids the complexity induced by the time delay between the laser beams and it can use less expensive CW laser sources. TDTR can also be implemented as FDTR by holding the delay stage at a fixed location [59].

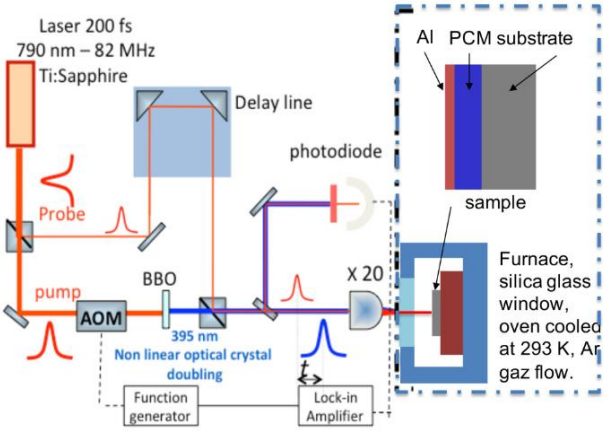

Figure 1.9: Scheme of TDTR experimental setup [60].

During the last decades, the thermoreflectance technique has been largely improved to allow the measurement of multiple thermal transport properties: in-plane and out-of-plane thermal conductivity [61]–[63], heat capacity [64]–[67] and thermal boundary resistance of interfaces [68]–[70]. Nevertheless, the TDTR is still subject of some drawbacks, such as the need of metal transducer layer and the smooth surfaces required to perform optimal measurements. In addition, the temperature sensitivity of the method is quite low compared to other techniques.

1.2.2.2 Imaging.

Thermoreflectance technique allows the acquisition of thermal images by three different approaches: The point scanning thermoreflectance technique [71]–[73], the CCD imaging thermoreflectance technique [74]–[77] and the laser scanning thermoreflectance technique [78]. The first one uses a focused laser source and a photodiode as detector coupled with a lock-in amplifier and the device under test is moved using a micrometric translation stage. A measurement is made at each scanned position. The second technique uses a diffuse light source to illuminate the whole surface of the device, and a CCD camera is used as a detector. Finally, the third technique uses a fast scanner made of two galvanometric mirrors, which enable to sweep a focused laser light on the device under test. Like in the point scanning thermoreflectance, the detector is made of a photodiode. A lock-in amplifier is used that yield in a good sensitivity but with the difference that in this technique it is the laser that is being rapidly moved using the fast scanner. The schematic representation of CCD imaging thermoreflectance and laser scanning thermoreflectance is presented in Figure 1.10. A comparison between the three techniques is presented in Table 1.2

a) b)

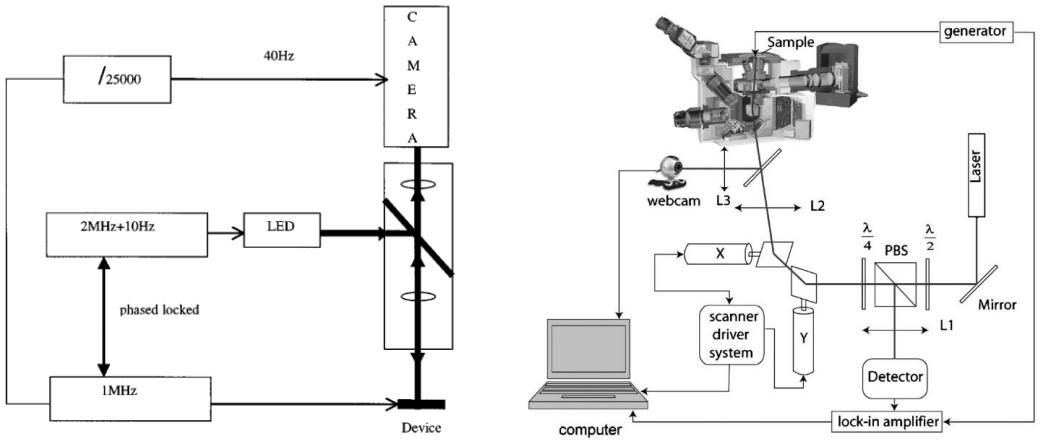

Figure 1.10: Scheme of a) CCD image thermoreflectance setup [76] and b) Scanning thermoreflectance microscopy setup [78].

Evaluated parameter	CCD technique	Point scanning measurement	Laser scanning technique
Measurement time by point [s]	0.1×10^{-6}	1	0.2×10^{-3}
Spatial resolution [nm]	Diffraction limit ~300	Limited by minimal scan step	Diffraction limit ~300
$\Delta R_f/R_f$ sensitivity	5×10^{-4}	10^{-6}	10^{-5}

Table 1.2 Performances of thermoreflectance techniques [78].

Figure 1.11 show the $\Delta R_f/R_f$ amplitude image obtained with the laser scanning thermoreflectance technique from a sample composed of nine 0.35 µm width resistors with a 0.8 µm distance between two consecutive resistors. The line cross section (A'-B') is plotted in Figure 1.11-b where it is possible to distinguish nine spikes corresponding to nine resistors.

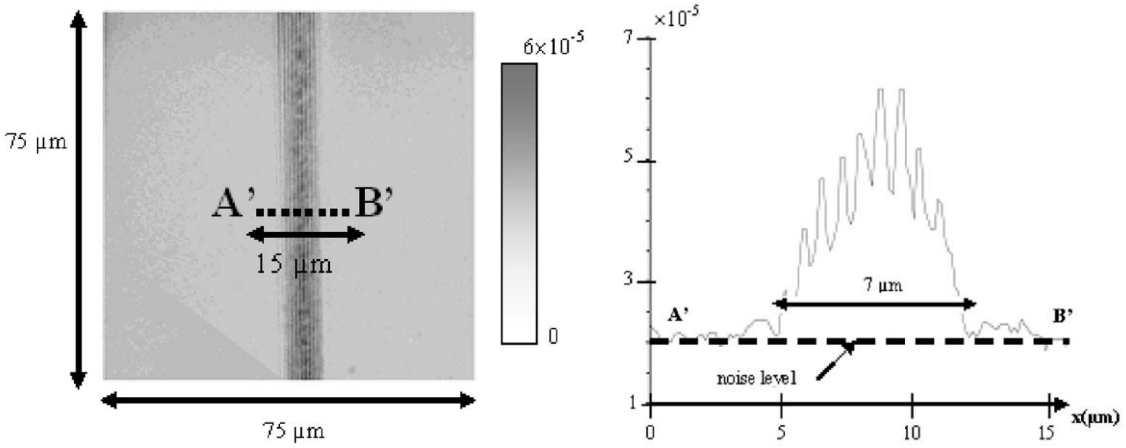

Figure 1.11: $\Delta R/R$ thermoreflectance image of sample with pixel size of 150 nm [78].

In [79] TDTR in point scanning configuration was used to image ~3 nm thick patterned titanium under 100 nm of gold on a silicon substrate (Figure 1.12-a). From phase images at six different modulation frequencies (Figure 1.12-b) the maps of thermal interface conductance between the gold film and the silicon substrate and the substrate thermal conductivity with a pixel size of 0.5 µm, are obtained (Figure 1.13).

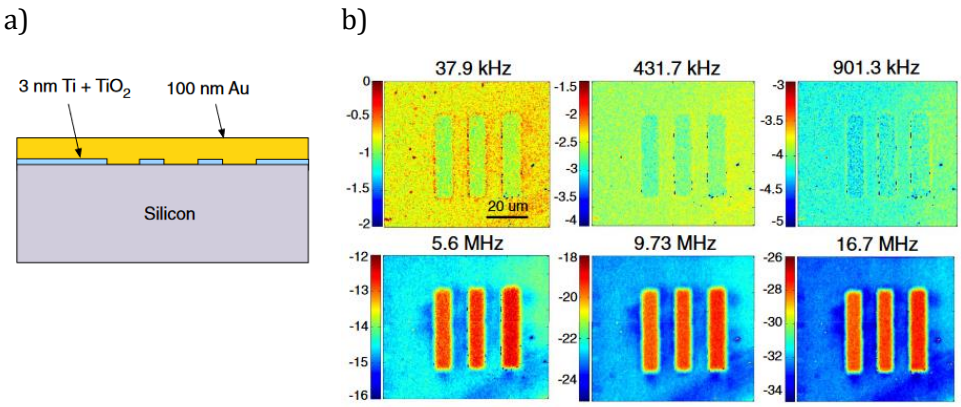

Figure 1.12: TDTR in point scanning configuration applied to patterned titanium-gold on a silicon substrate: a) scheme of the sample, b) phase images acquired at the six modulation frequencies [79].

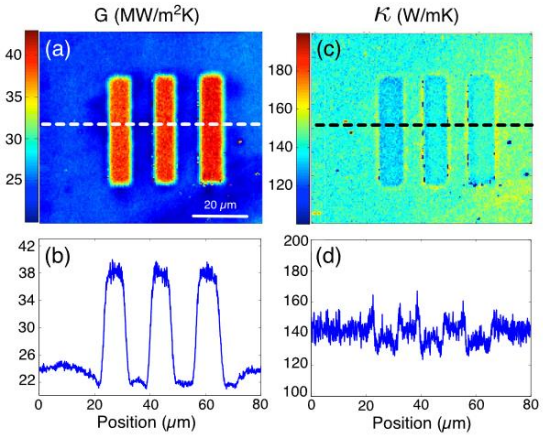

Figure 1.13: Results obtained from TDTR measurements presented in Figure 1.12: (a) Thermal interface conductance map. (b) Conductance across the path shown by the dashed line in (a). (c) Substrate thermal conductivity map. (d) Substrate thermal conductivity across the path shown by the dashed line in (c) [79].

1.2.3 Photothermal radiometry.

1.2.3.1 Principle.

Photothermal radiometry is a contactless thermal measurement technique originally proposed by Cowan [80] and fully developed by Nordal in 1979 [81]. It is based on the use of infrared detectors to measure the infrared radiation emitted by a surface in response to a transient

photothermal excitation. All bodies at a temperature higher than the absolute zero emit electromagnetic radiation due to the thermal agitation of charges in matter. The emitted thermal radiation is a function of the surface temperature T and is expressed according to the Stefan-Boltzmann law as:

$$M = \varepsilon\sigma T^4$$

where $\sigma_s = 5.67 \times 10^{-8}$ W·m^{-2}·K^{-4} is the Stefan-Boltzmann constant and ε is the emissivity of the surface. If the temperature variation is small enough one can stablish a linearized relationship between temperature and emitted radiation variation as:

$$\Delta M = 4\varepsilon\sigma T_0^3 \Delta T_\omega \tag{1.4}$$

Where T_0 expresses the constant increase of temperature and ΔT_ω is the periodic variation of the temperature. The spatial distribution of the excitation can be uniform or with a more complex form (Gaussian, for example)[82], [83]. In addition the flux excitation can be modulated [84] to perform the study in frequency domain of pulsed [85] to perform analysis in time domain. Figure 1.14 shows a typical configuration of the modulated photothermal radiometry (MPTR).

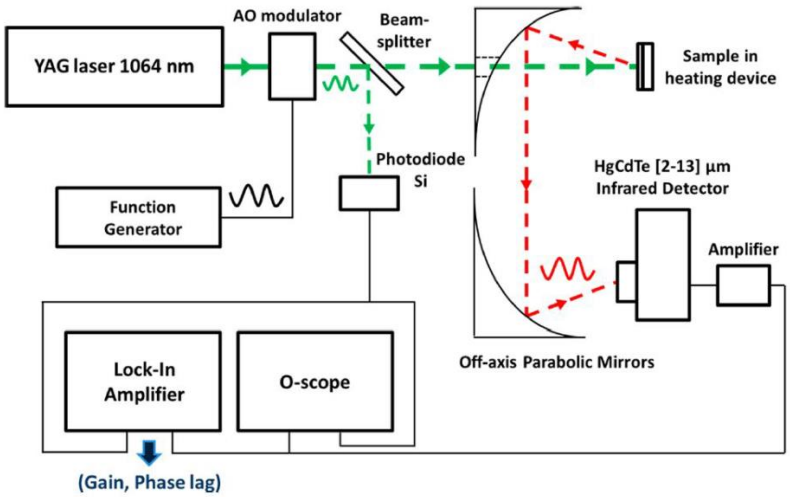

Figure 1.14 Scheme of MPTR setup.

The MPTR method has been extensively improved for both the experimental [86], [87] and theoretical [88]–[93] aspects and have been used for thermal characterization of bulk or thin films. The sample is usually capped with an additional transducer layer that improves the absorption and the emittance of the surface. In our Lab, the method has been used to measure the temperature dependent thermal conductivity of several chalcogenide alloys: $Ge_2Sb_2Te_5$ (GST) [94], GeTe [95] C-doped GeTe [96]. It has been also used to investigate the thermal boundary resistance at the SiO_2–GST interface and the role of Ti at the interface between TiN and GST [57].

The MPTR is based on monitoring the infrared radiation emitted from the sample surface consequently to a transient photothermal excitation. Considering a periodic heat flux φ, that is applied at the sample surface, initially in thermal equilibrium at temperature T_0, the heat flux is absorbed at the surface leading to a temperature variation into the sample. If one defines the periodic heat flux with frequency ω as:

$$\varphi = \varphi_0 cos(\omega t) \tag{1.5}$$

the temperature increase of the sample is expressed as:

$$\Delta T = \Delta T_0 + \Delta T_\omega cos(\omega t + \phi) \tag{1.6}$$

With ΔT_ω at the same frequency ω but with a phase lag ϕ induced by the thermal inertia of the sample. In this way, the sample temperature can be expressed as:

$$T = T_{\Delta 0} + \Delta T_\omega cos(\omega t + \phi) \tag{1.7}$$

where, $T_{\Delta 0} = T_0 + \Delta T_0$ is the new constant component in the sample temperature.

The emittance from the sample is thus expressed as:

$$M = M_0 + \Delta M = \varepsilon\sigma\left(T_{\Delta 0} + \Delta T_\omega cos(\omega t + \phi)\right)^4 \tag{1.8}$$

Assuming a weak enough disturbance φ, to produce a small temperature increase, the variation of the emitted radiation can be linearized as:

$$\Delta M \approx 4\varepsilon\sigma T_{\Delta 0}^3 \, \Delta T_\omega \cos(\omega t + \phi) \tag{1.9}$$

where the emittance is proportional to the temperature oscillation:

$$\Delta M \propto \Delta T_\omega \tag{1.10}$$

at the same frequency ω, and with the same phase lag ϕ.

In this way, it is possible to monitor the sample surface temperature variation, ΔT_ω, by measuring the radiant emittance ΔM from the excited surface with an infrared detector.

The modulated photothermal radiometry take advantage of the lock in amplifier to measure the amplitude $A(\omega)$ and the phase $\phi(\omega)$ from the signal captured by the infrared detector. In a general manner, the signal from the infrared detector $Q(\omega)$, measured by the lock-in in frequency domain can be expressed as:

$$Q(\omega) = A(\omega)e^{j\phi(\omega)} \tag{1.11}$$

where the amplitude of the signal, $A(\omega)$, is proportional to the emittance amplitude and thus, to the sample temperature variation:

$$A(\omega) \propto \Delta T_\omega \tag{1.12}$$

and the phase of the signal $\phi(\omega)$, is the delay introduced by the thermal behavior of the sample.

To perform absolute temperature measurements, the calibration of the measured amplitude vs the sample surface temperature requires knowing accurately the emissivity of the sample surface. It comes to be a difficult task, even more when the objective is study of inhomogeneous materials which have inhomogeneous optical properties. Nevertheless, the phase-lag $\phi(\omega)$, is also sensitive to the sample thermal properties and independent of the optical properties of the surface like the emissivity. The phase-lag measurement can be thus used directly as the explanatory variable within the parameter identification process.

The main inaccuracy of radiometric temperature measurements arises from the uncertainty in ε and from the influence of the background light. Fortunately, the surrounding light contributes

as a constant additive component to the thermal signal and is effectively cancelled by the lock-in process if it does not contain frequency components near the lock-in frequency (Appendix I).

1.2.3.2 Imaging.

The most extended technique for thermal imaging in contactless mode is the infrared (IR) thermography. It is based on the use of infrared sensitive camera for obtaining of thermal image of the sample surface. The IR thermography can be carried out in active or passive mode. Only the active mode provides information about thermal properties of the sample. The analyzed object is heated by an excitation source in a single pulse or periodically like in MPTR.

IR thermography is widely used as a nondestructive technique for quality inspection of structures or components in both, during manufacturing and in-service period. The best available spatial resolution in IR thermography is of order of several micrometers. IR thermography in pulsed and in lock-in mode have been applied for inspection and testing of materials [97], [98], crack detection [99], [100] and to the imaging of localized heat sources within electronic components [101], [102] or in chemical reactions [103].

An example of application of the IR thermography for the thermal characterization of materials is given in [104]. A grid of pulsed flying spots was used for estimation of the in-plane thermal diffusivity of heterogeneous anisotropic materials. Figure 1.15 shows the relaxing temperature field that reveals a highly heterogeneous nature of the studied material. The in-plane thermal diffusivity was estimated using the logarithmic parabolic method with an error lower than 4%.

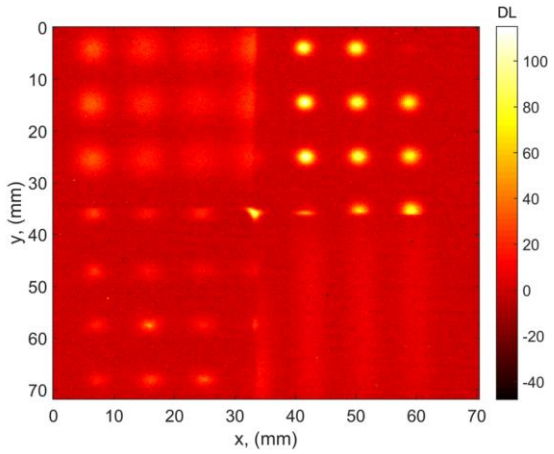

Figure 1.15: Temperature field during the relaxation of heterogeneous anisotropic materials studied in [104].

The pulsed spot was also used in [105] for estimation of the fields of in-plane thermal diffusivity in a homogeneous and orthotropic materials oriented out of the main axes. The studied material was a carbon/epoxy composite. Figure 1.16 shows the elliptic temperature field measured 1 s after the pulsed spot. It can be noticed that the isotherms are elliptical and angled compared to the main axes of the camera images. Using the logarithmic ellipsometric method, the authors could estimate the thermal diffusivity for orthotropic materials as well as the orientation angle with reference to the axes of the image.

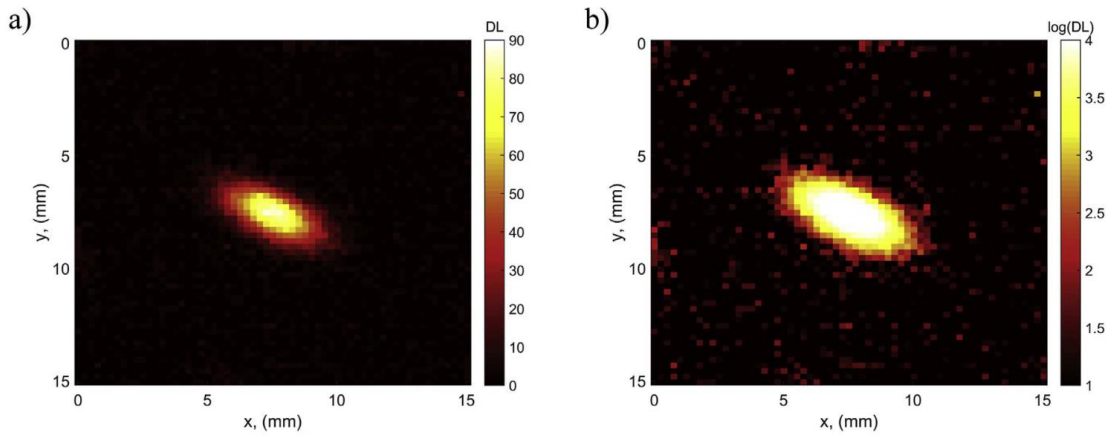

Figure 1.16: a) Measured temperature field at t = 1 s after the pulsed spot, b) logarithmic representation of the measured temperature field the same time [105].

In [106] the flying spot technique was used to determine the width of vertical cracks in AISI-304 stainless steel sample. Results with high accuracy, even for submicronic width cracks, were obtained with pixel resolution of 30 μm. Figure 1.17 shows a sequence of thermograms where the effect of the crack (0.56 μm in width) in the heat diffusion is clearly visible. The laser spot is motionless while the sample is moving to the left at a velocity of 3.56 mm/s. In order to improve the sensitivity in highly diffusive materials this technique was also used with a modulated heat source within the lock-in thermography mode [107]. Figure 1.18 shows the thermograms of amplitude and phase corresponding to an AISI-304 stainless steel sample moving to the right at constant velocity of 10 mm/s. The sample is excited by a laser beam modulated at 1 Hz. The amplitude shows the expected elongated shape corresponding to the dragging effect due to the sample motion. Astonishingly, the isophases seem circular similarly like in static measurement. The authors present that the amplitude and phase profiles in both parallel and perpendicular to the sample displacement direction, show a linear behavior. The slopes of those profiles permit obtaining the in-plane thermal diffusivity of the material.

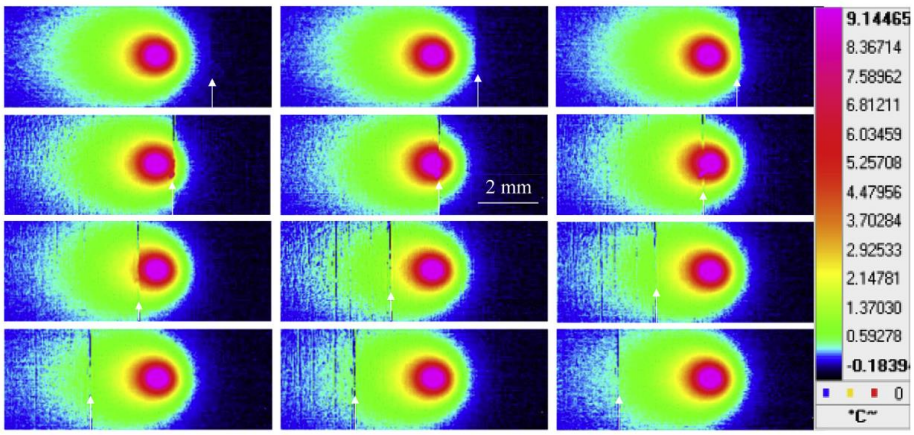

Figure 1.17: Sequence in time of thermograms from flying spot technique where the arrow indicates the position of the crack [106].

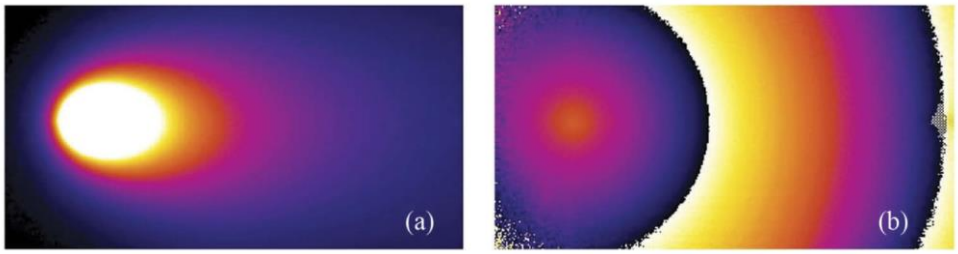

Figure 1.18: Thermograms of the amplitude (a) and phase (b) from lock-in thermography on moving sample [107].

Figure 1.19 shows a diagram of a classical experimental setup for lock-in measurements. The advantage of the lock-in thermography over the pulsed thermography is related to its averaging nature. Indeed, in the lock-in mode the sensitivity is improved considerably.

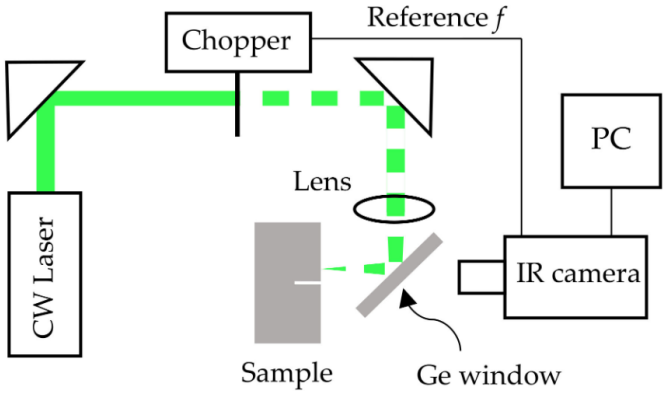

Figure 1.19: Diagram of the laser-spot lock-in thermography experimental setup [108].

The lock-in thermography allows to identify the in-plane and out-of-plane thermal diffusivity of samples in static condition [109] and moving at a constant velocity [107], [110]. A noise reduction below 1 mK can be achieved. The lock-in thermography has also been used to measure thermal diffusivity of filaments [111] and thermal boundary resistance in a two-layer system [112]. Using an infrared microscope objective, the IR thermography can reach a spatial resolution of 2.5 µm and the excitation frequencies of hundreds of Hz.

The main drawback of the IR thermography is the frame rate of the infrared cameras, which is limited to several kHz for high-speed cameras in sub-frame acquisition and several hundreds of Hz for most used cameras in full frame acquisition mode. Additionally, in the lock-in configuration a lower frequencies have to be considered to allow a good sampling. In fact, according to the sampling theorem, at least two samples per period are required. It must be doubled for each period in order to retrieve the in-phase and the quadrature signal if the dual-phase lock-in correlation is applied. Therefore the lock-in frequency f_{lk} is limited by the frame rate f_{ft} of the camera and must fulfill the relationship [113]:

$$f_{lk} \leq \frac{f_{ft}}{n} \tag{1.13}$$

where n is the number of frames evaluated in each lock-in period. Thus, according to the sampling theorem and without using under-sampling, the minimum possible number of samples

per period *n* is 4. The maximum possible lock-in frequency is thus a quarter of the frame rate of the camera.

1.3 Conclusions.

We have presented the main methods for thermal imaging dedicated to the thermal characterization at the microscale. Table 1.3 summarizes the advantages and drawbacks of those techniques, and Table 1.4 summarizes their spatial resolution.

Among the presented techniques, the SThM offers the best spatial resolution but its application is limited to materials with low thermal conductivity. The SThM brings the possibility to access the absolute values of the heat flux and the temperature. However, the method involves additional thermal parameters related to the contact itself. These parameters are difficult to assess accurately in practice and this becomes even more difficult in scanning mode.

The thermoreflectance has a good spatial resolution, with diffraction limit resolution around 300 nm and temporal resolution of picoseconds. The technique can be used for temperature imaging quite easily and with very fast rise time due to the use of CDD cameras. Nevertheless, the sensitivity of the technique is low. On the other hand, absolute measurements of the heat flux and the surface temperature are not easily accessible.

The lock-in IR thermography technique brings direct access to the phase-lag of the measured signal that is independent of optical properties. The sensitivity is higher than that of the thermoreflectance. However, the frame rate of the IR cameras limits its application to the low frequency range.

Techniques	advantages	Drawbacks
SThM	- Submicron resolution -Absolute temperature measurement - No sample preparation	- Contact resistance - Low frequency measurements - Low thermal conductivity sensitivity
Thermoreflectance	- In-plane and out-of-plane diffusion measurements - Nanometer scale thermal depth resolution - Time resolution of ps.	- Metal transducer needed - Complex and expensive experimental setup - Smooth surfaces required - Complex post-processing
Lock-in thermography	- In-plane and out-of-plane diffusion measurements - High temperature sensitivity - No sample preparation	- Time consuming - Low frequency measurements

Table 1.3: Advantages and drawbacks of thermal imaging techniques.

Techniques	resolution		
	Spatial	Temperature	Time
SThM	50 nm	50 mK	100 µs
Thermoreflectance	0.3 µm	10 mK	500 ps
Lock-in thermography	2.5 µm	10 µK	200 µs

Table 1.4: Spatial, temporal and temperature resolution of thermal imaging techniques.

Regarding this survey, we consider that there is a need to develop a high frequency scanning technique with a high spatial resolution to fill the gap between the existent thermal imaging techniques as illustrated in Figure 1.1.

Chapter 2:
Scanning Photothermal Radiometry (SPR).

2.1 Introduction.

We have seen different techniques for thermal characterization in contactless and contact mode. Among them, the measurement with best spatial resolution is the SThM. In addition the SThM is one of the most versatile techniques, since the sample under study don't need additional preparation like the transducer layer in thermoreflectance or 3-ω method. It can be applied to micro-structured materials like nanowire or fiber composites and assess materials in 3D geometries. Nevertheless, the method is limited to materials with low thermal conductivity. In addition, as with the lock-in thermography, the frequency range is limited to slow dynamics when using the modulation mode. It therefore deemed necessary to us to develop a high frequency scanning technique with a relatively easy implementation and data processing (if one compares with thermoreflectance) with high reliability and that can be used with a wide range of materials.

At the I2M lab there is a large experience with the application of contactless techniques based on self-emission for thermal characterization as the MPTR and PPTR techniques. However, it is limited to homogeneous surface, without the possibility to study complex geometries and perform thermal imaging of the thermal properties with heterogeneous surfaces. So, this work arises as a response to the need to analyze materials with complex geometry at high frequency and faces the problematic of thermal characterization of 3D structured materials with scanning thermal imaging.

In this chapter we will present two different scanning experiments, the first one is a contact method whereas the second one is a contactless method. Both techniques are based on the modulated photothermal radiometry as sensing principle. The self-emission subsequent to the periodic photothermal excitation on an opaque surface is sensed with an infrared mono detector.

The first part of the chapter will be dedicated to the scanning experiment in contact mode. In this experiment we use a home developed probe based on the use of an optical fiber. This fiber allows both to supply the modulated laser beam and to collect the IR emitted by a small transducer attached at the fiber end. The idea behind this probe is to generate and monitor the temperature change in a small volume at the end of the fiber that works as heater and sensor at the same time. The full experimental setup will be presented followed by its application and model identification. In this configuration we obtained reliable results regarding the differentiation between two different materials but its application remains at low frequency. Indeed, although the basic principle is simple, its practical implementation yields major technical challenges regarding mainly the contact conditions during the scan. Therefore, we decided to reduce the number or unknown variables involved within such an experiment and to change to a contactless technique. We think however that this contact method could be improved in the future and this is the raison why we reported the results we obtained using this technique.

Thus, in the second part of this chapter the scanning experiment in contactless mode will be detailed. In the contactless experiment we replace the fiber optic probe by a Cassegrain microscope objective. The microscopic objective allows to focus the laser beam directly over the

sample and collect the IR emitted by the surface. Several configurations have been tested in order to assess the spatial resolution and the sensitivity to the thermal properties of the sample. Since the technique presents remarkable results at the high frequency regime with high spatial resolution, this experiment appears as a very efficient complementary tool to classical IR thermography.

2.2 A first scanning experiment in contact mode based on the use of an optical fiber probe.

In the resistive probes used with the SThM, the main part of the heat flux is lost into the probe itself. We propose a new kind of probe without metallic connections based on photothermal excitation. The Joule effect used as the heat source in typical resistive probes is replaced by the photothermal excitation from a laser and the thermo-resistive effect used as the sensing phenomena is replaced by the probe emittance. The main idea is to generate and monitor the temperature change in a small volume located at one end of an optical fiber that works as the heater and the sensor at same time. By putting the probe tip in contact with the sample, a fraction of the generated heat flux will flow the investigated material whereas the other one will diffuse within the fiber. It is expected to have the most part of the source in the direction of the sample. Like in the MPTR technique, we will use the measured phase lag to determine the thermal properties of the material.

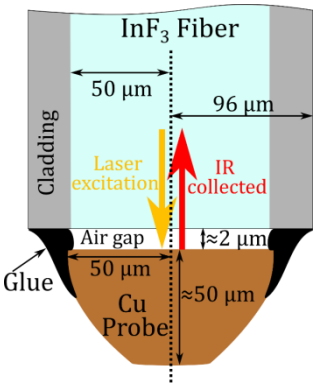

Figure 2.1 Scheme of fiber-based probe.

In order to fulfil the previous requirements, one practical solution is to hold the probe tip and provide a communication channel to supply the excitation flux and measure the emittance from the use of an optical fiber. Figure 2.1 shows a scheme of the concept, where a half sphere of copper (Cu) is glued at the end of the optical fiber. An air gap between the probe and the fiber is desired in order to reduce the heat diffusion from the tip to the fiber and therefore to promote the heat flow to the sample when it is in contact. In this way, when the photothermal excitation by the laser is sent through the fiber and heat the Cu probe attached on its end, there is a change in the probe's temperature and thus in the probe's emittance that is collected by the fiber. Like in the MPTR technique one can take advantage of the lock-in detection to measure the emittance variation on the probe consequent to a periodic excitation. This proposed technique is thus a mix of the SThM and MPTR techniques.

The optical fiber selected was an InF_3 fiber from Thorlabs. It has a transmission spectral range from 310 nm to 5.5 µm (Figure 2.2) that allows us to use a 1064 nm (Nd:YAG) laser as excitation source and collect the near IR from the probe in the 3-5 µm wavelength range from an InSb detector. A small piece of copper was glued at the end of a 100 µm core diameter InF_3 fiber leaving a space around 2 µm between the fiber and the copper tip. The probe radius is about 50 µm as revealed by optical images in Figure 2.3-b. The fiber probe was implemented within a homemade holder designed to mount the fiber probe in the optical table and provide a passive contact control during the scanning. The fiber is glued to the commercial ceramic ferrule leaving the probe tip to protrude above the level of the ferrule. A small coil spring push the ferrule out to be blocked by the support cage in contactless configuration. When the sample approaches the probe tip, the ferula and the spring are pressed. A scheme of the probe holder is presented in Figure 2.3-a in contact and contactless conditions and the handmade probe is shown in Figure 2.3-b.

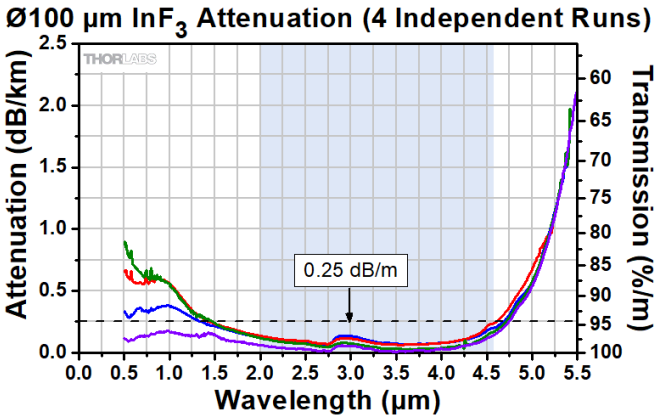

Figure 2.2 Measured attenuation of the Ø100 µm core InF_3 fiber provided by Thorlabs from four independent runs [114].

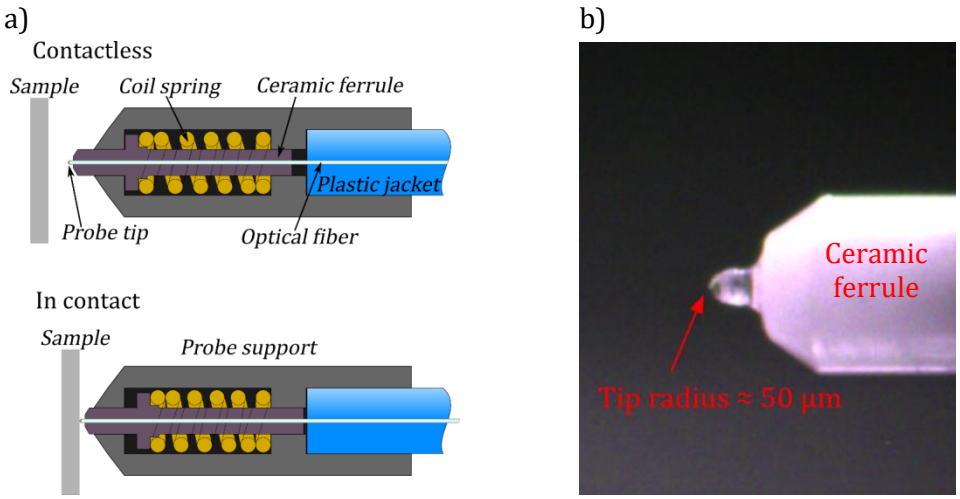

Figure 2.3 a) Scheme of fiber probe holder and the passive contact mechanism configuration in contact and contactless conditions; b) Optical image of the Cu probe tip deposited at the end of the 100 µm core diameter InF_3 optical fiber.

2.2.1 Complete experimental setup.

The scheme of the complete experimental setup is presented in Figure 2.4 where the path of the laser is represented in yellow and the path of the infrared signal is represented in red. A Nd:YAG laser (model VECTOR 1064-3000-30 from COHERENT) supplies a continuous laser beam that is sent through an acousto-optic (A-O) modulator to obtain the periodic excitation. The A-O modulator used is the model MT250-A0.5-1064 from AA optoelectronics with an amplitude modulation bandwidth of 15 MHz.

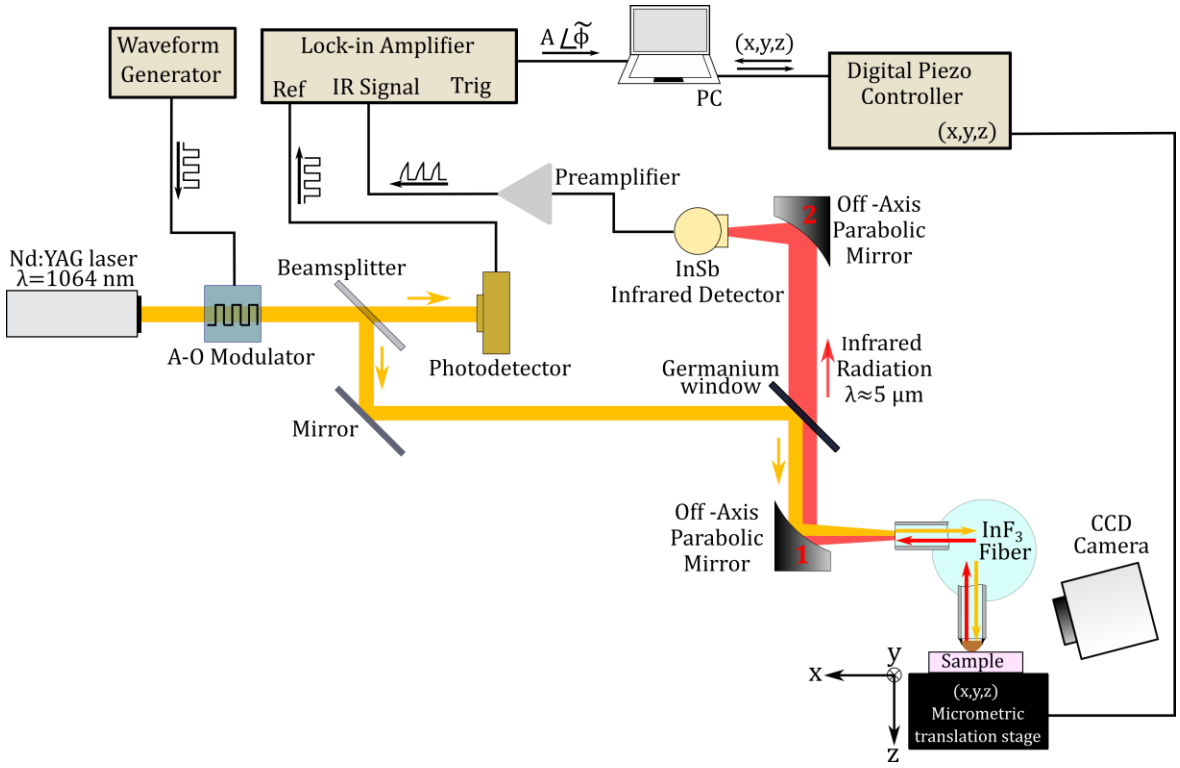

Figure 2.4 Scheme of experimental setup with fiber-based probe.

The A-O modulator allows driving the frequency and the power level of the laser that is used in the experiment with a single voltage wave. The voltage wave that controls the output of the A-O modulator is generated from a waveform generator (model 33510B from Agilent) and supplied to the A-O driver. The A-O modulator produces a periodic laser beam at the same frequency than that of the waveform generator. The power of the laser at the O-A modulator output is proportional to the voltage level of the control wave in the 0 to 1 V range, where 1V corresponds to the maximum output power. That means that a square signal with amplitude between 0 and 1 V corresponds to the 0-100% range in the output power of the A-O modulator without dependence on the operation frequency. Figure 2.5 shows the power delivered by the A-O modulator in function of the amplitude of the control wave.

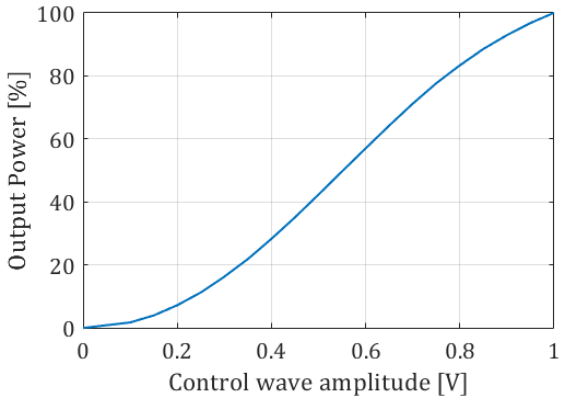

Figure 2.5: Output power vs. amplitude of the control wave from the waveform generator considering a Heaviside voltage.

In order to avoid a possible phase lag due to the waveform generator and the A-O modulator driver interconnection, a fast Si photodetector (PDA10A from Thorlabs) with 2.3 ns rise time is used as a reference for the lock-in amplifier measurements. At the 1st order output of the A-O modulator a beam splitter is used to take part of the laser to excite the photodetector. A germanium (Ge) window with transmission in the 3-12 µm range (Figure 2.6) is used to send the laser to the off-axis parabolic mirror 1.

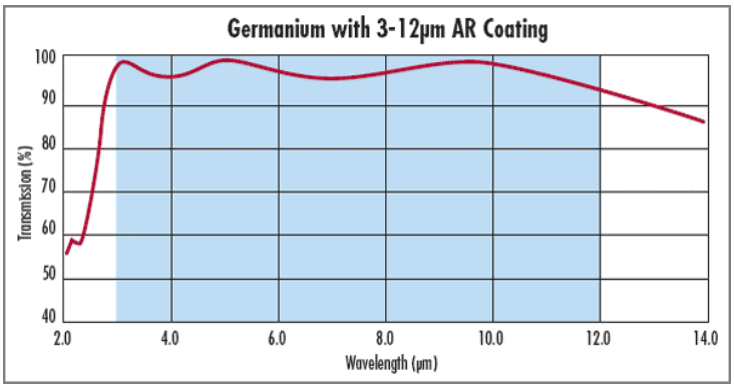

Figure 2.6 Ge window transmission from Edmund optics [115].

At the fiber end the laser heats the Cu probe and the IR emitted is collected within the fiber and conducted to the off-axis parabolic mirror 1. Therefore, the off-axis parabolic mirror 1 is used to focus the laser into the optical fiber and to collect the IR signal from the optical fiber. It avoids also possible reflection of the laser by the tip to go to the IR detector.

After passing through the Ge window, the collimated IR signal is focused on the IR detector by the off-axis parabolic mirror 2. The IR detector used in this experiment is the J10D-M204-R100U-60 (IRD) from Teledyne Judson Technologies. The IRD is made from an Indium Antimonide (InSb) photodiode with circular active area of 100 µm diameter and sensitivity range in the 1 to 5.5 µm wavelength region. The IRD is coupled with PA-9 amplifier from Teledyne Judson Technologies designed to operate from DC to 30 kHz.

The sample position is managed with a 3-axis piezoelectric translation stage (P-611K101 from PI) with travel range 100 µm × 100 µm × 100 µm. For contact measurements the sample is approached (moved along *z*-axis) to the probe with micrometric steeps controlled by the

piezoelectric stage and the contact is inspected visually with a CCD camera. A contact condition is assumed when it is appreciated that the probe is pushed a few micrometers by the sample.

2.2.2 Expected collected radiation.

Since the infrared radiation produced by the tip is collected by the optic fiber, we have to take into account that not all the radiation produced by the tip will reach the detector. The Numerical Aperture (NA) of the fiber limits the collected radiation to that inside of its margin angle. In addition, the transmission bandwidth of the optical fiber and the Ge window limit the transmitted radiation. The optical fiber transmits the light up to 5.5 μm and the Ge window transmission starts at 3 μm. This results in an available band from 3 μm to 5.5 μm in wavelength.

The power emitted from black body in the spectral range λ_1 to λ_2 is expressed as [116]:

$$M^0_{\lambda 1 \to \lambda 2} = \sigma T^4 (G_{0 \to \lambda 2} - G_{0 \to \lambda 1}) \tag{2.1}$$

With:

$$G_{0 \to \lambda} = \int_0^{\lambda T} \frac{M^0_\lambda}{\sigma T^4} d(\lambda T) \tag{2.2}$$

Where $G_{0 \to \lambda}$ is the fraction of the radiation emitted in the spectral band 0 to λ with respect to the total emittance (σT^4). M^0_λ is the spectral emittance of the blackbody defined as:

$$M^0_\lambda = \frac{C_1}{\lambda^5 \left(e^{\frac{C_2}{\lambda T}} - 1 \right)} \tag{2.3}$$

With $C_1 = 3.742 \times 10^8$ W·μm⁴·m⁻², $C_2 = 1.439 \times 10^4$ μm·K. Evaluating expression (2.2) for λ_1= 3 μm and λ_2=5.5 μm at the ambient temperature (T_0=300 K) and using relation (2.1) one obtains the power emitted of the black body in the available spectral band as:

$$M^0_{\lambda 1 \to \lambda 2} = 0.0261 \sigma T^4 \tag{2.4}$$

The NA of an optical fiber is the sinus of maximum angle at which the fiber can accept or emit light (Figure 2.7-a). InF_3 fiber has a NA=0.26, this leads to an acceptance angle (ϑ_a) of 15° as represented in Figure 2.7-b.

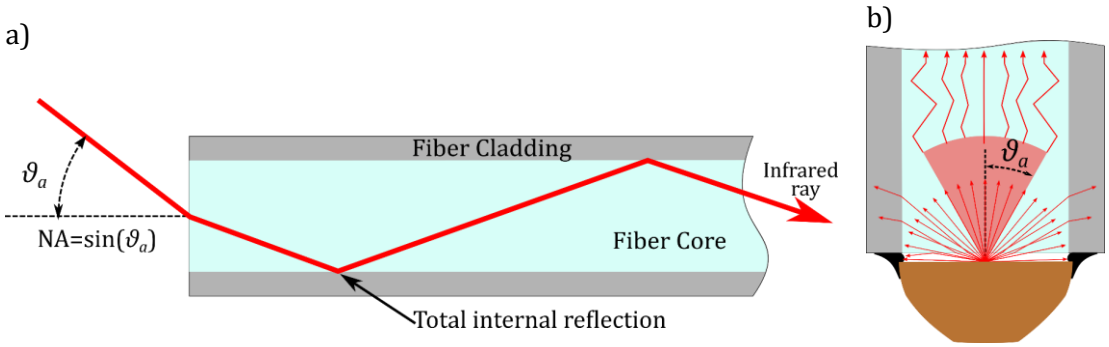

Figure 2.7: In scheme (a) the Numerical Aperture (NA) of a fiber is defined as the sine of the largest angle an incident ray can have for total internal reflectance in the core. In scheme (b) the angle of acceptance defines the cone of emitted radiation that will be transmitted by the optic fiber.

$M^0_{\lambda 1\to\lambda 2}$ is hemispheric emittance but we are only able to collect that inside the angle of 15°. Considering that the black body radiation is independent of the direction we can express the spectral band intensity of the emitted radiation as:

$$L_{\lambda 1\to\lambda 2} = \frac{M^0_{\lambda 1\to\lambda 2}}{\pi} \tag{2.5}$$

Thus, the radiation emitted inside a cone with angle of 15° is:

$$\overline{M}_{\lambda 1\to\lambda 2} = L_{\lambda 1\to\lambda 2}\int_{\psi=0}^{2\pi}\int_{\theta=0}^{\pi/12}\cos(\theta)\sin(\theta)\,d\theta\,d\psi = 0.067 M^0_{\lambda 1\to\lambda 2} \tag{2.6}$$

Finally considering a real body with the emissivity ε, the expression of the emittance captured by the fiber is expressed as:

$$\overline{M}_{\lambda 1\to\lambda 2} = 1.7\times 10^{-3}\,\varepsilon\sigma T^4 \tag{2.7}$$

Considering a temperature variation $T = T_0 + \Delta T$ and assuming the linear relationship where the variation in emittance is proportional to the temperature variation as $\Delta M = 4\varepsilon\sigma T_0^3 \Delta T$, one can estimate the variation of the emitted radiation and transmitted by the optical fiber:

$$\Delta M = 6.8\times 10^{-3}\varepsilon\sigma T_0^3\Delta T \tag{2.8}$$

and the total power as:

$$\Delta P = \Delta M \pi r_f^2$$

with r_f the radius of the fiber. Considering that the metallic tip has emissivity $\varepsilon = 0.1$, the available power collected and transmitted to the detector, resulting from a variation in temperature of 1 K is ΔP = 8.1 pW.

On the other hand, the noise equivalent power of the infrared detector is reported by the manufacturer equal to 0.8 pW [117]. This provides a theoretical value of signal to noise ratio of 10. It indicates that the experiment is viable even with the limited wavelength bandwidth that is not the optimal to work at ambient temperature.

2.2.3 Static measurements.

In order to verify the linear relationship between the measured emittance and the power supplied to the probe the first test was a frequency sweep in contactless condition for different power levels. As commented before we can control the power supplied to the probe via the A-O modulator, nevertheless we have no information of the efficiency of the laser-fiber coupling and the absorption coefficient of the tip. It is thus important to fulfill the linear relationship between the temperature and the emittance that is a requirement to use the phase lag for thermal characterization. For simplicity we will refer to the power supplied to the sample as a percentage of the maximum power (P%). For this experiment the maximum power was set in 20 mW, which means 20 mW = 100 P%. The measured amplitude and phase are presented in Figure 2.8.

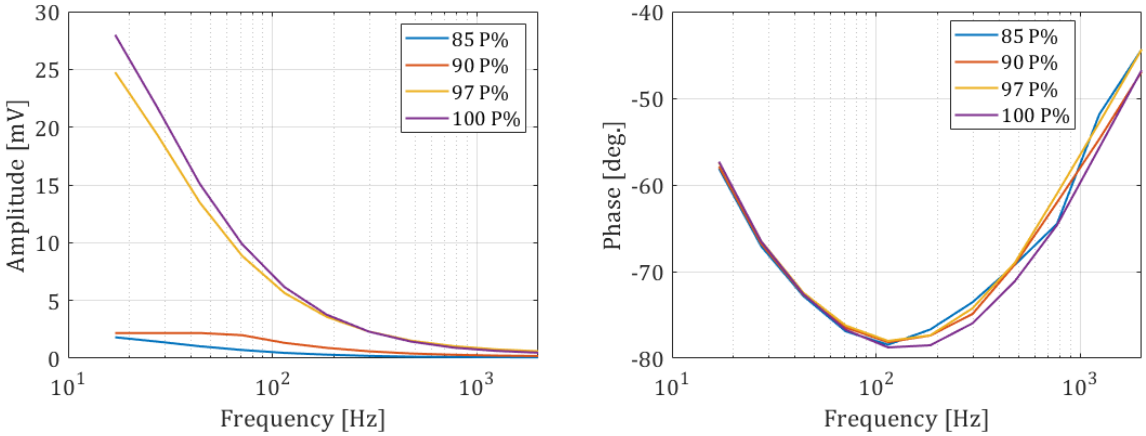

Figure 2.8: Amplitude and phase measured with four P%.

One observes that the measured phase is almost the same for frequency varying from 10 Hz to 100 Hz. Above this value the phase measurements start to spread with the maximum difference of 2 degrees at 2 kHz. Since the plots overlap and cross each other's and because of the large reduction in the amplitude of the signal we conclude that the phase variation comes from the noise measurement.

To test the experimental setup in contact mode and its capability to discriminate between two different materials we performed measurements on a silicon (Si) substrate with a 50 nm thick layer of SiO_2 and 20 nm thick gold (Au) strip deposited on the top as presented in Figure 2.9. This configuration is originally designed to work with the 3-ω configuration. A measurement in static mode was done over the zones I and II corresponding to the SiO_2 zone and Au zone respectively.

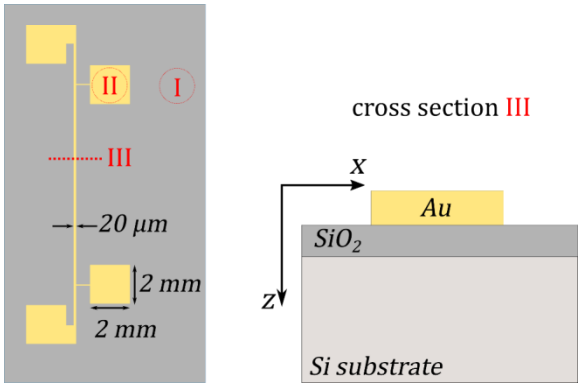

Figure 2.9: Scheme of the 3-ω sample used in the evaluation of fiber-based probe in contact mode.

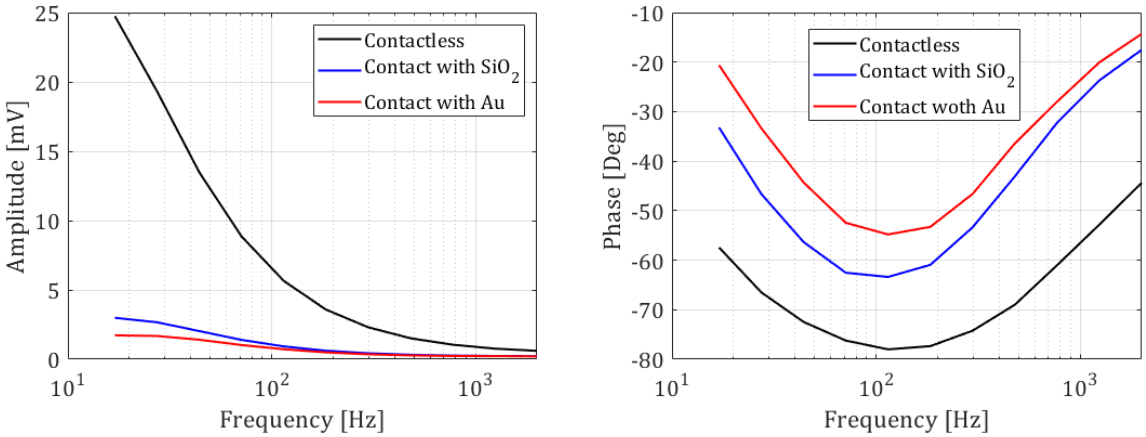

Figure 2.10: Frequency sweep in static mode of the fiber-based probe in out of contact condition, in contact with SiO_2 layer (zone I) and in contact with Au strip (zone II).

Figure 2.10 shows the measurements in static mode where it is possible to discriminate between the different contact materials. Frequency range is in the 20 Hz - 2 kHz. For higher frequencies the amplitude of the signal becomes too small and renders measurements noisy.

2.2.4 Measurements across the strip.

We performed a pseudo scanning measurement across the 20 μm width Au strip (the red line III in Figure 2.9) with two excitation frequencies, namely 27 Hz and 185 Hz. This measurement was done by consecutive static measurements with 2 μm space between each point and a total of 35 points was measured. For the line scanning process, the contact is stabilized at the first scan point and the *z* position is locked. Once the measurement is done, the probe is displaced along the *x*-axis to the next point without retracting the sample. Only after the last point measurement, the sample is retracted in *z*.

The normalized amplitude and phase from both scans are presented in Figure 2.11. The strip location and width are represented in yellow. Although the signal is very disturbed one can

identify the influence of the strip (the zone between red lines) that produce lower amplitude and higher phase with respect to the SiO_2.

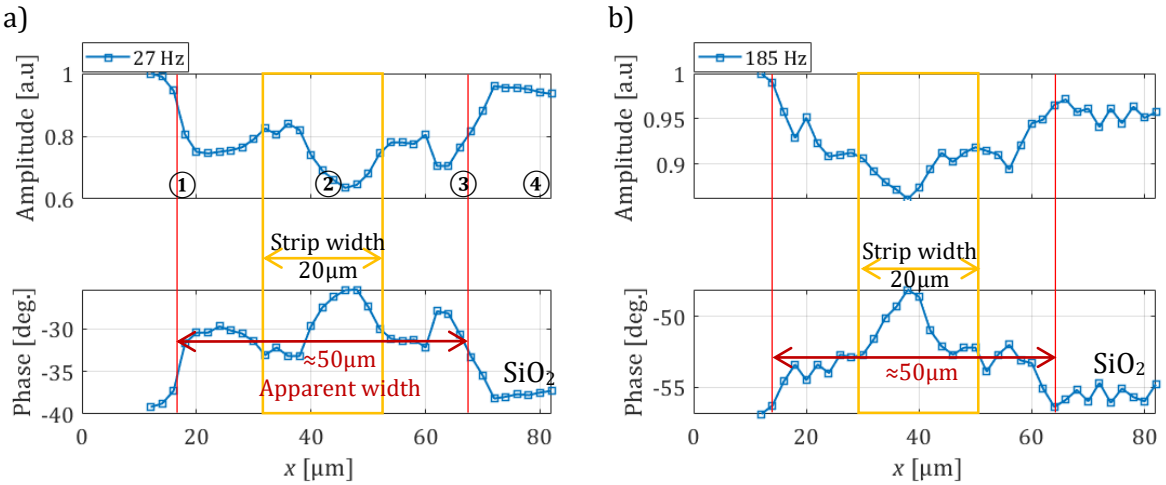

Figure 2.11: Scan across 20 µm in width Au strip (line III) over SiO_2 layer on Si substrate with: a) 27 Hz; b) 185 Hz excitation frequency.

Figure 2.12 shows a scheme of the contact conditions on the four points signaled in the scanning plot that help in the measurement interpretation. In ① the probe reaches the strip and it is in contact with the strip and substrate the same time. The same condition occurs in ③ with the probe leaving the strip. In ② the probe is only over the strip and finally, in ④ the probe is only in contact with the SiO_2.

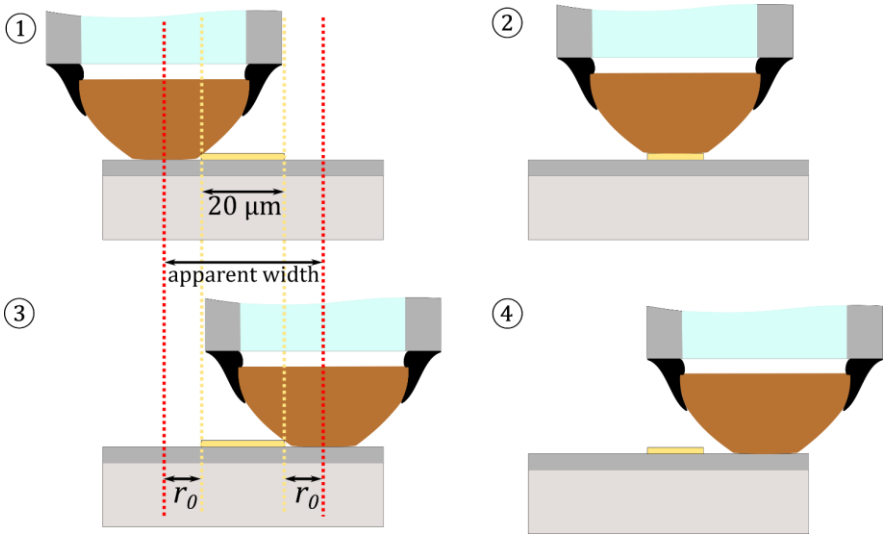

Figure 2.12: Scheme of the scanning process with four main positions indicated in scan plots.

The apparent width of the strip from the swiped line is estimated around 50 µm. This widening is generated by the size of the contact area between the sample and the probe as showed by specific configurations ① and ③ in Figure 2.12. Considering a circular contact area, the diameter could be estimated by subtracting the real size of the strip from the apparent width. The contact radius is thus around 15 µm. With this measurement we have an approximation of the contact area that will be used in the model of the experiment.

On the other hand, the noised signal could be generated by a change in the probe-sample contact condition since it is not controlled actively or by defects in the probe. The lowest value in amplitude observed close to the center of the strip, could suggest a better coupling between the tip and the sample. However, the scanning suggests a bad contact between the probe and the investigated surface.

2.2.5 Heat transfer model.

In a first approximation the fiber-based probe was modeled as a lumped capacitance coupled to a semi-infinite fin. The model is represented in Figure 2.13 using the formalism of thermal impedances. In this way the thermal impedance in $K \cdot W^{-1}$ of the hemispherical tip of the probe is described in the frequency domain as:

$$Z_t = \frac{1}{j\omega C_t}, \qquad \text{with } C_t = \rho C_{pt} V_t \tag{2.9}$$

where V_t is the volume of the tip that can be approximated as a half sphere. ρC_{pt} is the volumetric heat capacity of the copper tip and C_t is the capacitive effect of the tip at low frequencies. In the same way the thermal impedance of the fiber that acts as semi-infinite fin is described by:

$$Z_f = \frac{1}{\pi r_f^2 k_f \sqrt{\frac{j\omega\, \rho C_{pf}}{k_f} + \frac{2h_a}{r_f k_f}}} \tag{2.10}$$

where ρC_{pf} and k_f are the volumetric heat capacity and the thermal conductivity of the fiber. Parameter h_a is the heat transfer coefficient of the fin with the surrounding, that for natural convection is assumed around 5 $W \cdot m^{-2} \cdot K^{-1}$.

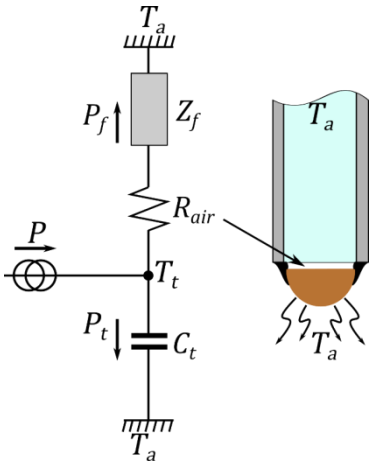

Figure 2.13: Impedance network representation of the fiber probe in contactless mode.

In this model the air gap between the coper tip and the fiber is considered as thermal resistance R_{air}. The thermal impedance of the probe that relates the thermal power P to the average temperature of the tip is thus expressed as:

$$Z_p = \frac{T_t}{P} = \left(\frac{1}{1/(Z_f + R_{air}) + j\omega C_t} \right) \tag{2.11}$$

One obtains the expression for the amplitude $T_t(\omega)$ and the phase $\phi(\omega)$ in contactless mode as:

$$T_t(\omega) = P\|Z_p\|, \qquad \phi(\omega) = \arg[Z_p] \tag{2.12}$$

The model was simulated with properties presented in Table 2.1 and the comparison with measurements of the phase in contactless condition is presented in Figure 2.14. One observes the agreement between the simulation and the measurement at frequency lower than 30 Hz. For higher frequencies the discrepancy between the two quantities is high since the copper tip cannot be considered as a lumped system anymore.

Material	k W·m^{-1}·K^{-1}	ρ kg·m^{-3}	C_p J·kg^{-1}·K^{-1}
Tip (Cu)	380	8933	385
Fiber	1	4000	800
Air	0.02	1	1000
Si	131	2329	700
SiO_2	1.4	2200	787

Table 2.1: Thermal properties of the probe and sample.

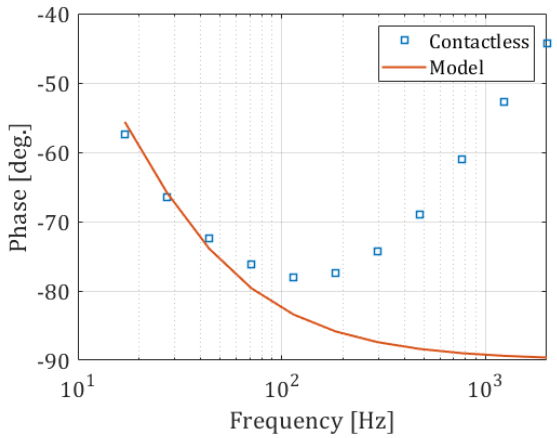

Figure 2.14: Comparison between phase measurements obtained in contactless condition and the simulation from the model based on the lumped body assumption for the tip.

The probe tip attached to the fiber and the air gap between them are probably acting as more complex systems. In addition, the handmade nature of the probe adds variables that are difficult to account in an analytical or even numerical model of the probe, as the exact dimension and shape of the probe tip, its proximity to the fiber and the interaction with the glue that was no considered in the model.

To overcome those difficulties, we propose using the measured transfer function of the probe from the previous contactless experiment. Therefore, the probe transfer function Z_e is expressed as:

$$Z_e(\omega) = \frac{T_t(\omega)e^{j\phi(\omega)}}{P} \tag{2.13}$$

The main drawback here is that we have no access to the absolute temperature $T_t(\omega)$ and power P since we have no information regarding the absorption coefficient of the tip. Thus, we modify the transfer function to introduce the relation between the measured amplitude $A(\omega)$ in volts from the lock-in and the temperature as:

$$Z_e(\omega) = \gamma A(\omega)e^{j\phi(\omega)} \tag{2.14}$$

With:

$$\frac{T_t(\omega)}{P} = \gamma A(\omega) \tag{2.15}$$

Where the left side of the previous expression is the magnitude of the thermal impedance defined in equation (2.34). To obtain an approximation of the γ coefficient one can use the fin-lumped model presented before and evaluate $\|Z_p\|$ at the lowest measured frequency where the model shows an acceptable reliability. In this way the γ coefficient is obtained as:

$$\gamma = \frac{\|Z_p(\omega_{min})\|}{A(\omega_{min})} = 3.24 \times 10^5 \ \mathrm{K \cdot W^{-1} \cdot V^{-1}} \tag{2.16}$$

From this measured thermal impedance Z_e, one can extract the thermal impedance Z_f of the fiber alone assuming the lumped tip at low frequency. This thermal impedance Z_e can then be used to model the heat transfer in contact mode as showed in Figure 2.15.

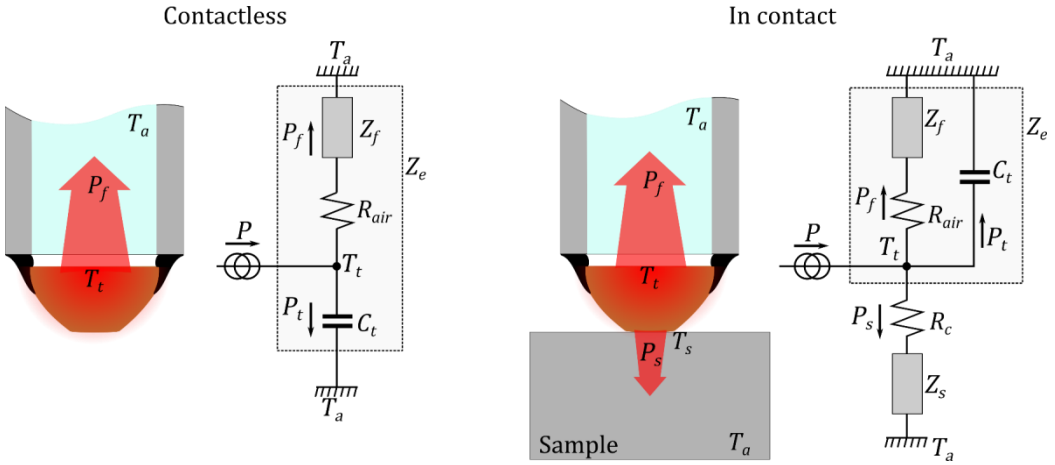

Figure 2.15: Thermal impedance network of the probe in contactless and in contact modes for low frequencies.

In this network the thermal resistance, R_c, is introduced to take into account the contact resistance between the tip and the material. Z_s is the thermal impedance of the sample expressed as:

$$Z_s = \frac{2}{k_s}\int_0^\infty \frac{J_1(\alpha r_0)^2}{\alpha\sqrt{\alpha^2 + \frac{j\omega}{a_s}}}\, d\alpha + R_{th} \tag{2.17}$$

Where R_{th} is the thermal resistance of the deposit over the substrate. r_0 is the contact radius, k_s and a_s are the thermal conductivity and diffusivity of the sample and J_1 is the Bessel function

of the first kind and order 1. From the thermal impedance network one can see that the total thermal impedance of the probe-sample system:

$$Z = \frac{T_t}{P} = \left(\frac{1}{1/Z_e + 1/Z_s}\right) \tag{2.18}$$

And the phase lag is calculated as:

$$\phi(\omega) = \arg[Z] \tag{2.19}$$

Using the phase lag one can identify R_c by fitting the model to the experiments in contact condition. The parameter identification procedure is presented in section 3.6.

From measurements in the SiO_2 zone the contact resistance is estimated as: $R_{cI} = 8.4 \times 10^{-6}$ m²·K·W⁻¹ and from measurements in the Au zone one gets $R_{cII} = 4 \times 10^{-6}$ m²·K·W⁻¹. The comparison between the simulation and the experiment is presented in Figure 2.16.

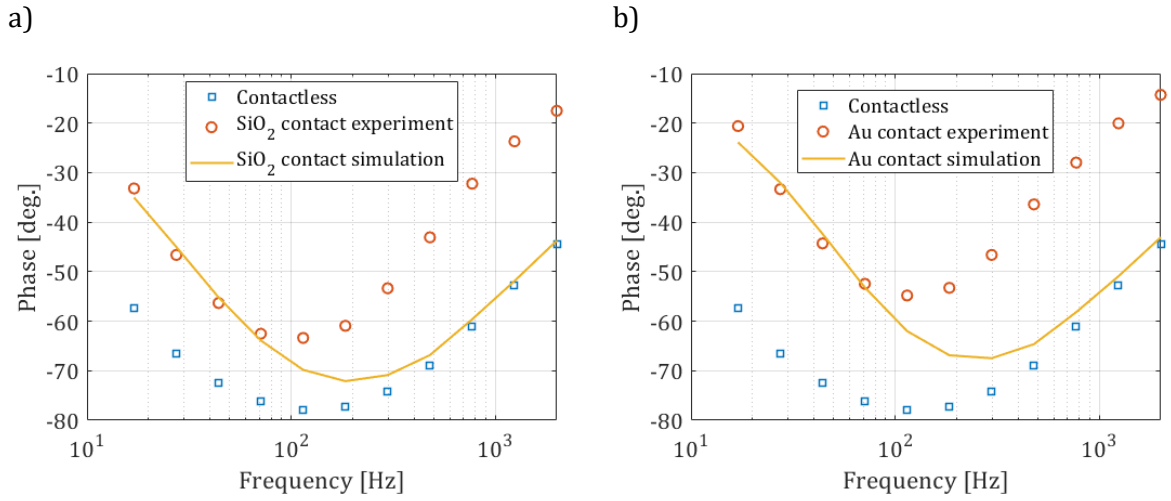

Figure 2.16: Phase comparison between experiment and simulation in contact with a) SiO_2 zone and b) Au zone.

As expected, the model is valid only in the low frequency range under 80 Hz. In addition, the large contact resistance is a consequence of the poor contact condition between the tip and the sample surface that is also obvious in the scanning measurements presented above. Although the area of contact is large it is possible that the effective contact takes place at randomly distributed points on the tip surface like represented by the scheme in Figure 2.17.

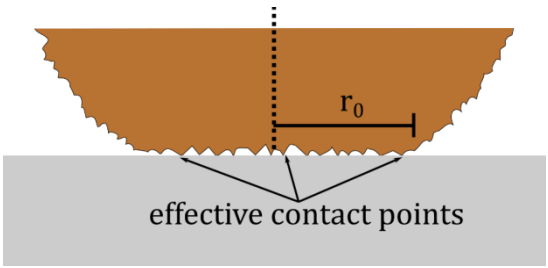

Figure 2.17: Schematic representation of the probe-sample contact.

From the experiments carried out, we found that the developed setup is applicable only at very low frequencies and it is clear that the probe and experimental setup needs to be improved. The

size of the probe tip has to be reduced to extend the lumped body approximation to higher frequencies and the contact force has to be accurately controlled in order to get measurements in constant conditions. In addition, the thermal insulation from the optical fiber has to be promoted and the signal to noise ratio improved to be able to measure the signal at high frequencies.

Improve the experimental setup implies solving several technical challenges that involve micromachining techniques which require much more time to design and study the thermal exchange at small scale on this kind of fibers. On the other hand, the reduction in size will inevitably lead to the similar behavior that NSOM-probes, which are extremely fragile and its fabrication and operation requires complex and expensive experimental setup. In addition, with such type of probe the measurements are done under contact conditions, that implies to face the complexity on the tip-sample interaction. This problematic has been proven on SThM probes and play an important role in the results of the experiments and is varying in function of the studied material.

To overcome to the complexity involved in contact mode studies, we have chosen to explore the application of a contactless method based on photothermal radiometry in a scanning configuration. We have taken the modulated photothermal radiometry as starting point to develop a new experimental setup in order to extend the frequency and sensitivity range for thermal characterization of materials with micrometric or even sub micrometric structures with 3D geometries. In addition, if the material is opaque to the excitation laser, the use of proper emission to estimate the thermal properties brings the possibility to work without any transducer avoiding the introduction of additional layer's interactions and unknown parameters in the model of the sample. The use of light as a probe to measure the thermal response of the sample allows work in a high frequency range. Thus, a second experimental setup for imaging the thermal properties of materials will be presented next.

2.3 A second scanning experiment in contactless mode based on Photothermal Radiometry.

In this contactless experiment we replace the fiber optic probe by a Cassegrain microscope objective. The microscope objective allows to focus the laser beam directly over the sample and collect the IR emitted by the surface.

In the optical arrangement, three bands of the light spectrum are exploited: the visible spectrum, the laser with wavelength, λ = 1064 nm, and the emitted infrared radiation which maximum power is centered around $\lambda \approx 10$ µm at the ambient temperature. The use of a reverse Cassegrain microscope objective with reflectance > 96% over 240 nm–20 µm wavelength operation region makes it possible to focus the laser beam over the sample surface and to collect the emitted infrared radiation from the same sample surface consequently to the periodic photothermal excitation. It makes it also possible to obtain the visible image of the sample which is used to place the sample in the area of interest.

As for the previous experimental setup, the use of lock-in amplifier allows to measure the amplitude and the phase of the signal from the IR detector with reference to the signal obtained

from the photodetector. Finally, the scanning system based on the piezo translation platform allows the acquisition of images from one-pixel sensor measurements.

2.3.1 SPR experimental setup.

The schematic view of the experimental setup is presented in Figure 2.18. The setup is composed by three sections: the optical arrangement, the measurement stage and the scanning stage, all integrated in the homemade user interface installed on the PC (LabView).

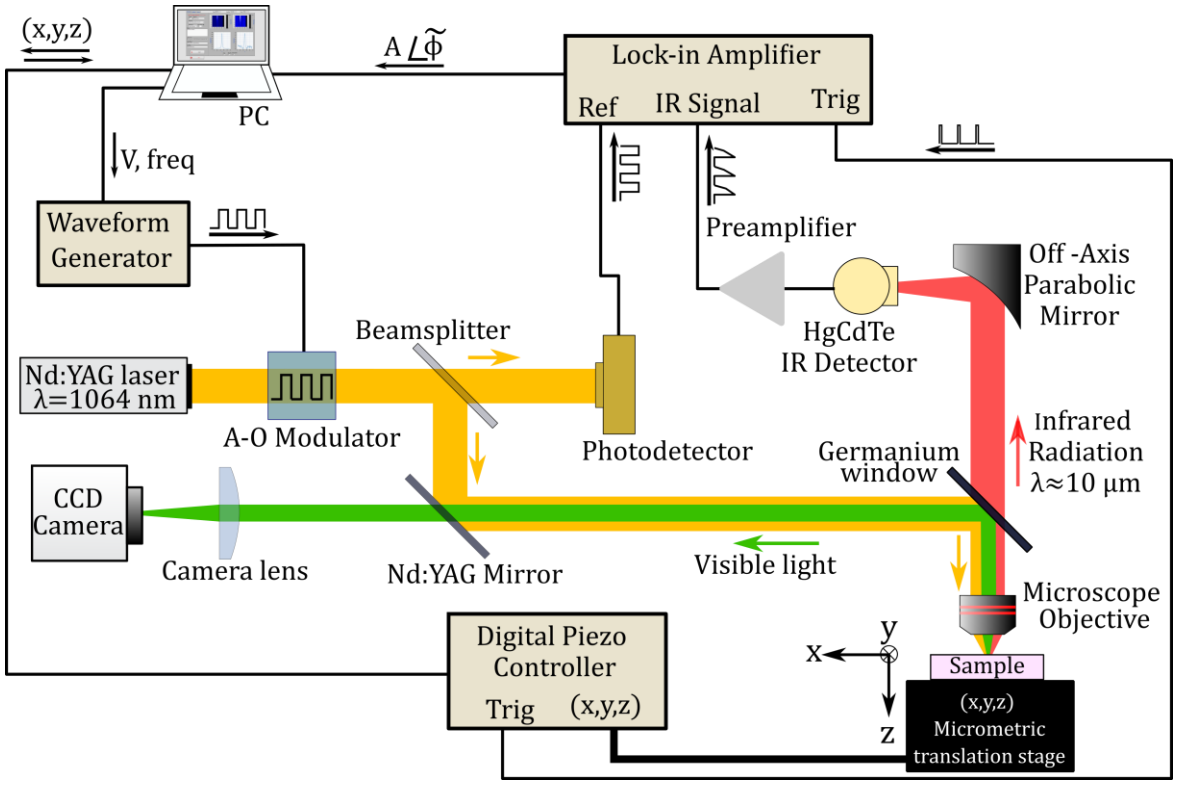

Figure 2.18: Diagram of the experimental setup.

Starting with the optical part of the setup, the excitation source is represented in yellow in Figure 2.18, the laser beam is emitted in a continuous wave mode by the Nd:YAG laser. The continuous laser beam is sent through the A-O modulator to generate the periodic heat flux. A waveform generator drives the frequency and the power delivered by the A-O modulator. This brings the possibility to control the power supplied to the sample in a simple way during the experiments without modifying the spot radius. After the A-O modulator a beamsplitter send a fraction of the laser to the reference photodetector and the remaining part is sent by a Germanium window to the Cassegrain microscope objective which focuses the laser onto the sample surface located at the focal plane of the microscope objective. The laser spot on the sample surface is circular and provides heat flux with a Gaussian distribution. The full characterization of the heat source is addressed in section 2.3.2. The surface heat flux leads to the temperature variation and so on the change of the emittance. Illustrated in red in Figure 2.18, the emitted infrared radiation is collected by the same Cassegrain microscope objective and sent to the germanium window. Up to here, the heating laser and the collected IR signal have the same path. It is the germanium

window who separates the infrared signal from the laser, since it is transparent for infrared light, but semitransparent for the laser wavelength. The infrared signal goes through the germanium window and reaches the off-axis parabolic mirror to be focused at the infrared detector.

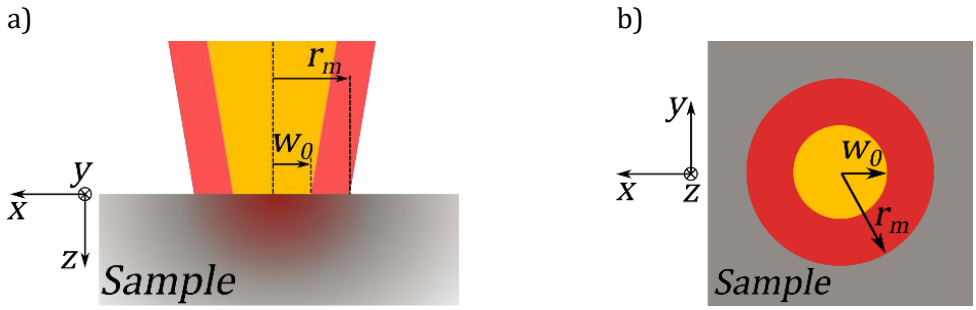

Figure 2.19: In yellow, the focused laser incident on the sample with spot radius of w_0 at sample surface and in red, the emittance from the sample collected with effective radius r_m at sample surface in a lateral view (a) and top view (b).

In Figure 2.19 one can observe in more details the formation of two concentric circular areas over the sample surface. In yellow is represented the heating area with radius, w_0, produced by the focused laser impinging the sample. The measurement region is depicted with radius r_m. It corresponds to the area that the sensor can see over the sample surface.

The visible image of the sample surface is obtained by a CCD camera. The path of the visible light is represented in green in Figure 2.18. The visible wavelengths are collected by the microscope objective and reflected by the germanium window through Nd-YAG mirror, transparent for them and finally focused on the camera.

To measure the infrared signal, two infrared detectors were used, both of them of J15D12 series from Teledyne Judson Technologies. These detectors are based on HgCdTe semiconductor compound with a square active area. The J15D12 detectors are sensitive in 2-12 µm wavelength range with detection peak at 11 µm. One detector was the J15D12-M204-S500U-60 (IRD-1) with an active area of 500 µm width, the second one was the J15D12-M204-S01M-60 (IRD-2) with active area of 1 mm width. In order to simplify the model and analysis, the active area will be considered as a circular area with diameter equal to the width of each detector.

The signal delivered by the infrared detector is amplified before to be sent to the lock-in amplifier. The lock-in uses the signal from the photodetector as reference to measure the amplitude and phase of the infrared signal. The lock-in amplifier used in the setup is the SR830 from Stanford Research Systems that have a frequency range from 1 mHz to 102 kHz. This gives the possibility to work in a wide frequency range beyond the possible for an infrared camera. Nevertheless, the phase measured by the lock-in amplifier takes into account the phase lag induced by the detector and the associated amplifier, thus, a calibration has to be done in order to obtain the real phase lag from the thermal behavior of the sample and this calibration procedure is detailed in section 2.3.5.

The measurement process requires that the surface of the sample under investigation be placed at the focal plane of the microscope objective, perpendicular to the propagation axis of the beam.

The sample is fixed on a micrometric translation stage in order to monitor its location. The translation stage allows scanning the sample surface by translation in the focal plane while the laser beam remains static. In this way, an image of the sample surface is constructed from point to point measurements with the mono-pixel sensor. More details about the scanning configuration are provided in section 2.3.6.

2.3.2 Heat source.

The radius of the heating area is an important parameter for further analysis of the obtained measurements. As mentioned before the heating area is the laser spot formed at the sample surface. Considering that the sample surface is located at the focal point of the microscope objective, the target parameter is the minimum radius produced by the objective, usually called beam waist w_0.

Since the laser employed as heat source operates in the fundamental mode (TEM_{00}), the beam has a Gaussian intensity profile. The laser propagation direction is denoted by z-axis in Figure 2.20 (a). Figure 2.20 (b) shows the intensity profile of the beam where φ_0 is the maximum flux power and y_0 is the center position of the distribution, the beam radius w, is defined at the power corresponding to $1/e^2$ of the maximum. Although only the y-axis is presented here the same distribution is applicable in the x-axis since a circular transversal profile of the laser is considered.

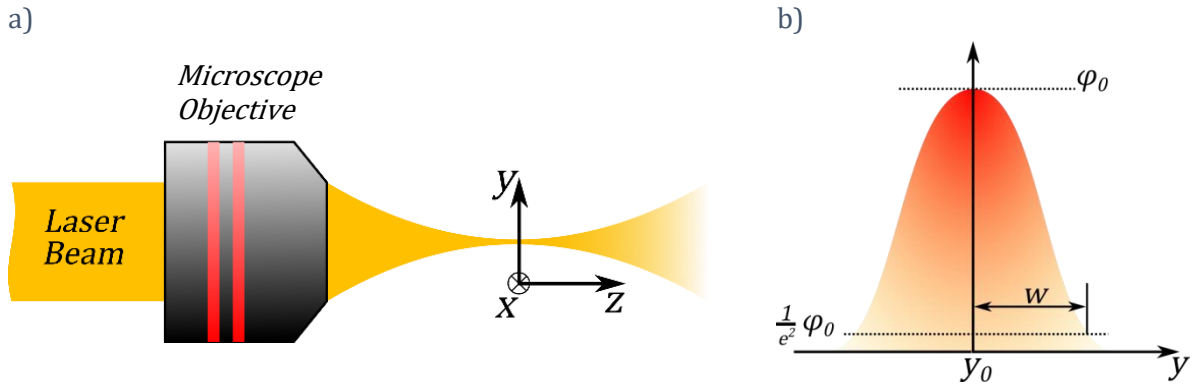

Figure 2.20 (a) Gaussian beam propagation. (b) Transversal Intensity distribution of the Gaussian beam.

In order to determine the spot radius of the focused laser, the knife-edge method for laser beam characterization has been implemented. It allows quick, inexpensive and accurate determination of the beam parameters. This technique consists in moving a knife's edge perpendicular to the direction of propagation of the laser beam and record the total transmitted power as a function of the knife's edge position like show Figure 2.21.

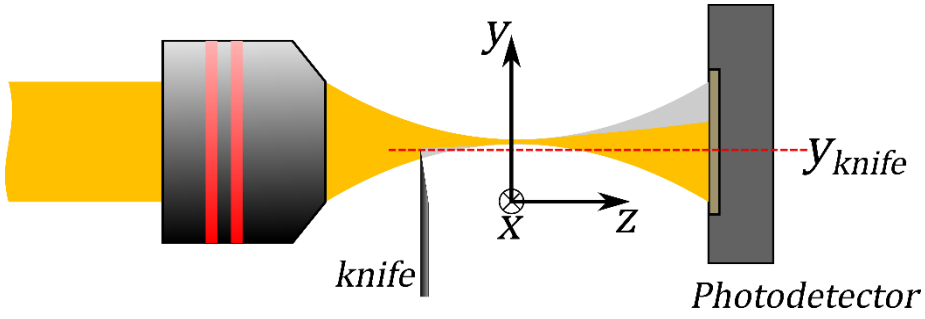

Figure 2.21: Scheme of knife-edge experiment.

For the analysis one supposes that the knife's edge is moved from -∞ to +∞ along the y-axis in a fixed position for the z-axis and that the length of the knife in x-axis direction is infinite. While the knife's edge is moving the power captured by the detector will decrease from a total power P_{max} to 0. The amount of power viewed by the photodetector can be expressed as function of the position of the knife's edge, y_{knife}.

To reach the expression one starts by expressing the transversal power density distribution of the beam in function of the (x, y) position as:

$$\varphi(x,y) = \varphi_0 e^{-\frac{2(x-x_0)^2}{w^2}} e^{-\frac{2(y-y_0)^2}{w^2}} \tag{2.20}$$

Where w is the beam radius, φ_0 is the maximum flux density and x_0 and y_0 are the central position of the Gaussian distribution in the x-axis and y-axis respectively. From here, integrating the power density distribution one obtains the total available power as:

$$P_{max} = \varphi_0 \int_{-\infty}^{+\infty} e^{-\frac{2(x-x_0)^2}{w^2}} dx \int_{-\infty}^{+\infty} e^{-\frac{2(y-y_0)^2}{w^2}} dy \tag{2.21}$$

$$P_{max} = \frac{\varphi_0 \pi}{2} w^2 \tag{2.22}$$

When the knife is blocking a portion of the beam from -∞ to y_{knife}, the power transmitted is expressed as:

$$P(y_{knife}) = \varphi_0 \int_{-\infty}^{+\infty} e^{-\frac{2(x-x_0)^2}{w^2}} dx \int_{y_{knife}}^{+\infty} e^{-\frac{2(y-y_0)^2}{w^2}} dy \tag{2.23}$$

With:

$$\int_{-\infty}^{+\infty} e^{-\frac{2(x-x_0)^2}{w^2}} dx = \sqrt{\frac{\pi}{2}} w \tag{2.24}$$

and:

$$\int_{y_{knife}}^{+\infty} e^{-\frac{2(y-y_0)^2}{w^2}} dy = \frac{1}{2}\sqrt{\frac{\pi}{2}} w \left(1 - \operatorname{erf}\left(\frac{\sqrt{2}(y_{knife} - y_0)}{w}\right)\right) \tag{2.25}$$

the power reaching the sensor as a function of the position of the knife in the y-axis is expressed as:

$$P(y_{knife}) = \frac{\varphi_0 \pi}{4} w^2 \left(1 - \text{erf}\left(\frac{\sqrt{2}(y_{knife} - y_0)}{w}\right)\right) \tag{2.26}$$

Normalizing it by the total power P_{max}, the expression of the normalized power captured by the photodetector is:

$$P_n(y_{knife}) = \frac{1}{2}\left(1 - \text{erf}\left(\frac{\sqrt{2}(y_{knife} - y_0)}{w}\right)\right) \tag{2.27}$$

In order to determine the beam radius $w(z)$ at a given position along the beam propagation z axis, one only has to perform the knife-edge experiment and fit the obtained curve with the equation (2.27).

Figure 2.22 shows the data from the knife-edge measurements (red squares) and the fitted curve using equation (2.27) (black line), where the two parameters w and y_0 were adjusted to obtain optimal fit. For this particular case the obtained diameter of the beam is 13.62 µm.

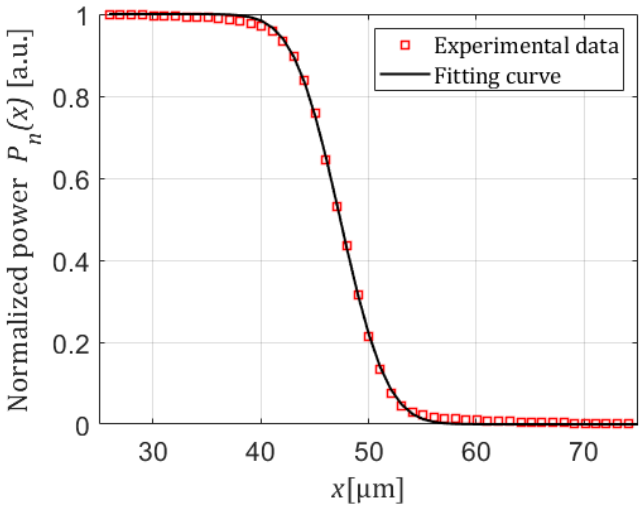

Figure 2.22 Experimental data from one knife-edge measurement (at $z = 25$ µm) and fitting curve (equation (2.27)) with optimal parameters $w = 6.81$ µm and y_0 =47.3 µm.

Considering a focused beam, it is obvious that the width of the intensity profile changes along the z-axis. Referring to Figure 2.23, the section with the smallest width is located at z_0 and the minimum radius, w_0, is called beam waist. The spot radius at distance $(z - z_0)$ from the beam waist expands as a hyperbola, which has the form:

$$w(z) = w_0 \sqrt{1 + \left(\frac{z - z_0}{z_R}\right)^2} \tag{2.28}$$

Parameter z_R is the Rayleigh range and it is the distance from the waist for which the beam area has doubled with radius $w(z_0 \pm z_R) = \sqrt{2} w_0$. The distance within $z_0 - z_R$ to $z_0 + z_R$ can be considered the region over which the beam is approximately collimated.

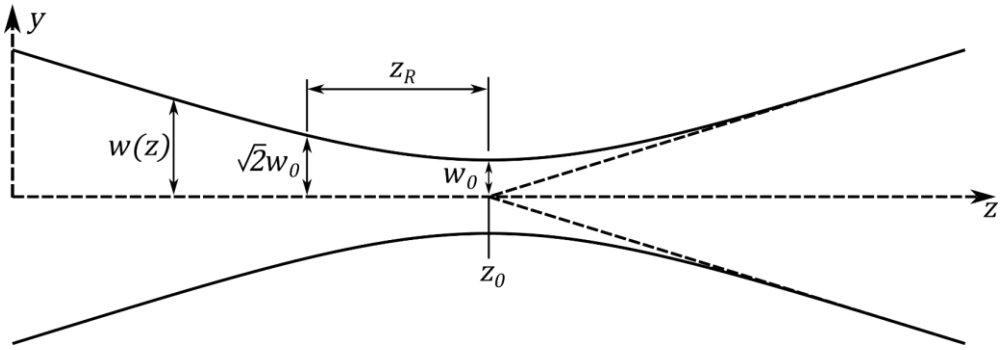

Figure 2.23 Diagram of Gaussian beam propagation near to the focal plane.

Therefore, to estimate the minimal spot radius and its location, one must apply the knife-edge method in different positions (z_i) around the focal plane of the microscope objective as presented in Figure 2.24 in order to get the beam radius $w(z_i)$ corresponding to each position. Finally, one fits the obtained values with equation (2.28) to extract the parameters w_0, z_0 and z_R.

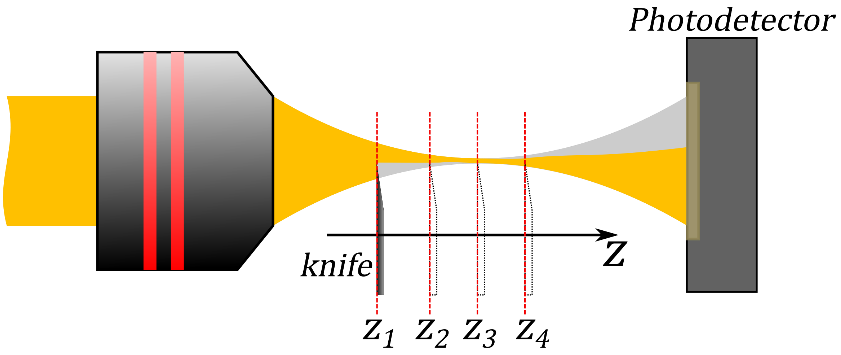

Figure 2.24 Representation of the beam radius measurement procedure with knife-edge method for several positions in z-axis.

In the laser beam characterization procedure, the knife-edge method was applied in 26 sections around the focal plane in z-axis with separation of 1 μm between each one. Thus, the experimental protocol covered a total of 25 μm distance along laser beam propagation axis.

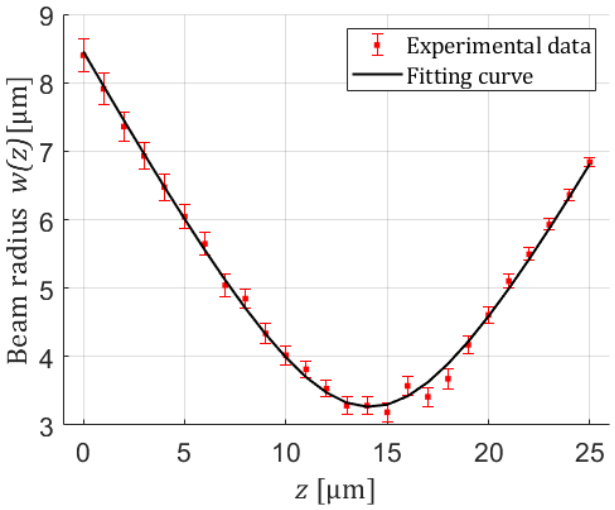

Figure 2.25 Experimental data from $w(z)$ measurements and fitting curve with equation (2.28) with optimal parameters $w_0 = 3.3$ µm, $b = 5.9$ µm and $z_0 = 14.14$ µm

The experimental measurements and the parameter identification process leads to the beam propagation curve shown in Figure 2.25. where the dots represent the experimental data and the black line represent the fitting curve with equation (2.28). The optimal values for the three parameters are: w_0= 3.3 µm, z_R=5.9 µm and z_0=14.1 µm.

2.3.3 Measurement area.

The measurement area is an important parameter for processing of data obtained from the experimental setup, since the measurement is highly sensitive to this parameter. The correct interpretation of the measurements will depend of the accuracy of this parameter and it is required to feed the thermal model in the parameter identification procedure.

The measurement area is the area over the sample that is seen by the sensor. In order to obtain the aimed area, one has to assess the magnification of the optical system, m, and apply it to the detector diameter D. In this way, the radius r_m, of the aimed area will be:

$$r_m = \frac{D}{2m} \tag{2.29}$$

The optical arrangement in the measurement chain is composed of two elements, the microscope objective with a focal length, f_{obj}=5 mm and the off-axis parabolic mirror with focal length f_{opm}=200 mm. The sample is placed at the focal plane of the microscope objective and the detector is placed at the focal plane of the off-axis parabolic mirror as shown in Figure 2.26.

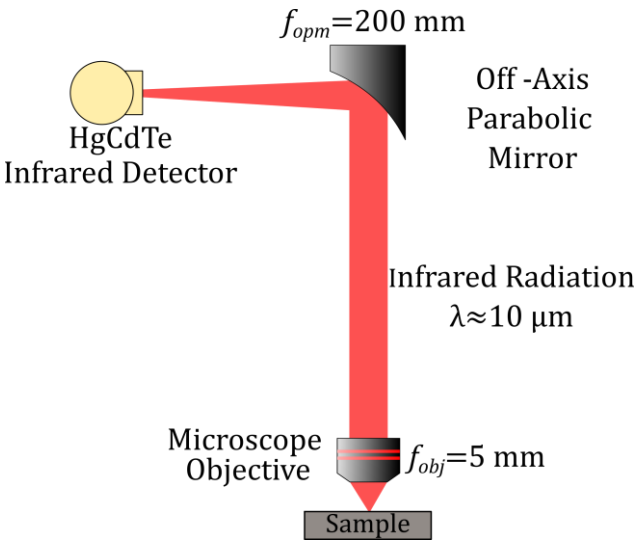

Figure 2.26: Optical arrangement for measurement of the infrared radiation.

Thus, the magnification of the optical collection system from the sample to the detector is given by the ratio of the focal lengths as:

$$m = \frac{f_{opm}}{f_{obj}} = 40 \tag{2.30}$$

The IRD-1 has an active area with diameter D= 500 μm so the measurement area on the sample surface has a radius r_m= 6.25 μm and for the IRD-2 with D= 1 mm one obtains r_m= 12.5μm.

2.3.4 Optical Alignment.

From the heat source characterization, one knows not only the size of the heating area but also its position in the z-axis. Thus, one can set this point as the new origin on the z-axis (the 0 mark) to make it coincident with focal plane. In this way with a well-defined measurement plane at position z=0 one can align the infrared detector and the visible camera to visualize the same point.

To align the infrared detector, it is mounted on a 3-axis displacement stage and placed at the focal distance of the off-axis parabolic mirror, obviously one does not place the detector at the exact focal point position but close to it, and the best position is researched by moving the detector with the micrometric translation stage in three axes. Since the knife is heated by the laser spot, it is emitting infrared radiation. Thus, one can follow the signal until reaching the maximum amplitude possible. It means that the detector aims the most heated area over the knife surface and this area is coinciding with the heat source. This procedure ensures that the measurement and heated area are aligned and their location is known.

The next step is the alignment of the visible camera in order to obtain an in-focus image of the knife and the laser spot. The magnification of the visible image is also 40x since a lens with focal length of 200 mm is used which is the same as focal length of the off-axis parabolic mirror. Once the three elements are aligned and fixed, one no longer has to worry about finding the correct position of the sample with the knife-edge method when one changes the sample. From now, it is only a question to get a sharp in-focus image from the visible camera which indicates that the sample is at the focal plane. In practice the sample can move in a 1 μm range and maintain an in-

focus image, without visible difference, this is because of the depth of field of the system. Nevertheless, this variation doesn't introduce a significant error in the measurements. It is discussed in details in the chapter dealing with applications.

2.3.5 Detector calibration.

The signal captured by the infrared detector is amplified before entering to the lock-in amplifier. To reach the best performance, each detector is coupled with a dedicated preamplifier. For the IRD-1 a PA-300 amplifier from Teledyne Judson Technologies is used. The PA-300 amplifier is designed to work in the 200 Hz to 100 kHz frequency range. A homemade amplifier with a frequency band ranging from 0.05Hz to 380 kHz is used with the IRD-2. These preamp stages add phase lag to the signal measured by the lock-in amplifier in function of frequency, f in Hz. Thus, the phase lag measured by the lock-in is expressed as:

$$\tilde{\phi}(f) = \phi(f) + \phi_D(f) \tag{2.31}$$

In this relation $\tilde{\phi}$ is the measured phase lag, ϕ is the thermal induced phase lag and ϕ_D is the phase lag introduced by the preamp stage in the measurement chain.

In order to avoid the influence of the measurement chain, the adding phase lag was measured experimentally. Figure 2.27 shows the experimental setup for the phase lag calibration. The infrared detector is exited directly by a laser source after the frequency modulation. The same laser source that excited the photodetector is used as reference. Since the detector is excited directly by the laser, there is no thermal phase lag in the measurements and only the influence of the measurement chain is measured.

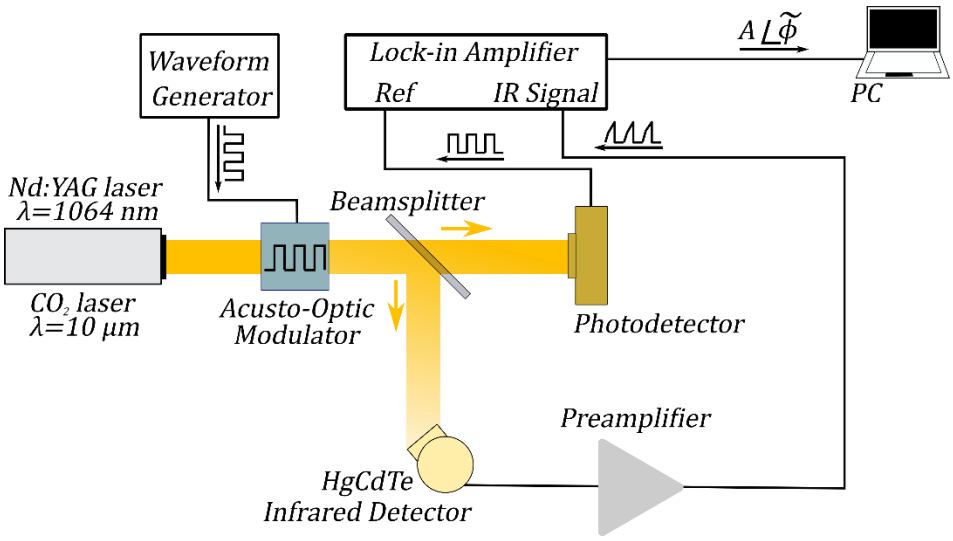

Figure 2.27: Scheme of the setup for calibration of the measurement chain phase lag.

A sweep in 200 Hz–100 kHz frequency range is done and the value for the phase lag in degrees as function of frequency is obtained.

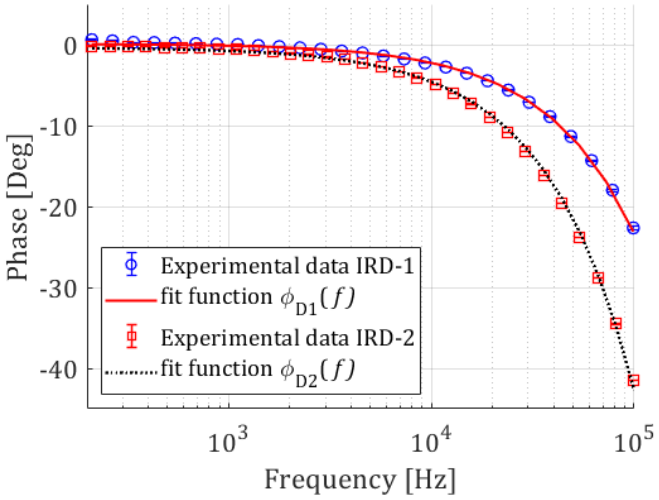

Figure 2.28: Phase lag calibration curve for the two infrared detectors.

The found function, ϕ_{D1}, that describes the phase lag of the IRD-1 chain is:

$$\phi_{D1}(f) = -2.34 \times 10^{-4} f + 0.09 \tag{2.32}$$

and the phase lag in the IRD-2 chain is described by:

$$\phi_{D2}(f) = -4.23 \times 10^{-4} f - 0.35 \tag{2.33}$$

Using the above relations, one can subtract the influence of the measurement chain from the lock-in measurements in order to obtain the phase lag corresponding to the thermal diffusion in the sample:

$$\phi = \tilde{\phi} - \phi_{Di} \tag{2.34}$$

2.3.6 The scanning configuration.

The previous paragraphs describe the manner for obtaining a one spot measurement. The imaging of sample surface is obtained by pixel by pixel measurements with the infrared sensor by scanning the sample surface.

In the scanning process the sample surface is translated at constant velocity in plane perpendicular to the laser beam propagation axis. For this, the sample is mounted over a 3-axis piezoelectric translation stage (P-611K101 from PI) with travel range 100 µm × 100 µm × 100 µm. The piezoelectric translation stage is equipped with a driver unit, the E-517 Digital Piezo Controller, which enables the control of the position and the displacement velocity with sub-micron precision. This precision displacement system is equipped with position sensors which allow knowing the position of the plate while a feedback loop guarantees the exact and well repeatable positioning of the plate, thus avoiding a possible phenomenon of hysteresis.

The scanning is performed on the sample surface parallel to the xy-plane and coincident with the focal plane of the laser beam. The scanned area is defined by the length L, along the x-axis and the width W, along the y-axis, as shown in Figure 2.29. That means that if we fix the frame of reference at one point on the sample surface, for the x-axis direction the spot is displaced from a

given initial point, x_0, to $x_0 + L$, where the position of the spot is defined by its center point. The same occurs in the y-axis direction, where the spot goes from y_0 as initial point to $y_0 + W$ at the end of the scanning.

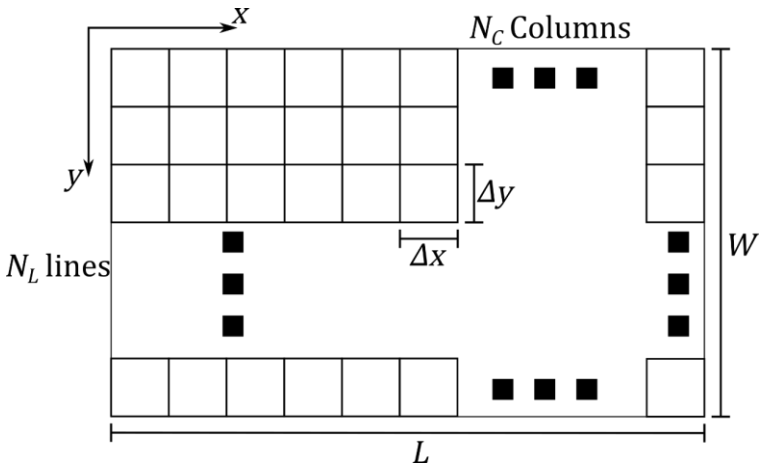

Figure 2.29: Scheme of the scanning - sampling process.

In the scanning process the area is divided in N_L lines along the y-axis and the lines are divided in N_C sampling segments equally distributed along the x-axis. The lines are scanned one by one from top to down, and each line from left to right.

Given the line length L, and the number of sampling segments, the sampling interval, Δx, is defined as the portion of the line that is measured at each segment, it is equivalent to the scanning resolution in the x-axis direction and is expressed as:

$$\Delta x = \frac{L}{N_C} \tag{2.35}$$

In the same way the sampling interval, Δy, corresponds to the scanning resolution in the y-axis direction, and is expressed as:

$$\Delta y = \frac{W}{N_L} \tag{2.36}$$

From this, the obtained image is recorded as a matrix of $N_L \times N_C$ pixels, with a well-defined pixel size. It is important to remark that this pixel size doesn't have to be equal to or limited in by the spot size which was defined as $2r_m$. Even more, smaller pixel will improve the image resolution and the capability to detect geometries smaller than the probe size.

In addition, there is a difference in the physical implications between the x-direction resolution and the y-direction resolution. To explain it, one has to keep in mind that each line is scanned at constant velocity, v, and the lock-in amplifier is continuously measuring. So that, the value obtained for each segment Δx contains the average of the information recorded along the travel though this segment, from x_0 to $x_0 + \Delta x$. On the other hand, the resolution in y-axis direction means that the distance between two consecutive lines (with the center of the spot as reference) is equal to Δy, but there is no velocity implication in this direction.

The selected velocity in the scanning process affects the measurements in two different ways, one is linked to the thermal behavior of the sample when it is submitted to a motion heat flux and the second is linked to the data acquisition of the lock-in. One will deal with the first one in the chapter 3 since it is related to the mathematical model. For the second one, it is important to remember that the lock-in is based on a phase sensitive detector following by a low pass filter which is defined by its time constant. The time constant is the necessary time that the filter needs to reach the final value and a narrower filter needs a higher time constant. In the lock-in, a narrower bandwidth will remove noise sources very close to the reference frequency, a wider bandwidth allows these signals to pass, so, one can select a bigger time constant in order to get more accurate measurement, especially for signals with low signal to noise ratio. Thus, one has to take into account the lock-in acquisition configuration when the scanning velocity is selected. In addition, for the lowest limit of the time constant one has to consider the excitation frequency used in the study since it's needed to reach a stationary thermal behavior at each location on the surface.

If one defines the sampling time, Δt, as the necessary time to travel the sampling interval Δx, the scan velocity is obtained as:

$$v = \frac{\Delta x}{\Delta t} \tag{2.37}$$

On the other hand, the time constant, T_C, is the time required for the lock-in to perform the measurement of amplitude and phase. Thus, in order to have consistent measurements, one must set the time constant as the minimum sampling time. In other words, the sampling time must satisfy the condition:

$$\Delta t \geq T_C \tag{2.38}$$

Otherwise the information from two consecutive pixels or more will be overlapped and this will lead to wrong results, since the pixel resolution will be lost. In the experiments presented in this work we choose $T_c = \Delta t$.

The total time required to scan one line is thus:

$$t = N_C \times \Delta t \tag{2.39}$$

With these parameters one can configure the E-517 controller to perform the scanning line by line at constant velocity, v, from x_0 to $x_0 + L$.

In addition, because the probe is not subject of wears, one can sweep the same line as many times as needed in order to improve the average result before to jump to the next one. In this way one can obtain better experimental results than in a simple sweep configuration. Thus, the SL parameter is introduced as the number of sweeps per line that are averaged for the final result. Table 2.2 collects all parameters involved in the scanning process.

Parameter	Description
L	Scan length
W	Scan width
Δx	Sampling interval x-axis
Δy	Sampling interval y-axis
Δt	Sampling time
v	Scan velocity
f	Excitation frequency
SL	Sweeps by line

Table 2.2: Summary of scanning parameters.

2.3.7 Scanning-Measurement synchronization.

To synchronize the data acquisition from the lock-in with the sampling interval, the E-517 Digital Piezo Controller was programed to send a trigger signal when the platform has traveled the sampling interval.

The trigger behavior from the piezo controller in this configuration is represented in Figure 2.30. The graphic shows that a trigger pulse is written whenever the axis has covered the distance set as trigger steep.

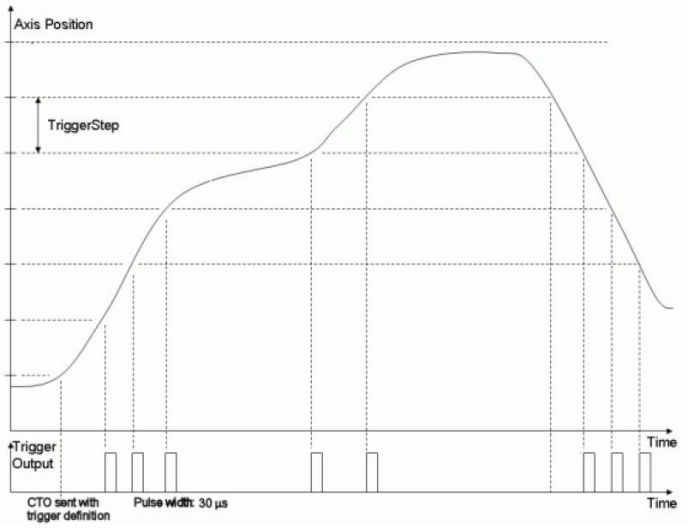

Figure 2.30: E-517 trigger behavior.

On the other hand, the lock-in is configured to record the amplitude and phase each time it is triggered on. The recorded data are added to the storage buffer and the buffer is read and flushed after scanning each line. The SR830 can store up to 16383 points in the buffer and the maximum sampling rate is 512 Hz. This sampling rate sets the lowest limit for the sample time, which has to be always $\Delta t \geq 2$ms.

2.4 Conclusions.

In this chapter we have presented two scanning experiments a first one in contact mode and a second one in contactless mode. Both are based on the modulated photothermal radiometry.

In the contact mode experiment we proposed a new kind of probe based on the use of an optical fiber working at both the wavelength of the laser and that of the infrared emission. The idea behind the probe is to generate and monitor the temperature change in a small tip that works as the heater and the sensor at the same time. For this we design a probe based on a optical fiber with a small metallic tip attached at the end. The metallic tip is heated with a modulated laser supplied trough the fiber and the IR emitted is collected by the same fiber. Under this configuration it was possible to discriminate the contact between the probe and two different materials. Nevertheless, because of the size of the metallic tip, only the analysis of the data at frequency below 80 Hz could be used to achieve the thermal characterization of the investigated materials. Although the basic idea is simple, its implementation is challenging and we think that it would take too much time to find the suitable technological solutions.

We have therefore chosen to develop a contactless method based on modulated photothermal radiometry in a scanning configuration, namely SPR. Thus, a second scanning experimental configuration was presented in this chapter. In the SPR we replace the optical fiber probe by a Cassegrain microscope objective. The reflective microscope objective allows to focus the laser beam directly over the sample and to collect the IR emitted as consequence. After the description of the experimental setup, we showed the characterization of the spot formed by the microscope objective on the sample surface and the aimed area from the IR detector. In addition, we showed the calibration of the infrared detectors used in order to correct the phase lag induced by the measurement chain at high frequencies. Finally, we presented a detailed description of the scanning process and the parameters involved. We define the configuration and the synchronization of the sweep at constant velocity and the data acquisition.

Chapter 3:
Model describing the experimental measurement.

3.1 Introduction.

In this chapter we will focus on the mathematical model that describes the heat transfer process in the sample under investigation with the experimental conditions presented in the previous chapter. The simulated quantities (amplitude and phase) will be compared with the experimental results in the parameter identification process using an inverse procedure.

As pointed out with the description of the scanning configuration, the scanning velocity is a fundamental parameter in the data acquisition process, and it has to be taken into account in the scan parameter selection. This parameter must be considered with respect to the frequency of the photothermal excitation, the time constant for the integration of the measurement within the lock-in amplifier and with the sampling time. All together those parameters will lead to a possible smoothness of the measured signal according to the spatial resolution. Now as starting point, we will show that the velocity used in the experiment is too slow to significantly modify the heat diffusion profile in the investigated medium. Therefore, the amplitude and phase at the aimed area by the IR detector can be calculated with the model for motionless conditions. The analysis of the experiments in contactless mode will be done assuming the sample is an opaque material and the photothermal excitation is absorbed on its surface. Thus, the modulated laser can be modeled as a boundary heat source at the sample surface.

In order to verify the correct operation of the setup and to validate the experimental assumptions, measurements will be performed on a known stainless-steel bulk sample. The sample will behave as a semi-infinite medium submitted to a Gaussian heat flux on its surface and the analytical solution for the measured temperature will be derived. The calculated temperature produced by a Gaussian heat flux will be compared with the ones obtained considering a uniform and point heat flux. In addition, the analytical solution for the semi-infinite media in static conditions will be compared with the numerical model for the semi-infinite media that moves at constant velocity with respect to the photothermal source. This numerical solution will be obtained from the finite element method (FEM) using the software Comsol Multiphysics.

Then, an analytical solution is presented for the multilayer sample. This model is developed in order to simulate the behavior of the 3-ω sample in static condition and verify the correct operation of the SPR before the scanning. Indeed, in the high frequency regime the stack of layers cannot be treated as a thermal resistance as it is the case at the low frequency regime.

Finally, in the last section of this chapter the general formulation of the parameter identification method used in this work will be presented. It is classically based on an inverse procedure based on the nonlinear least square technique.

3.2 The influence of the scan velocity.

We have established that the scanning is performed at constant velocity that is an important parameter regarding the experimental data processing. We will analyze the influence of the velocity in the thermal response of the sample and its impact in the measured temperature by the IR detector.

A number of problems in configuration of heating by a fixed source over uniformly moving medium may be solved by integration of the solutions for instantaneous sources. In the present case, a periodic heat flux is applied as:

$$\varphi = \varphi_0 \cos(\omega t) \tag{3.1}$$

Where ω is the angular frequency, defined as: $\omega = 2\pi f$, with frequency f in Hz. The average temperature over the measured area, which is assumed to be a disk, is obtained using the convolution between the average impulse response over the heated disk and the heat flux as:

$$T(x,y,z,t) = \int_0^t \bar{h}(t-\tau)\, \varphi_0 \cos(\omega\tau)\, d\tau \tag{3.2}$$

To define the average impulse response, we will start by presenting the impulse response for a motionless disk heat source of radius w_0 at the surface of a semi-infinite medium as [27], [118]:

$$h(x,y,z,t) = \frac{1}{2\rho C_p \sqrt{\pi}(at)^{3/2}} \int_0^{w_0} r' e^{\frac{x^2+y^2+z^2+r'^2}{4at}} I_0\left(\frac{\sqrt{x^2+y^2}\, r'}{2at}\right) dr' \tag{3.3}$$

Where ρC_p is the volumetric heat capacity, a is the thermal diffusivity and I_0 is the modified Bessel function of first kind and order 0. Now, let's consider the source is moving at constant velocity v in the reference frame of the sample. Then the impulse response can be written as:

$$h(x,y,z,t) = \frac{1}{2\rho C_p \sqrt{\pi}(at)^{3/2}} \int_0^{w_0} r' e^{\frac{(x-vt)^2+y^2+z^2+r'^2}{4at}} I_0\left(\frac{\sqrt{(x-vt)^2+y^2}\, r'}{2at}\right) dr' \tag{3.4}$$

We have to remember that the heat source (the laser spot) is in a fixed position and the sample is moving along the x-axis at constant velocity v. For the reference fixed at the center of the heat source, the temperature profile is moving because the sample is moving. Thus, we are interested in the temperature distribution around the heat source. Therefore, it is more convenient to have the frame of reference fixed on the heat source (blue frame in Figure 3.1).

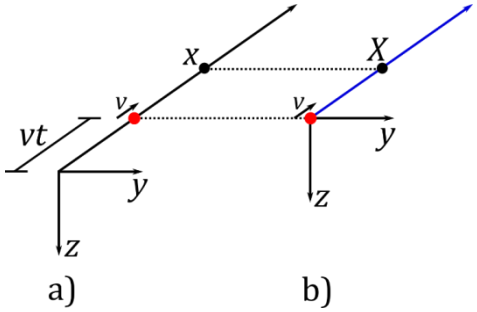

Figure 3.1: Moving heat source: (a) coordinates *x, y, z* fixed on the sample and (b) moving coordinates fixed on the heat source *X , y, z*.

As shown in Figure 3.1 the change in frame of reference can be done introducing a new coordinate X defined by:

$$X = x - vt \;\rightarrow x = X + vt \tag{3.5}$$

The impulse response in this case is written as:

$$h(X,y,z,t) = \frac{1}{2\rho C_p \sqrt{\pi}(at)^{3/2}} \int_0^{w_0} r' e^{\frac{(X+vt)^2+y^2+z^2+r'^2}{4at}} I_0\left(\frac{\sqrt{(X+vt)^2+y^2}\, r'}{2at}\right) dr' \tag{3.6}$$

Where X denotes the coordinate of the source at time t in the frame of reference fixed to the source. One must notice that:

$$e^{\frac{(X+vt)^2}{4at}} \approx e^{\frac{X^2}{4at}}, \qquad \text{when } \left(\frac{Xv}{2a} + \frac{v^2 t}{4a}\right) \ll 1 \tag{3.7}$$

It is possible to evaluate the behavior over one period of time using the characteristic length for the heat diffusion. With the modulated excitation at frequency f, the period is $\tau = 1/f$, and the characteristic length of the system is the diffusion length: $l_h = \sqrt{a/\pi f}$.

Therefore, one can state that:

$$\left(\frac{Xv}{2a} + \frac{v^2 t}{4a}\right) = \left(\frac{l_h v}{2a} + \left(\frac{l_h v}{2a}\right)^2\right) \tag{3.8}$$

Hence, one can recognize the thermal version of the Péclet number (P_e) in expression (3.8) that represents the ratio of heat transfer by convection to heat transfer by conduction and that is defined as: $P_e = l_h v/a$

Thus, one can say that:

$$e^{\frac{(X+vt)^2}{4at}} \approx e^{\frac{X^2}{4at}}, \qquad \text{when } P_e \ll 1 \tag{3.9}$$

Figure 3.2 shows the Péclet number for thermal diffusivity $a = 10^{-7}$ m²·s⁻¹ (notice that for higher values of a, P_e will be lower), using two values for the velocity and the frequency in the range available for scanning in the SPR experiment, namely, $v = 1$,and 20 µm s⁻¹, and the 1 to 100 kHz frequency rage. It demonstrates that in these conditions the Péclet number is largely lower than 1, $P_e \ll 1$.

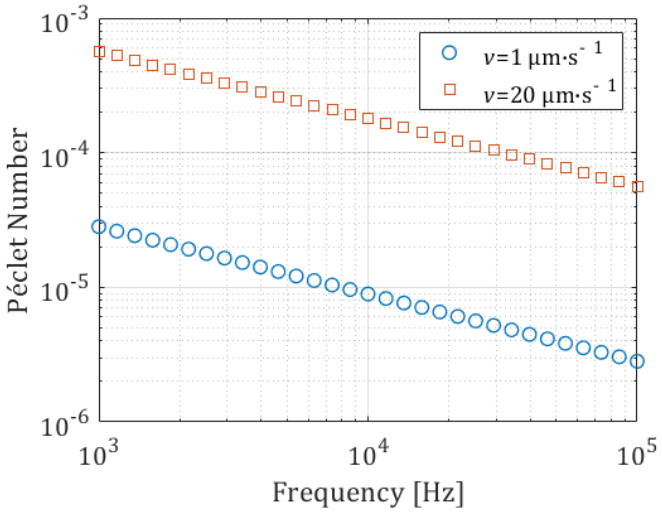

Figure 3.2: Péclet number for two scan velocities v and thermal diffusivity $a = 1 \times 10^{-7}$ m²·s⁻¹ according to frequency range exploited in the SPR measurement.

On this basis, it can be considered that the impulse response for a moving sample at z=0 is that calculated in the motionless configuration as:

$$h(r,t) = \frac{1}{2\rho C_p \sqrt{\pi}(at)^{3/2}} \int_0^{w_0} r' e^{-\frac{r^2+r'^2}{4at}} I_0\left(\frac{r\,r'}{2at}\right) dr' \tag{3.10}$$

with $r^2 = X^2 + y^2$.

The average impulse response over the measurement disk with radius r_m is thus:

$$\bar{h}(t) = \frac{1}{\rho C_p \sqrt{\pi}\,(at)^{3/2}\, r_m^2} \int_0^{r_m} \int_0^{w_0} r' e^{-\frac{r^2+r'^2}{4at}} I_0\left(\frac{r\,r'}{2at}\right) dr' r dr \tag{3.11}$$

Since the work is based on a modulated excitation and can be approximated as a motionless configuration, one can predict the influence of the diffusion length in the experimental configuration. If one compares r_m with the diffusion length of different materials as a dimensionless ratio r_m/l_h, plotted in Figure 3.3, one observes the values close to the unity at different frequencies. Thus, although the dimension of the sample in radial coordinate could be considered infinite, the measurement area is in the same order of magnitude at different excitation frequency. That suggests that the measurement setup will be sensitive to the heat diffusion for a wide range of materials.

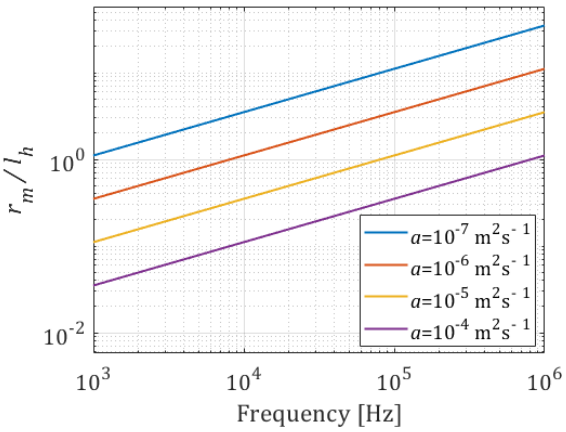

Figure 3.3: Dimensionless ratio r_m/l_h with $r_m = 6.25$ µm for different thermal diffusivity values: $a = 10^{-7}, 10^{-6}, 10^{-5}, 10^{-4}$ m²·s⁻¹.

As it is usual for a new experimental setup, first it was applied on a well know material in order to validate the experimental configuration. To perform this validation, the measurement on a steel bulk sample was performed.

In order to perform the bulk sample study, one will start by modeling the general case of the heat transfer in an orthotropic and semi-infinite media. Although the actual configuration of the experimental setup limits its operation up to 100 kHz, the analysis of the model will be in a wider range in order to have a full picture of the behavior.

3.3 Heat transfer in a semi-infinite media submitted to a heat flux with Gaussian distribution.

The previous investigation does not account for the spatial distribution of the heat source at the surface of the sample. We will start by the general description of the heat transfer in a material with orthotropic thermal conductivity in semi-infinite configuration. As the heat flux spot is circular in geometry, the system has cylindrical rotational symmetry around the z axis. The solution of the heat diffusion equation will therefore be made in the 2D axisymmetric cylindrical coordinates (r, z), as depicted in Figure 3.4.

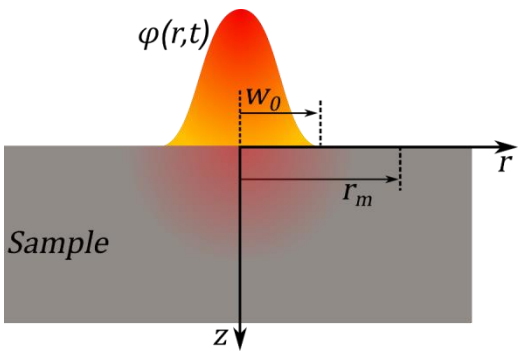

Figure 3.4: Geometrical representation of a semi-infinite sample submitted to a Gaussian heat flux on its top surface.

As it has already been established in Chapter 2 (section 2.3.2 Heat source) the heat flux, $\varphi(r,t)$, is applied over the sample surface. The shape of the spot is a disk with radius w_0 with a Gaussian power density distribution. If we consider a periodic excitation, the heat flux on the sample surface is described as:

$$\varphi(r,t) = \varphi_0 \sin(\omega t)\, e^{-2\left(\frac{r}{w_0}\right)^2} \tag{3.12}$$

Considering the thermal conductivity directionally dependent, one defines k_r as the thermal conductivity along the radial coordinate (r) or in plane, and k_z as the thermal conductivity in transverse (z) coordinate or out of plane. Then, the periodic temperature on the sample surface is (see appendix III):

$$\theta_0(r,\omega) = \frac{\varphi_0 w_0^2}{4k_z} \int_0^\infty \frac{\alpha}{\beta} e^{-\frac{(\alpha w_0)^2}{8}} J_0(\alpha r)\, d\alpha \tag{3.13}$$

With $\beta = \sqrt{\frac{\rho C_p p + k_r \alpha^2}{k_z}}$

Where J_0 is the Bessel function of the first kind of order 0. Finally, the expression for the average temperature on a disk of radius r_m is

$$\bar{\theta}_G(j\omega) = \frac{\varphi_0(\omega) w_0^2}{2k_z r_m} \int_0^\infty \sqrt{\frac{k_z}{\rho C_p\, j\omega + k_r \alpha^2}}\; e^{-\frac{(\alpha w_0)^2}{8}} J_1(\alpha r_m)\, d\alpha \tag{3.14}$$

Where J_1 is the Bessel function of the first kind of order 1 and ρC_p is the volumetric heat capacity of the material at constant pressure. The integral is computed numerically using the global adaptive quadrature and default error tolerances (routine INTEGRAL in MATLAB).

From equation (3.14), one can express the amplitude and the phase of the periodic temperature variation as:

$$\left\|\bar{\theta}_G(\omega)\right\| = \sqrt{\mathbf{Re}[\,\bar{\theta}_G(j\omega)] + \mathbf{Im}[\bar{\theta}_G(j\omega)]} \tag{3.15}$$

$$\phi_G(\omega) = \arg[\bar{\theta}_G(\omega)] \;= \arctan\left[\frac{\mathbf{Im}[\bar{\theta}_G(j\omega)]}{\mathbf{Re}[\,\bar{\theta}_G(j\omega)]}\right] \tag{3.16}$$

As mentioned in chapter 2, we have no access to the absolute measurement because, in general, we don't know the optical properties of the material under study. Nevertheless, it is possible to see the amplitude signal as a normalized magnitude with respect to its maximum value in the frequency sweep. In this way one can write the definition of normalized amplitude, Θ, as a dimensionless amplitude:

$$\Theta_G(\omega) = \frac{\left\|\bar{\theta}_0(j\omega)\right\|}{\max\left(\left\|\bar{\theta}_0(j\omega)\right\|\right)} \tag{3.17}$$

With the presented model for the superficial temperature expressed in equation (3.14) one can evaluate the reduced sensitivity function in order to see the influence of the different parameters in different frequency regions and their correlation. One can define the vector of parameters, $\boldsymbol{a}$, as:

$$\boldsymbol{a} = [w_0, r_m, k_r, k_z] \tag{3.18}$$

The reduced sensitivity function of the amplitude is defined as:

$$S_{\Theta_G}(a_i, \omega) = a_i \frac{\partial \Theta_G(a_i, \omega)}{\partial a_i} \approx a_i \frac{\Theta_G(a_i, \omega) - \Theta_G(a_i - \Delta a_i, \omega)}{\Delta a_i} \tag{3.19}$$

And for the phase is:

$$S_{\phi_G}(a_i, \omega) = a_i \frac{\partial \phi_G(a_i, \omega)}{\partial a_i} \approx a_i \frac{\phi_G(a_i, \omega) - \phi_G(a_i - \Delta a_i, \omega)}{\Delta a_i} \tag{3.20}$$

In order to analyze the possible application of the method to a wide range of materials, we have considered a constant volumetric heat capacity as: $\rho C_p = 3$ MJ·m^{-3}·K^{-1}, while the thermal conductivity varies as $k_z = 0.3, 150, 300$, W·m^{-1}·K^{-1}and $k_r = 0.1, 50, 280$ W·m^{-1}·K^{-1}. In this way, diffusivity values in the 10^{-4} to 10^{-7} m^2·s^{-1} range are obtained. With radiuses w_0=3.3 µm and r_m=6.25 µm, the sensitivity function is calculated using a variation of ten percent of the fixed value for each parameter ($\Delta a_i = a_i \times 0.1$).

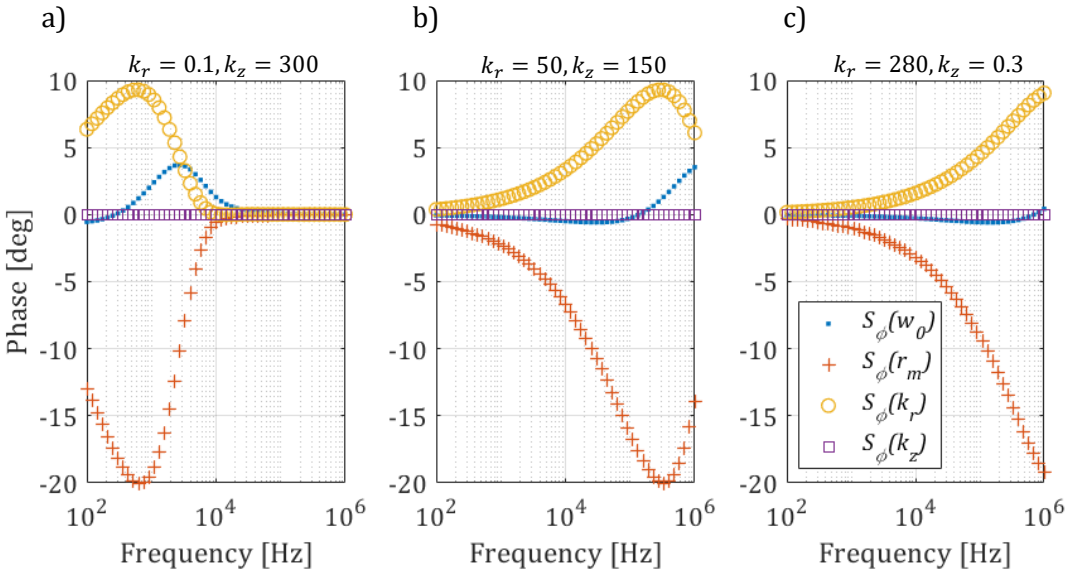

Figure 3.5: Reduced sensitivity function $S_\phi(a_i)$ using $\rho C_p = 3$ MJ·m^{-3}·K^{-1}, calculated for parameters: $w_0 = 3.3$ µm, $r_m = 6.25$ µm and a) $k_r = 0.1$ W·m^{-1}·K^{-1}, $k_z = 300$ W·m^{-1}·K^{-1}; b) $k_r = 50$ W·m^{-1}·K^{-1}, $k_z = 150$ W·m^{-1}·K^{-1}; c) $k_r = 280$ W·m^{-1}·K^{-1}, $k_z = 0.3$ W·m^{-1}·K^{-1}.

Figure 3.5 shows the phase sensitivity curves S_{ϕ_G} for the four parameters with three different pairs for thermal conductivity (k_r, k_z). It can be noticed that under this configuration the model is not sensitive to the out-of-plane thermal conductivity (purple square) in the investigated frequency range. On the other hand, the model shows an important sensitivity to the in-plane thermal conductivity, whose maximum is displaced to higher frequencies for higher thermal conductivity. This frequency shift of the most sensitive zone is related with the increase of the diffusion length for higher thermal diffusivity and its relation with the size of the measurement spot. As shown in Figure 3.3, r_m/l_h>2 take place at higher frequency for higher thermal diffusivity and this mark the transition to the 1D behavior (Figure 3.9-a).

In addition, Figure 3.5 shows that the influence of the measurement radius is more important than the in-plane thermal conductivity. Thus, one has to pay attention to the measurement area since the results will be highly dependent on this parameter. The influence of the heating radius appears lower than that of the measurement radius, and becomes close to zero for highly conductive materials.

The sensitivity plots for the normalized amplitude S_{Θ_G} are presented in Figure 3.6, here one observes a similar behavior that on the phase.

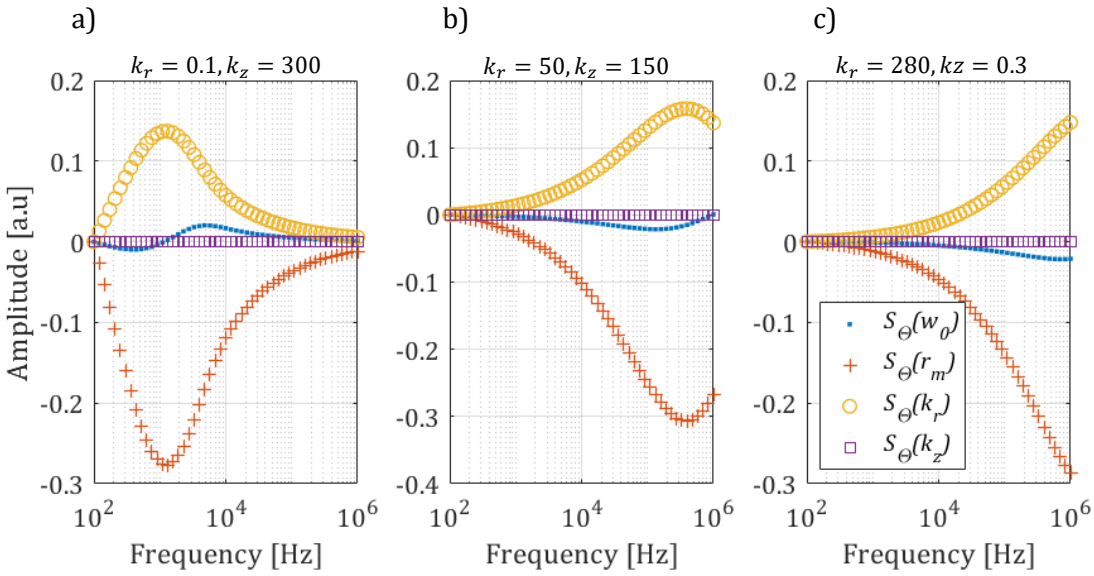

Figure 3.6: Reduced sensitivity function $S_\Theta(a_i)$ using $\rho C_p = 3$ MJ·m^{-3}·K^{-1}, calculated for parameters: $w_0 = 3.3$ µm, $r_m = 6.25$ µm and a) $k_r = 0.1$ W·m^{-1}·K^{-1}, $k_z = 300$ W·m^{-1}·K^{-1}; b) $k_r = 50$ W·m^{-1}·K^{-1}, $k_z = 150$ W·m^{-1}·K^{-1}; c) $k_r = 280$ W·m^{-1}·K^{-1}, $k_z = 0.3$ W·m^{-1}·K^{-1}.

Because the model is only sensitive to the in-plane thermal conductivity, a simplification of the model can be done in order to work with an isotropic approach. Nevertheless, it is important to note that the lack of sensitivity to the out-of-plane component of the thermal conductivity is a particular result of the normalization of the amplitude. If one knows the optical properties of the sample, then amplitude of absolute temperature variation can be measured and the influence of the out-of-plane component of the thermal conductivity will be observable on the sensitivity plot for the amplitude.

3.3.1 Simplification for isotropic assumption.

In the case of an isotropic material the in-plane and out-of-plane thermal conductivity are equal. So, one can define a unique thermal conductivity, k, and make:

$$k_z = k_r = k \tag{3.21}$$

Under this assumption the equation (3.13) becomes:

$$\theta_0(r,\omega) = \frac{\varphi_0 w_0^2}{4k_z}\int_0^\infty \frac{\alpha}{\sqrt{\frac{\rho C_p\, j\omega}{k}+\alpha^2}} e^{-\frac{(\alpha w_0)^2}{8}} J_0(\alpha r)\, d\alpha \tag{3.22}$$

and introducing the thermal diffusivity $a = k/\rho C_p$, the average temperature on a disk of radius r_m is expressed as:

$$\bar{\theta}_g(j\omega) = \frac{\varphi_0(\omega) w_0^2}{2kr_m}\int_0^\infty \frac{1}{\sqrt{\frac{j\omega}{a}+\alpha^2}}\, e^{-\frac{(\alpha w_0)^2}{8}} J_1(\alpha r_m)\, d\alpha \tag{3.23}$$

Thus, phase and amplitude in function of frequency are calculated as:

$$\phi_g(\omega) = \arg\left[\,\bar{\theta}_g(j\omega)\right] \tag{3.24}$$

$$\Theta_g(\omega) = \frac{\left\|\bar{\theta}_g(j\omega)\right\|}{\max\left(\left\|\bar{\theta}_g(j\omega)\right\|\right)} \tag{3.25}$$

As for the orthotropic case, one can use $\phi_g(\omega)$ to evaluate the reduced sensitivity function (equation (3.20)) for phase, $S_{\phi_g}(a_i,\omega)$, with the parameters, $\boldsymbol{a} = [w_0, r_m, k]$ and ρC_p=3 MJ·m^{-3}·K^{-1}. Because no effect of k_z was observed, we will use k=k_r= 0.1, 50, 280 W·m^{-1}·K^{-1} to evaluate the sensitivity. The obtained plots are shown in Figure 3.7.

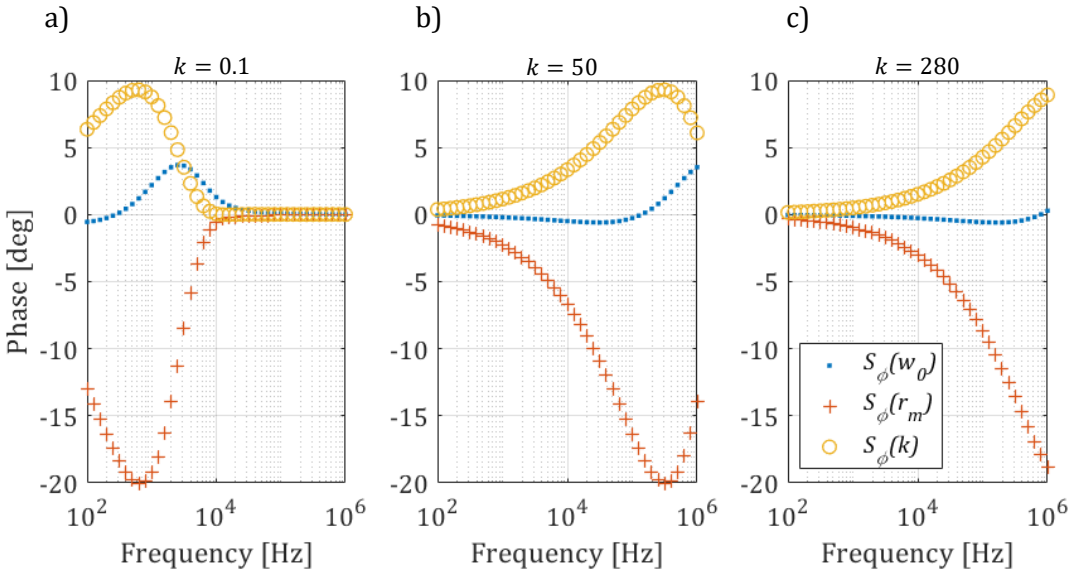

Figure 3.7: Reduced sensitivity function $S_{\phi g}\,(a_i)$ for isotropic material using ρC_p = 3 MJm^{-3}K^{-1}, calculated for parameters: w_0 = 3.3 µm, r_m = 6.25 µm and a) k = 0.1 Wm^{-1}K^{-1}; b) k = 50 Wm^{-1}K^{-1}; c) k = 280 Wm^{-1}K^{-1}.

As expected, the sensitivity to the thermal conductivity in the isotropic model is equal to the one obtained for the radial thermal conductivity in the orthotropic one. In addition, the reduced sensitivity plots suggest a correlation between r_m and k_r at almost all frequencies. The correlation is more obvious when we calculate the ratio of the sensitivity functions, $S_{\phi g}(k)/S_{\phi g}(r_m)$, as presented in Figure 3.8.

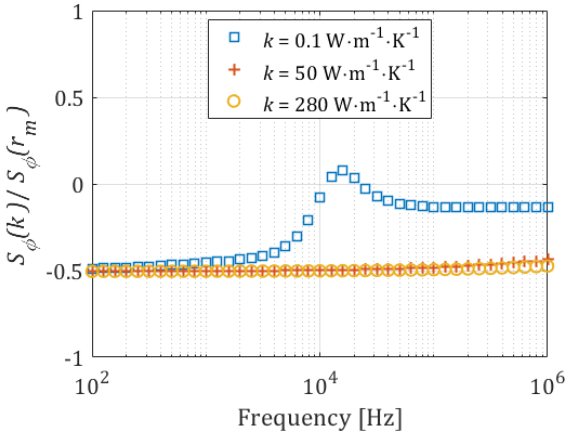

Figure 3.8: Ratio of the reduced sensitivity functions ($S_{\phi g}(k)/S_{\phi g}(r_m)$) with three different thermal conductivities.

One can observe that for high thermal conductivities the ratio is constant in all frequency range. At low frequency, k=0.1 W·m^{-1}·K^{-1}, there is a small variation between two constant levels that corresponds to the frequency range at which the sensitivity approaches zero.

Figure 3.9 shows the plots obtained for the phase and amplitude with both models (equation (3.14) for orthotropic model and equation (3.23) for isotropic model), with the isotropic thermal conductivity equal to the orthotropic in-plane thermal conductivity.

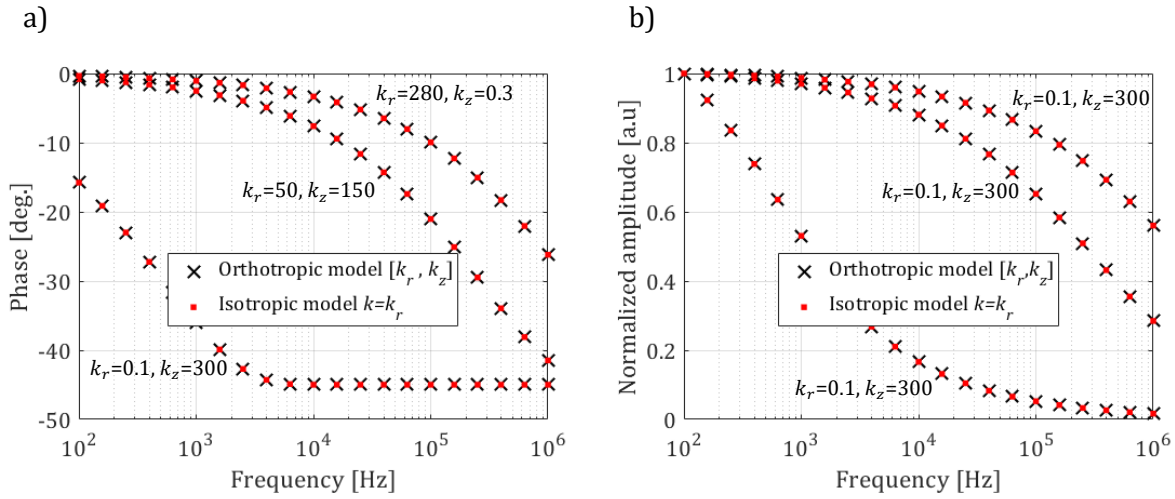

Figure 3.9: Comparison of phase (a) and amplitude (b) of orthotropic model (equation (3.14)) and isotropic model (equation (3.23)) for a semi-infinite media.

The previous analysis shows that in a semi-infinite medium, the model considering orthotropic thermal conductivity is mainly sensitive to the in-plane heat diffusion. In addition, because of the low influence of the out-of-plane thermal conductivity, the simplification to an isotropic model can be made.

In the other hand, one can wonder about the influence of the flux spatial distribution that in reality could be not a perfect Gaussian profile. Thus, in order to have an approximation of how the distribution profile influence the calculated quantities (amplitude and phase), we will model the heat flux as a uniform distribution and as a point source.

3.3.2 Uniform disk Heat flux and punctual heat flux.

Considering the flux distribution, φ_u, applied on the sample surface as a uniform disk of radius w_0, the expression for the heat flux after Laplace and Henkel transform is:

$$\tilde{\psi}(\alpha, p) = \mathcal{H}\left[\mathcal{L}[\varphi_u(r,t)]\right] = \frac{\varphi_0 w_0 J_1(\alpha w_0)}{\alpha} \tag{3.26}$$

Using the expression of the uniform heat flux in the boundary condition applied on the sample surface the temperature expressed by equation (3.22) becomes:

$$\theta_0(r, j\omega) = \frac{\varphi_0 w_0^2}{k} \int_0^\infty \frac{J_1(\alpha w_0)}{\sqrt{\alpha^2 + \frac{j\omega}{a}}} J_0(\alpha r)\, d\alpha \tag{3.27}$$

And the expression for the average temperature on a disk of radius r_m in function of the excitation frequency ω is:

$$\bar{\theta}_u(j\omega) = \frac{2\varphi_0(\omega) w_0}{k r_m} \int_0^\infty \frac{J_1(\alpha w_0)\, J_1(\alpha r_m)}{\alpha\sqrt{\alpha^2 + \frac{j\omega}{a}}}\, d\alpha \tag{3.28}$$

The phase of the periodic temperature variation is:

$$\phi_u = \arg[\bar{\theta}_u(j\omega)] \tag{3.29}$$

The normalized amplitude of the periodic temperature variation is:

$$\Theta_u(\omega) = \frac{\left\|\bar{\theta}_u(j\omega)\right\|}{\max\left(\left\|\bar{\theta}_u(j\omega)\right\|\right)}$$

In addition, when the radius of the heat source is lower than the diffusion length, the heat source can be approached to the punctual source. Thus, if $w_0 \ll \sqrt{a/\omega}$, $\forall\omega$, the solution on (3.27) comes to that of the point heat source at the surface of a semi-infinite medium as:

$$\theta_P(r, j\omega) = \frac{\varphi_0(\omega)}{8k\pi r}\, e^{-\sqrt{\frac{j\omega}{a}} r} \tag{3.30}$$

The average temperature on the area viewed by the detector of equivalent radius r_m is:

$$\bar{\theta}_P(j\omega) = \frac{\varphi_0(\omega)}{4k\pi r_m^2 \sqrt{\frac{j\omega}{a}}} \left(1 - e^{-r_m\sqrt{\frac{j\omega}{a}}}\right) \tag{3.31}$$

and the phase and amplitude of this temperature are:

$$\phi_P = \arg[\bar{\theta}_P(j\omega)] \tag{3.32}$$

$$\Theta_P(\omega) = \frac{\left\|\bar{\theta}_P(j\omega)\right\|}{\max\left(\left\|\bar{\theta}_P(j\omega)\right\|\right)} \tag{3.33}$$

3.3.3 Comparison of models with: Gaussian, Uniform and Punctual heat flux excitation.

In order to investigate how the flux spatial distribution modifies the average temperature at the area aimed by the IR detector one compares the three models. The first one with Gaussian heat flux distribution of radius w_0 (equation (3.23)), the second with uniform disk heat flux distribution of radius w_0 (equation (3.28)) and the last one with a point heat source (equation (3.31)).

Figure 3.10 shows the calculated plots for the phase and the normalized amplitude from the three models. For the calculation, we used: $w_0 = 3.3$ µm, $r_m = 6.25$ µm, $\rho C_p = 3$ MJ·m^{-3}·K^{-1} and $k = 0.3, 30, 300$ W·m^{-1}·K^{-1}. In the normalized amplitude (Figure 3.10a) there is no significant variation between models since the total power absorbed by the material is the same in the three configurations.

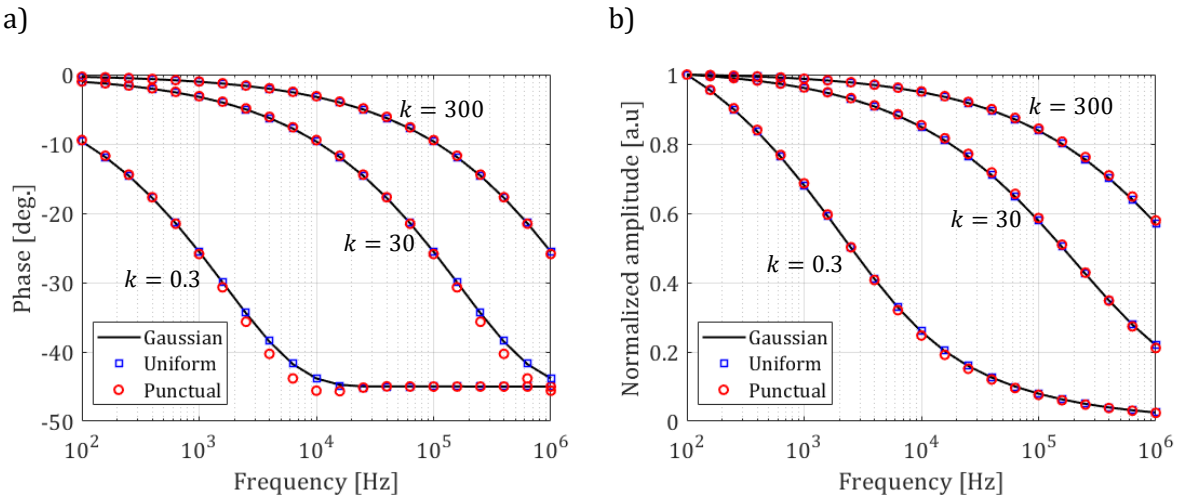

Figure 3.10: (a) Phase lag and (b) normalized amplitude from the three models for surface sample temperature: Gaussian (circle), Uniform (square), Point (dot). The thermal conductivities considered are: $k = 0.3,\ 30,\ 300$ Wm^{-1}K^{-1}.

On the calculated phase plots (Figure 3.10a), one can see that there is no significant difference between the uniform and Gaussian heat flux distribution. Nevertheless, for the point source assumption it is noticed the leak of the spatial source distribution near the transition zone to the 1D behavior (the most sensitive zone for w_0 in Figure 3.7). In the point source model, the transition to the 1D behavior takes place at lower frequency. This phase shift becomes more evident when the absolute difference between the two plots is represented, with the absolute phase difference defined as:

$$\phi(\omega)_{Diff} = \mathrm{abs}(\phi_P(\omega) - \phi_G(\omega)) \tag{3.34}$$

Figure 3.11 shows the absolute difference of the phase between the point source model and the Gaussian source model, where one can observe the increase on the phase difference at the frequency corresponding to the transition zone.

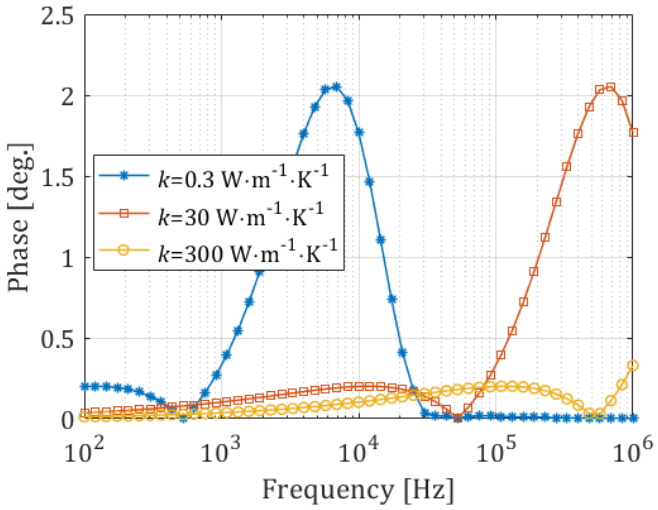

Figure 3.11: Absolute phase difference between point heat source and Gaussian heat source model.

It is interesting to notice that the maximum value of this difference is not driven by change in thermal conductivity of the materials. The maximum difference is fixed by the radius of the heat source area and how bigger is the measurement radius in comparison. A measurement radius $r_m = 2w_0$ leads to higher difference than $r_m = 3w_0$. Figure 3.12 shows the phase difference between the Gaussian heat source and the others two models for the two-measurement radiuses ($r_m = 6.25, 12.5$ µm) used in the experiments. In this case $k = 0.3$ W·m^{-1}·K^{-1} value was used. One has to remember that higher values of thermal conductivity push the plot to the right (to higher frequencies) but does not change its shape.

A) b)

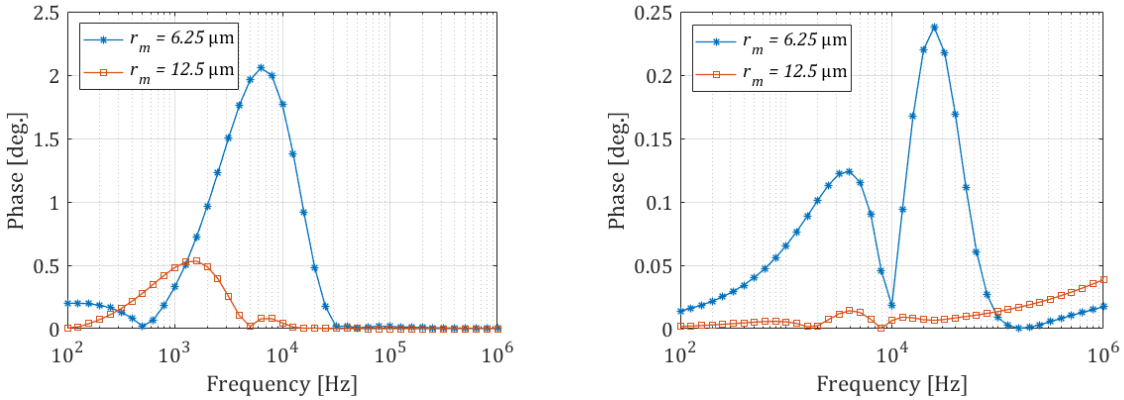

Figure 3.12: Absolute phase difference between: a) point heat source and Gaussian heat source models; b) uniform heat source and Gaussian heat source models.

Finally, one can say that the variation induced by the change on the flux distribution from Gaussian to uniform is always lower than 0.25 degrees for the phase considering all kind of materials and an excitation frequency up to 1 MHz. Thus, one can say that the shape of the heat flux distribution does not introduce an important variation in the measured phase as long as its characteristic size is known and the measurement radius is twice bigger than the heating radius.

3.4 A comparison between the analytical solution and that from the FEM.

The general formulation of the finite element method is presented and used to calculate the temperature of a semi-infinite media that is moving at constant velocity v_x in the x-axis direction, like occurs during the experiments. This model is built and solved using the FEM software COMSOL.

In the modulated heat flux configuration, the transient part of the heat equation, involving both diffusion and convection, becomes a source term as:

$$\begin{gathered} j\omega\rho C_p\theta(M,j\omega) + \rho C_p v\,\nabla\theta(M,j\omega) = k\Delta\theta(M,j\omega), M \in \Omega \\ v = [v_x, v_y, v_z] \end{gathered} \tag{3.35}$$

Where $\nabla\theta$ is the gradient of the temperature and $\Delta\theta$ is the Laplacian of temperature. The equation is solved using the non-linear stationary solver. As said previously, the complex term $j\omega\rho C_p\theta(M,j\omega)$ is considered as a source term. The heat flux, φ_0, is imposed as the boundary condition at the top surface of the domain as a disk of radius w_0= 3.3 µm. In addition, in order to simulate a wide range of frequencies without increase too much the size of the domain, we used an infinite element surrounding the region of interest. Infinite elements represent a region that is stretched along certain coordinate axes with the effect of approximating an infinitely large domain [119]. Figure 3.13 shows the geometry and mesh of the domain build for the simulation of the semi-infinite media moving at constant velocity.

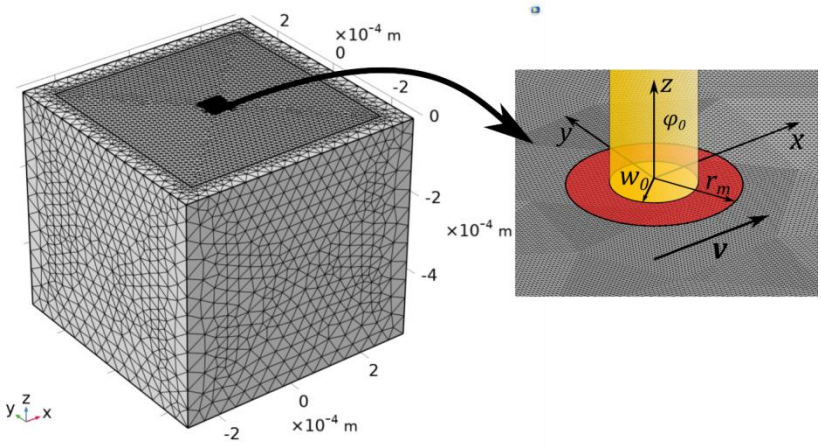

Figure 3.13: a) Geometry and mesh of the domain used in the FEM simulation of the semi-infinite media moving at constant velocity and submitted to a uniform heat flux distribution on its top surface.

The FEM model was used to calculate the phase over a disk of radius r_m=6.25 µm on the top surface. In the simulation, only the velocity along x-axis is considered ($v_y = v_z = 0$) with v_x=1, 5, 20 µms^{-1}. This solution is compared with the obtained one from the analytical model for the semi-infinite sample submitted to a Gaussian heat flux (equation (3.23)). For those calculations we used: $\rho C_p = 3$ MJ·m^{-3}·K^{-1} and $k = 0.3, 30, 300$ W·m^{-1}·K^{-1}. The results are presented in Figure 3.14.

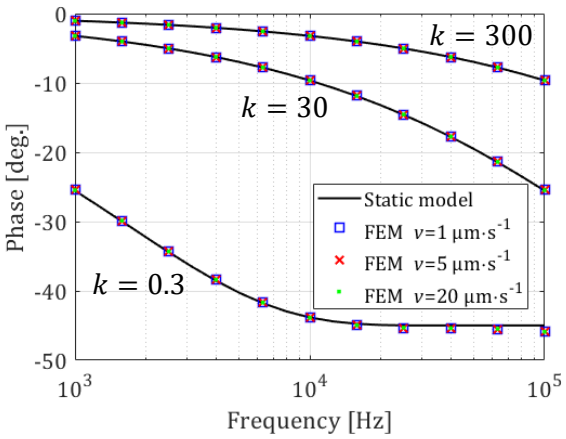

Figure 3.14: Comparison between analytical static model (equation (3.23)) and FEM model with constant velocities v = 1, 5, 20 µms^{-1} for three thermal conductivities k = 0.3, 30, 300 Wm^{-1}K^{-1}.

With this comparison one can verify that the influence of the scan velocity in the scanning process is negligible with respect to the thermal response of the sample. But still being an important parameter with respect to the data acquisition process as reported in the previous chapter.

The FEM approach presented here is not mandatory since we are fully confident with the analytical solution. Nevertheless, it will be used later to simulate the heat transfer within more complex geometries where no analytical approach can be implemented.

3.5 Multilayer material.

This section presents the solution for heat transfer in a multilayer sample based on the thermal quadrupole method [120]. This model is developed in order to simulate the heat diffusion in such configurations in the next chapter (as the 3-ω sample).

Let's consider the general case of a stack of finite layers deposited over a subtract of thickness e_s. In practice the thickness of the substrate is much larger that the diffusion length, for all the investigated frequency ranges. Thus, the substrate can be considered as semi-infinite in z direction. Each layer is defined by its thermal properties and the thickness, e_i, along the z coordinate, all of them are considered of the same size, r_L, along the r coordinate, as shown in Figure 3.15.

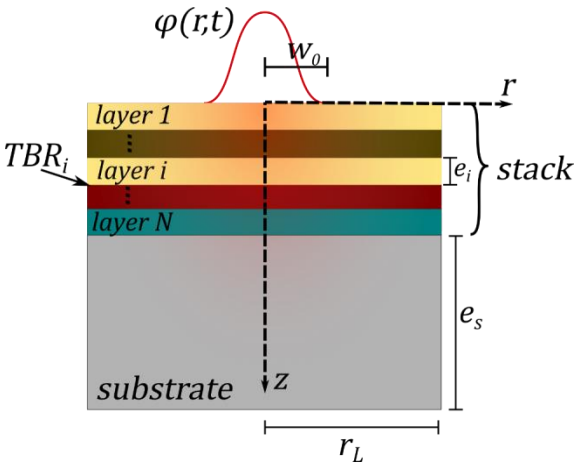

Figure 3.15: Schematic representation of a multilayer stack over a substrate.

In general, whatever its position in the stack, the layer will have an input heat flux, in the case of the first layer this flux will be the laser excitation, and for any other layer, that will be the output flux of the precedent one. In the same way each layer will be in contact with the next one trough a thermal interface resistance that will relate the output flux and temperature of two adjacent layers and in the case of the last one with the substrate.

Basing on the solution of heat transfer for a single layer (see appendix IV), the thermal quadrupole method allows generalizing the notation for a given layer i in the stack of N layers as:

$$\begin{bmatrix} \tilde{\theta}_{in}^{i} \\ \tilde{\psi}_{in}^{i} \end{bmatrix} = M^{i} \begin{bmatrix} \tilde{\theta}_{out}^{i} \\ \tilde{\psi}_{out}^{i} \end{bmatrix}, \qquad \text{with } M^{i} = e^{\beta_i e_i} \begin{bmatrix} A^{i} & B^{i} \\ C^{i} & D^{i} \end{bmatrix} \tag{3.36}$$

with:

$$A^{i} = D^{i} = \frac{1 + e^{-2\beta e}}{2}, \qquad B^{i} = \frac{1 - e^{-2\beta e}}{2k_z\beta}, \qquad C^{i} = k_z\beta\frac{1 - e^{-2\beta e}}{2} \tag{3.37}$$

where $A^{i}, B^{i}, C^{i}, D^{i}$ are defined in function of the properties of the layer i. The matrix for thermal contact resistance between the layers is defined as:

$$\begin{bmatrix} \tilde{\theta}_{out}^{i} \\ \tilde{\psi}_{out}^{i} \end{bmatrix} = M_R^{i} \begin{bmatrix} \tilde{\theta}_{in}^{i+1} \\ \tilde{\psi}_{in}^{i+1} \end{bmatrix} \tag{3.38}$$

with:

$$M_R^{i} = \begin{bmatrix} 1 & TBR_i \\ 0 & 1 \end{bmatrix}$$

where TBR_i, is the thermal contact resistance at the interface between the layer i and the layer i+1. It is thus possible to relate the top surface of the stack with the surface of the substrate, through the global matrix (M) for the stack of N layers as:

$$\begin{bmatrix} \tilde{\theta}_0 \\ \tilde{\psi}_0 \end{bmatrix} = M \begin{bmatrix} \tilde{\theta}_s \\ \tilde{\psi}_s \end{bmatrix} \tag{3.39}$$

with:

$$M = \begin{bmatrix} A & B \\ C & D \end{bmatrix} = M^1 M_R^1 M^2 M_R^2 \dots M^N M_R^N$$

and:

$$\begin{bmatrix} \tilde{\theta}_0 \\ \tilde{\psi}_0 \end{bmatrix} = \begin{bmatrix} \tilde{\theta}_{in}^1 \\ \tilde{\psi}_{in}^1 \end{bmatrix}, \qquad \begin{bmatrix} \tilde{\theta}_s \\ \tilde{\psi}_s \end{bmatrix} = \begin{bmatrix} \tilde{\theta}_{out}^N \\ \tilde{\psi}_{out}^N \end{bmatrix}$$

where $\tilde{\psi}_0$, is the imposed heat flux at the sample surface (top of the stack) and $\tilde{\psi}_s$ is the heat exchange with the semi-infinite substrate.

In the case of Gaussian distribution, the imposed heat flux is:

$$\tilde{\psi}_0 = \frac{\varphi_0 w_0^2}{4} e^{-\frac{(\alpha w_0)^2}{8}} \tag{3.40}$$

and the rear heat flux is:

$$\tilde{\psi}_s = k_s \beta_s \tilde{\theta}_s \tag{3.41}$$

$\tilde{\theta}_s$ is the temperature at substrate surface and k_s its thermal conductivity. In the same way β_s is defined with the thermal properties of the substrate.

Equation (3.39) leads to the functional form for $\tilde{\theta}_0$:

$$\tilde{\theta}_0 = \frac{A(\alpha, j\omega) + k_s \beta_s B(\alpha, j\omega)}{C(\alpha, j\omega) + k_s \beta_s D(\alpha, j\omega)} \frac{\varphi_0 w_0^2}{4} e^{-\frac{(\alpha w_0)^2}{8}} \tag{3.42}$$

Thus, the expression of the average periodic temperature on the sample surface on a disk of radius r_m is:

$$\bar{\theta}_{ML}(j\omega) = \frac{\varphi_0(\omega)\, w_0^2}{r_L^2} \left(\frac{1}{2} Z_M(\alpha_0, j\omega) + \sum_{n=1}^{N} \frac{J_0(\alpha_n r_m)\, e^{-\frac{(\alpha_n w_0)^2}{8}}}{r_m\, J_0(\alpha_n r_L)^2 \alpha_n} Z_M(\alpha_n, j\omega) \right) \tag{3.43}$$

with:

$$Z_{ML}(\alpha_n, p) = \frac{A(\alpha_n, j\omega) + k_s \beta_s B(\alpha_n, j\omega)}{C(\alpha_n, j\omega) + k_s \beta_s D(\alpha_n, j\omega)} \tag{3.44}$$

and the phase is defined as:

$$\phi_{ML}(\omega) = \arg[\bar{\theta}_{ML}(j\omega)] \tag{3.45}$$

3.6 Parameter identification.

The estimation of the seek thermal properties using the scanning photothermal radiometry method is based on the solution of an inverse problem. The classical approach consists in minimizing the measured quantity (the phase) with the calculated one using the different approaches presented in this chapter, either analytical or discrete. This minimization can be achieved using different techniques. In this work we will use a gradient based nonlinear

optimization method: The Levenberg-Marquardt method. In this case, the minimization acts on the quadratic gap between experimental and calculated data.

The calculated can be either amplitude or phase lag in the form represented by the vector:

$$\boldsymbol{Y}(\boldsymbol{a}, K_i) \tag{3.46}$$

with the seek parameters:

$$\boldsymbol{a} = [a_i]_N \tag{3.47}$$

Where a_i could be either a thermal resistance, a thermal conductivity, a thermal boundary resistance or other unknown parameter related to the experimental configuration used. K_i represents the set of known parameters controlled in the experiment, for example the operation frequency. The length of the vector is the number of investigated frequencies.

Accordingly, the measured data are components of the vector $\boldsymbol{Q}(K_i)$. Thus, the objective function to minimize is expressed as:

$$F(\boldsymbol{a}) = \sum_{i=1}^{M} er_i^2 \tag{3.48}$$

with:

$$er_i = \mathbf{Y}(\boldsymbol{a}, K_i) - \mathbf{Q}(K_i) \tag{3.49}$$

To minimize F, the Levenberg-Marquart algorithm is based on the following iterative method:

$$a^k = a^{k-1} - (J^T J + \mu\, I)^{-1} J^T E \tag{3.50}$$

Where $E = [er_i]_M$ is the vector of residuals and J is the Jacobian $M \times N$ matrix:

$$J = \left[\boldsymbol{S_Q}(a_i)\right] \tag{3.51}$$

With the vector $\boldsymbol{S}_Q$ denotes the sensitivity function:

$$\boldsymbol{S}_Q(a_i) = \left[\frac{\partial \boldsymbol{Q}}{\partial a_i}\right]_M \tag{3.52}$$

The parameter μ is used to control the condition number of the matrix to be inverted. When one moves towards the minimum of the functional, the value of μ decreases in order to accelerate the convergence while ensuring the inversion of the matrix.

It must be recalled that if the sensitivity functions $\boldsymbol{S}_Q(a_i)$ of parameters a_i are linearly independent, the minimization of F, leads to a global minimum and then to the optimal values for a_i. In such a case, the linear least square technique can be implemented. However, this configuration will not be met in the present work.

The approximate standard deviation, $\sigma(a_i)$, of the identified values can be calculated using the covariance matrix for a_i at the end of the iterative minimization process and the residuals, E, that are expected to be comparable to the noise measurement assuming the model is unbiased.

$$\sigma(a_i) = \sqrt{\frac{\mathrm{cov}(a_i)\; E^T E}{N}} \tag{3.53}$$

where:

$$\mathrm{cov}(a_i) = (\boldsymbol{S}(a_i)^T \boldsymbol{S}(a_i))^{-1} \tag{3.54}$$

3.7 Conclusions.

In this chapter, analytical and discrete models have been derived to solve the heat transfer process related to the photothermal radiometry scanning experiment presented in chapter 2.

As a main result, we showed that the velocity of the sample relatively to the photothermal excitation does not significantly modify the calculated amplitude and phase. Therefore, those two quantities can be calculated considering a motionless configuration.

The analytical solution of heat transfer in an orthotropic semi-infinite media submitted to a Gaussian heat flux was then presented. The sensitivity study carried out in this configuration obviously demonstrates that the model is sensitive only to the in plane thermal properties. This sensitivity study shows also a high sensitivity to the measurement radius. Therefore, this parameter must be mastered for the use of the experimental measurements. The carried-out analysis also highlighted the correlation between measurement radius and in plane thermal conductivity.

Additionally, in order to assess the influence of the spatial distribution of the photothermal excitation, the solutions considering a uniform heat flux and a punctual one were presented. The comparison of the phase calculated with these models shows a not significant difference between this resulting from Gaussian distribution and that when a uniform heat flux of the same radius is applied. This behavior appears naturally when the measurement area becomes bigger than the heating spot. Nevertheless, the heat flux distribution has to be taken into account when the measurement and heating areas are of similar radius.

As the application part deals with multilayer materials, the description of the heat transfer using the quadrupole formalism is also presented in this chapter.

Finally, the method used for identification of the seek parameter is recalled. It is based on minimization of the gap between measured quantity and the calculated one from the model. The Levenberg Marquardt method is applied in this work.

Chapter 4:
Applications of the SPR experiment.

4.1 Introduction.

In chapter 3 we have presented the heat transfer model describing measurement using the experimental setup of modulated photothermal radiometry in scanning and contactless mode, designated as SPR, whose description was detailed in section 2.3, chapter 2. In this chapter we will present its application to several configurations of sample in order to assess the performance and capabilities of the technique. Due to the type of application addressed, the chapter will be divided into two segments: motionless experiments and scanning experiments.

The interest in motionless experiments is to compare the results of the new setup with the results from known experiments like the HotDisk and the 3-omega setup in order to assess the performance of the SPR before passing to the image acquisition with the scanning mode and validate the obtained data.

Thus, in the first section the new experimental setup will be used on a steel bulk sample, previously characterized with commercial Hot Disk, in order to validate the experimental configuration and signal processing. In this configuration we will show how the experimental parameters affect the measurements and the conditions required to obtain reliable results. Then, the motionless configuration will be applied on a multilayer thin strip typically used in the 3-ω method for thermal characterization of thin films. We will present the results obtained using the 3-ω mode and we will face them to the results obtained from the SPR in motionless configuration. The film under investigation is a chalcogenide alloy used in phase change memory devices.

In the scanning experiment section, we will first present the characterization of an interface perpendicular to the surface formed by the mechanical junction of two pieces of steel. We will show that the SPR technique allows to reach the quantitative estimation of the thermal boundary resistance at this interface. Then, we will present an application of the SPR to the 3-ω sample that was used in static mode already. Finally, we will show an application of the SPR to the thermal surface imaging of composite samples to assess the capability of the technique in terms of spatial accuracy.

Obviously, all those experiments, and mainly the ones realized in scanning, illustrate the capability of such SPR experiment to deal with configurations where the classical imaging by thermography is difficult to implement in terms of spatial resolution and frequency of the photothermal excitation.

4.2 Motionless experiments.

4.2.1 Assessment of the performance of the setup on bulk sample.

To test the performance of the experimental setup, a known stainless steel (SST) sample was used to run a thermal characterization study. The SST properties are presented in Table 4.1, where

the thermal conductivity was measured with the Hot-Disk TPS2500S apparatus using 102003-F1 sensor.

Properties	Value
ρC_p	4 MJ·m^{-3}·K^{-1} [121]
k	14.45 ± 0.99 W·m^{-1}·K^{-1} (measured)
Thickness	2 mm
Width	12 mm

Table 4.1: Properties of the stainless-steel sample (SST).

In [84] it was reported that 1 µm roughness affects the phase measured at high frequencies from a bulk sample in classical MPTR setup. It was shown that the roughness behaves as layer deposited on the top of the sample and additional characterization has to be done to consider it. In order to reduce the influence of the surface roughness the sample was polished before the experiments. The polishing was done firstly with abrasive papers of silicon carbide grain with grit: 800, 1200, 2400 and 4000. Then, three polishing suspensions with 3, 1 and 0.3 µm particle size were used. After polishing, measurements with AFM showed that the surface roughness is lower than 100 nm (see Figure 4.1 and Table 4.2), which is much lower than the characteristic length of the used wavelength (1064 nm) and the measurement radius (6.25 µm). The sample is assumed to behave as a semi-infinite media for the investigated frequency range.

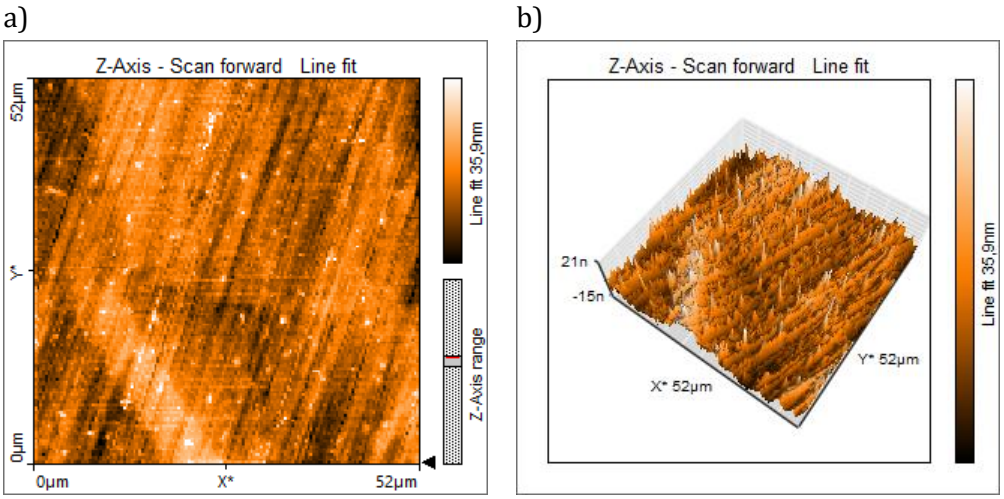

Figure 4.1: AFM images on SST sample in (a) 2D and (b) 3D view.

Parameter	Value	Description
Sa	4 nm	Roughness Average
Sq	5 nm	Root Mean Square
Sy	85 nm	Peak-Valley Height
Sp	65 nm	Peak Height
Sv	-20 nm	Valley depth

Table 4.2: Results from area roughness measured and calculated with Nanosurf EasyScan-2 AFM tool.

In the present work we will use two configurations for the experimental setup, both with the same operation principle and general description. The two versions of the experimental

arrangement differ in the infrared sensor used and in the angle of incidence (AOI) of the laser and IR signal over the Ge window. For the experimental configuration with IRD-1 the AOI over the Ge window was around 20° and for the second version, the experimental configuration with IRD-2, the AOI was around 45°.

Experimental configuration with IRD-1.

The initial configuration of the experimental setup was based on the IRD-1, and to promote the transmission of the infrared signal in the Ge window we look for a low AOI, since the best transmission is at 0°. The real experimental setup is presented in Figure 4.2.

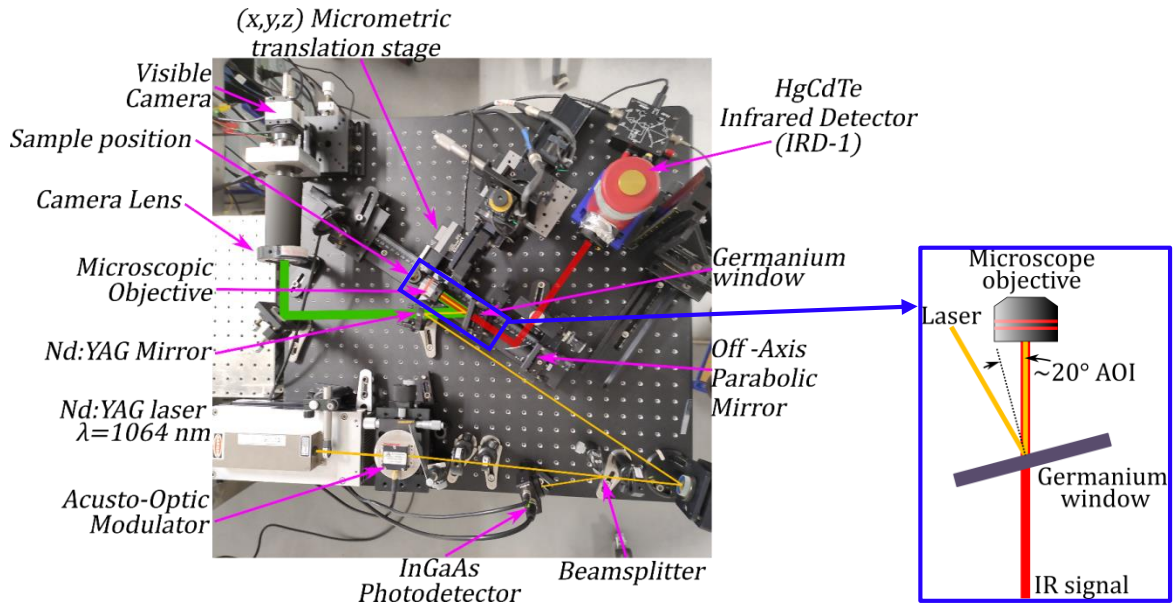

Figure 4.2: Experimental setup with infrared detector IRD-1. The yellow line represents the laser beam, the red line represents the IR signal and the green line represents the visible.

We first investigated the thermal response in static mode. We used the SST sample with the objective to estimate the thermal conductivity in a wide frequency range and to compare the results with the expected value.

The sample surface was placed at the focal plane, with heated area of radius $w_0 = 3.3$ μm. To simplify the problem, the measurement area was considered as a circular area with radius $r_m = 6.25$ μm. Thereby, the average temperature over the aimed area is expressed by equation (3.22).

We have control of the power supplied to the sample by means of the A-O modulator. With the maximum power defined as P=100 mW, one can set any desired power percentage (P%) to perform the experiment (see Figure 2.5 [1]). Nevertheless, we have no idea of the power absorbed by the sample since it is dependent of the absorptivity of the sample that is unknown. On the other

[1] Although the voltage to %P ratio in Figure 2.5 is not exactly linear, by simplicity and given that the real absorbed power is unknown, we will assume a linear ratio with P%=V*100, where V is the amplitude in volts of the signal supplied to the A-O modulator.

hand, the measurement principle is based on the assumption of linear relationship between the surface temperature and the emittance, which is classically verified at low temperature variations. Bearing this in mind, the power supplied to the sample in the experimental measurements has to be low enough to fulfil the linear assumption but in addition it should be high enough to give an accurate measurement of the thermal response.

From the sensitivity plots presented in Figure 3.7(b), one gets that the most sensitive region for samples with thermal diffusivity $\approx 10^{-5}$ $m^2 \cdot s^{-1}$ is the 40-100 kHz range. This was the selected frequency range for the measurements. Figure 4.3 show the measured amplitude in μV and phase-lag in degrees for different supplied P%. The amplitude, as expected, increase with the power and a clean signal is observed, even for low power excitation.

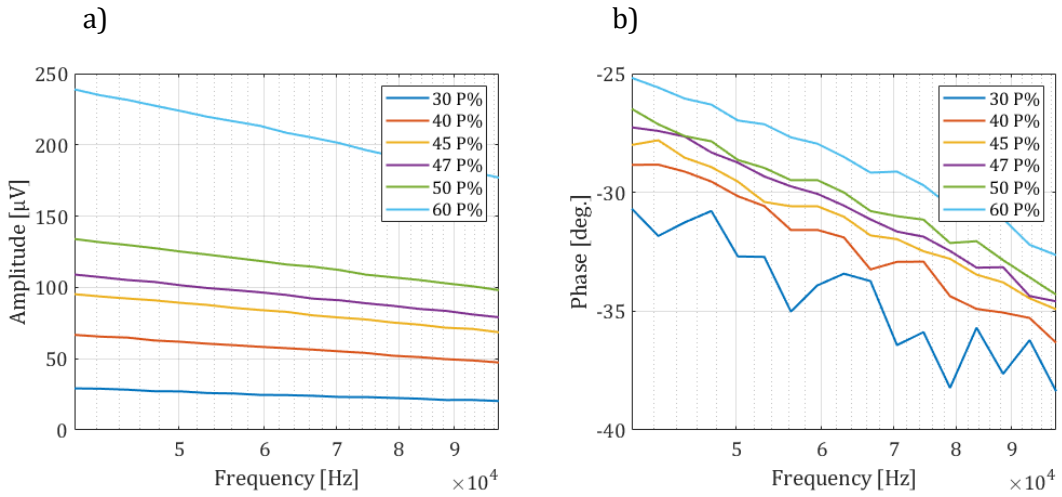

Figure 4.3: Amplitude (a) and phase (b) measured of SST sample for diferent P%.

In the phase plot (Figure 4.3-b) one can see that for low power (30 P%) the measured phase is much more noisy than the obtained for higher values of power. In addition, there is an offset in the phase for different power level, the power increase pushes the phase up. It is clear that the phase behavior is not typical that of a linear system where the phase is independent of the power. In addition, based on the simulations of the non-linear relation between temperature an emittance (see appendix V), one expects that the phase decrease when higher power is applied that is contrary to the observed behavior.

We used the experimental measurements of the phase-lag and that calculated from the model for the semi-infinite media presented in equation (3.24), to implement the parameter identification process to estimate the thermal conductivity. This is possible because it is assuming that the volumetric heat capacity is well known, otherwise the identified property will be the thermal diffusivity, since it is directly related to the phase-lag. The result that approaches the best the reference value measured from the Hot Disk was found at 47 P% with estimated thermal conductivity equal to 14.77 ± 0.76 $W \cdot m^{-1} \cdot K^{-1}$. The plots for this power level are presented in Figure 4.4 where the experimental measurements for the phase and normalized amplitude are squares and the simulated plots from the fitted model are solid lines. One can see that the experiment match with the model for both phase and amplitude, but the phase shows a discrepancy at low frequency that is induced by the noise captured by the IR detector. It is important remark that the amplitude in Figure 4.4, is not used in the parameter identification

process but it matches with the theoretical behavior for that experimental condition and this provides confidence on the results.

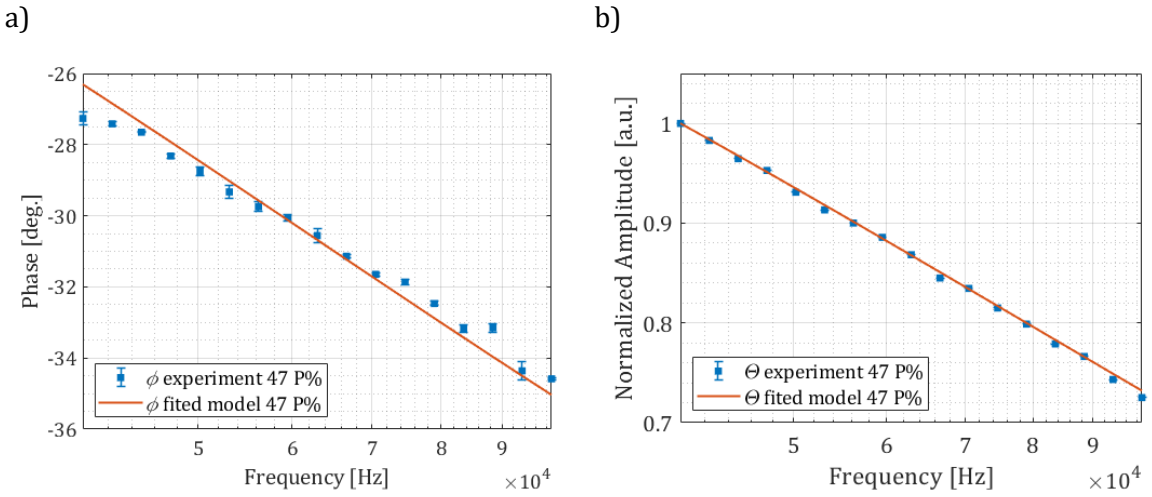

Figure 4.4: Phase and amplitude measured for the SST sample and the results of fitted model.

In order to see the influence of the optical arrangement in the estimated thermal conductivity the sample was moved out-of-focus in a range of ±2.5 µm around the focal plane, with steps of 0.5 µm, like show the scheme in Figure 4.5 a). The phase-lag was measured for each position and the estimated thermal conductivity k is presented in Figure 4.5 b). This shows that a possible misalignment with the focal plane around ±1µm produce a variation in the estimated thermal conductivity lower than 1%.

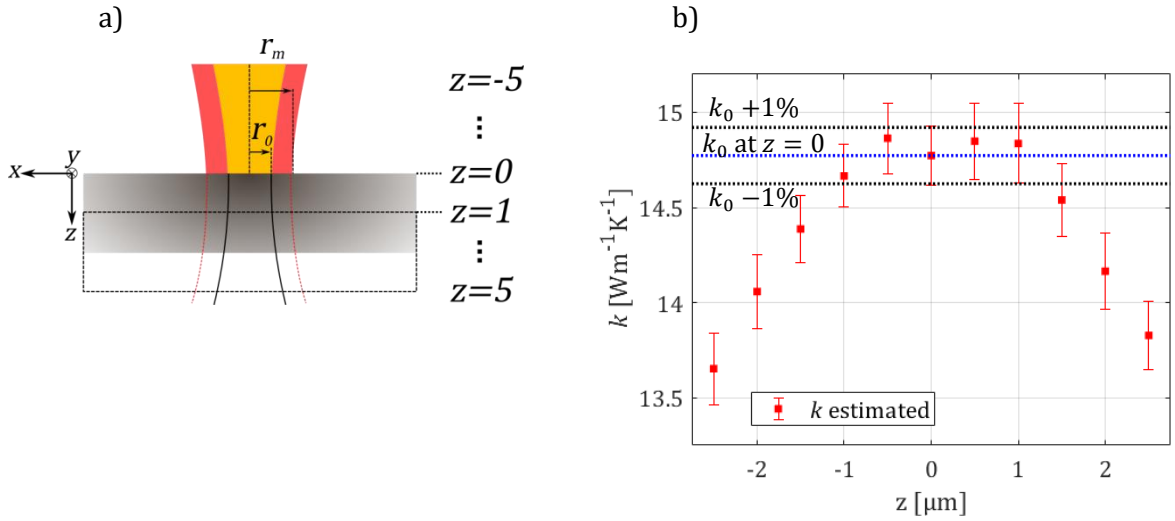

Figure 4.5: a) Schematic representation of out of focus sample displacement. b) Estimated thermal conductivity (k) for different sample position in z, with the focal plane at z=0, r_m = 6.25 µm and power at 47 P%.

Considering that power variation introduces an offset in the measured phase as presented before in Figure 4.3. We compared the fitting curve with the measurements for power higher than 47 %P and one observes that the experimental points are crossing the line of the fitted model (points at the right of the middle frequency are below the line and points on the right are above the line). Figure 4.6 shows the experimental points and the fitted model for the phase at 60 P%

where this phenomenon is observed. In the other hand, the phase measured at lower power (blue squares in Figure 4.6) show a better distribution around the fitted model, although the signal is noisier. Thus, reducing the white noise by increasing the power leads to a phase shift.

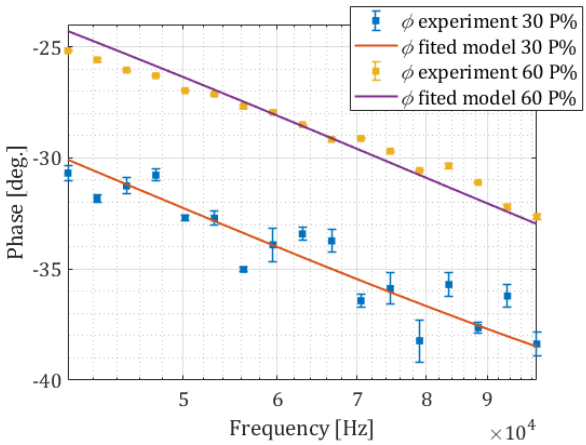

Figure 4.6: Comparison of measured phase and simulated phase with fitted model for low power and high power.

The difference in the slope suggest the measurements are biased. Since the properties of the material are known and the heating radius was experimentally measured, we decided to estimate the effective measurement radius from the experimental data. Indeed, we assumed that the noise measurement affects strongly the measured signal from the detector in this 2D axi-symmetric configuration as shown in Figure 4.7. Using the minimization procedure with r_m as the unknown parameter we estimated an effective measurement radius of about 7.39±0.09 µm at 30 P% and 5.56±0.03 µm at 60 P% (Figure 4.8) with a relation between measured points and fitted model similar that the exhibited in Figure 4.4 and Figure 4.6. According to the bias observed at high P% one can say that the real measurement radius is closer to 7.39 µm than to 6.25 µm, but the signal at low power is more perturbed, that produce high standard deviation on the identified r_m (Figure 4.8).

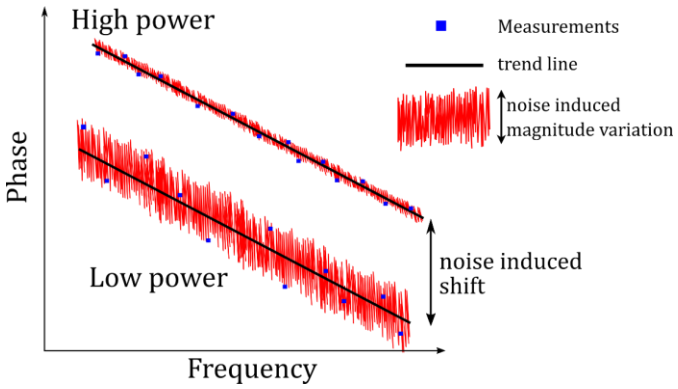

Figure 4.7: Influence of the noise in the phase measured. At high power the variation of the phase measured is lower as consequence of better signal but the trend line is shifted.

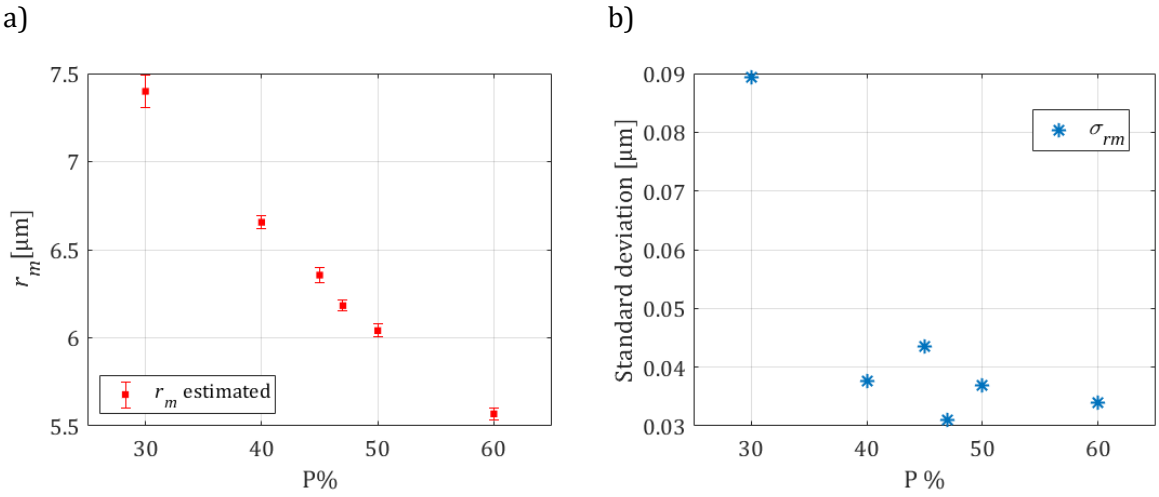

Figure 4.8: a) Estimated r_m according to the power; b) Standard deviation of the estimated r_m according with the power.

It is known that the temperature variation is bigger at lower frequencies and as consequence the emittance is bigger. So that, a better signal to noise ratio and thus a better estimation of the measurement radius should be possible at low frequencies. The lowest value in the swept frequency range is 200 Hz, that is also the lower limit for the detector amplifier.

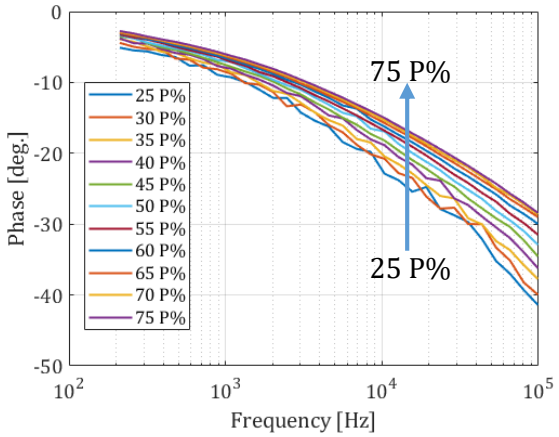

Figure 4.9: Phase measured from SST sample for several P% in the 200 Hz to 100 kHz frequency range where the effect of the power is visible. It reduces the white noise but also add a phase shift.

Figure 4.9 shows measurements in the full frequency range, where a similar behavior with respect to the previous analysis is observed. In addition, the phase shift between different P% is not constant with the frequency since the difference is lower at lower frequency. Estimating the measurement radius from those measurements we found that the measured and simulated phase follow the same slope difference that in the previous analysis, with the measured points crossing the simulated plot (Figure 4.10-a). It is similar for all P% tested in Figure 4.10-b where the phase error[2] between the experimental points and the fitted model are presented in function of the

[2] Phase error was calculated as the difference between the phase simulated with the fitted model and the phase measured: $\phi_{error} = \phi_{\text{fited model}} - \phi_{\text{experiment}}$.

frequency. This demonstrates that the phase deviation varies not only with the power but also with the frequency.

In addition, considering the full frequency range, we found that for 30 P% the measurement radius is estimated in 8.49±0.18 µm, but the fit between measured and calculated values presented in Figure 4.10-a is not as good as previously (showed in Figure 4.6).

a) b)

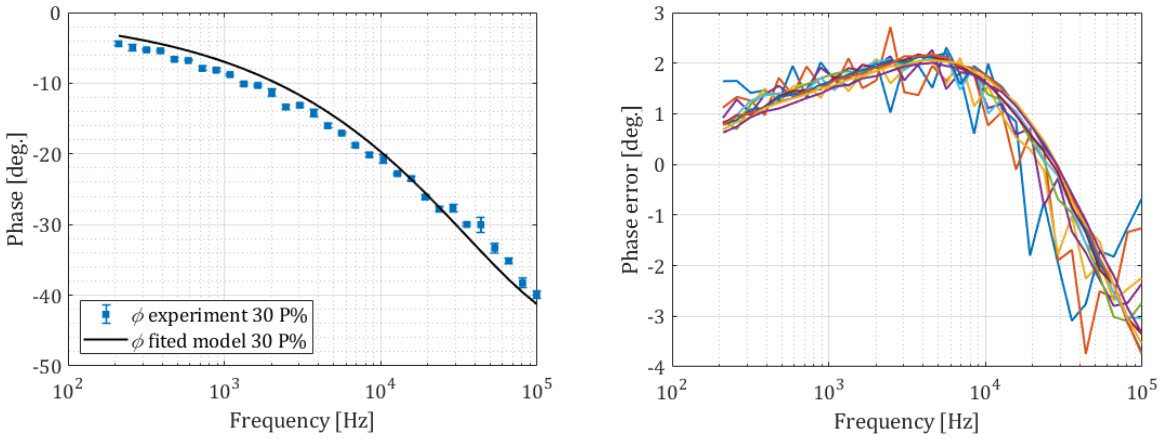

Figure 4.10: a) Experimental phase and fitted model in 200 Hz to 100 kHz frequency range for SST sample at 30 P%. b) Phase error between the experimental phase and its fitted model for all the tested P% presented in Figure 4.9.

In the analytical model the measurement area is considered as a disk although the real shape of the detector sensitive element is a square. Then, we performed a numerical simulation of the heat transfer within a semi-infinite media using the finite element method (FEM) with Comsol Multihysics software. The heat source is a disk with radius w_0, and we calculated the phase over two concentric areas, a circle of radius $r_c = 6.25$ µm, and a square of width $2b = 2r_c = 12.5$ µm.

The phases for both areas are represented in Figure 4.11 where one can see that the difference between them increases with the frequency, but they never cross. Thus, the shape of the sensor does not explain the observed bias along the frequency. In addition, it was found that the phase difference induced by the shape of the sensor can be compensated by increasing the diameter of the circular area to cover the same area. Since the area of the square is $A_s = 4b^2$, the equivalent circular area will have radius $r_e = \sqrt{4b^2/\pi}$. In this way the square measurement area with side of 12.5 µm can be modeled with the equivalent circular area with radius $r_e = 7.05$ µm. The results of the FEM simulation for this equivalent configuration are also presented in Figure 4.11. With the bigger equivalent radius one can explain the behavior observed at high frequency (Figure 4.6) where the effective measurement radius is 7.3 µm but that does not explain the bias at low frequencies (Figure 4.10).

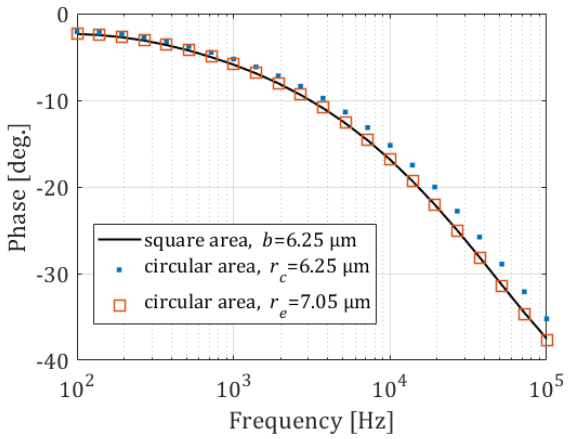

Figure 4.11: Comparison of phases calculated using FEM for the semi-infinite sample SST considering three measurement areas: a disk of radius $r_c = 6.25$ µm, a square of $2b$=12.5 µm width and a second disk of radius r_e=7.05 µm.

Using $r_m = 7.05$ µm in the analytical model to simulate the phase and compare it with the data set presented in Figure 4.9, we found that the measurements match with the calculated values but in different frequency ranges with respect to the value of P% as reported in Figure 4.12. In the plot the model with $r_m = 7.05$ µm is presented as black line and the experimental measurements as squares.

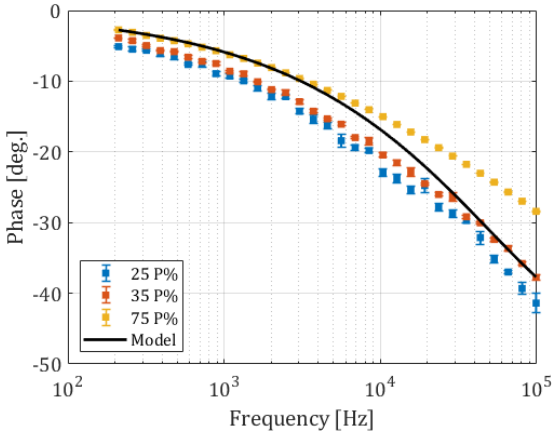

Figure 4.12: Comparison between modeled phase with r_m=7.05 µm and experimental phase at 25 P%, 35 P% and 75 P%.

It is thus clear that the detector was recording more than the sample surface emittance. An additional signal may be produced by the germanium window used to separate the infrared signal and the laser. Indeed, the sample has a good reflectivity and it is thus possible that the microscope objective collects a part of the reflected laser and send it to the germanium window increasing the magnitude of the background noise. This additional signal has the same frequency that the emitted one from the surface and it is therefore not filtered by the lock-in.

In order to check this assumption, we removed the sample and left the laser dispersing in the space in front of the microscopic objective. We measured then the signal captured by the infrared detector. The phase of the measured signal is presented in Figure 4.13-a. One can see that for

frequencies above 20 kHz the measured phase is close to the random noise behavior but for lower frequencies there is a clear tendency around 150 degrees. In Figure 4.13-b one can see the evolution of the amplitude with the lowest value around 1µV for high frequency.

a) b)

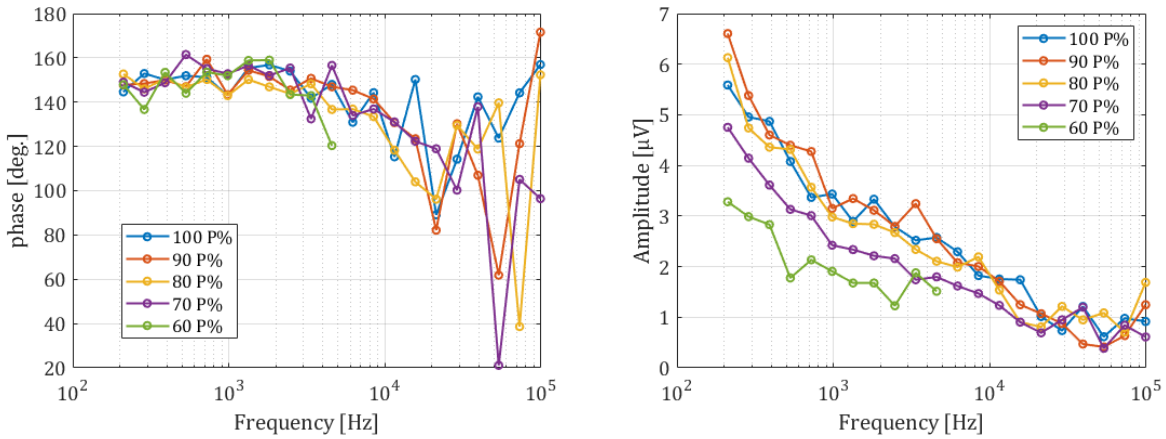

Figure 4.13: Phase (a) and amplitude (b) of background noise signal generated by the germanium window measured without sample.

From the evolution of the noise and the comparison between the model and the experiments presented in Figure 4.12, we conclude that an additional thermal signal from the germanium window is superposed with the signal from the sample surface. This explains why the amplitude of both signals varies with the power or the frequency of the laser.

In order to limit the influence of the germanium window heating it is advised to work at high frequency and with lower power. Using only the frequencies above 20 kHz in the data set presented in Figure 4.9, we estimate the measurement radius for all P% and the best fit was found at 35P% with estimated $r_m = 7.18 \pm 0.67$ µm. This estimated radius is close to the equivalent value found by the numerical simulation and the difference could be explained from the background noise or from the imperfections in the optical arrangement.

It is important to note that the heating of the germanium window is lower for samples with better emissivity and/or lower thermal conductivity since the signal from the sample is the dominant one.

Experimental configuration with IRD-2.

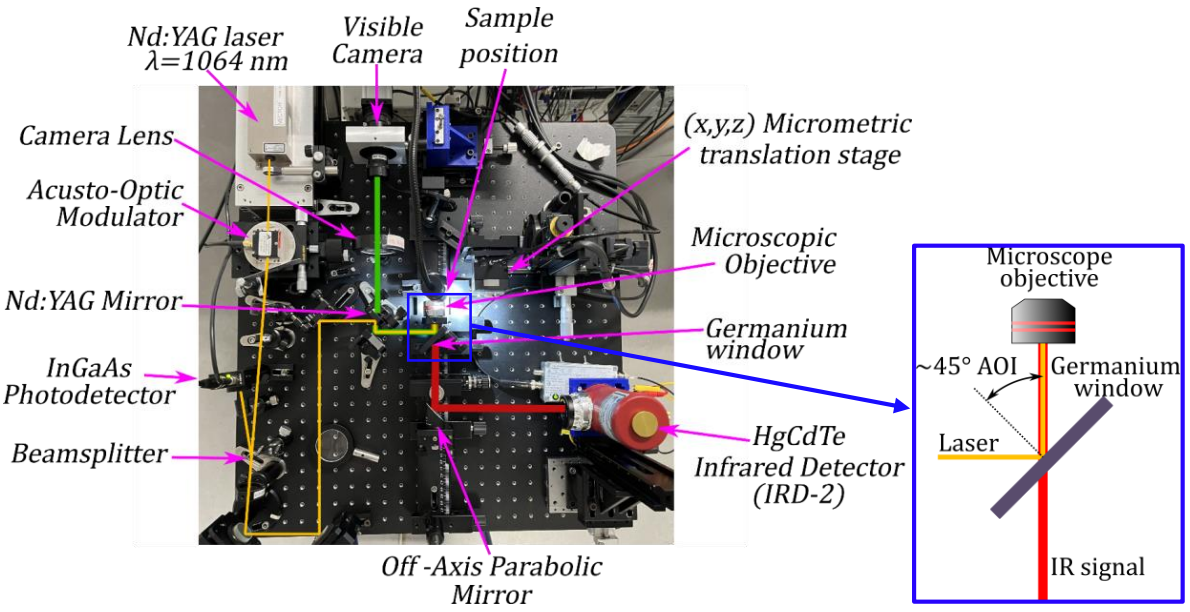

Figure 4.14: Experimental setup with infrared detector IRD-2. The yellow line represents the laser beam, the red line represents the IR signal and the greed line represents the visible light.

In order to avoid the influence of the germanium window and reduce the variation of the estimated measurement radius we increase the angle of incidence of the laser over the germanium window to 45° (Figure 4.14), originally around 20° (Figure 4.2). In addition, because the IRD-1 was no more available, this detector was replaced by the IRD-2 (with a square active area four times larger). To change the angle of incidence of the laser on the germanium window the spatial distribution of the experimental setup was modified, but the general description and principle remain the same. In this experimental configuration the radius of the heating area was measured equal 2.7 µm and the maximum applied power over the sample surface at 100 % was reduced to P_2= 40 mW. The change in the laser spot radius is observed because the laser alignment is not the same as the optical elements were moved and realigned.

With this configuration one decreases the phase variation with respect to P%. However, the exponential decay of the amplitude and the reduction on the transmissivity of the Ge window due to the increase of AOI lead to a strong decrease of the sensitivity at frequencies above 10 kHz. Figure 4.15-a show the experimental and calculated phase for 40P_2%. Figure 4.15-b reports the estimated r_m for three different P_2% showing a variation of 1 µm in the 40 P_2% to 60 P_2% range. The central value of $r_m = 15.46 \pm 0.13$ µm is higher than the expected equivalent value (14.1 µm) from the optical magnification. This variation is probably caused by imperfections in the optical arrangement of elements. But we have to consider also that it is influenced by the heating of the germanium window.

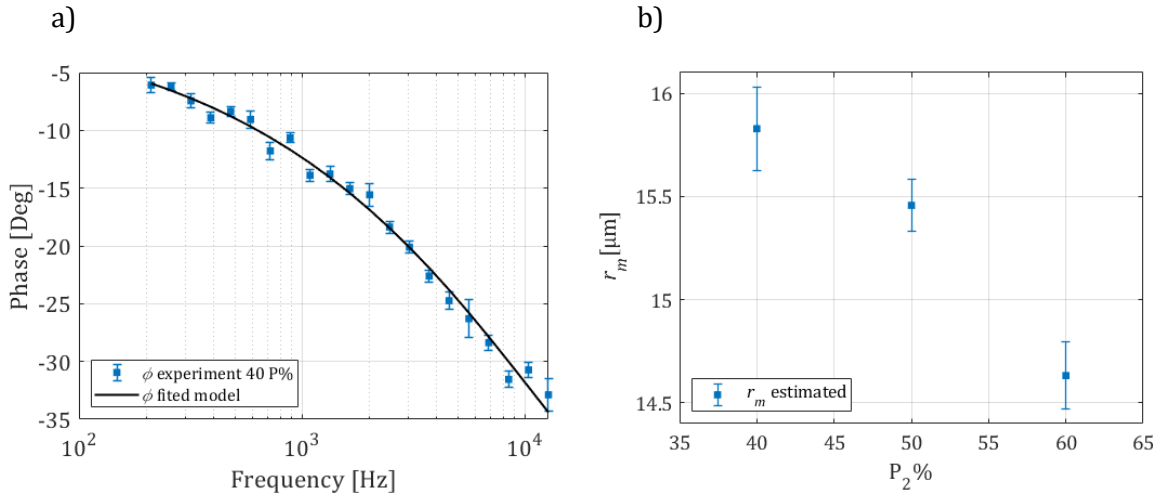

Figure 4.15: (a) Experimental phase and fitted model for SST sample at 40 P%; (b) estimated r_m for 40 P$_2$%, 50 P$_2$% and 60 P$_2$%.

Although the variation of the estimated radius was reduced, the general tendency remains. In addition, it was shown that the sensitivity of the setup is related to the emissivity of the sample. So more work is needed to improve the capability and efficiency of the experimental setup. However, under correct configuration the technique has shown potential for studies of thermal properties at high frequency and with high spatial resolution as we will show in the following sections.

4.2.2 Application on the 3-ω sample.

To verify that the measurement radius estimated from the SST sample is extensible to others applications, we used a 3-ω sample in static configuration.

The 3-ω samples were developed at CEA-LETI laboratory with the aim of measuring the thermal conductivity of the amorphous Ge-rich $Ge_2Sb_2Te_5$ (GGST) phase-change alloy by its potential application in PCRAM (Phase-change Random Access Memory) devices capable to operate at the high temperature (>150 °C) required in automotive applications [5] .

The used samples have been fabricated with four different thicknesses (100, 200, 300, and 400 nm) of the GGST layer deposited over a silicon (Si) substrate covered by a 400 nm thick Si_3N_4 (SiN) passivation layer. The heater is made of 400 nm platinum (Pt) layer deposited over the GGST layer with a 20 nm titanium (Ti) adhesion layer and 25 nm SiN passivation layer. The schematic representation of the stack is presented in Figure 4.16 with a representation of the heater pattern with heater length L=4 mm and width W=20 µm. The thermal properties are collected in Table 4.3.

Material	k W·m^{-1}·K^{-1}	ρ kg·m^{-3}	C_p J·kg^{-1}·K^{-1}
Si	164	2330	700
Pt	72	21350	130
Ti	13	4500	540
Si_3N_4	1.3	2370	673

Table 4.3: Thermal Properties (Thermal Conductivity (k), Density (ρ) and Specific Heat (C_p)) of the different materials involved in the 3-ω sample.

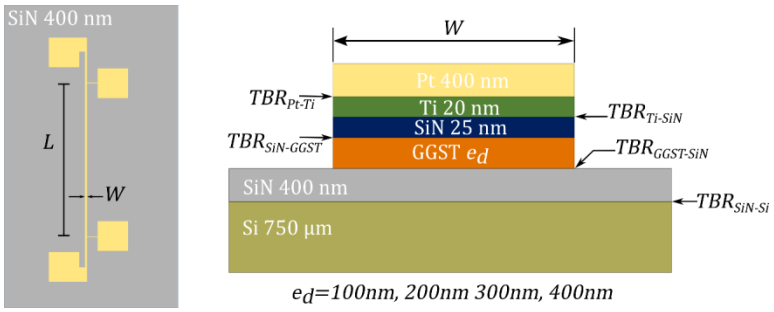

Figure 4.16: Schema of the 3-omega pattern and stack composition.

The next paragraph presents the 3-ω measurement performed in order to obtain the thermal conductivity of the GGST material before the use of the same sample for testing of the SPR capabilities.

4.2.2.1 Thermal conductivity measurement of GGST phase change alloy using the 3-ω method.

In general, the 3-ω sample has two external connection pads to supply the electric current to the strip and two internal connections used to measure the voltage generated by the current flowing through the strip. In the experiment, a modulated current with frequency ω is sent through the metallic strip, next, the Joule effect generate a heat flux into the strip and leads to a temperature rise with frequency 2ω. Finally, the temperature variation changes the resistance of the strip and this variation appears as a strip voltage at 3ω frequency. To perform the 3-ω measurements we use the experimental setup developed in the lab [27] and [122]. Its schematic view is presented in Figure 4.17.

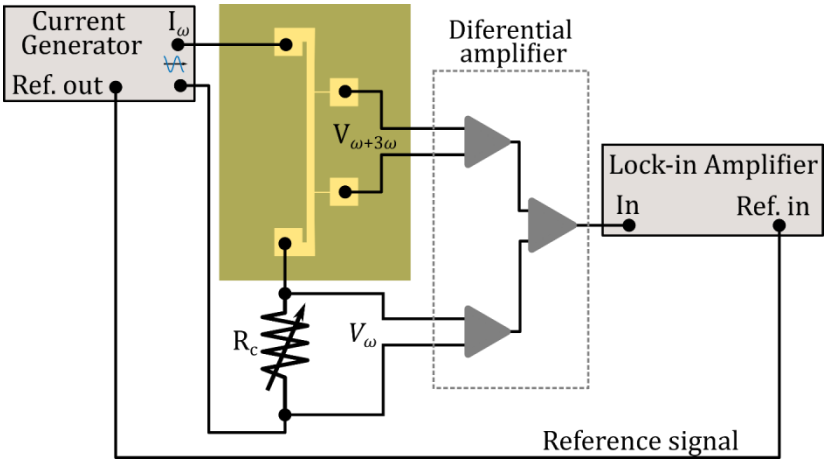

Figure 4.17: Scheme of experimental arrangement for the 3-ω measurement.

4.2.2.1.1 The 3-ω technique.

The AC current generator supplies the current in the form:

$$i = i_0 \cos(\omega t) \tag{4.1}$$

The heat power generated in the strip by Joule effect is thus

$$\begin{aligned} P = Ri^2 &= Ri_0^2 \cos^2(\omega t) = \frac{Ri_0^2}{2}(1 + \cos(2\omega t)) \\ &= P_{2\omega}(1 + \cos(2\omega t)) \end{aligned} \tag{4.2}$$

In this relation R is the electrical resistance of the strip which varies with the temperature as:

$$R = R_0(1 + \alpha_R \Delta T) \tag{4.3}$$

and α_R is the temperature coefficient of the electrical resistance, R_0 being the electric resistance at the reference temperature.

Since P is the total power applied to the sample on the whole surface at the bottom of the metallic strip and assuming the disturbance is small enough to ensure the linear heat transfer in the material, the average temperature rise of the strip is expressed as:

$$\Delta T = \Delta T_0 + \Delta T_{2\omega}(2\omega t + \phi) \tag{4.4}$$

Therefore, the voltage measured between the inner pads is:

$$\begin{aligned} V = Ri &= R_0(1 + \alpha_R \Delta T) i_0 \cos(\omega t) \\ &= R_0\big(1 + \alpha_R(\Delta T_0 + \Delta T_{2\omega} \cos(2\omega t + \phi))\big) i_0 \cos(\omega t) \\ &= V_0 \cos(\omega t)\,(1 + \alpha_R \Delta T_0) + V_\omega \cos(\omega t + \phi) + V_{3\omega} \cos(3\omega t + \phi) \end{aligned} \tag{4.5}$$

with:

$$V_0 = R_0 i_0, \qquad V_\omega = \frac{\alpha_R R_0 i_0}{2} \Delta T_{2\omega}, \qquad V_{3\omega} = \frac{\alpha_R R_0 i_0}{2} \Delta T_{2\omega} \tag{4.6}$$

Previous equation shows that the first term gives no information on $\Delta T_{2\omega}$ and in the second term it appears at the same frequency that the first term, making it impossible to discriminate between them. Only the third term with frequency at third harmonic permits to measure the amplitude and the phase related to $\Delta T_{2\omega}$. Thus, measuring $V_{3\omega}$ with the lock-in amplifier one can calculate $\Delta T_{2\omega}$ as:

$$\Delta T_{2\omega} = \frac{2\,V_{3\omega}}{\alpha R_0 i_0} = \frac{2\,V_{3\omega}}{\alpha\,V_0} \tag{4.7}$$

The main difficulty to overcome in the method is the measurement of $V_{3\omega}$ that is very low compared to V_0, thus, we used a differential stage that allow decreasing the first harmonic before entering a lock-in amplifier for seeking the third harmonic of the signal.

Since we know that $\Delta T_{2\omega} \propto P_{2\omega} = Ri^2/2$ and $Ri^2 \propto V_{3\omega}/Ri$ it results that:

$$V_{3\omega} \propto Ri^3 \tag{4.8}$$

Thus, in order to check that the experimental setup is operating properly, the third harmonic of the voltage is measured as a function of the current. This calibration allows to define the good current range and verify the state of the strip. Figure 4.18 shows the obtained points for three frequencies and for each sample thickness fitted with function in the form $V_{3\omega} = a \times i^b$.

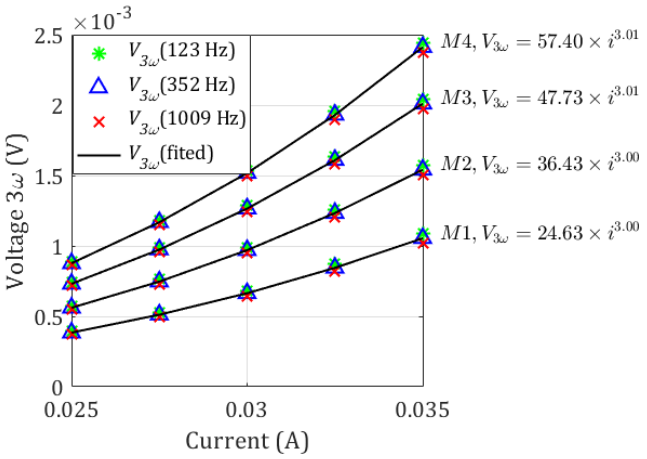

Figure 4.18: Measured $V_{3\omega}$ vs current at different frequencies for samples $M1 \rightarrow e_{GGST} =$ 100 nm, $M2 \rightarrow e_{GGST} = 200$ nm, $M3 \rightarrow e_{GGST} = 300$ nm and $M4 \rightarrow e_{GGST} = 400$ nm thick GGST layer.

4.2.2.1.2 The temperature coefficient of the electrical resistance.

The temperature coefficient of the electrical resistance α_R, is defined as the variation of resistance induced in the metallic heater when the temperature is increased by 1 K. It can be obtained experimentally by measuring the electrode resistance as a function of the temperature.

To perform the calibration at room temperature, the device is placed on a hot plate at temperature ranging between 19-28 °C. The obtained curve is shown in Figure 4.19, with the electrical resistance, R, linearly related to the temperature change, ΔT, as:

$$R = m\,\Delta T + R_0 \tag{4.9}$$

Where m is the slope of the linear fitting. Comparing with equation (4.3) one can obtain the temperature coefficient of resistance as:

$$\alpha_R = \frac{m}{R_0} \tag{4.10}$$

For the Pt strip, the obtained value is $\alpha_R = 2.3 \times 10^{-3}\ \mathrm{K}^{-1}$.

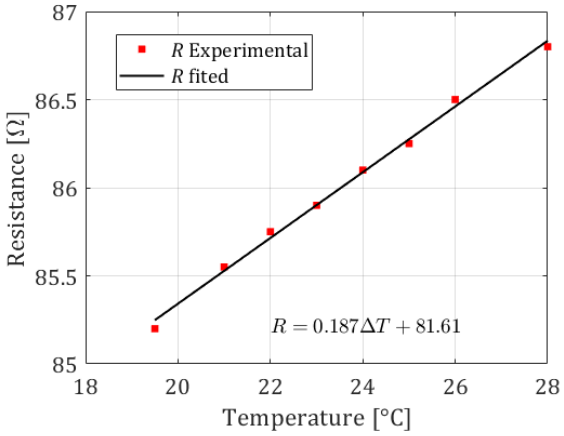

Figure 4.19: Measurement of electrical resistance according to the temperature.

4.2.2.1.3 Evaluation of thermal conductivity and thermal boundary resistance.

Because the thicknesses of the stack deposit deposited over the substrate are lower than the diffusion length in the frequency range of the study (100 to 1000 Hz), the sum of all the layers is viewed as a thermal resistance, R_{Th}. Thus, the temperature rise of the sample can be expressed as:

$$\bar{\theta}(2\omega) = P\left(\frac{1}{2\pi k l}\left(\frac{1}{2}\ln\left(\frac{a}{b^2}\right) - \frac{1}{2}\ln(2\omega) + 0.923 - \frac{j\pi}{4}\right) + \frac{R_{th}}{4bl}\right) \tag{4.11}$$

where k is the thermal conductivity of the substrate, b is the half width of the strip and l is the half of its length. The detailed model is presented in Appendix I.

Using the absolute temperature measurements ($\Delta T_{2\omega}$) and the equation (4.11), we implemented the identification procedure to estimate the total thermal resistance of the stack R_{Th} for each sample with four different thickness.

The thermal resistance of the deposit is expressed according to the thermal conductivity of each layer n composing the deposit and the thermal boundary resistances, (TBR_n) between the layers as:

$$R_{Th} = \sum \frac{e_n}{k_n} + \sum TBR_n \tag{4.12}$$

In order to discriminate the thermal conductivity of the GGST layer, it is necessary to consider four thicknesses of this layer. Therefore, we can express the obtained thermal resistance (R_{Th}) as a function of the thickness of the desired layer e_{GGST} and an aditional constant thermal resiatance (R_T), which thakes in to account the thermal resistance of the other layers and the thermal

boundary resistance of all interfaces (TBR_i). Thus for each sample constituted with varying thickness of the investigated layer it is obtained:

$$R_{Th}(e_{GGST}) = \frac{e_{GGST}}{k_{GGST}} + R_T \tag{4.13}$$

with:

$$R_T = \sum_{n=1}^{N-1} \frac{e_n}{k_n} + TBR_T, \qquad n \neq \text{GGST} \tag{4.14}$$

In this relation e_n and k_n denote the thickness and thermal conductivtviy of the layer n different of the GGST layer, TBR_T is the sum of all termal boundary resistances in the stack and N denotes the number of layers constituting the deposit.

It is easy to see in equation (4.13) that the thermal conductivity k_{GGST} is the inverse of the slope of the line equation and the thermal resistance R_T is the value of R_{Th} extrapolating the regression line at e_{GGST}=0. Thus, the termal conductivity is obtained by linear regression of the obtained from experiments R_{Th} according to the thickness e_{GGST}. The experimental results and the fitted line are presented in Figure 4.5.

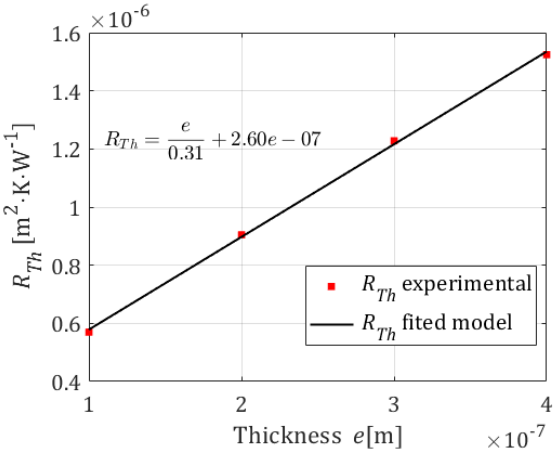

Figure 4.20: Thermal resistance vs layer thickness for the GGST material. Experimental measurements in red squares, and fitting line in black.

The found value for GGST thermal conductivity is $k_{GGST} = 0.31 \pm 0.03$ m^2KW^{-1}. This is consistent with the reported value [5] and the measured with MPTR and PPTR in the amorphous state of GGST at ambient conditions.

4.2.2.2 SPR measurement in motionless mode on the 3 ω sample.

The SPR was applied in motionless mode in order to measure the phase and compare it with the model for multilayer material at high frequencies. This comparison was intended to verify that the measurements with SPR are consistent. The measurements in static condition were done at the center of the square contact pad of 2 mm width of the 3-ω pattern. Because the size of the contact pad is much larger than the diffusion length of the Pt in the 5-100 kHz frequency range,

when measuring at the center, it can be approximated as an infinite extension in the radial direction. Thus, the thermal response can be simulated with the multilayer model presented in chapter 3.

A variation in power was applied to confirm the linear behavior. The phase measured at different P% in motionless condition is reported in Figure 4.21. It is important remark that the effect of the germanium window heating seems negligible in this power range since the phase variation is very low.

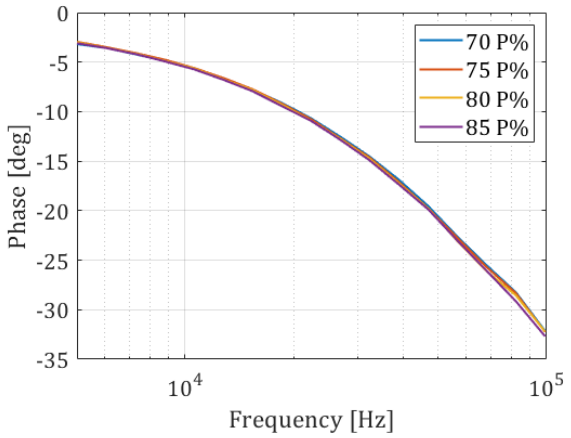

Figure 4.21 Phase measured on the 3-ω sample (400 nm GGST) for several %P.

On the other hand, the expected value of phase can be calculated with the model for the multilayer sample presented in section 3.5, with $w_0 = 3.3$ µm and $r_m = 7.18$ µm. In the model it is considered the five-layer stack over the substrate. The phase is calculated with expression (3.45), in the first instance with a thermal resistance interface $TBR = 0$ for all layer interfaces and then with $TBR_{SiN-Si} = 2 \times 10^{-8}$ m²·K·W⁻¹ and $TBR = 5 \times 10^{-8}$ m²·K·W⁻¹ for other interfaces. The aim is to test the TBR influence on the model response. The simulated phase from both models (with and without *TBR*) are plotted with measurements in Figure 4.22-a. In this plot, the effect of the *TBR*s is more evident at high frequency. In addition, the reduced sensitivity plot for the *TBR*s shows that the TBR_{Ti-SiN} largely dominates over the others.

a) b)

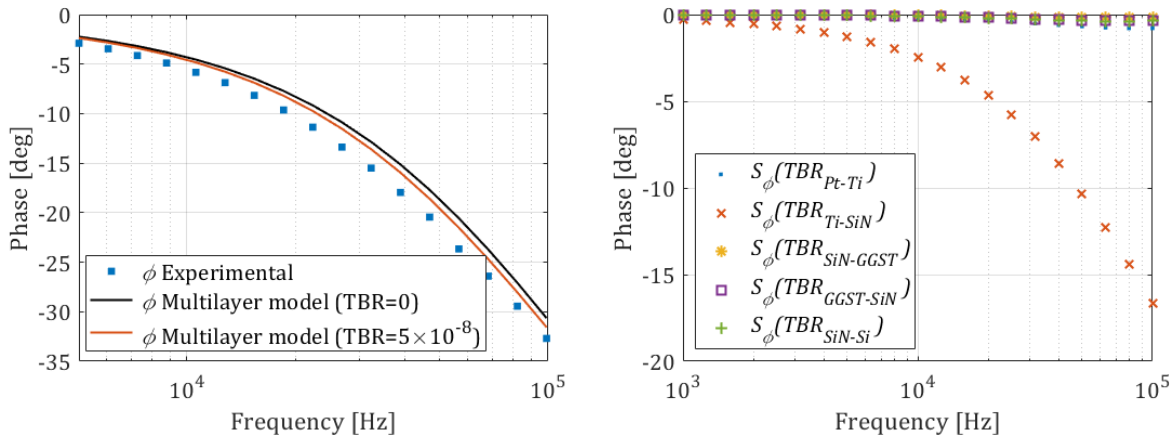

Figure 4.22: a) Comparison between experimental and simulated phase; b) Sensitivity curves for *TBR* in the 400 nm thick GGST sample obtained with multilayer model.

Figure 4.22 shows that the measurements are very close to the theoretical value of the phase and both follow the similar trend. Nevertheless, we cannot discard the possibility that the heating of the germanium window biased the results, although in a minor degree.

From measurements in motionless mode we have shown that under the correct condition, the SPR is capable to measure accurately the phase from proper thermal emission of the sample as result of the periodic excitation. Based on the presented analysis we will present the application of SPR technique for thermal image acquisition which is the main interest of this work.

4.3 Scanning experiments.

4.3.1 Scanning across contact interface perpendicular to the surface.

We performed a scanning across the contact interface formed by the mechanical junction of two metallic parts. For this application the experimental configuration with the IRD-2 was used. The sample was made of two stainless steel parts pressed between the bolt and the nut, as shown in Figure 4.23-a. To get a flat surface to perform the scan the sample was first polished. Figure 4.23-b show the SEM image of the contact interface where it is observed that there are zones where the contact interface width is lower than 0.5µm.

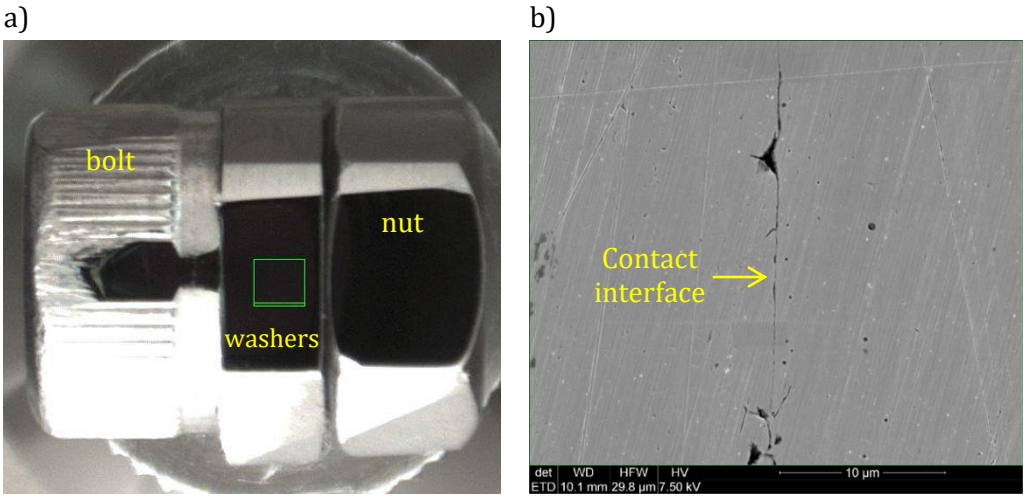

Figure 4.23: Sample configuration (a) and SEM image of contact interface (b).

Because of the homogeneity of the sample in the visible image of the experimental setup, it is difficult to locate the same point on both SEM and SPR image. Therefore, for the scanning measurement we look for the region where the contact fades in visible image, meaning that the zone has a thinner interface. The selected scanning region is presented in Figure 4.24. Because of the poor illumination and the low quality image, the contact line is not as well defined as in the SEM image but it is easily distinguishable at the bottom and top of the image. The red rectangle shows the scan zone were the first scan line is coincident with the top line of the rectangle and the last one is coincident with the bottom line. One can see that the contact interface seems disappear in the top region of the scanning zone that will be the objective of the study.

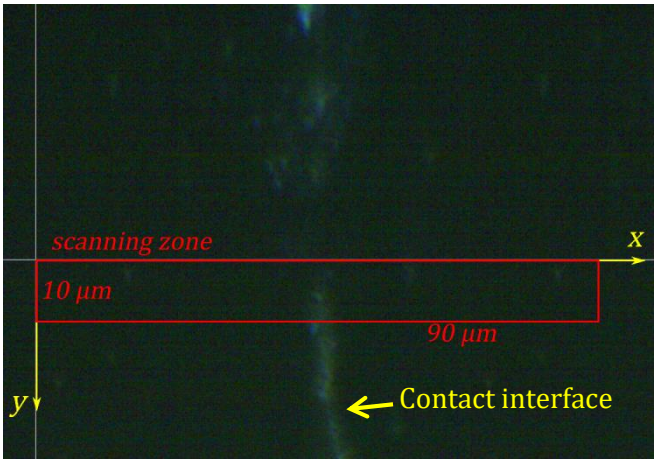

Figure 4.24: Image of the scanning zone.

The scanning was performed with the parameters presented in Table 4.4. To reduce the noise in the image each line was swept three times and the measurements were averaged.

Parameter	Value
L	90 µm
W	10 µm
Δx	1 µm
Δy	1 µm
Δt	1 s
v	1 µm/s
f	8.4 kHz
SL	3

Table 4.4: Scan parameters for the image presented in Figure 4.25.

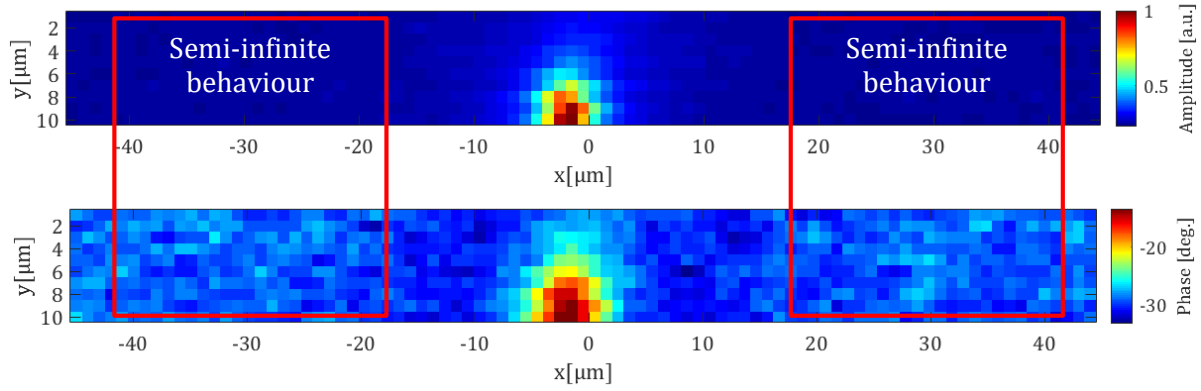

Figure 4.25: Amplitude and phase scan of the contact interface between two stainless steel parts pressed mechanically.

In the scanning images, the effect of the interface is clearly evidenced on the amplitude and the phase, around zero position in *x*-axis. On the edges of the image, one observes a more uniform distribution as expected for the semi-infinite media behavior. Figure 4.26 show the comparison between the scan lines at the top (y=0) and bottom (y=10) of the image. Because the width of the contact interface is much smaller than the measurement radius and the sampling interval, it is not possible to identify the width of the interface. But its effects are clearly evidenced and can provide information about the thermal contact resistance.

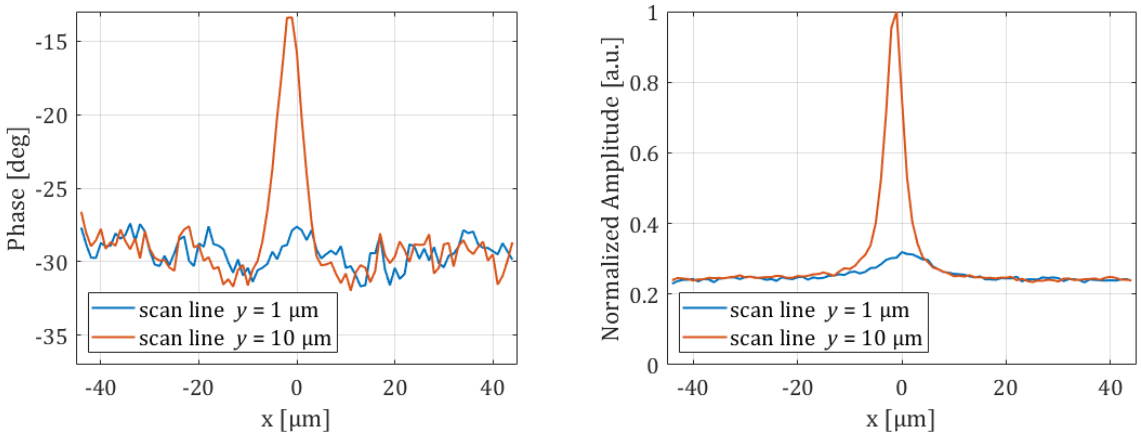

Figure 4.26: Phase and amplitude comparison between first and last scan line in Figure 4.25.

Parameter	Value
L	90 µm
Δx	0.5 µm
Δt	1 s
v	0.5 µm/s
f	8.4 kHz
SL	20

Table 4.5: Scan parameters for the line y=1 µm.

We chose the first line (y=1 µm) in the scan image to perform an estimation of the TBR at the contact interface by comparing the measured phase with that calculated from a FEM simulation. We improved the signal noise ratio by performing 20 sweeps by line. The scanning configuration is presented in Table 4.5 and the results are presented in Figure 4.27 as SL 20 and compared with SL 3 (the data from the scan image at y=1 µm) where the reduction of the noise is appreciable and the symmetric behavior is clear, with a valley at each side of the maximum phase, this symmetrical behavior is consistent with the theory and similar results obtained with thermoreflectance presented in [71]. To avoid the possible influence of the background noise, the measurement radius was estimated using the average phase from the semi-infinite region on the scan image (Figure 4.25) and the analytical model for semi-infinite media, obtaining $r_m = 15 \pm 0.2$ µm. Thus, the phase was calculated over a circular area with this radius and the excitation laser was modeled as a disk heat flux with radius of 2.75 µm at the surface.

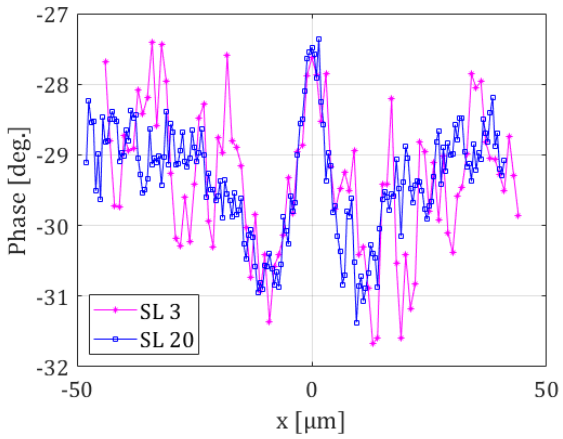

Figure 4.27: Comparison between scan with 20 sweeps by line (SL20 in blue) and scan with 3 sweeps by line (SL3 in magenta).

The finite elements model was built as the contact of two stainless steel blocks with the same dimensions surrounded by a semi-infinite domain and a thermal contact resistance (TBR) is introduced at the interface.

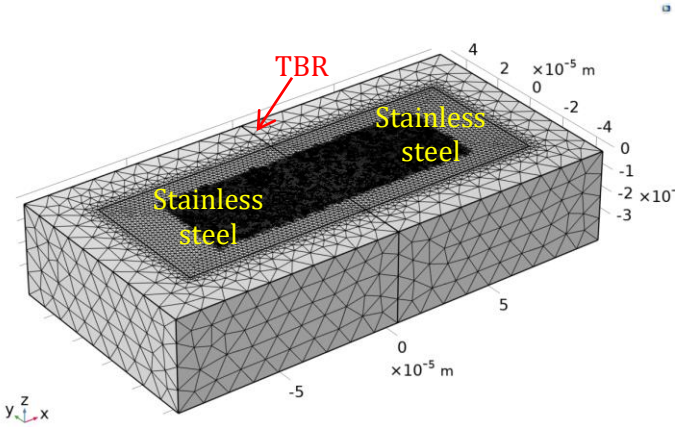

Figure 4.28: Model of the contact interface with the finite element method in COMSOL.

The TBR values have been considered as: 5×10^{-8}, 5×10^{-7}, 5×10^{-6}, 5×10^{-5} $m^2 \cdot K \cdot W^{-1}$, with results reported in Figure 4.29-a. The thermal boundary resistance produces a reduction in the phase whom the minimum value is at around x=±10 µm far from the contact interface, which is consistent with the experiments.

a) b)

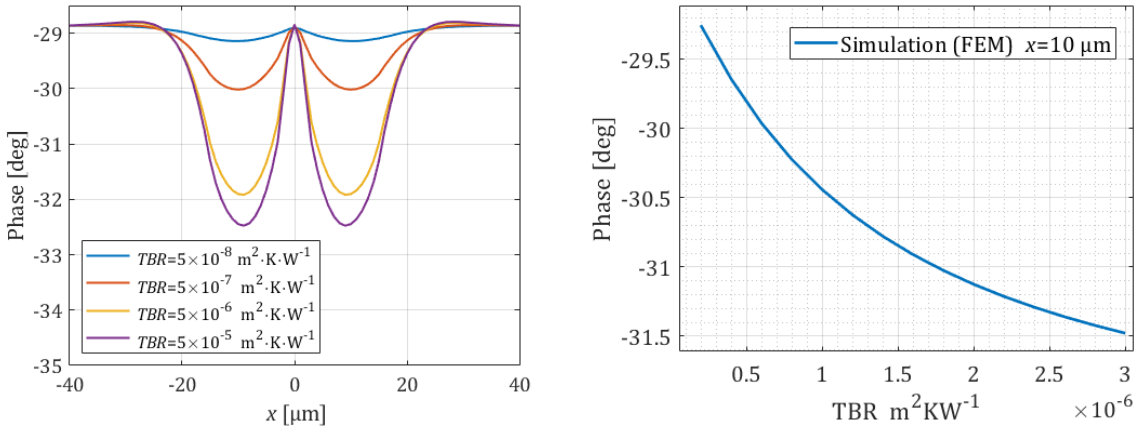

Figure 4.29: a) Phase vs position for $= 5 \times 10^{-8},\ 5 \times 10^{-7},\ 5 \times 10^{-6},\ 5 \times 10^{-5}$ m²·K·W⁻¹; b) minimum phase calculated at x=10 µm vs TBR.

The minimum phase variation as function of TBR is shown Figure 4.29-b. Therefore, one can adjust the TBR to reach the best fit between the calculated and measured phase. It is obtained the value: $TBR = 1.3 \times 10^{-6}$ m²·K·W⁻¹. The comparison between the experimental and simulated scan is presented in Figure 4.30. One can see that the measurements and simulation match well with exception of the center zone (x=0) that is coincident with the contact interface. At this point the system simulated is completely symmetric because the measurement is equally distributed in both sides of the interface. Thus, the TBR does not modify the heat diffusion because it has not thickness and diffusion cannot take place on it. In the other hand, the real contact interface has a non-null thickness that modifies the measured phase.

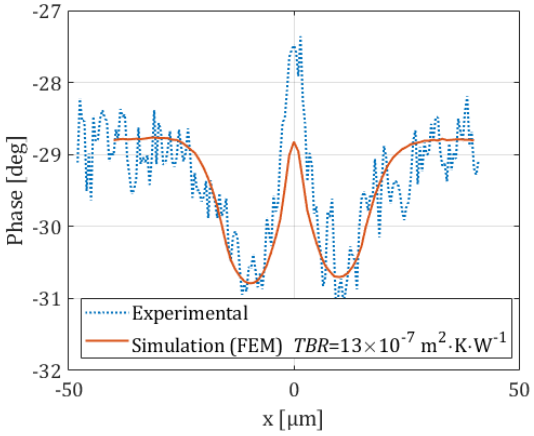

Figure 4.30: Comparison between the experimental scan and simulated scan with TBR = 13×10^{-7} m²·K·W⁻¹.

To consider the thickness of the interface, the geometry of the FEM was modified by introduction of a thin layer between the blocks playing the role of the contact interface. In addition, a perfect contact between the interface layer and both stainless steel blocks were assumed. Under the simplest assumption, that the space between two solids is filled by air the thermal properties of the air were used in the interface layer to model the contact interface ($k = 0.026$ W·m⁻¹·K⁻¹, ρ =1 kg·m⁻³, C_p =1000 J·kg⁻¹·K⁻¹).

One can relate the previously estimated TBR with the thermal conductivity and the thickness of the interface layer as:

$$TBR = e_c/k_c \tag{4.15}$$

Using relation (4.15) one can estimate the thickness of the interface layer as 0.033 μm. This value, although possible for some regions does no reproduce the increase in phase observed experimentally. Observing the evolution of the phase in the scan image (Figure 4.25 and Figure 4.26) it could be expected that the phase increase (at $x = 0$) with the thickness of the contact interface. In order to keep the TBR constant we can define the thermal conductivity as function of the thickness $k_c = e_c/TBR$. In this way we calculated the maximum phase for some pairs (e_c, k_c) that result 13×10^{-7} m²·K·W⁻¹. For simplicity we keep the density and heat capacity of the air in the simulations. Figure 4.31 shows the results for different thickness of the interface layer.

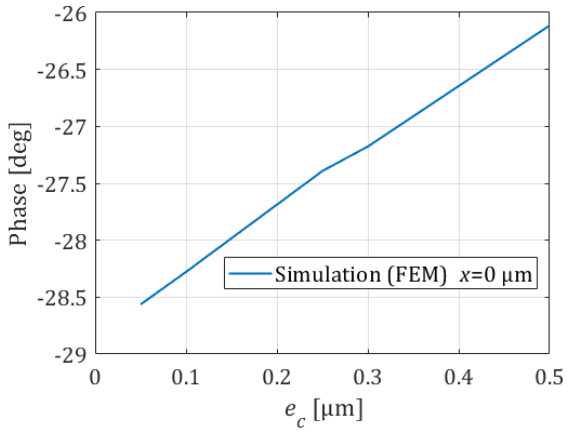

Figure 4.31: Phase calculated at x=0 versus the thickness of the layer interface.

One can see that a close value to the measured phase (27.5°) is obtained with $e_c = 0.25$ μm what implies $k_c = 0.19$ W·m⁻¹·K⁻¹. Thus, we take this value to perform a scan simulation. The results are presented in Figure 4.32 and compared with the experimental measurements where a good match is observed.

In order to examine the influence of the measurement shape (probe shape), the same model was used to calculate the phase over a square area of $2b$=26.8 μm in width. A difference of 0.1° between the phase obtained using the square and the circular probe is observed in the semi-infinite region. A small difference in the phase at the valley region with respect to the probe shape is also observed. Nevertheless, the general behavior remains the same. In the normalized amplitude plot (Figure 4.32-b) we observe a larger variation in the magnitude of the signal with respect to the semi-infinite region that is produced by the increase of the temperature.

a) b)

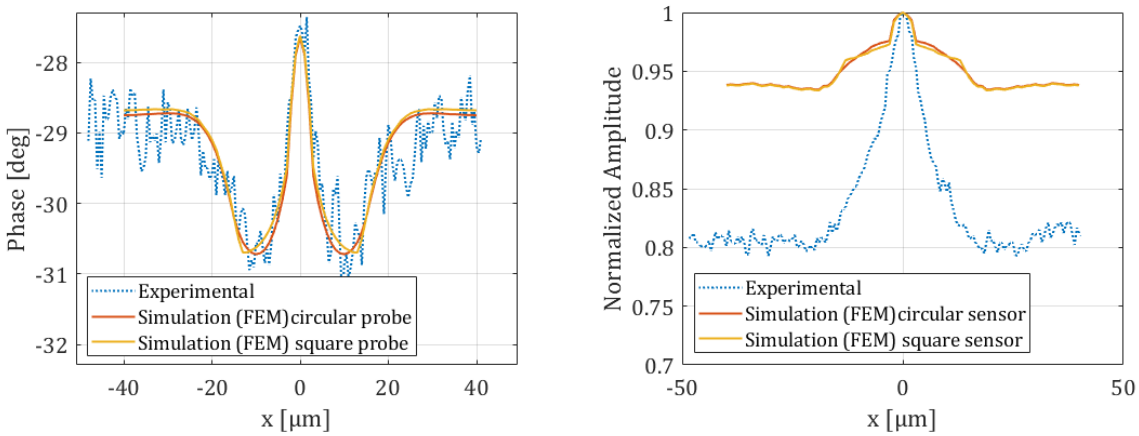

Figure 4.32: a) Comparison between experimental and calculated using numerical simulation phase according to the probe shape (circular and square) of equal area. b) Comparison between experimental and calculated using numerical simulation amplitude.

Through this qualitative comparison between the model and the measurements we could approach an approximation of the thermal contact resistance occurring at the metallic contact and evaluate its thickness. It was done with the assumption of known volumetric heat capacity (ρC_p of air). The study shows the potential of the SPR measurement for the quantitative analysis of thermal interfaces vertical to the surface.

4.3.2 Scanning across the 3-ω pattern.

The thin metallic strip from the 3-ω sample is used for the image acquisitions with the SPR in order to assess the spatial resolution using the experimental configuration of the IRD-1. For this purpose, the strip of 50 µm in width and of 400 nm in GGST thickness was used. The scanning parameters are presented in Table 4.6.

Parameter	Value
L	100 µm
W	4 µm
Δx	0.5 µm
Δy	0.5 µm
Δt	0.1 s
v	5 µm/s
f	99 kHz
SL	5

Table 4.6: Scanning parameters for strip of 50 µm in width and 400 nm in GGST thickness (results presented in Figure 4.33).

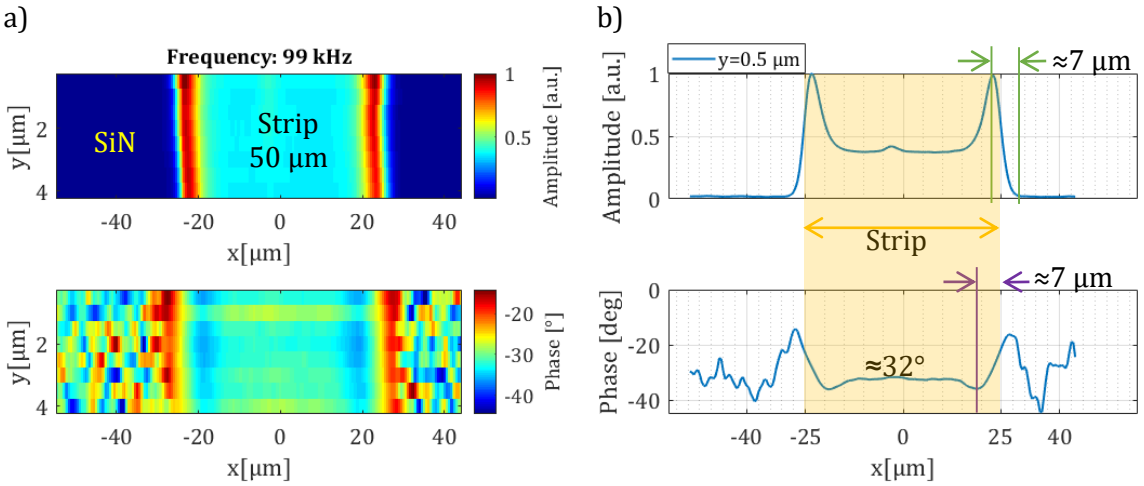

Figure 4.33: Scan images of amplitude and phase acquired with 99kHz excitation frequency.

The scans of amplitude and phase measured are shown in Figure 4.33-a. The strip is clearly visible on the two images. On the amplitude cross section (First line, $y = 0.5\ \mu m$) showed in Figure 4.33-b top, one can easily note the strip region raising over the substrate. Here, it is important to remember that this raising is not related to the height of the metallic region but to the change in the emittance and thermal properties. One can also identify a transition zone corresponding to the edges, where the measuring spot is over the substrate and the strip at same time. The width of this zone between the maximum amplitude and the beginning of the flat level inside or outside of the strip, is estimated to be around 7 µm (green dimensions) and is related to the size of the measurement spot. One can see the temperature increase at the edge of the strip with respect of the central zone due the heat confinement effect when the laser is close to the edge. In addition, the horizontal distance between the maximum amplitude and the edge of the wire (≈ 2 µm) could be related with the size of the heat source. At this point (on the right edge for example) the laser is fully on the strip but tangent to the edge and the strip reaches the maximum temperature by the confinement effect. When laser moves to the right the power deposited on the strip decreases and also its temperature.

On the phase cross section plot (Figure 4.33-b low) one can identify the zones inside the strip where the effect of the heat confinement is visible as a reduction in the phase with minimum phase located around 7 µm. Because of the low sensitivity of the phase with respect to the heating area there is no clear indication of the heating radius. The phase plot in the section corresponding to the substrate with SiN layer is noisy with an average value around 30°. This noisy signal is the consequence of the very low amplitude that does not allow an accurate measurement. The reduction in amplitude is related to higher thermal conductivity of the substrate with respect to the stack and to the lower power absorbed because it is semitransparent to the excitation laser. The semitransparency of the subtract also explain the average value of the phase that is lower than the expected one from an opaque media with high thermal conductivity.

In order to verify the reliability of those measurements, the scan data are compared with the ones calculated from the model. First, the phase measured at the central area of the wire is comparable with the measurements done at the center of the square contact pad of the 3-ω

pattern, where there is no effect of the edges. This is because at 99 kHz the diffusion length of the Pt is about 9 µm which is much lower that the width of the strip.

To verify the behavior observed at the strip edges is not an optical artefact produced by the geometry the strip, we compared the measured values along the scan with the calculated ones. We have already shown that the scan velocity used is too low to influence the heat distribution in the sample. In addition, because of the small Δx we can consider that the area used for this test is invariant with Δt. Thus, the scanning can be represented as static measurements at consecutive fixed points and to simulate the scanning it is enough to calculate the static response of the model with the probe at consecutive locations.

The heat transfer within the multilayer strip was simulated using the finite element method (FEM) with the COMSOL software. The full stack was introduced in the model with the substrate behaving as a semi-infinite domain. The heat flux was introduced as a boundary heat source applied on the top surface and considered as a circular uniform distribution of radius 3.3 µm. The phase and amplitude were calculated over a disk area of radius 7.18 µm (value obtained from SST sample for the IRD-1). Figure 4.34 shows the segment of the strip modeled using the FEM.

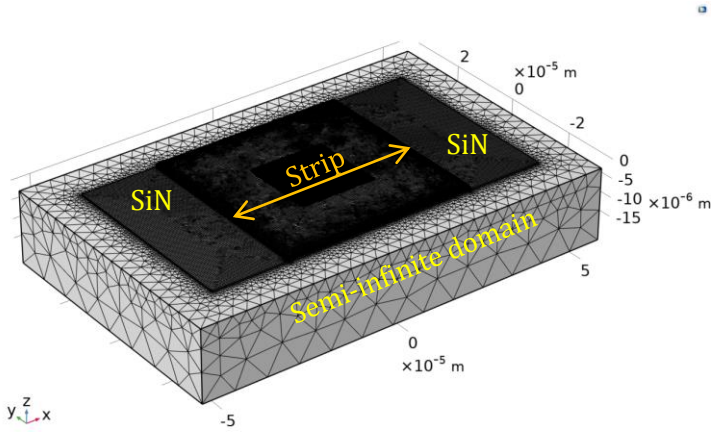

Figure 4.34: Model of the 3-ω strip with the finite element method in COMSOL.

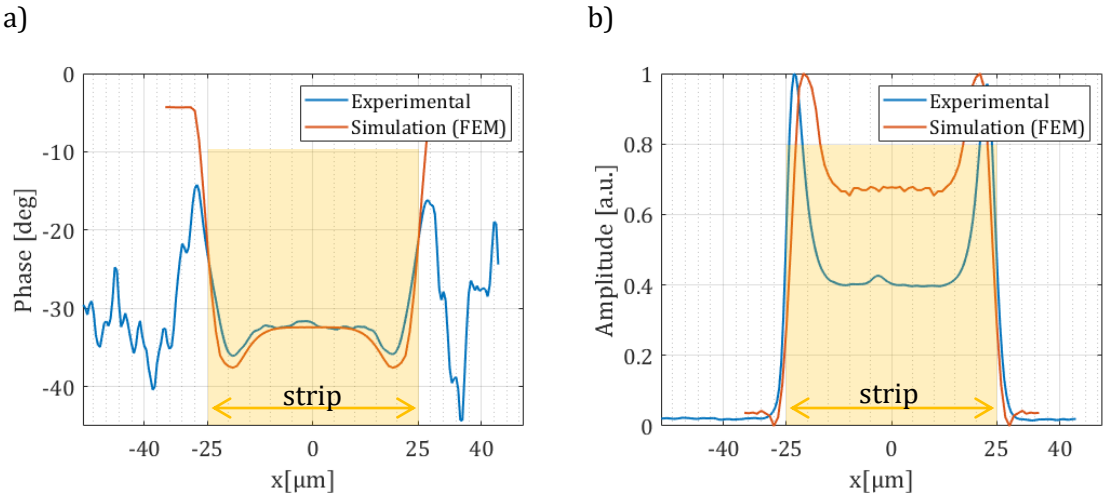

Figure 4.35: (a) Phase and (b) amplitude comparison between simulated and experimental scanning of 50 µm wide strip.

The results of the simulation and the measured scan are compared in Figure 4.35 (a) for the phase and (b) for the amplitude. On the phase plot one can see the similar evolution on both signals for the region inside the strip but a large difference in the substrate region. This difference comes from the semitransparent behavior of the substrate that is not accounted with the simulation. In addition, because of the low signal, the measured phase could be influenced by the background noise. On the normalized amplitude plot one can see that the measured signal at the edges is more than doubled relative to the center but in simulation the difference is lower than the half. Although the amplitude is no used in the quantitative analysis the large increase of the signal suggests a high temperature increase at the edges.

To further challenge the spatial resolution capabilities, one strip with 300 nm width was scanned, with the same scan configuration as used for the 50 µm wide strip (Table 4.6). Figure 4.36-a shows the obtained image. The contrast between the strip and the substrate is clearly visible, in both amplitude and phase. On the cross section, one can identify the region related to the strip, as a peak in the amplitude plot and a flat region in the phase plot, similar to those for the larger strip.

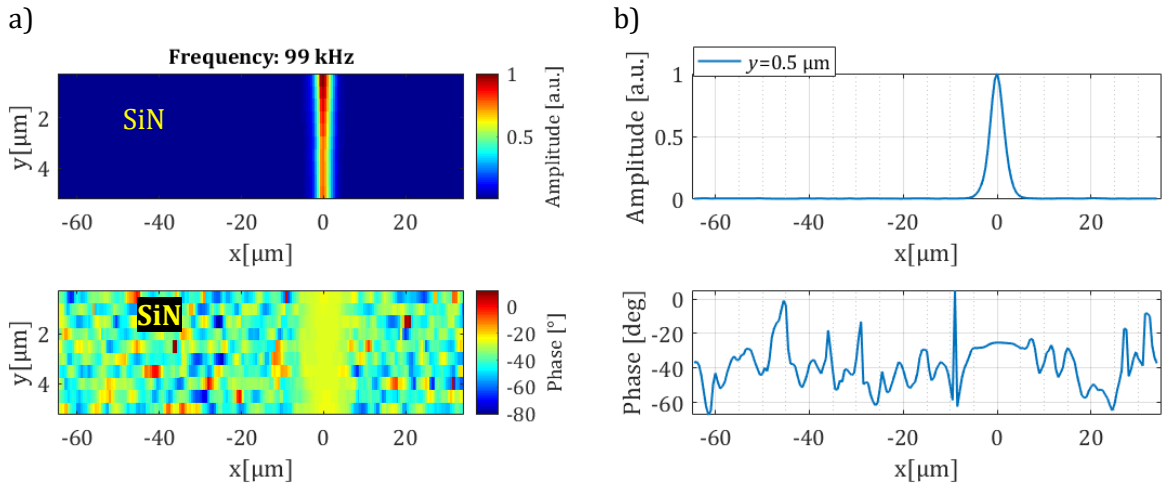

Figure 4.36: (a) Scan image of the 300 nm wide 3-ω strip with 400 nm thick GGST layer. (b) Amplitude and phase plot of first scan line (y=0.5 µm).

Figure 4.37 show a comparison between the FEM simulation of scanning and the experimental data. It is evident that, unlike for the 50 µm strip, the phase measured has a large difference with the simulation. This difference is a consequence of the probe size and the phase value in the substrate zone. One has to remember that the probe is sensing in a large area and provides an average value of all inside this area. Since the measurement area is much larger than the emitter we have a signal highly influenced by the substrate behavior. Similar behavior is observed on the edges of the 50 µm strip where the phase is about 25° like in the central region of the 0.3 µm strip phase plot.

a) b)

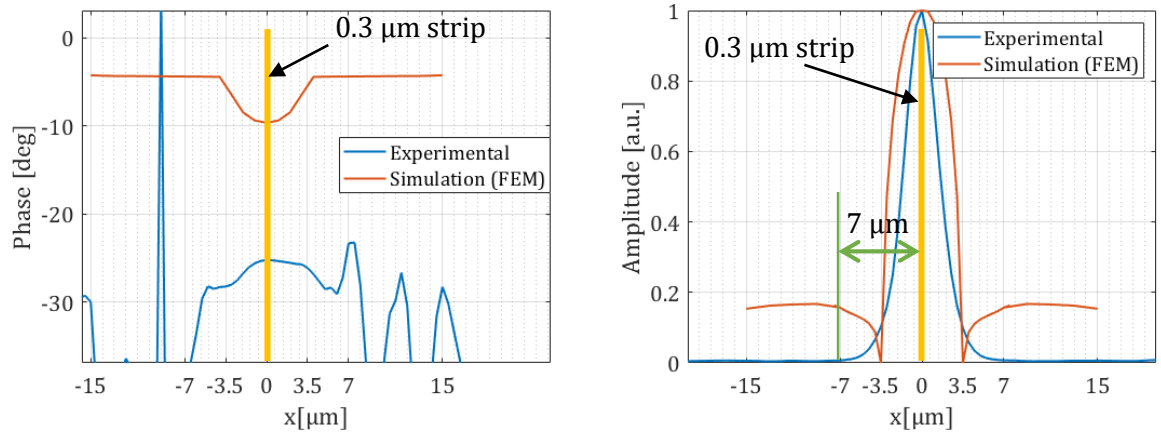

Figure 4.37: (a) Phase and (b) amplitude comparison between the simulated and experimental scanning of 300 nm wide strip.

In the amplitude plot one can see that the measured signal is wider than the strip in both experimental and simulation. The widening effect is also a result of the probe size that is bigger that the strip. The signal starts rising up where the probe starts to cover the strip and reach the maximum at the center position. As a result, it is observed a signal with a width resulting from superposition of the probe and the strip. Similar behavior occurs in the 50 µm strip but here is more evident because the strip is much smaller than the probe size.

From the scanning across the contact interface and the scanning of the 3-ω strip we conclude that the measurements from SPR setup can be used to perform a quantitative analysis if the geometry of the sample are known and the materials are opaque. Under this condition the model of the sample can be compared directly with the measurements at the corresponding position without need of any previous treatment. And this is valid for structures even smaller than the probe size.

Further studies have to be done to extend the analysis to semitransparent media where the main challenge is the characterization of optical parameters of materials.

4.3.3 Imaging on composite materials.

In this section we present the thermal contrast images acquired with SPR on three different composite materials: silica fibers in pyrocarbon matrix, carbon fibers in aluminum matrix and carbon fibers in epoxy matrix.

Silica Fiber-Pyrocarbon composite (SF-PyC).

Lamellar pyrocarbons (PyC) are used as interphases or matrices of carbon/carbon and ceramic-matrix composites in several high-temperature aerospace applications. Depending on their organization at the nanoscale, they can have a variety of mechanical and thermal properties. Hence, it is important to know the properties of these matrices at the micrometer scale in order to improve and control the composite behavior at the macroscopic scale.

a) b)

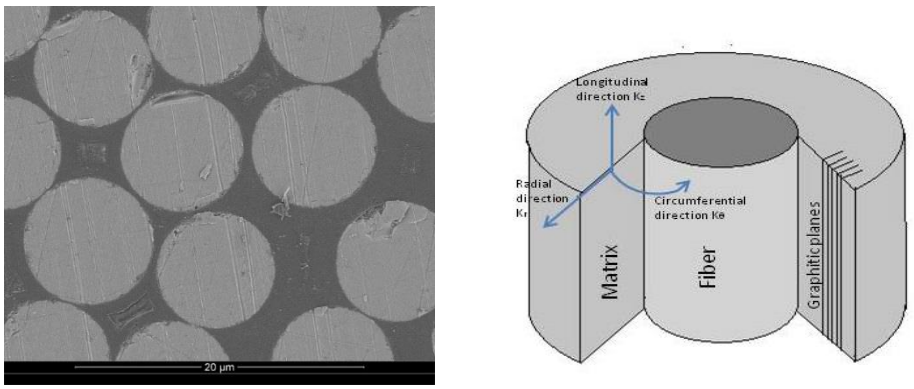

Figure 4.38: a) SEM image of the Composite Structure; b) Scheme of the silica fiber surrounded by the lamellar PyC matrix.

Material	k W·m^{-1}·K^{-1}	ρ kg·m^{-3}	C_p J·kg^{-1}·K^{-1}
Silica Fiber	1.1	2200	748
PyC	20	2100	748

Table 4.7: Properties of the silica fiber and PyC present in the composite sample.

The composite consists of an as-deposited regenerative laminar (ReL) PyC [123] deposit made on glass fibers as presented in Figure 4.38. The general orientation of the graphitic sheets is concentric around the fibers. The sample has been previously studied with SThM [27]. Where the measurements achieved when the probe is in contact with the PyC lead to identify the effective thermal conductivity ($k = \sqrt{k_r^2 + k_z^2}$), without possibility to identify the orthogonal components individually. Table 4.7 shows the obtained effective thermal conductivity for the PyC and the additional thermal properties of the sample reported in the study.

In order to test the capability to discriminate between different materials, we select an area over the PyC sample where a fiber could be easily distinguished from the matrix in the visible image. The scanned area is framed with a red square in Figure 4.39-a; where the target fiber close to the right edge of the scanned area can be identified. The used scan parameters are presented in Table 4.8 and the obtained images for five excitation frequencies in the 1-100 kHz range are presented in Figure 4.39 b-f.

Parameter	Value
L	30 µm
W	15 µm
Δx	0.5 µm
Δy	0.5 µm
Δt	0.3 s
v	1.6 µm/s
SL	1

Table 4.8: Scanning parameters for the PyC composite imaging and presented in Figure 4.39.

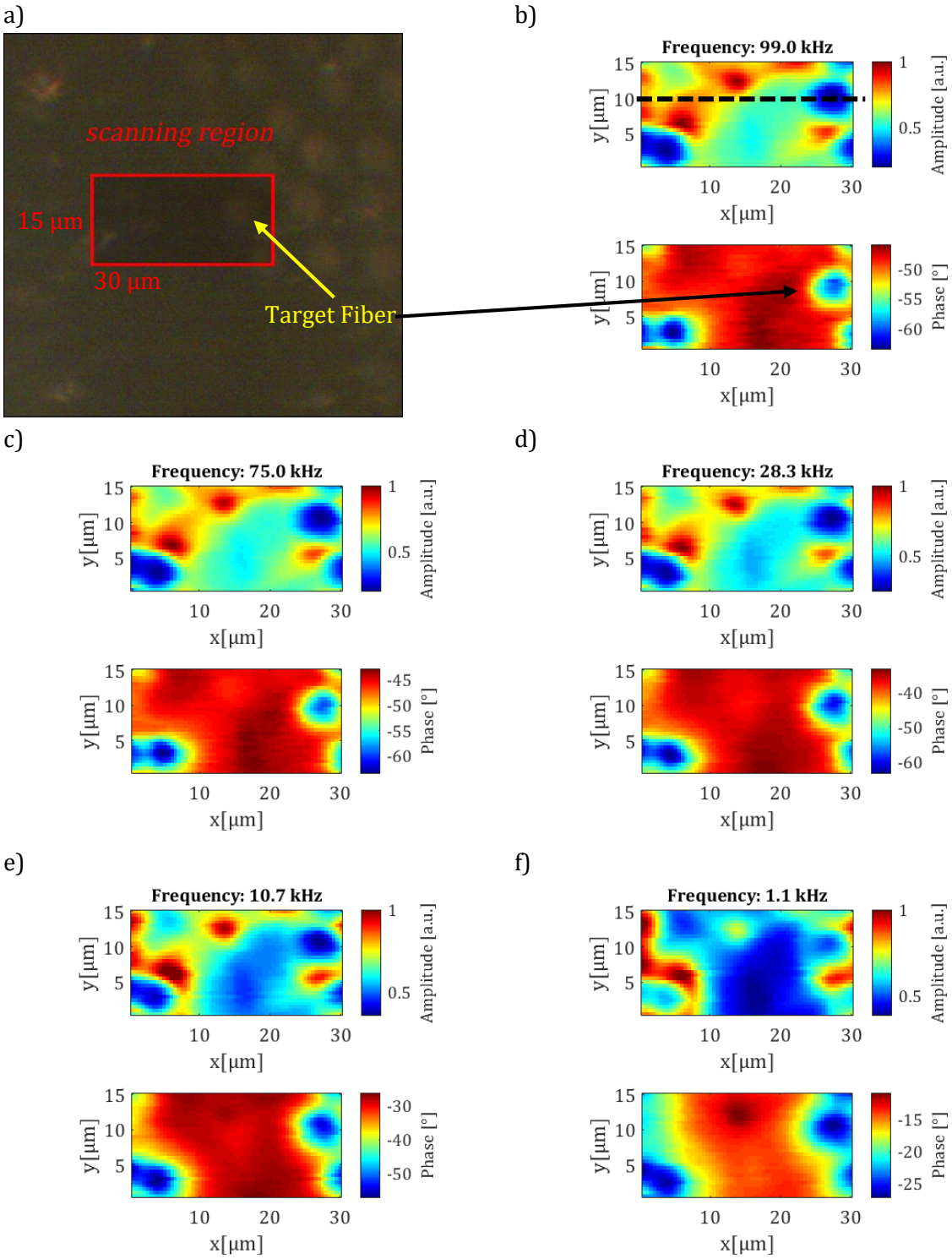

Figure 4.39: a) Visible image of the scanned area on the PyC composite sample. Obtained images of amplitude and phase on the scanned area using different excitation frequency: b) 99 kHz; c)75 kHz; d)28.3 kHz; e) 10.7; f) 1.1 kHz.

Figure 4.39 shows the amplitude and phase acquired at different excitation frequency. The silica fiber is clearly distinguished from the substrate in both signals. In addition to the target fiber, it is possible to identify more structures behind the surface that are more or less well defined

according to the excitation frequency. This is explained by the difference in the diffusion length of each frequency measurement. Another remarkable difference between the scan at high frequency and the one done at low frequency linked with the diffusion length is the definition of the phase image that is clearly better at high frequency. This effect is better appreciated in the line plot as presented in Figure 4.40-b where the phase slope near to the fiber (blue shadow region) becomes shorter and steeper for high frequency. The plots in Figure 4.40 correspond to the black dashed line in amplitude image in Figure 4.39-b.

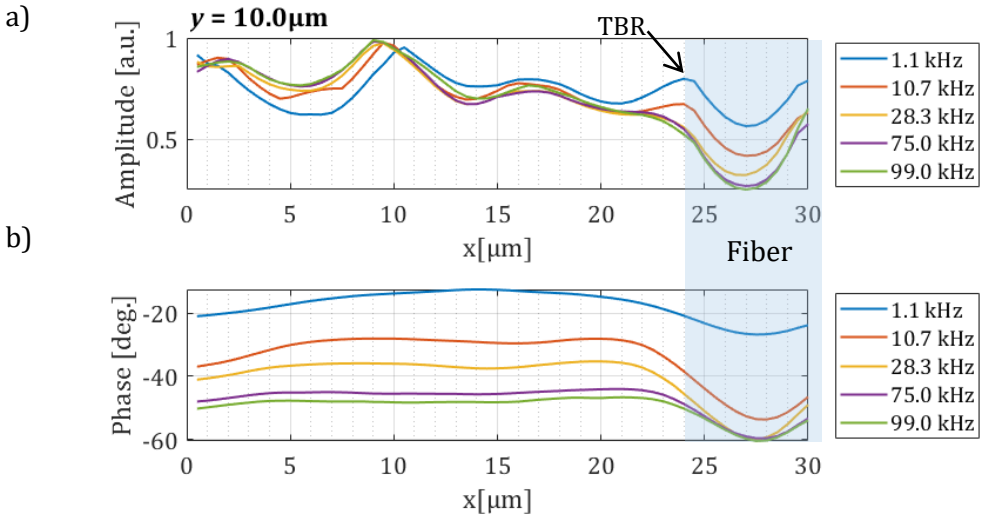

Figure 4.40: Frequency comparison of scan line at y=10 µm for (a) amplitude and (b) phase. Blue shadow represents the fiber region.

On the other hand, in the amplitude plots it clearly appears the increase in temperature due to the TBR at the interface between the matrix and the fiber. This TBR is clearly visible at low frequency, but it vanished at high frequency. Although the fiber has lower than the matrix thermal conductivity an amplitude decrease is observed at its location. In fact, the absorbed power is lower given to the semitransparency.

A quantitative analysis is limited according to the complex structure of the sample. We cannot assume a homogenous geometry more than few micrometers around the silica fiber. From the frequency scans more fibers behind a thin surface layer of PyC are visible. In addition, the simulation should involve the absorption properties of the sample. Nevertheless, the capability of the SPR to differentiate between different types of material is demonstrated.

Carbon Fiber-Aluminium composite.

To further challenge the sensitivity of the SPR the Carbon Fiber –Aluminum (CF-Al) composite material made of carbon fibers surrounded by an aluminum matrix was scanned. In this experiment we pretend to differentiate between two materials with high thermal conductivity. A zone including a single fiber is selected. Figure 4.41 shows the visible image of the CF-Al composite where the area with target carbon fiber is framed with red rectangle. The fiber can be easily distinguished in the center of the marked zone. The parameters used for scanning are collected in Table 4.9.

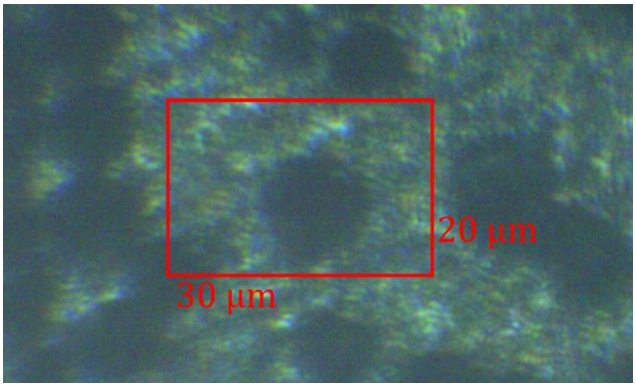

Figure 4.41: Visible image of the CF-Al composite. The SPR scanned zone is delimited with red rectangle.

Parameter	Value
L	30 µm
W	20 µm
Δx	0.5 µm
Δy	0.5 µm
Δt	0.3 s
v	1.6 µm/s
f	8.5 kHz
SL	5

Table 4.9: SPR scanning parameters used for the CF-Al composite imaging.

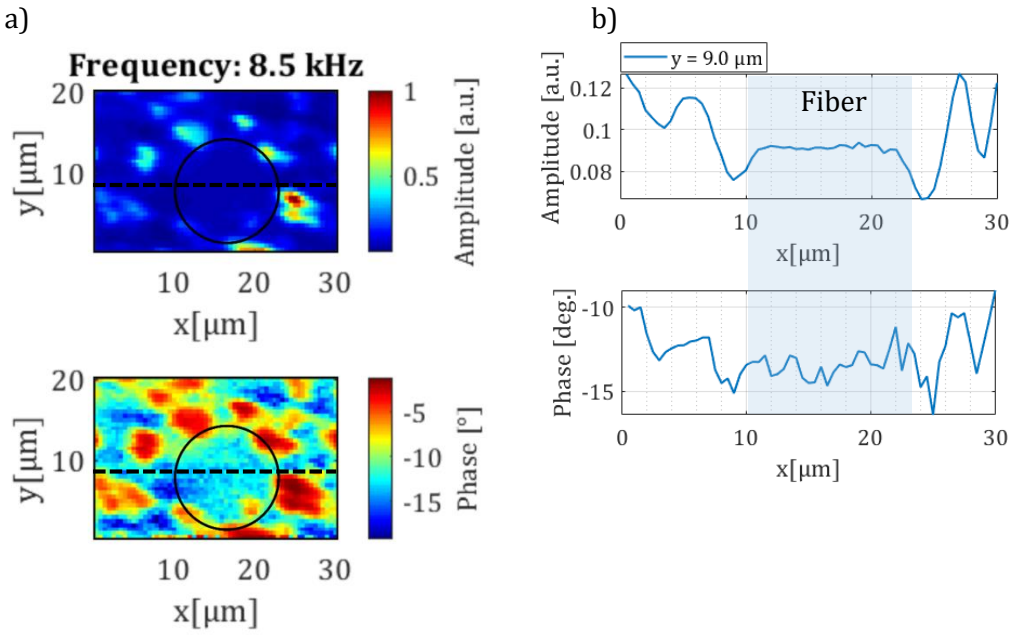

Figure 4.42: a) Amplitude and phase measured by SPR on the CF-Al composite at 8.5 kHz excitation frequency. b) Amplitude and phase measured at y=9 µm scanline (black dashed line on amplitude and phase image).

The images of amplitude and phase from the experiment are presented in Figure 4.42. The amplitude and phase images do not exhibit the position of the fiber as clearly as in the visible

image. In fact, it is expected at the position of the black circle marked on these images. Nevertheless, on the amplitude plot from the dashed line, the fiber zone becomes clear as a flat region.

Because of the high thermal conductivity of the sample, the temperature increase is low and the measured IR signal is largely biased by the noise generated by the germanium window, thus the quantitative analysis seems delicate.

Carbon Fiber - Epoxy composite.

Finally, we present the scanning images obtained on a Carbon Fiber-Epoxy (CF-E) composite. In this case, the carbon fiber is surrounded by an epoxy matrix. Again, the selected zone to perform the scanning contains an easily identifiable vertical structure surrounded by a random configuration. The visible image of the CF-E composite is presented in Figure 4.43. The SPR scanning was carried out with 53.5 kHz excitation frequency with two different velocities.

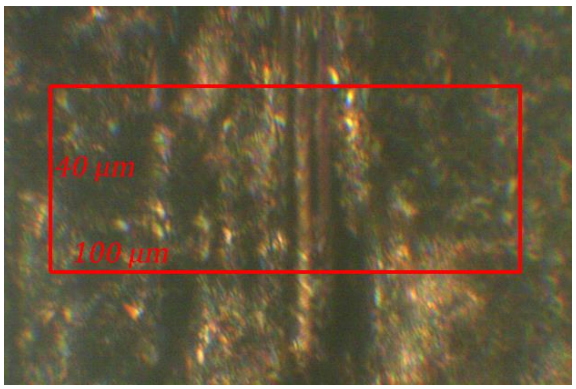

Figure 4.43: Image of CF-E sample with the scan zone is marked by a red square.

As indicated previously, the scan velocity is an important parameter regarding the data acquisition process. It is directly related with sampling time and thus to the time constant selected on the lock-in since the maximum T_c is set by Δt. We tested this relation on this sample in order to check how it affects the results in heterogeneous material. The used scan parameters are listed in Table 4.10.

Parameter	Value
L	100 µm
W	40 µm
Δx	0.2 µm
Δy	0.2 µm
f	53.5 kHz
SL	1

Table 4.10: Scanning parameters used in SPR imaging of the CF-E composite. Visible image presented in Figure 4.44.

With sampling interval of 0.2 µm, we will first set a velocity of 6.6 $\mu m \cdot s^{-1}$ that limit the time constant to 30 ms. The second velocity used is 2 $\mu m \cdot s^{-1}$ and thus the time constant can be as

large as 100 ms. Under these conditions we obtain the amplitude and phase images presented in Figure 4.44 for each velocity. The target fiber can be easily identified in all the thermal images. Nevertheless, observing the images acquired at lower velocity one can note the improvement in the definition as the result of larger time constant selected.

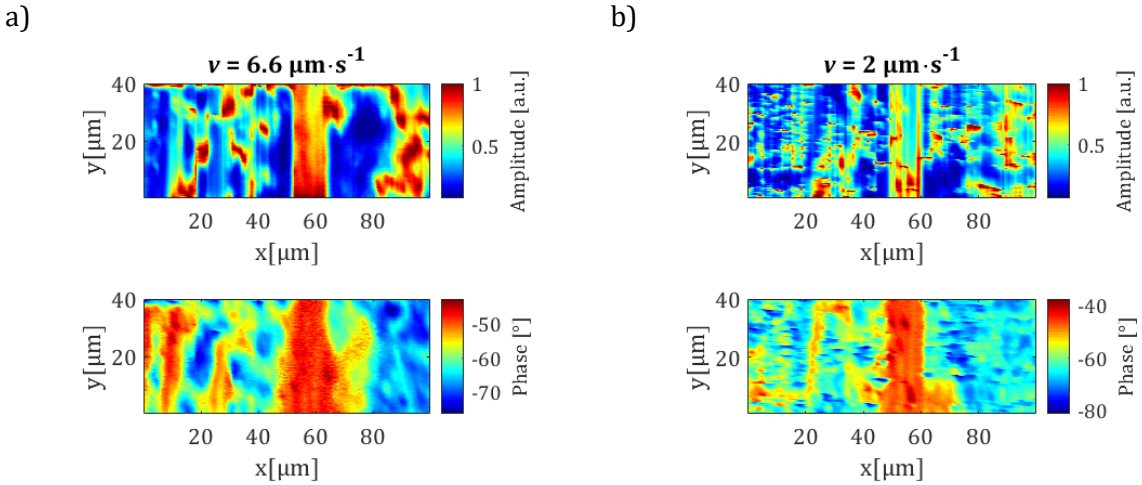

Figure 4.44 Amplitude and phase images obtained by SPR on CF-E composite with two scanning velocities: a) v = 6.6 µm · s^{-1} and b) v = 2 µm · s^{-1}.

The thermal image shows that the composite sample is very heterogeneous, which makes a geometric description difficult. This fact and the semitransparent behavior of the epoxy matrix makes complicate to perform a quantitative analysis of this sample.

4.4 Conclusions.

This chapter was dedicated to present the application of the SPR setup with two main objectives: the first to establish the reliability of the setup and the second to show its capabilities in the acquisition of thermal images at high frequency, up to 100 kHz, that is higher than the frequency reachable with IR thermography.

In the first part of the chapter, we showed the experiments carried out in static configurations. Those experiments were realized in order to compare the results of the new setup with the results obtained from well-known measurements like the Hot Disk and the 3-omega method. The used samples were the stainless-steel SST bulk material and the chalcogenide phase change GGST alloy in thin film on silicon substrate configuration respectively.

The measurements on SST exhibited that the germanium window used to separate the IR radiation from the laser wavelength can bias significantly the results if the IR signal from the sample becomes weak compared to the one from the germanium window. It appears that a correct selection of power and frequency range is crucial to the reliability of the measurements. In addition, we used the measurements on the SST sample and the semi-infinite media model to estimate the real measurement area of the setup. Once all the parameters of the experiment were characterized, another validation in static mode has been realized using the multilayer sample designed for the 3-ω method measurement. Thus additionally, the 3-ω technique was used to

measure the thermal conductivity of the GGST layer within the multilayer structure. A good agreement was found with the value obtained using the SPR in static condition at high frequencies up to 99 kHz.

Once the SPR was validated from static condition, the scanning experiments for thermal image acquisition were performed and presented in section 4.3. The first application was the estimation of the thermal boundary resistance at the interface between two metallic parts. We showed that the SPR measurements allow the quantitative estimation of this TBR. This suggests that the procedure could be applied to the thermal characterization of thin layers' perpendicular to the plane surface of the sample. Next, we assessed the spatial resolution of the SPR by scanning across the narrow strip of the 3-ω sample. Because the strip has a known geometry, it allows a comparison between the experimental data and those from a discrete model using the FEM. We tested two strips, the first one of 50 µm width and the second of 300 nm. It was observed that if the sample is opaque the SPR is able to differentiate structures smaller than 300 nm even though the probe is bigger.

The high resolution of the SPR comes from the combination of two factors that generate a contrast on the 3D structured material. The first one is the difference between the heat source radius and the probe radius that makes the setup highly sensitive to the in-plane diffusion even in static conditions. The second factor is the spatial sampling interval, which when lower than the probing diameter leads to the overlapping of the measurements and renders the image formation sensitive to objects narrower than the probing spot.

We conclude that the measurements from the SPR setup can be used to perform a quantitative analysis if the geometry of the sample is known and materials are opaque. Under those conditions the solution of a model of the heat transfer within the sample can be compared directly with the measurements at the corresponding position through an identification process.

Finally, we presented the measurements on three composite samples to show that the SPR offers very good performances in the thermal imaging of materials at high frequency.

Chapter 5:
General Conclusions and perspectives.

5.1 Conclusions

The basic idea of this work was the need to perform imaging the thermal properties of heterogeneous materials at the microscale and at high frequency. Thus, we have presented two different scanning experiment proposals in order to achieve this goal. The first one in contact and the second one in contactless mode. Both proposals are based on the modulated photothermal radiometry as sensing principle. The IR emission of an opaque surface heated by a periodic photothermal excitation is sensed with an infrared detector. Both techniques are also based on scanning of the surface with a micrometric spatial resolution. In this way, a thermal mapping of the surface within a high frequency range can be carried out. It was therefore important to check if those techniques are more accurate and sensitive than other well-known techniques, namely, the imaging thermoreflectance and the IR thermography. Those techniques are recalled in chapter 1 together with the SThM contact method.

In chapter 2, we proposed a new kind of contact scanning method inspired by the SThM technique with the main objective to address the problem of heat leakage into the probe. The proposed approach is based on an optical fiber with transmittance in the NIR and the MIR in order to carry the laser illumination to the investigated surface and to collect the IR emission from this heated surface to a detector. Making an analogy with the SThM comes to say that the Joule effect used as heat source in typical resistive probe is replaced by the photothermal excitation from a modulated laser and the thermo-resistive effect used as the sensing phenomena is replaced by the probe emittance. The main idea is to generate and monitor the temperature change in a well-insulated and small tip that works as the heater and the sensor at the same time. Therefore, a small piece of metal is attached at the end on the optical fiber in order to play the role of the optical-to-thermal transducer. The correct selection of fiber allows to supply the photothermal heat source to the transducer and, at the same time, to collect the infrared radiation generated by this transducer. We showed that this setup allowed differentiating the contact between two different materials. Nevertheless, the low signal level and the thermal inertia of the probe allows measurements only in low frequency range, with 2 kHz as the maximum frequency. In addition, the random nature of the contact between the transducer and the investigated surface makes the measurements in the developed configuration uncertain.

The idea behind this first experiment was quite simple, but its application faces technical challenges that are not easy to overcome, like the reduction of the probe tip size and the probe-sample contact control. An alternative to avoid the first one is to remove the transducer at the end of the fiber and heat and measure directly on the sample. This kind of solution will allow the reduction of the probe size with the reduction of the optical fiber aperture as it occurs in SNOM technique. Nevertheless, it leads to probe which becomes extremely fragile and the experimental operation requiring complex and expensive experimental setup to control the distance between the probe and the surface during the scanning. In addition, because the measurements must be done in the near field, the sample-fiber interaction has to be considered in the data analysis.

Although, we don't rule out addressing this kind of solution in the future. In fact, we did not have enough experience to face these challenges in a period of time suitable with the PhD duration.

Therefore, we decided to switch to a contactless photothermal radiometry technique with the implementation of a scanning configuration for thermal image acquisition. Thus, the second experimental setup was developed and presented in this work: the SPR.

In the SPR arrangement, we replaced the optical fiber probe by a Cassegrain microscope objective. The use of a reverse Cassegrain microscope objective makes it possible to focus the laser beam over the sample surface and collect the emitted infrared radiation from the same sample surface consequently to the periodic photothermal excitation. The thermal contrast image of sample is obtained by implementing a pixel-by-pixel mapping.

The SPR setup was detailed in chapter 2, where the characterization of the heating spot and a first approximation to the measurement area were presented. In this chapter were also defined the parameters involved in the scanning process and the synchronization between the scan constant velocity and the data acquisition time interval.

Although the scanning is carried out at constant velocity, we showed in chapter 3 that its very small value does not affect significantly the thermal response viewed by the detector comparing to the motionless configuration. Thus, the scanning process can be simulated using models for motionless conditions. In addition, we show a comparison between the analytical solution for the semi-infinite media in static conditions and the numerical model for the semi-infinite media that moves at constant velocity with respect to the photothermal source. We show also that the experimental configuration provides a large sensitivity to the in-plane heat diffusion.

The high in-plane sensitivity is one of the factors involved in the micrometric resolution of the SPR even when the probe size is relatively large. The second factor is the reduced sampling interval reached with the piezoelectric translation stage. Using a sampling interval lower than the probing diameter leads to the overlapping of the aimed area and renders the image formation sensitive to objects narrower than the probing spot. This was put in evidence in the different applications of the SPR presented in chapter 4.

In the first part of chapter 4 we presented the applications in motionless conditions carried out with the objective to assess the performances of the SPR and to validate the associated model. From this study, we found that the germanium window, used to separate the collected IR radiation from the laser radiation, could bias significantly the results if the IR signal from the sample is weaker than the one generated by the Ge window. The signal generated by the germanium window produces a shift in the measured phase that modify the value of the estimated parameter. Thus, a correct selection of power and frequency is crucial with regards to the reliability of the measurements. This problem arises particularly with materials of high thermal conductivity or low emissivity, since this will result in a low IR signal.

From the scanning across the contact interface between two steel pieces and the scanning of the 3-ω strip we concluded that the measurements from the SPR setup can be used to perform a quantitative analysis if the geometry of the sample is well known. Under this condition, the model can be faced with the measurements at the corresponding position without the need of previous

data processing. The comparison is at the basis of the minimization technique implemented to perform the parameter identification process.

With the scanning across the contact interface we were able to estimate the TBR and the procedure could be applied to the thermal characterization of thin layers perpendicular to the plane surface of the sample. Since the geometry of the 3-ω sample is known, we used it to assess the resolution of the SPR. It allows a comparison between the experimental data and those from the numerical simulation of two strips of 50 µm and 300 nm width. It was shown that the SPR is able to differentiate structures smaller than the probe size. In addition, it was observed that if the sample is opaque the SPR allows a quantitative analysis.

The application of the SPR on the composite materials showed the potential advantage of the technique to perform the thermal characterization of complex 3D micro structured materials. In addition, the sensitivity to high thermal conductivity materials was tested. Table 5.1 summarizes the main parameters of the developed setup and the values used in the present work.

Parameter	Limits	Used	Sample
Frequency	Up to 100 kHz	99 kHz	3-ω strip
			Silica fiber-Pyrocarbon
		53.3 kHz	Carbon fiber-Epoxy
		8.5 kHz	SST contact interface
			Carbon fiber- Aluminium
Spatial sampling resolution	Limited by scan step	0.2 µm	Carbon fiber-Epoxy
	10 nm	0.5 µm	3-ω strip
			Silica fiber-Pyrocarbon
			Carbon fiber- Aluminium
		1 µm	SST contact interface
Sampling time	≥ 2 ms	0.03 s	Carbon fiber-Epoxy
		0.1 s	3-ω strip
		0.3 s	Silica fiber-Pyrocarbon
			Carbon fiber- Aluminium
		1	SST contact interface
Scan velocity	1 µm to 20 µm	6.6 $\mu m \cdot s^{-1}$	Carbon fiber-Epoxy
	(Related to IR signal level)	5 $\mu m \cdot s^{-1}$	3-ω strip
		1.6 $\mu m \cdot s^{-1}$	Silica fiber-Pyrocarbon
			Carbon fiber- Aluminium
		1 $\mu m \cdot s^{-1}$	SST contact interface
Material diffusivity	(Related to IR signal level)	10^{-7} - 10^{-6}	Silica fiber (6.6×10^{-7})
			Aluminium (9×10^{-5})

Table 5.1: Parameters used in the thermal image acquisition by SPR.

5.2 Perspectives

The developed SPR setup permits to carry out the thermal mapping of materials in the actual state. However, the different analysis and assessments realized in this work highlighted that the obtained measurements must be dealt carefully when quantitative estimation is targeted. This fact leads to several, experimental and theoretical, perspectives arising from the realized work.

Firstly, the bias induced by the heating of the germanium window must be mastered in order to be able to perform a quantitative analysis on high thermal conductivity materials at high frequencies. A potential solution is to increase the laser beam size that is reflected on the germanium window before to be focused on the sample surface. This could allow to reduce the heat flux density and thus to decrease the heating on the germanium window. Thus, the design and test of a new optical configuration is required in order to avoid the germanium window interference and keep the desired magnification provided by the microscope objective.

Another solution could be researched by adapting the excitation source wavelength with that corresponding to the maximum reflectivity of the germanium window. In addition, the use of different wavelength as excitation source, and why not with different filters, could provide the opportunity to test different materials with opaque behavior in different wavelength range.

Secondly, in the actual configuration, the setup is limited in maximum operation frequency by the SR830 lock-in amplifier which works up to 100 kHz. There is thus potential to increase the accessible frequency range by the use of a lock-in with larger frequency range and of an appropriate infrared detector whose market announced performances are going up to 100 MHz.

In addition, since the method is contactless, it can also be implemented for high temperature characterizations.

On the other hand, this work can be extended to the analysis of semitransparent materials by using of adequate models taking into account the volume interaction of light and matter. This of course implies the knowledge of optical properties of the material or materials if one considers a composite.

Finally, from the theoretical point of view, the aspects of coupling of the image processing techniques with the mapped thermal images, obtained using spatial scanning step lower than the probing spot size, are to be investigated. For information, a collaborative work in this sense was undertaken with the Image and Signal Processing team of the IMS laboratory of University of Bordeaux.

Appendix.

I. The lock-in amplifier.

The experimental principle is based on the measurement of variation of emittance from the sample surface. This variation has to be low enough to ensure the linearity assumption between the temperature and the emittance. In general, the electric voltage issued from the infrared detector is small and drown in noise, which can be several times higher than the signal itself. In this case the measurement by lock-in amplifier becomes essential.

The lock-in amplifiers are used to detect and measure periodic signals as low as several nanovolts. Accurate measurements may be made even when the signal is obscured by a noise thousands times higher. Lock-in amplifier uses a technique known as phase-sensitive detection to extract the signal amplitude and phase at a specific reference frequency. Noise signals, at frequencies other than the reference frequency, are rejected and do not affect the measurement. Figure A- 1 shows a scheme of the principle of lock-in amplifier measurement.

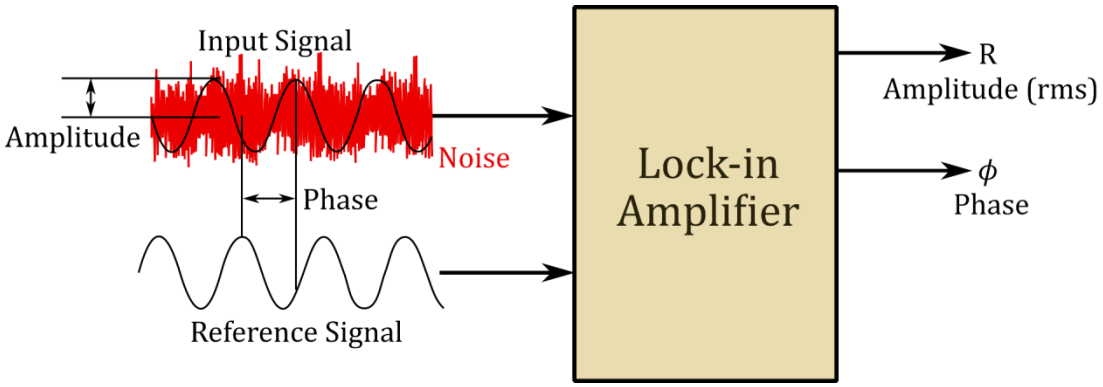

Figure A- 1: Lock-in amplifier permits to extract the signal amplitude and phase in extremely noisy environments [124].

Lock-in measurement requires a frequency reference that is fixed in our case by periodic heating during the experiment and the signal to be measured. Lock-in amplifier uses a phase-locked-loop (PLL) to generate its internal reference signal driven by the experiment reference (in our case, the signal viewed by the reference photodetector). The PLL in the lock-in locks the internal reference oscillator to this external reference, resulting in a reference sine wave at ω_{ref} with a fixed phase shift of ϕ_{ref}. One can define the reference signal as:

$$Q_{ref} = A_{ref}\sin(\omega_{ref}t + \phi_{ref}) \qquad \text{(A - 1)}$$

On the other hand, the signal to be measured (in our case, the signal from the infrared detector) is composed of useful signal and noise at all other frequencies. As an example, one considers that the measured signal with amplitude A has a frequency ω and phase $\tilde{\phi}$ and is expressed as:

$$Q = A\sin(\omega t + \tilde{\phi}) \qquad \text{(A - 2)}$$

The lock-in amplifies the signal and then multiplies it by the lock-in reference using a phase-sensitive detector (PSD) or multiplier. The output of the PSD is simply the product of two sine waves.

$$\begin{aligned} Q_{PSD} &= A_{ref}\sin\left(\omega_{ref}t + \phi_{ref}\right) \times A\sin\left(\omega t + \tilde{\phi}\right) \\ &= \frac{1}{2}A_{ref}\,A\cos\left(\left(\omega - \omega_{ref}\right)t + \tilde{\phi} - \phi_{ref}\right) \\ &\quad - \frac{1}{2}A_{ref}\,A\cos\left(\left(\omega + \omega_{ref}\right)t + \tilde{\phi} + \phi_{ref}\right) \end{aligned} \tag{A - 3}$$

The PSD output is constituted of two AC signals, one at frequency $\omega - \omega_{ref}$ and the other at frequency $\omega + \omega_{ref}$. However, if ω equals ω_{ref}, the component at $\omega - \omega_{ref}$ frequency will be in fact a DC signal. Now, if the PSD output is filtered by a low pass filter, the AC signals are removed and the filtered PSD output will be:

$$\begin{aligned} Q_{PSD} &= \frac{1}{2}AA_{ref}\cos\left(\tilde{\phi} - \phi_{ref}\right) \\ Q_{PSD} &= R\cos\left(\tilde{\phi} - \phi_{ref}\right) \end{aligned} \tag{A - 4}$$

This DC signal is proportional to the amplitude of measured signal and the phase difference between the signal and the lock-in reference $\left(\tilde{\phi} - \phi_{ref}\right)$. One can adjust the phase reference to set it at zero and the signal will be proportional to the phase of the measured signal. This phase dependency can be eliminated by adding a second PSD. If the second PSD multiplies the signal with the reference oscillator shifted by 90°, its low pass filtered output will be:

$$\begin{aligned} Q_{PSD2} &= \frac{1}{2}AA_{ref}\sin\left(\tilde{\phi} - \phi_{ref}\right) \\ Q_{PSD2} &= \mathrm{R}\sin\left(\tilde{\phi}\right) \end{aligned} \tag{A - 5}$$

In this manner one obtains two outputs, one proportional to $\cos\left(\tilde{\phi}\right)$ and the other proportional to $\sin\left(\tilde{\phi}\right)$. Denoting the first output *X* and the second *Y*, these two quantities represent the signal as a vector relative to the lock-in reference oscillator as:

$$\begin{aligned} X &= R\cos\left(\tilde{\phi}\right) \\ Y &= R\sin\left(\tilde{\phi}\right) \end{aligned} \tag{A - 6}$$

The magnitude *R* of the signal is then computed as:

$$R = \sqrt{X^2 + Y^2} \tag{A - 7}$$

and its phase $\tilde{\phi}$, is:

$$\tilde{\phi} = \tan^1\left(\frac{X}{Y}\right) \tag{A - 8}$$

Figure A- 2 shows the functional block diagram of the SR830 DSP Lock-in amplifier used in this work.

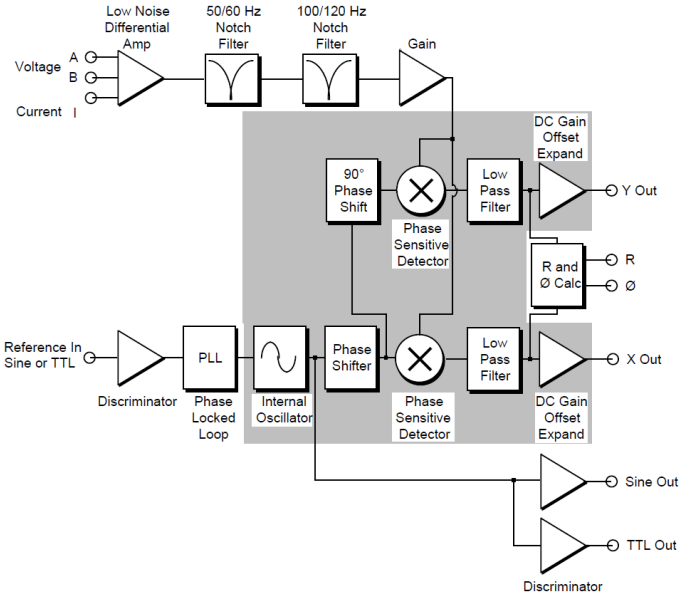

Figure A- 2 The functional block diagram of the SR830 DSP Lock-In Amplifier [125]

The PSD and low pass filter only detect signals whose frequencies are very close to the lock-in reference frequency. Noise signals at frequencies far from the reference are attenuated at the PSD output by the low pass filter. Their attenuation depends upon the low pass filter bandwidth and roll-off. A narrower bandwidth will remove noise sources very close to the reference frequency; a wider bandwidth allows these signals to pass. The low pass filter bandwidth determines the bandwidth of detection and the lock-in amplifiers have traditionally set the low pass filter bandwidth by setting the time constant.

II. Principle and model of the 3-ω method.

This paragraph presents the principle and model for the 3-ω method. We used the 3-ω patterns of phase change material (GGST) in order to have a multilayer reference sample for thermal properties and at the same time a well-defined geometrical configuration for scanning experiment.

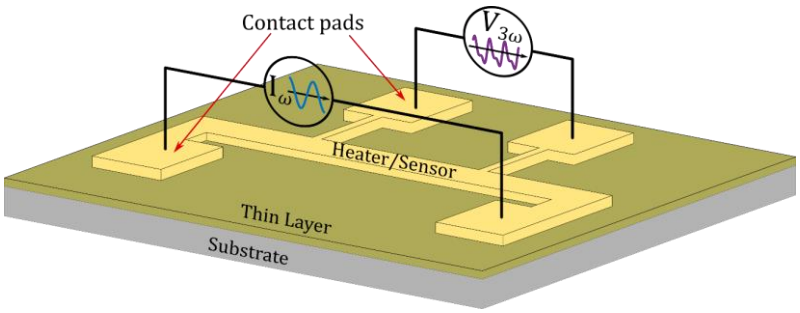

Figure A- 3 Schematic representation of the principle of 3-ω measurement.

For measurements by the 3-ω method, a thin metallic strip is deposited on the top surface of the sample. When a thin layer on a substrate is studied, the strip is deposited on the layer. The strip supplied with an electrical current acts as a heater and at the same time as temperature sensor. Obviously, for dielectric materials, the heater is deposited directly on the surface of the sample but if the sample is an electrically conducting material, then an insulating layer between the heater and the sample is mandatory in order to insulate it from the sample material. Figure A- 3 shows a typical configuration of the 3-ω pattern. One distinguishes two external connection pads to supply the electric current to the strip and two internal pads used to measure the voltage generated by the current flowing through the strip. In the experiment, a modulated current with frequency ω is used. Therefore, the Joule effect generates a heat flux within the strip and leads to a temperature oscillation at frequency 2ω. This temperature variation results in the strip resistance change which can be followed through the strip voltage at 3-ω frequency.

The heater/sensor being very thin, it is assumed that it is thermalized at each time and its temperature is that of the sample surface. It is also considered that the generated heat flux is transmitted completely to the sample. The heat flux is applied on the sample surface in the shape of a rectangular strip. In general, it is admitted that the strip is infinite since its length *2l* (order of millimeters) is very large compared to its width *2b* (order of micrometers), as represented in Figure A- 4.

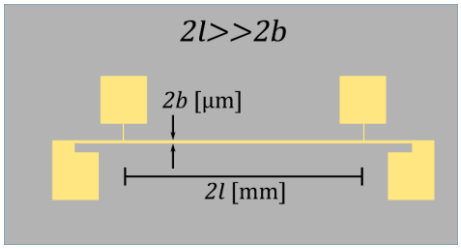

Figure A- 4: A schematic view of a typical pattern used in the 3-ω technique.

For classical values of the thicknesses $e_d < 1\mu m$, the deposit behaves as a thermal resistance, RT. Indeed, considering the thermal diffusivity range (10^{-5} - 10^{-7}) m^2s^{-1}, the thermal diffusion length is l_h>> 1µm in the 100 Hz - 1kHz frequency range, as plotted in Figure A- 5. On the other hand, the substrate thickness e_s, is generally much larger than the diffusion length in the same frequency region, thus the substrate behaves as a semi-infinite media.

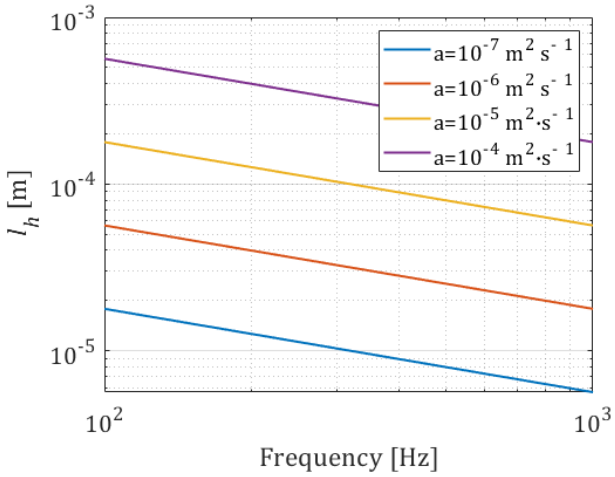

Figure A- 5: Heat diffusion length for four different values of the thermal diffusivity (a) according to the frequency.

Considering all the above, the problem is described in the 2D coordinates (x, z) as shown in Figure A- 6.

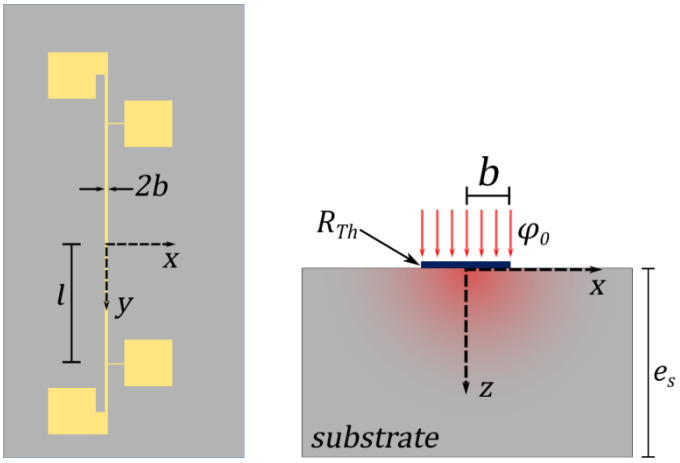

Figure A- 6: Geometrical consideration of the 3-ω measurement.

The system of partial differential equations reflecting the diffusion of heat in the semi-infinite domain is:

$$\rho C_p \frac{\partial T(x,z,t)}{\partial t} = k\left(\frac{\partial^2 T(x,z,t)}{\partial x^2} + \frac{\partial^2 T(x,z,t)}{\partial z^2}\right) \quad \text{(A - 9)}$$

$$\text{at: } 0 < x < \infty, \qquad 0 < z < \infty, \qquad t > 0$$

with boundary conditions:

$$-k\frac{\partial T(x,z,t)}{\partial z} = \varphi(z,t), \qquad \text{at } z = 0 \text{ and } t > 0 \quad \text{(A - 10)}$$

$$\frac{\partial T(x,z,t)}{\partial x} = 0, \qquad \text{at } x = 0 \text{ and } x \to \infty \quad \text{(A - 11)}$$

$$T(r,z,t) = 0, \qquad \text{when } z \to \infty \text{ and } x \to \infty \text{ for } t > 0 \quad \text{(A - 12)}$$

and initial condition:

$$T(x,z,t) = 0, \qquad 0 \le z < \infty, 0 < x < \infty, t = 0 \quad \text{(A - 13)}$$

By applying the Laplace transform on equation (A - 9) one obtains the new system of partial differential equations as follows:

$$\frac{p}{a}\theta(x,z,p) = \frac{\partial^2 \theta(x,z,p)}{\partial x^2} + \frac{\partial^2 \theta(x,z,p)}{\partial z^2} \quad \text{(A - 14)}$$

with boundary conditions:

$$-k\frac{\partial \theta(x,z,p)}{\partial z} = \psi\,(x,p), \qquad \text{at } z = 0 \quad \text{(A - 15)}$$

$$\frac{\partial \theta(x,z,p)}{\partial x} = 0, \qquad \text{at } x = 0 \quad \text{(A - 16)}$$

$$\theta(x,z,p) = 0, \qquad \text{when } z \to \infty \text{ and } x \to \infty \tag{A - 17}$$

The cosine Fourier transform (see [126]) on the temperature upon the x coordinate is:

$$\tilde{\theta}(\alpha,z,p) = \int_0^\infty \theta(r,z,p)\cos(\alpha x)dx \tag{A - 18}$$

$$\tilde{\psi}(\alpha,z,p) = \int_0^\infty \psi(r,z,p)\cos(\alpha x)dx \tag{A - 19}$$

Applying this integral transform to relation (A - 14) one obtains:

$$\frac{\partial^2\tilde{\theta}(\alpha,z,p)}{\partial z^2} - \beta\tilde{\theta}(\alpha,z,p) = 0, \qquad 0 < z < \infty \tag{A - 20}$$

with $\beta = \sqrt{\frac{p}{a} + \alpha^2}$ and:

$$-k\frac{\partial\tilde{\theta}(\alpha,z,p)}{\partial z} = \tilde{\psi}\,(\alpha,p), \qquad \text{at } z = 0 \tag{A - 21}$$

$$\theta(\alpha,z,p) = 0, \qquad \text{when } z \to \infty \tag{A - 22}$$

where the heat flux is:

$$\tilde{\psi}(\alpha,p) = \frac{\varphi_0\sin(\alpha b)}{a} \tag{A - 23}$$

The general solution of differential equation (A - 20) is expressed as:

$$\tilde{\theta}(\alpha,z,p) = Ae^{\beta z} + Be^{-\beta z} \tag{A - 24}$$

The boundary condition when $z \to \infty$ implies that A=0. Thus:

$$\tilde{\theta}(\alpha,z,p) = Be^{-\beta z} \tag{A - 25}$$

Using this expression for $\tilde{\theta}$ in the boundary condition at $z = 0$ leads to:

$$B = \frac{\varphi_0\sin(\alpha b)}{\alpha k\beta} \tag{A - 26}$$

Finally, one obtains the solution:

$$\tilde{\theta}(\alpha,z,p) = \frac{\varphi_0\sin(\alpha b)}{\alpha k\beta}e^{-\beta z} \tag{A - 27}$$

The inverse Fourier transform allows to retrieve the periodic temperature as:

$$\theta(x,z,p) = \frac{2}{\pi}\int_0^\infty \tilde{\theta}(\alpha,z,p)\cos(\alpha x)\,d\alpha \tag{A - 28}$$

Thus:

$$\theta(r,z,p) = \frac{2\varphi_0}{\pi k}\int_0^\infty \frac{\sin(\alpha b)}{\alpha\beta}e^{-\beta z}\cos(\alpha x)\,d\alpha \tag{A - 29}$$

at the sample surface, $z = 0$ it is:

$$\theta_0(x,p) = \frac{2\varphi_0}{\pi k}\int_0^\infty \frac{\sin(\alpha b)}{\alpha\beta}\cos(\alpha x)\,d\alpha \tag{A - 30}$$

and the average temperature on the sensor is:

$$\bar{\theta}_0(p) = \frac{1}{b}\int_0^b \theta_0(x,p)\,dx \tag{A - 31}$$

Thus:

$$\bar{\theta}_0(p) = \frac{2\varphi_0}{\pi k b}\int_0^\infty \left[\frac{\sin(\alpha b)}{\alpha\beta}\int_0^b \cos(\alpha x)\,dx\right]d\alpha = \frac{2\varphi_0}{\pi k b}\int_0^\infty \frac{\sin^2(\alpha b)}{\alpha^2\beta}d\alpha \tag{A - 32}$$

Finally, by replacing $p = j\omega$ and considering $\varphi_0 = \frac{P}{4bl}\sin(\omega t)$, where P is the total supplied power. One obtains the expression of the average temperature in function of frequency as:

$$\bar{\theta}_0(j\omega) = \frac{P(\omega)}{2\pi k b^2 l}\int_0^\infty \frac{sin^2(\alpha b)}{\alpha^2\sqrt{\frac{j\omega}{a}+\alpha^2}}\,d\alpha \tag{A - 33}$$

When $\sqrt{a/\omega} \gg 2b$, a simplified form of relation is found as:

$$\bar{\theta}(\omega) = \frac{P(\omega)}{2\pi k l}\left(\frac{1}{2}\ln\left(\frac{a}{b^2}\right) - \frac{1}{2}\ln(\omega) + 0.923 - \frac{j\pi}{4}\right) \tag{A - 34}$$

When the thickness of the sample is not so large as compared to l_h, the boundary condition (A - 22) must take into account the value of e_s , and the model (A - 27) becomes:

$$\tilde{\theta}(\alpha,z,p) = \frac{\varphi_0(j\omega)\sin(\alpha b)}{\alpha k\beta\tanh(\beta e_s)}e^{-\beta z} \tag{A - 35}$$

And the expression for the average temperature is:

$$\bar{\theta}(j\omega) = \frac{P(\omega)}{2\pi k b^2 l}\int_0^\infty \frac{\sin^2(\alpha b)}{\alpha k\sqrt{\frac{j\omega}{a}+\alpha^2}\tanh\left(\sqrt{\frac{j\omega}{a}+\alpha^2}e_s\right)}\,d\alpha \tag{A - 36}$$

Finally, adding the thermal resistance corresponding to the deposit on the substrate, one obtains the temperature magnitude as:

$$\Delta\bar{\theta}(\omega) = \frac{P(\omega)}{2bl}\left\|\frac{1}{2\pi k b}\int_0^\infty \frac{\sin^2(\alpha b)}{\alpha k\sqrt{\frac{j\omega}{a}+\alpha^2}\tanh\left(\sqrt{\frac{j\omega}{a}+\alpha^2}e_s\right)}\,d\alpha + \frac{R_{Th}}{2}\right\| \tag{A - 37}$$

The integral is numerically computed using the global adaptive quadrature and default error tolerances (routine INTEGRAL in MATLAB).

III. Heat transfer in a semi-infinite media submitted to a heat flux with Gaussian distribution.

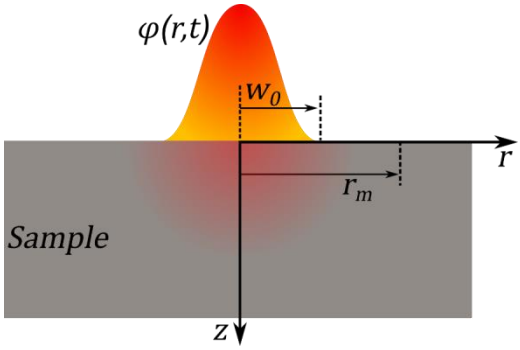

Figure A- 7: Geometrical representation of a semi-infinite media submitted to a Gaussian heat flux on its top surface.

Figure A- 7 presents the geometrical scheme of a semi-infinite media submitted to a heat flux $\varphi(r,t)$ on its top surface. The shape of the heat spot is a disk with radius w_0 and a Gaussian power density distribution. The system has thus the cylindrical rotational symmetry around the z axis. The solution of the heat diffusion equation is therefore obtained in the 2D axisymmetric cylindrical coordinates (r,z).

Considering the temporal variation of the laser as a Dirac pulse $\delta(t)$, the heat flux on the sample surface is:

$$\varphi(r,t) = \varphi_0 \delta(t)\, e^{-2\left(\frac{r}{w_0}\right)^2} \tag{A - 38}$$

When the thermal conductivity of the media is directionally dependent, one defines k_r as in plane thermal conductivity and k_z as out of plane thermal conductivity. The system of partial differential equations describing the diffusion of heat in the media is:

$$\rho C_p \frac{\partial T(r,z,t)}{\partial t} = \frac{k_r}{r}\frac{\partial}{\partial r}\left(r\frac{\partial T(r,z,t)}{\partial r}\right) + k_z\left(\frac{\partial^2 T(r,z,t)}{\partial z^2}\right) \tag{A - 39}$$

$$\text{at:}\quad 0 < r < \infty, \qquad 0 < z < \infty, \qquad t > 0$$

with boundary conditions:

$$-k_z \frac{\partial T(r,z,t)}{\partial z} = \varphi(r,t), \qquad \text{at}\ \ z = 0\ \ \text{and}\ \ t > 0 \tag{A - 40}$$

$$\frac{\partial T(r,z,t)}{\partial r} = 0, \qquad \text{at}\ \ r = 0\ \ \text{and}\ r \to \infty \tag{A - 41}$$

$$T(r,z,t) = 0, \qquad \text{when}\ \ z \to \infty\ \ \text{and}\ \ r \to \infty\ \ \text{for}\ t > 0 \tag{A - 42}$$

and initial condition:

$$T(r,z,t) = 0, \qquad 0 \le z < \infty, \qquad 0 < r < \infty, t = 0 \tag{A - 43}$$

In equation (A - 39), ρC_p is the volumetric heat capacity of the material at constant pressure. The Laplace transform is applied to the time variable t of the temperature and the heat flux as:

$$\theta(r,z,p) = \mathcal{L}[T(r,z,t)] = \int_0^\infty T(r,z,t)\, e^{-pt} dt \tag{A - 44}$$

$$\psi(r,p) = \mathcal{L}[\varphi(r,t)] = \int_0^\infty \varphi(r,z,t)\, e^{-pt} dt \tag{A - 45}$$

with p being the Laplace variable. The use of the Laplace transform has the advantage that allows passing to the frequency domain with the equivalence $p = j\omega$, when the initial temperature is zero. Thus, applying the Laplace transform to equation (A - 39) one obtains:

$$\rho C_p p \frac{\partial \theta(r,z,p)}{\partial t} = \frac{k_r}{r}\frac{\partial}{\partial r}\left(r\frac{\partial \theta(r,z,p)}{\partial r}\right) + k_z \frac{\partial^2 \theta(r,z,p)}{\partial z^2} \tag{A - 46}$$

with boundary conditions:

$$-k_z \frac{\partial \theta(r,z,p)}{\partial z} = \psi\,(r,p), \qquad \text{at} \;\; z = 0 \tag{A - 47}$$

$$\frac{\partial \theta(r,z,p)}{\partial r} = 0, \qquad \text{at} \;\; r = 0 \tag{A - 48}$$

$$\theta(r,z,p) = 0, \qquad \text{when} \;\; z \to \infty \;\; \text{and} \;\; r \to \infty \tag{A - 49}$$

and with heat flux:

$$\psi(r,p) = \varphi_0\, e^{-2\left(\frac{r}{w_0}\right)^2} \tag{A - 50}$$

Due to the cylindrical symmetry, the Hankel transform is applied over to the r space variable for the temperature and the heat flux. By definition, these transforms are written:

$$\tilde{\theta}(\alpha,z,p) = \mathcal{H}[\theta(r,z,p)] = \int_0^\infty \theta(r,z,p)\, r J_0(\alpha r) dr \tag{A - 51}$$

$$\tilde{\psi}(\alpha,z,p) = \mathcal{H}[\psi(r,z,p)] = \int_0^\infty \psi(r,z,p)\, r J_0(\alpha r) dr \tag{A - 52}$$

with J_0 denoting the Bessel function of the first kind and order 0. Applying this integral transform to relation (A - 46) one obtains:

$$\rho C_p p \tilde{\theta}(\alpha,z,p) = -k_r \alpha^2 \tilde{\theta}(\alpha,z,p) + k_z \frac{\partial^2 \tilde{\theta}(\alpha,z,p)}{\partial z^2} \tag{A - 53}$$

Thus:

$$\frac{\partial^2 \tilde{\theta}(\alpha,z,p)}{\partial z^2} - \left(\frac{\rho C_p p + k_r \alpha^2}{k_z}\right)\tilde{\theta}(\alpha,z,p) = 0, \qquad 0 < z < \infty \tag{A - 54}$$

with boundary condition:

$$-k_z \frac{\partial \tilde{\theta}(\alpha,z,p)}{\partial z} = \tilde{\psi}\,(\alpha,p), \qquad \text{at} \;\; z = 0 \tag{A - 55}$$

$$\theta(\alpha, z, p) = 0, \qquad \text{when } z \to \infty \tag{A - 56}$$

where the heat flux is:

$$\tilde{\psi}(\alpha, p) = \frac{\varphi_0 w_0^2}{4} e^{-\frac{(\alpha w_0)^2}{8}} \tag{A - 57}$$

If one defines:

$$\beta^2 = \frac{\rho C_p p + k_r \alpha^2}{k_z} \tag{A - 58}$$

The solution for the differential equation (A - 53) is expressed as:

$$\tilde{\theta}(\alpha, z, p) = Ae^{\beta z} + Be^{-\beta z} \tag{A - 59}$$

The boundary condition when $z \to \infty$ implies that A=0. Thus:

$$\tilde{\theta}(\alpha, z, p) = Be^{-\beta z} \tag{A - 60}$$

Replacing the obtained expression for $\tilde{\theta}$ in the boundary condition (A - 55) leads to:

$$k_z B \beta e^{-\beta z} = \frac{\varphi_0 w_0^2}{4} e^{-\frac{(\alpha w_0)^2}{8}}, \qquad \text{at } z = 0 \tag{A - 61}$$

Thus:

$$B = \frac{\varphi_0 w_0^2}{4 k_z \beta} e^{-\frac{(\alpha w_0)^2}{8}} \tag{A - 62}$$

Finally, one obtains the solution:

$$\tilde{\theta}(\alpha, z, p) = \frac{\varphi_0 w_0^2}{4 k_z \beta} e^{-\frac{(\alpha w_0)^2}{8}} e^{-\beta z} \tag{A - 63}$$

The inverse Hankel transform allows retrieving the periodic temperature as:

$$\theta(r, z, p) = \int_0^\infty \tilde{\theta}(\alpha, z, p)\ \alpha J_0(\alpha r) d\alpha \tag{A - 64}$$

thus:

$$\theta(r, z, p) = \frac{\varphi_0 w_0^2}{4 k_z} \int_0^\infty \frac{\alpha}{\beta} e^{-\frac{(\alpha w_0)^2}{8}} e^{-\beta z}\ J_0(\alpha r)\ d\alpha \tag{A - 65}$$

at the sample surface at $z = 0$ is:

$$\theta_0(r, p) = \frac{\varphi_0 w_0^2}{4 k_z} \int_0^\infty \frac{\alpha}{\beta} e^{-\frac{(\alpha w_0)^2}{8}} J_0(\alpha r)\ d\alpha \tag{A - 66}$$

The average temperature viewed by the detector on the area of radius r_m is:

$$\bar{\theta}_0(p) = \frac{1}{\pi r_m^2} \int_0^{r_m} \theta_0(r, p)\ r\ 2\pi dr \tag{A - 67}$$

Replacing equation (A - 66) in (A - 67) leads to:

$$\bar{\theta}_0(p) = \frac{\varphi_0 w_0^2}{2k_z r_m^2} \int_0^\infty \left[\frac{\alpha}{\beta} e^{-\frac{(\alpha w_0)^2}{8}} \int_0^{r_m} J_0(\alpha r)\, r dr \right] d\alpha \quad \text{(A - 68)}$$

Since:

$$\int_0^{r_m} J_0(\alpha r)\, r dr = \frac{r_m}{\alpha} J_1(\alpha r_m) \quad \text{(A - 69)}$$

One obtains:

$$\bar{\theta}_0(p) = \frac{\varphi_0 w_0^2}{2k_z r_m} \int_0^\infty \frac{1}{\beta} e^{-\frac{(\alpha w_0)^2}{8}} J_1(\alpha r_m)\, d\alpha \quad \text{(A - 70)}$$

Where J_1 is the Bessel function of the first kind of order 1. Finally, with $p = j\omega$ and considering now $\varphi = \varphi_0 \sin(\omega t)$. The expression for the average temperature at the aimed area in function of the excitation frequency ω is:

$$\bar{\theta}(j\omega) = \frac{\varphi_0(\omega) w_0^2}{2k_z r_m} \int_0^\infty \sqrt{\frac{k_z}{\rho C_p\, j\omega + k_r \alpha^2}}\, e^{-\frac{(\alpha w_0)^2}{8}} J_1(\alpha r_m)\, d\alpha \quad \text{(A - 71)}$$

IV. Heat transfer in a layer.

Let's consider a layer material of thickness e in z and radius r_L in r direction with a general input and output heat fluxes and temperatures as represented in Figure A- 8.

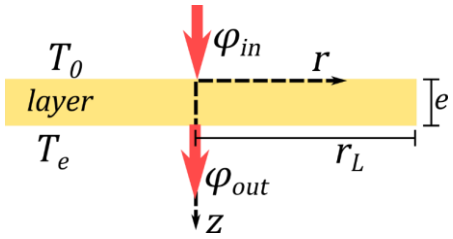

Figure A- 8: General representation of heat inputs and outputs for one layer.

The expression for diffusion of heat in this layer is:

$$\rho C_p \frac{\partial T(r,z,t)}{\partial t} = \frac{k_r}{r}\frac{\partial}{\partial r}\left(r\frac{\partial T(r,z,t)}{\partial r}\right) + k_z\left(\frac{\partial^2 T(r,z,t)}{\partial z^2}\right) \qquad \text{(A - 72)}$$

$$\text{at:}\quad 0 < r < r_L, \qquad 0 < z < e, \qquad t > 0$$

with boundary conditions:

$$-k_z\frac{\partial T(r,z,t)}{\partial z} = \varphi_{in}(r,t), \qquad \text{at}\ \ z = 0\ \text{ and }\ t > 0 \qquad \text{(A - 73)}$$

$$-k_z\frac{\partial T(r,z,t)}{\partial z} = \varphi_{out}(r,t), \qquad \text{at}\ \ z = e\ \text{ and }\ t > 0 \qquad \text{(A - 74)}$$

$$\frac{\partial T(r,z,t)}{\partial r} = 0, \qquad \text{at}\ \ r = 0\,, r = r_L\,, 0 < z < e \qquad \text{(A - 75)}$$

and initial condition:

$$T(r,z,t) = 0, \qquad 0 \le z < e, 0 < r < r_L, t = 0 \qquad \text{(A - 76)}$$

The Laplace transform is applied to the time variable t and the Henkel transform is applied to the space variable r on the temperature and the heat flux density respectively as:

$$\tilde{\theta}(\alpha,z,p) = \mathcal{H}\big[\mathcal{L}[T(r,z,t)]\big] = \int_0^{r_L}\int_0^{\infty} T(r,z,t)\, e^{-pt}\, rJ_0(\alpha r)\, dt\, dr \qquad \text{(A - 77)}$$

$$\tilde{\psi}(\alpha,z,p) = \mathcal{H}\big[\mathcal{L}[\varphi(r,t)]\big] = \int_0^{r_L}\int_0^{\infty} \varphi(r,t)\, e^{-pt}\, rJ_0(\alpha r)\, dt\, dr \qquad \text{(A - 78)}$$

where p, is the Laplace variable, α is the Henkel variable and J_0 is the Bessel function of the first kind and first order.

Applying the integral transforms, one obtains:

$$\frac{\partial^2\tilde{\theta}(\alpha,z,p)}{\partial z^2} - \beta\tilde{\theta}(\alpha,z,p) = 0, \qquad 0 < z < \infty \qquad \text{(A - 79)}$$

With $\beta = \sqrt{\frac{\rho C_p p + k_r \alpha^2}{k_z}}$ and:

$$-k_z \frac{\partial \tilde{\theta}(\alpha, z, p)}{\partial z} = \tilde{\psi}_{\text{in}}(\alpha, p), \qquad \text{at} \quad z = 0 \tag{A - 80}$$

$$-k_z \frac{\partial \tilde{\theta}(\alpha, z, p)}{\partial z} = \tilde{\psi}_{out}(\alpha, p), \qquad \text{at} \quad z = e \tag{A - 81}$$

$$J_1(\alpha R) = 0, \qquad \text{at } 0 < z < e \tag{A - 82}$$

The general solution for the differential equation (A - 79) is:

$$\tilde{\theta}(\alpha, z, p) = K_1 \cosh \beta z + K_2 \sinh \beta z \tag{A - 83}$$

Constants K1 and K2 are determined from boundary conditions and using the quadrupole formalism [120], the transformed heat flux and temperature can be expressed according to:

$$\begin{bmatrix} \tilde{\theta}_0 \\ \tilde{\psi}_{in} \end{bmatrix} = \begin{bmatrix} A & B \\ C & D \end{bmatrix} \begin{bmatrix} \tilde{\theta}_e \\ \tilde{\psi}_{out} \end{bmatrix} \tag{A - 84}$$

where $\tilde{\theta}_0 = \tilde{\theta}(z = 0)$, and $\tilde{\theta}_e = \tilde{\theta}(z = e)$, and:

$$A = D = \cosh(\beta e), \qquad B = \frac{\sinh(\beta e)}{k_z \beta}, \qquad C = k_z \beta \sinh(\beta e) \tag{A - 85}$$

The temperature and flux on both sides of the slab are linearly related. In [127] it was reported that replacing the hyperbolic functions by the respective exponential representation permits avoiding the overflow in the numeric computation for βe>700. So that

$$\begin{bmatrix} \tilde{\theta}_0 \\ \tilde{\psi}_{in} \end{bmatrix} = e^{\beta e} \begin{bmatrix} A & B \\ C & D \end{bmatrix} \begin{bmatrix} \tilde{\theta}_e \\ \tilde{\psi}_{out} \end{bmatrix},$$
$$A = D = \frac{1 + e^{-2\beta e}}{2}, \qquad B = \frac{1 - e^{-2\beta e}}{2k_z \beta}, \qquad C = k_z \beta \frac{1 - e^{-2\beta e}}{2} \tag{A - 86}$$

Considering output impedance Z_{out} as:

$$Z_{out} = \frac{\tilde{\theta}_e}{\tilde{\psi}_{out}} \tag{A - 87}$$

Equation (3.39) leads to the functional form for $\tilde{\theta}_0$:

$$\tilde{\theta}_0 = \frac{A(\alpha, p) + B(\alpha, p)/Z_{out}}{C(\alpha, p) + D(\alpha, p)/Z_{out}} \tilde{\psi}_{in} \tag{A - 88}$$

The inverse Hankel transform allows retrieving the periodic temperature:

$$\theta(r, z, p) = \int_0^\infty \tilde{\theta}(\alpha, z, p)\, \alpha J_0(\alpha r) d\alpha \tag{A - 89}$$

The values of α are solutions of the relationship (A - 82), which is a transcendental equation with an infinite number of solutions approximated as:

$$\alpha_0 = 0, \qquad \alpha_n r_L \approx \pi\left(n + \frac{1}{4}\right) - \frac{3}{8\pi\left(n + \frac{1}{4}\right)} \tag{A - 90}$$

It leads to replace the integral of the relation 3.110 by a discrete sum and the inverse Hankel transform is then written:

$$\theta(r, z, p) = \sum_{n}^{\infty} \frac{2J_0(\alpha_n r)}{r_L^2 J_0(\alpha_n r_L)^2} \tilde{\theta}\,(\alpha, z, p) \tag{A - 91}$$

Finally, the average temperature viewed by the detector on area of equivalent radius r_m is:

$$\bar{\theta}_0(p) = \sum_{n=0}^{\infty} \frac{4J_0(\alpha_n r_m)}{r_m r_L^2 J_0(\alpha_n r_L)^2 \alpha}\ \tilde{\theta}_0(\alpha, p) \tag{A - 92}$$

Considering that $\lim_{\alpha \to 0} J_1(\alpha r_m) = \frac{r_m}{2}$ and by truncating the infinite series to a sufficiently large N value one gets:

$$\bar{\theta}_0(p) = \frac{\tilde{\psi}_{in}(\alpha_0, p)}{2r_L^2} Z(\alpha_0, p) + \sum_{n=1}^{N} \frac{4J_0(\alpha_n r_m)}{r_m r_L^2\, J_0(\alpha_n r_L)^2 \alpha_n} \tilde{\psi}_{in}(\alpha_n, p)\, Z(\alpha_n, p) \tag{A - 93}$$

where:

$$Z(\alpha_n, p) = \frac{A(\alpha_n, p) + B(\alpha_n, p)/Z_{out}}{C(\alpha_n, p) + D(\alpha_n, p)/Z_{out}} \tag{A - 94}$$

Finally, with $p = j\omega$, and $\varphi = \psi_0 \sin(\omega t)$. The expression of the periodic temperature amplitude on the sample surface is:

$$\bar{\theta}_0(j\omega) = \frac{\tilde{\psi}_0(\alpha_0, j\omega)}{2r_L^2} Z(\alpha_0, j\omega) + \sum_{n=1}^{N} \frac{4J_0(\alpha_n r_m)}{r_m r_L^2\, J_0(\alpha_n r_L)^2 \alpha_n} \tilde{\psi}_0(\alpha_n, j\omega)\, Z(\alpha_n, j\omega) \tag{A - 95}$$

V. Emittance calculation.

In order to examine the effect of the non-linear relationship between the emittance and the surface temperature one can compare the total emittance variation with that from the linear assumption. The emittance from the sample surface is given as:

$$\begin{aligned} M &= M_0 + \Delta M = \varepsilon\sigma(T_{\Delta 0} + \Delta T_\omega)^4 \\ &= \varepsilon\sigma\left(T_{\Delta 0}^4 + 4T_{\Delta 0}^3\Delta T_\omega + 6T_{\Delta 0}^2\Delta T_\omega^2 + 4T_{\Delta 0}\Delta T_\omega^3 + \Delta T_\omega^4\right) \end{aligned} \quad \text{(A - 96)}$$

where ε is the emissivity and $\sigma = 5.67 \times 10^{-8}$ $\mathrm{Wm^{-2}K^{-4}}$ is the Stefan-Boltzmann constant. With the constant level emittance due the average temperature increase as:

$$M_0 = \varepsilon\sigma T_{\Delta 0}^4 \quad \text{(A - 97)}$$

And the total emittance variation with nonlinear relationship with the temperature variation is expressed as:

$$\Delta M = \Delta M_{NL} = \varepsilon\sigma(4T_{\Delta 0}^3\Delta T_\omega + 6T_{\Delta 0}^2\Delta T_\omega^2 + 4T_{\Delta 0}\Delta T_\omega^3 + \Delta T_\omega^4) \quad \text{(A - 98)}$$

where, $T_{\Delta 0} = T_0 + \Delta T_0$ is the constant component in the sample temperature because the average temperature increase when it is submitted to the periodic power flux and ΔT_ω is the temperature variation. When ΔT_ω is lower than few Kelvins $\Delta M_{NL} \to \Delta M_L$ that is the condition for the linear assumption, thus:

$$\Delta M \approx \Delta M_L = 4\varepsilon\sigma T_{\Delta 0}^3\Delta T_\omega \quad \text{(A - 99)}$$

With ΔT_ω obtained with equation (3.23) as $\Delta T_\omega = \overline{\theta_g}(j\omega)$.

The DC component of the emittance is coming from the initial temperature and the DC component of the sample temperature, described as $\Delta T_0 = \overline{\theta_g}(\omega = 0)$

$$\Delta T_0 = \frac{\varphi_0}{\pi k r_m}\int_0^\infty \frac{1}{\alpha}\; e^{-\frac{(\alpha w_0)^2}{8}} J_1(\alpha r_m)\, d\alpha \quad \text{(A - 100)}$$

Assuming initial temperature $T_0 = 300$ K, ε=0.2 and $\varphi_0 = \frac{2P}{\pi r^2}$, where P is the total power. The phase of the total emittance variation generated at the sample surface can be calculated as:

$$\phi_{\Delta M_{NL}} = \arg[\Delta M_{NL}(j\omega)] \quad \text{(A - 101)}$$

And the phase of the emittance variation under linear assumption as:

$$\phi_{\Delta M_L} = \arg[\Delta M_L(j\omega)] \quad \text{(A - 102)}$$

The average phase calculated over a disk of radius $r_m = 6.25$ µm for five power levels applied on heated area $w_0 = 3.3$ µm is presented in Figure A- 9. It is shown that increasing the power produces an increase in the temperature variation and decrease in the phase of the emittance. The maximum temperature variation produced at low frequency is noted as ΔT_{max}.

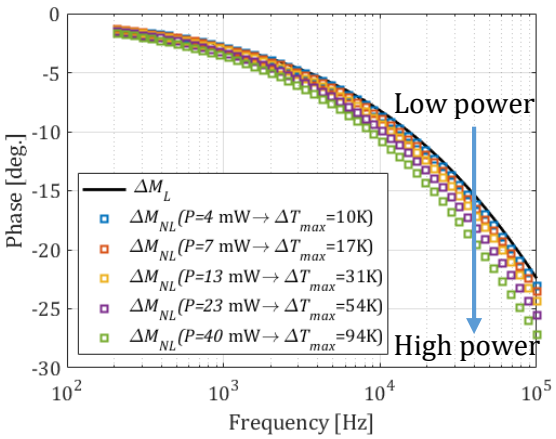

Figure A- 9: Comparison between phase of emittance variation under linear assumption (ΔM_L) and the total emittance variation with nonlinear relationship with the temperature (ΔM_{NL}) for different powers.

For better appreciation, the phase difference between the linear and nonlinear emittance is calculated as $\phi_{\Delta M_{NL}} - \phi_{\Delta M_L}$ and presented in Figure A- 10.

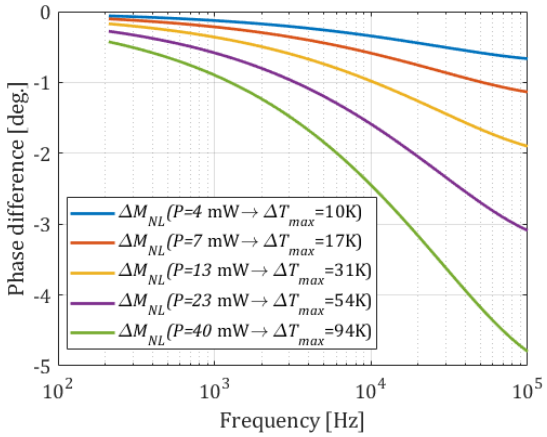

Figure A- 10: Phase difference ($\phi_{\Delta M_{NL}} - \phi_{\Delta M_L}$) for different powers.

Bibliography

[1] Z. M. Zhang, *Nano/Microscale Heat Transfer*. Cham: Springer International Publishing, 2020. doi: 10.1007/978-3-030-45039-7.

[2] L. D. Hicks and M. S. Dresselhaus, 'Thermoelectric figure of merit of a one-dimensional conductor', *Phys. Rev. B*, vol. 47, no. 24, pp. 16631–16634, Jun. 1993, doi: 10.1103/PhysRevB.47.16631.

[3] E. Perros, 'Caractérisation locale du transfert de chaleur aux interfaces solide-solide dans les milieux isolants', Université Paris sciences et lettres, 2017. [Online]. Available: https://pastel.archives-ouvertes.fr/tel-02280102

[4] J. Doumouro, 'Caractérisation de la laine de verre : étude des transferts de chaleur entre fibres de verre à l'échelle micrométrique', Université Paris sciences et lettres, 2020. [Online]. Available: http://www.theses.fr/2020UPSLS008/document

[5] A. Lisa SERRA, 'Nouvelle génération de mémoire à changement de phase non volatile pour des applications à très basse consommation', Doctoral dissertation, Université Grenoble Alpes, 2021.

[6] C. C. Williams and H. K. Wickramasinghe, 'Scanning thermal profiler', *Appl. Phys. Lett.*, vol. 49, no. 23, pp. 1587–1589, 1986, doi: 10.1063/1.97288.

[7] A. Majumdar, J. P. Carrejo, and J. Lai, 'Thermal imaging using the atomic force microscope', *Appl. Phys. Lett.*, vol. 62, no. 20, pp. 2501–2503, 1993.

[8] R. J. Pylkki, P. J. Moyer, and P. E. West, 'Scanning Near-Field Optical Microscopy and Scanning Thermal Microscopy', *Jpn. J. Appl. Phys.*, vol. 33, no. Part 1, No. 6B, pp. 3785–3790, Jun. 1994, doi: 10.1143/jjap.33.3785.

[9] R. B. Dinwiddie, R. J. Pylkki, and P. E. West, 'Thermal conductivity contrast imaging with a scanning thermal microscope', *Therm. Conduct.*, vol. 22, pp. 668–690, 1994.

[10] G. Mills, H. Zhou, A. Midha, L. Donaldson, and J. M. R. Weaver, 'Scanning thermal microscopy using batch fabricated thermocouple probes', *Appl. Phys. Lett.*, vol. 72, no. 22, pp. 2900–2902, 1998, doi: 10.1063/1.121453.

[11] Y. Zhang, P. S. Dobson, and J. M. R. Weaver, 'Batch fabricated dual cantilever resistive probe for scanning thermal microscopy', *Microelectron. Eng.*, vol. 88, no. 8, pp. 2435–2438, 2011, doi: https://doi.org/10.1016/j.mee.2011.02.040.

[12] P. G. Royall, V. L. Kett, C. S. Andrews, and D. Q. M. Craig, 'Identification of Crystalline and Amorphous Regions in Low Molecular Weight Materials Using Microthermal Analysis', *J. Phys. Chem. B*, vol. 105, no. 29, pp. 7021–7026, Jul. 2001, doi: 10.1021/jp010441k.

[13] 'AFM Probes | Kelvin Nanotechnology'. https://www.kntnano.com/probes/ (accessed Jun. 07, 2020).

[14] B. A. Nelson and W. P. King, 'Measuring material softening with nanoscale spatial resolution using heated silicon probes', *Rev. Sci. Instrum.*, vol. 78, no. 2, p. 023702, Feb. 2007, doi: 10.1063/1.2435589.

[15] M. E. Mcconney, D. D. Kulkarni, H. Jiang, T. J. Bunning, and V. V. Tsukruk, 'A New Twist on Scanning Thermal Microscopy', 2012, doi: 10.1021/nl203531f.

[16] S. J. Kim, T. Ono, and M. Esashi, 'Thermal imaging with tapping mode using a bimetal oscillator formed at the end of a cantilever', *Rev. Sci. Instrum.*, vol. 80, no. 3, 2009, doi: 10.1063/1.3095680.

[17] O. Nakabeppu, M. Chandrachood, Y. Wu, J. Lai, and A. Majumdar, 'Scanning thermal imaging microscopy using composite cantilever probes', *Appl. Phys. Lett.*, p. 694, 1995, doi: 10.1063/1.114102.

[18] Y. Zhang, W. Zhu, F. Hui, M. Lanza, T. Borca-Tasciuc, and M. Muñoz Rojo, 'A Review on Principles and Applications of Scanning Thermal Microscopy (SThM)', *Adv. Funct. Mater.*, vol. 30, no. 18, p. 1900892, 2020, doi: 10.1002/adfm.201900892.

[19] S. Gomès, A. Assy, and P.-O. Chapuis, 'Scanning thermal microscopy: A review', *Phys. Status Solidi A*, vol. 212, no. 3, pp. 477–494, 2015, doi: 10.1002/pssa.201400360.

[20] H. M. Pollock and A. Hammiche, 'Micro-thermal analysis: techniques and applications', *J. Phys. Appl. Phys.*, vol. 34, no. 9, pp. R23–R53, May 2001, doi: 10.1088/0022-3727/34/9/201.

[21] G. Wielgoszewski and T. Gotszalk, 'Chapter Four - Scanning Thermal Microscopy (SThM): How to Map Temperature and Thermal Properties at the Nanoscale', vol. 190, P. W. Hawkes, Ed. Elsevier, 2015, pp. 177–221. doi: https://doi.org/10.1016/bs.aiep.2015.03.011.

[22] J. Bodzenta, A. Kaźmierczak-Bałata, and K. Harris, 'Quantitative thermal measurement by the use of scanning thermal microscope and resistive thermal probes', *J. Appl. Phys.*, vol. 127, no. 3, p. 31103, 2020, doi: 10.1063/1.5125062.

[23] G. Eloise, 'Microscopie thermique à sonde locale : étalonnages, protocoles de mesure et applications quantitatives sur des matériaux nanostructurés', Doctoral dissertation, Université de Lyon, 2020.

[24] P. Tovee, M. Pumarol, D. Zeze, K. Kjoller, and O. Kolosov, 'Nanoscale spatial resolution probes for scanning thermal microscopy of solid state materials', *J. Appl. Phys.*, vol. 112, no. 11, p. 114317, 2012, doi: 10.1063/1.4767923.

[25] Y. Zhang, E. E. Castillo, and R. J. Mehta, 'A noncontact thermal microprobe for local thermal conductivity measurement', *Rev Sci Instrum*, vol. 82, p. 24902, 2011, doi: 10.1063/1.3545823.

[26] Y. Zhang, W. Zhu, and T. Borca-Tasciuc, 'Sensitivity and spatial resolution for thermal conductivity measurements using noncontact scanning thermal microscopy with thermoresistive probes under ambient conditions', 2021, doi: 10.1093/oxfmat/itab011.

[27] Indrayush De, 'Thermal characterization of nanostructures using scanning thermal microscopy', Doctoral dissertation, UNIVERSITÉ DE BORDEAUX, 2017.

[28] F. Menges, P. Mensch, H. Schmid, H. Riel, A. Stemmer, and B. Gotsmann, 'Temperature mapping of operating nanoscale devices by scanning probe thermometry', *Nat. Commun.*, vol. 7, no. 1, p. 10874, Apr. 2016, doi: 10.1038/ncomms10874.

[29] P. S. Dobson, J. M. R. Weaver, and G. Mills, 'New Methods for Calibrated Scanning Thermal Microscopy (SThM)', in *SENSORS, 2007 IEEE*, Oct. 2007, pp. 708–711. doi: 10.1109/ICSENS.2007.4388498.

[30] K. Edinger, T. Gotszalk, and I. W. Rangelow, 'Novel high resolution scanning thermal probe', *J. Vac. Sci. Technol. B Microelectron. Nanometer Struct.*, vol. 19, no. 6, p. 2856, 2001, doi: 10.1116/1.1420580.

[31] E. Nasr Esfahani, F. Ma, S. Wang, Y. Ou, J. Yang, and J. Li, 'Quantitative nanoscale mapping of three-phase thermal conductivities in filled skutterudites via scanning thermal microscopy', *Natl. Sci. Rev.*, vol. 5, no. 1, pp. 59–69, Jan. 2018, doi: 10.1093/nsr/nwx074.

[32] L. Shi, O. Kwon, A. C. Miner, and A. Majumdar, 'Design and batch fabrication of probes for sub-100 nm scanning thermal microscopy', *J. Microelectromechanical Syst.*, vol. 10, no. 3, pp. 370–378, 2001, doi: 10.1109/84.946785.

[33] A. Bontempi, T. P. Nguyen, R. Salut, L. Thiery, D. Teyssieux, and P. Vairac, 'Scanning thermal microscopy based on a quartz tuning fork and a micro-thermocouple in active mode (2ω method)', *Rev. Sci. Instrum.*, vol. 87, no. 6, p. 63702, 2016, doi: 10.1063/1.4952958.

[34] K. Kim *et al.*, 'Quantitative scanning thermal microscopy using double scan technique', *Appl. Phys. Lett.*, vol. 93, no. 20, p. 203115, 2008, doi: 10.1063/1.3033545.

[35] K. Yoon *et al.*, 'Measuring the thermal conductivity of residue-free suspended graphene bridge using null point scanning thermal microscopy', *Carbon*, 2014, doi: 10.1016/j.carbon.2014.04.051.

[36] G. S. Shekhawat *et al.*, 'Micromachined Chip Scale Thermal Sensor for Thermal Imaging', 2018, doi: 10.1021/acsnano.7b08504.

[37] L. Aigouy, E. Saïdi, and L. Lalouat, 'AC thermal imaging of a microwire with a fluorescent nanocrystal: Influence of the near field on the thermal contrast ARTICLES YOU MAY BE INTERESTED IN', *J Appl Phys*, vol. 106, p. 74301, 2009, doi: 10.1063/1.3233940.

[38] L. Aigouy, L. Lalouat, and M. Mortier, 'Note: A scanning thermal probe microscope that operates in liquids ARTICLES YOU MAY BE INTERESTED IN', 2011, doi: 10.1063/1.3567794.

[39] B. Samson, L. Aigouy, P. Löw, C. Bergaud, B. J. Kim, and M. Mortier, 'ac thermal imaging of nanoheaters using a scanning fluorescent probe', 2008, doi: 10.1063/1.2832673.

[40] E. Saïdi *et al.*, 'Scanning thermal imaging by near-field fluorescence spectroscopy', *Nanotechnology*, vol. 20, no. 11, p. 115703, Mar. 2009, doi: 10.1088/0957-4484/20/11/115703.

[41] S. Lefèvre, J.-B. Saulnier, C. Fuentes, and S. Volz, 'Probe calibration of the scanning thermal microscope in the AC mode', *Superlattices Microstruct.*, vol. 35, no. 3, pp. 283–288, 2004, doi: https://doi.org/10.1016/j.spmi.2003.11.004.

[42] S. Lefèvre and S. Volz, '3ω-scanning thermal microscope', *Rev. Sci. Instrum.*, vol. 76, no. 3, p. 33701, 2005, doi: 10.1063/1.1857151.

[43] M. Muñoz Rojo, S. Grauby, J.-M. Rampnoux, O. Caballero-Calero, M. Martin-Gonzalez, and S. Dilhaire, 'Fabrication of Bi_2Te_3 nanowire arrays and thermal conductivity measurement by 3ω-scanning thermal microscopy', *J. Appl. Phys.*, vol. 113, no. 5, p. 054308, Feb. 2013, doi: 10.1063/1.4790363.

[44] J. L. Battaglia, I. De, A. Saci, A. Kusiak, and V. Sousa, 'Thermal investigation of a phase change memory device at the nanoscale', in *Journal of Physics: Conference Series*, Oct. 2016, vol. 745, no. 3. doi: 10.1088/1742-6596/745/3/032098.

[45] M. Chirtoc, J. Gibkes, R. Wernhardt, J. Pelzl, and A. Wieck, 'Temperature-dependent quantitative 3ω scanning thermal microscopy: Local thermal conductivity changes in NiTi microstructures induced by martensite-austenite phase transition', *Rev. Sci. Instrum.*, vol. 79, no. 9, p. 093703, 2008, doi: 10.1063/1.2982235.

[46] S. Lefèvre, S. Volz, J.-B. Saulnier, C. Fuentes, and N. Trannoy, 'Thermal conductivity calibration for hot wire based dc scanning thermal microscopy', *Rev. Sci. Instrum.*, vol. 74, no. 4, pp. 2418–2423, 2003, doi: 10.1063/1.1544078.

[47] A. Saci, J.-L. Battaglia, A. Kusiak, R. Fallica, and M. Longo, 'Thermal conductivity measurement of a Sb_2Te_3 phase change nanowire', *Appl. Phys. Lett.*, vol. 104, no. 26, p. 263103, Jun. 2014, doi: 10.1063/1.4884604.

[48] J.-L. Battaglia *et al.*, 'Thermal resistance measurement of In3SbTe2 nanowires', *Phys. Status Solidi A*, vol. 214, no. 5, p. 1600500, 2017, doi: 10.1002/pssa.201600500.

[49] I. De, J.-L. Battaglia, and G. L. Vignoles, 'Thermal properties measurements of a silica/pyrocarbon composite at the microscale', *J. Appl. Phys.*, vol. 120, no. 24, p. 245101, Dec. 2016, doi: 10.1063/1.4972974.

[50] C. A. Paddock and G. L. Eesley, 'Transient thermoreflectance from thin metal films', *J. Appl. Phys.*, vol. 60, no. 1, pp. 285–290, Jul. 1986, doi: 10.1063/1.337642.

[51] S. Sandell, E. Chávez-Ángel, A. El Sachat, J. He, C. M. Sotomayor Torres, and J. Maire, 'Thermoreflectance techniques and Raman thermometry for thermal property characterization of nanostructures', *J. Appl. Phys.*, vol. 128, no. 13, p. 131101, Oct. 2020, doi: 10.1063/5.0020239.

[52] Z. ChungWei, B. KeDong, W. JianLi, N. ZhongHua, and C. YunFei, 'Measurement of thermal boundary conductance between metal and dielectric materials using femtosecond laser transient thermoreflectance technique', p. 6, 2012.

[53] Z. Tian, A. Marconnet, and G. Chen, 'Enhancing solid-liquid interface thermal transport using self-assembled monolayers', *Appl. Phys. Lett.*, vol. 106, no. 21, p. 211602, May 2015, doi: 10.1063/1.4921758.

[54] J. A. Tomko, D. R. Boris, S. G. Rosenberg, S. G. Walton, and P. E. Hopkins, 'Thermal conductance of aluminum oxy-fluoride passivation layers', *Appl. Phys. Lett.*, vol. 115, no. 19, p. 191901, Nov. 2019, doi: 10.1063/1.5120028.

[55] E. Ziade, M. Goni, T. Sato, P. Czubarow, and A. J. Schmidt, 'Thermal conductance of nanoscale Langmuir-Blodgett films', *Appl. Phys. Lett.*, vol. 107, no. 22, p. 221603, Nov. 2015, doi: 10.1063/1.4937010.

[56] J. Yang *et al.*, 'Thermal conductance imaging of graphene contacts', *J. Appl. Phys.*, vol. 116, no. 2, p. 023515, Jul. 2014, doi: 10.1063/1.4889928.

[57] J.-L. Battaglia, A. Kusiak, A. Saci, R. Fallica, A. Lamperti, and C. Wiemer, 'Effect of a thin Ti interfacial layer on the thermal resistance of $Ge_2Sb_2Te_5$-TiN stack', *Appl. Phys. Lett.*, vol. 105, no. 12, p. 121903, Sep. 2014, doi: 10.1063/1.4896325.

[58] P. Jiang, X. Qian, and R. Yang, 'Tutorial: Time-domain thermoreflectance (TDTR) for thermal property characterization of bulk and thin film materials', *J. Appl. Phys.*, vol. 124, no. 16, p. 161103, Oct. 2018, doi: 10.1063/1.5046944.

[59] A. J. Schmidt, R. Cheaito, and M. Chiesa, 'A frequency-domain thermoreflectance method for the characterization of thermal properties', *Rev. Sci. Instrum.*, vol. 80, no. 9, p. 094901, Sep. 2009, doi: 10.1063/1.3212673.

[60] J. L. Battaglia, A. Kusiak, and K. Ghosh, 'The use of photothermal techniques for thermal conductivity and thermal boundary resistance measurements of phase-change chalcogenides alloys', *J. Appl. Phys.*, vol. 129, no. 5, Feb. 2021, doi: 10.1063/5.0020983.

[61] X. Zheng, D. G. Cahill, and J.-C. Zhao, 'Thermal Conductivity Imaging of Thermal Barrier Coatings', *Adv. Eng. Mater.*, vol. 7, no. 7, pp. 622–626, 2005, doi: 10.1002/adem.200500024.

[62] J. P. Feser, J. Liu, and D. G. Cahill, 'Pump-probe measurements of the thermal conductivity tensor for materials lacking in-plane symmetry', *Rev. Sci. Instrum.*, vol. 85, no. 10, p. 104903, Oct. 2014, doi: 10.1063/1.4897622.

[63] J. Liu, G.-M. Choi, and D. G. Cahill, 'Measurement of the anisotropic thermal conductivity of molybdenum disulfide by the time-resolved magneto-optic Kerr effect', *J. Appl. Phys.*, vol. 116, no. 23, p. 233107, Dec. 2014, doi: 10.1063/1.4904513.

[64] J. Liu, J. Zhu, M. Tian, X. Gu, A. Schmidt, and R. Yang, 'Simultaneous measurement of thermal conductivity and heat capacity of bulk and thin film materials using frequency-dependent transient thermoreflectance method', *Rev. Sci. Instrum.*, vol. 84, no. 3, p. 034902, Mar. 2013, doi: 10.1063/1.4797479.

[65] C. Wei, X. Zheng, D. G. Cahill, and J.-C. Zhao, 'Invited Article: Micron resolution spatially resolved measurement of heat capacity using dual-frequency time-domain thermoreflectance', *Rev. Sci. Instrum.*, vol. 84, no. 7, p. 071301, Jul. 2013, doi: 10.1063/1.4815867.

[66] X. Wang, C. D. Liman, N. D. Treat, M. L. Chabinyc, and D. G. Cahill, 'Ultralow thermal conductivity of fullerene derivatives', *Phys. Rev. B*, vol. 88, no. 7, p. 075310, Aug. 2013, doi: 10.1103/PhysRevB.88.075310.

[67] X. Xie, D. Li, T.-H. Tsai, J. Liu, P. V. Braun, and D. G. Cahill, 'Thermal Conductivity, Heat Capacity, and Elastic Constants of Water-Soluble Polymers and Polymer Blends', *Macromolecules*, vol. 49, no. 3, pp. 972–978, Feb. 2016, doi: 10.1021/acs.macromol.5b02477.

[68] R. B. Wilson, B. A. Apgar, W.-P. Hsieh, L. W. Martin, and D. G. Cahill, 'Thermal conductance of strongly bonded metal-oxide interfaces', *Phys. Rev. B*, vol. 91, no. 11, p. 115414, Mar. 2015, doi: 10.1103/PhysRevB.91.115414.

[69] B. F. Donovan *et al.*, 'Thermal boundary conductance across metal-gallium nitride interfaces from 80 to 450 K', *Appl. Phys. Lett.*, vol. 105, no. 20, p. 203502, Nov. 2014, doi: 10.1063/1.4902233.

[70] B. C. Gundrum, D. G. Cahill, and R. S. Averback, 'Thermal conductance of metal-metal interfaces', *Phys. Rev. B*, vol. 72, no. 24, p. 245426, Dec. 2005, doi: 10.1103/PhysRevB.72.245426.

[71] F. Lepoutre *et al.*, 'Micron-scale thermal characterizations of interfaces parallel or perpendicular to the surface', *J. Appl. Phys.*, vol. 78, no. 4, pp. 2208–2223, 1995, doi: 10.1063/1.360137.

[72] A. Mandelis, A. Williams, and E. K. M. Siu, 'Photothermal wave imaging of metal-oxide-semiconductor field-effect transistor structures', *J. Appl. Phys.*, vol. 63, no. 1, pp. 92–98, Jan. 1988, doi: 10.1063/1.340468.

[73] M. G. Burzo, P. L. Komarov, and P. E. Raad, 'Noncontact transient temperature mapping of active electronic devices using the thermoreflectance method', *IEEE Trans. Compon. Packag. Technol.*, vol. 28, no. 4, pp. 637–643, 2005.

[74] S. Grauby, A. Salhi, L.-D. Patino Lopez, W. Claeys, B. Charlot, and S. Dilhaire, 'Comparison of thermoreflectance and scanning thermal microscopy for microelectronic device temperature variation imaging: Calibration and resolution issues', *Microelectron. Reliab.*, vol. 48, no. 2, pp. 204–211, Feb. 2008, doi: 10.1016/j.microrel.2007.04.008.

[75] A. Ziabari *et al.*, 'Full-field thermal imaging of quasiballistic crosstalk reduction in nanoscale devices', *Nat. Commun.*, vol. 9, no. 1, Art. no. 1, Jan. 2018, doi: 10.1038/s41467-017-02652-4.

[76] S. Grauby, B. C. Forget, S. Holé, and D. Fournier, 'High resolution photothermal imaging of high frequency phenomena using a visible charge coupled device camera associated with a multichannel lock-in scheme', *Rev. Sci. Instrum.*, vol. 70, no. 9, pp. 3603–3608, Sep. 1999, doi: 10.1063/1.1149966.

[77] M. Farzaneh *et al.*, 'CCD-based thermoreflectance microscopy: principles and applications', *J. Phys. Appl. Phys.*, vol. 42, no. 14, p. 143001, Jul. 2009, doi: 10.1088/0022-3727/42/14/143001.

[78] S. Grauby, A. Salhi, J.-M. Rampnoux, H. Michel, W. Claeys, and S. Dilhaire, 'Laser scanning thermoreflectance imaging system using galvanometric mirrors for temperature measurements of microelectronic devices', *Rev. Sci. Instrum.*, vol. 78, no. 7, p. 074902, Jul. 2007, doi: 10.1063/1.2757473.

[79] J. Yang, C. Maragliano, and A. J. Schmidt, 'Thermal property microscopy with frequency domain thermoreflectance', *Rev. Sci. Instrum.*, vol. 84, no. 10, p. 104904, Oct. 2013, doi: 10.1063/1.4824143.

[80] R. D. Cowan, 'Proposed Method of Measuring Thermal Diffusivity at High Temperatures', *J. Appl. Phys.*, vol. 32, no. 7, pp. 1363–1370, Jul. 1961, doi: 10.1063/1.1736235.

[81] P.-E. Nordal and S. O. Kanstad, 'Photothermal radiometry', *Phys. Scr.*, vol. 20, no. 5–6, p. 659, 1979.

[82] S. Brahim, J. L. Bodnar, and P. Grossel, 'Thermal diffusivity measurement by photothermal radiometry under random excitation and parametric analysis', *J. Phys. Conf. Ser.*, vol. 214, p. 012065, Mar. 2010, doi: 10.1088/1742-6596/214/1/012065.

[83] J.-L. Battaglia, A. Kusiak, M. Bamford, and J.-C. Batsale, 'Photothermal radiometric characterization of a thin deposit using a linear swept-frequency heat flux waveform', *Int. J. Therm. Sci.*, vol. 45, no. 11, pp. 1035–1044, Nov. 2006, doi: 10.1016/j.ijthermalsci.2006.02.005.

[84] A. Cappella, 'Caractérisation thermique à haute température de couches minces pour mémoires à changement de phase depuis l'état solide jusqu'à l'état liquide', 2012. [Online]. Available: http://www.theses.fr/2012BOR14500/document

[85] J. L. Battaglia *et al.*, 'The periodic pulse photothermal radiometry technique within the front face configuration', *Meas. J. Int. Meas. Confed.*, vol. 158, Jul. 2020, doi: 10.1016/j.measurement.2020.107691.

[86] J. Ishii, Y. Shimizu, K. Shinzato, and T. Baba, 'High-speed infrared radiation thermometry for microscale thermophysical property measurements', *Int. J. Thermophys.*, vol. 26, no. 6, pp. 1861–1872, Nov. 2005, doi: 10.1007/s10765-005-8601-8.

[87] N. Horny, M. Chirtoc, A. Fleming, G. Hamaoui, and H. Ban, 'Kapitza thermal resistance studied by high-frequency photothermal radiometry', *Appl. Phys. Lett.*, vol. 109, no. 3, p. 033103, Jul. 2016, doi: 10.1063/1.4959084.

[88] H. G. Walther and T. Kitzing, 'Systematic errors of locally resolved photothermal radiometric measurements', *J. Appl. Phys.*, vol. 84, no. 3, pp. 1163–1167, Aug. 1998, doi: 10.1063/1.368180.

[89] A. Mandelis, J. Batista, and D. Shaughnessy, 'Infrared photocarrier radiometry of semiconductors: Physical principles, quantitative depth profilometry, and scanning imaging of deep subsurface electronic defects', *Phys. Rev. B*, vol. 67, no. 20, p. 205208, May 2003, doi: 10.1103/PhysRevB.67.205208.

[90] S. Paoloni and D. Fournier, 'Novel approach for the analysis of infrared photothermal microscopy data', *Rev. Sci. Instrum.*, vol. 74, no. 1, pp. 523–525, Jan. 2003, doi: 10.1063/1.1512991.

[91] S. André, B. Rémy, D. Maillet, A. Degiovanni, and J.-J. Serra, 'Modulated photothermal radiometry applied to semitransparent samples: Models and experiments', *J. Appl. Phys.*, vol. 96, no. 5, pp. 2566–2575, Sep. 2004, doi: 10.1063/1.1774260.

[92] M. Depriester, P. Hus, S. Delenclos, and A. H. Sahraoui, 'New methodology for thermal parameter measurements in solids using photothermal radiometry', *Rev. Sci. Instrum.*, vol. 76, no. 7, Jul. 2005, doi: 10.1063/1.1942532.

[93] R. Fuente, E. Apiñaniz, A. Mendioroz, and A. Salazar, 'Simultaneous measurement of thermal diffusivity and optical absorption coefficient using photothermal radiometry. I. Homogeneous solids', *J. Appl. Phys.*, vol. 110, no. 3, p. 033515, Aug. 2011, doi: 10.1063/1.3614524.

[94] J.-L. Battaglia *et al.*, 'Thermal characterization of the SiO2-Ge2Sb2Te5 interface from room temperature up to 400°C', *J. Appl. Phys.*, vol. 107, no. 4, p. 044314, Feb. 2010, doi: 10.1063/1.3284084.

[95] K. Ghosh, A. Kusiak, P. Noé, M. C. Cyrille, and J. L. Battaglia, 'Thermal conductivity of amorphous and crystalline GeTe thin film at high temperature: Experimental and theoretical study', *Phys. Rev. B*, vol. 101, no. 21, Jun. 2020, doi: 10.1103/PhysRevB.101.214305.

[96] A. Kusiak, J. L. Battaglia, P. Noé, V. Sousa, and F. Fillot, 'Thermal conductivity of carbon doped GeTe thin films in amorphous and crystalline state measured by modulated photo thermal radiometry', *J. Phys. Conf. Ser.*, vol. 745, no. 3, Oct. 2016, doi: 10.1088/1742-6596/745/3/032104.

[97] R. Yang and Y. He, 'Optically and non-optically excited thermography for composites: A review', *Infrared Phys. Technol.*, vol. 75, pp. 26–50, Mar. 2016, doi: 10.1016/j.infrared.2015.12.026.

[98] F. Ciampa, P. Mahmoodi, F. Pinto, and M. Meo, 'Recent Advances in Active Infrared Thermography for Non-Destructive Testing of Aerospace Components', *Sensors*, vol. 18, no. 2, Art. no. 2, Feb. 2018, doi: 10.3390/s18020609.

[99] N. W. Pech-May, A. Oleaga, A. Mendioroz, A. J. Omella, R. Celorrio, and A. Salazar, 'Vertical cracks characterization using lock-in thermography: I infinite cracks', *Meas. Sci. Technol.*, vol. 25, no. 11, p. 115601, Nov. 2014, doi: 10.1088/0957-0233/25/11/115601.

[100] K. Sebastian, A. Melnikov, K. Sivagurunathan, X. Guo, X. Wang, and A. Mandelis, 'Non-destructive lock-in thermography of green powder metallurgy component inhomogeneities: A predictive imaging method for manufactured component flaw prevention', *NDT E Int.*, vol. 127, p. 102603, Apr. 2022, doi: 10.1016/j.ndteint.2022.102603.

[101] Ch. Schmidt, F. Altmann, and O. Breitenstein, 'Application of lock-in thermography for failure analysis in integrated circuits using quantitative phase shift analysis', *Mater. Sci. Eng. B*, vol. 177, no. 15, pp. 1261–1267, Sep. 2012, doi: 10.1016/j.mseb.2012.02.011.

[102] J. Bauer, O. Breitenstein, and J.-M. Wagner, 'Lock-in Thermography: A Versatile Tool for Failure Analysis of Solar Cells', *EDFA Tech. Artic.*, vol. 11, no. 3, pp. 6–12, Aug. 2009, doi: 10.31399/asm.edfa.2009-3.p006.

[103] M. Ryu *et al.*, 'Infrared thermo-spectroscopic imaging of styrene radical polymerization in microfluidics', *Chem. Eng. J.*, vol. 324, pp. 259–265, Sep. 2017, doi: 10.1016/j.cej.2017.05.001.

[104] L. Gaverina, J. C. Batsale, A. Sommier, and C. Pradere, 'Pulsed flying spot with the logarithmic parabolas method for the estimation of in-plane thermal diffusivity fields on heterogeneous and anisotropic materials', *J. Appl. Phys.*, vol. 121, no. 11, Mar. 2017, doi: 10.1063/1.4978919.

[105] L. Gaverina, A. Sommier, J. L. Battaglia, J. C. Batsale, and C. Pradere, 'Pulsed Flying Spot Elliptic method for the estimation of the thermal diffusivity field of orthotropic materials', *Int. J. Therm. Sci.*, vol. 125, pp. 142–148, Mar. 2018, doi: 10.1016/j.ijthermalsci.2017.11.017.

[106] J. González, A. Mendioroz, A. Sommier, J. C. Batsale, C. Pradere, and A. Salazar, 'Fast sizing of the width of infinite vertical cracks using constant velocity Flying-Spot thermography', *NDT E Int.*, vol. 103, pp. 166–172, Apr. 2019, doi: 10.1016/j.ndteint.2019.03.003.

[107] A. Salazar *et al.*, 'Lock-in thermography on moving samples: amazing mismatch between amplitude and phase', *Quant. InfraRed Thermogr. J.*, vol. 17, no. 4, pp. 279–286, Oct. 2020, doi: 10.1080/17686733.2019.1655248.

[108] M. Colom, J. Rodríguez-Aseguinolaza, A. Mendioroz, and A. Salazar, 'Sizing the depth and width of narrow cracks in real parts by laser-spot lock-in thermography', *Materials*, vol. 14, no. 19, Oct. 2021, doi: 10.3390/ma14195644.

[109] T. Ishizaki and H. Nagano, 'Measurement of 3D thermal diffusivity distribution with lock-in thermography and application for high thermal conductivity CFRPs', *Infrared Phys. Technol.*, vol. 99, pp. 248–256, Jun. 2019, doi: 10.1016/j.infrared.2019.04.023.

[110] M. Colom, A. Bedoya, A. Mendioroz, and A. Salazar, 'Measuring the in-plane thermal diffusivity of moving samples using laser spot lock-in thermography', *Int. J. Therm. Sci.*, vol. 151, May 2020, doi: 10.1016/j.ijthermalsci.2020.106277.

[111] A. Mendioroz, R. Fuente-Dacal, E. Apiñaniz, and A. Salazar, 'Thermal diffusivity measurements of thin plates and filaments using lock-in thermography', *Rev. Sci. Instrum.*, vol. 80, no. 7, p. 074904, Jul. 2009, doi: 10.1063/1.3176467.

[112] T. Ishizaki, T. Igami, and H. Nagano, 'Measurement of local thermal contact resistance with a periodic heating method using microscale lock-in thermography', *Rev. Sci. Instrum.*, vol. 91, no. 6, Jun. 2020, doi: 10.1063/5.0002937.

[113] O. Breitenstein, W. Warta, and M. C. Schubert, *Lock-in Thermography: Basics and Use for Evaluating Electronic Devices and Materials Third Edition*, 3rd ed., vol. 10. Springer, 2018. Accessed: Apr. 04, 2022. [Online]. Available: http://www.springer.com/series/4076

[114] 'Multimode Fluoride Fiber Optic Patch Cables'. https://www.thorlabs.com (accessed Nov. 18, 2022).

[115] 'TECHSPEC Germanium (Ge) Windows'. https://www.edmundoptics.fr/p/25mm-dia-x-1mm-thick-3-12mum-ar-coated-ge-window/26495/ (accessed Nov. 18, 2022).

[116] J.-L. Battaglia, A. Kusiak, and C. Pradère, *Introduction aux transferts thermiques-3e éd.: Cours et exercices corrigés*. Dunod, 2020.

[117] 'Indium Antimonide Detectors'. https://www.teledynejudson.com/products/indium-antimonide-detectors (accessed Dec. 10, 2022).

[118] H. S. Carslaw and J. C. Jaeger, 'Conduction of heat in solids', *Oxf. Clarendon Press 1959 2nd Ed*, 1959.

[119] COMSOL Documentation: Infinite Element Implementation'. https://doc.comsol.com/6.0/docserver/#!/com.comsol.help.comsol/comsol_ref_definitions.17.121.html (accessed Nov. 28, 2022).

[120] D. Maillet, S. Andre, J. C. Batsale, A. Degiovanni, and C. Moyne, *Thermal quadrupoles: solving the heat equation through integral transforms*. John Wiley & Sons Incorporated, 2000.

[121] 'Stainless Steel 304 - 1.4301 Data Sheet thyssenkrupp Materials (UK)', *Materials UK*. https://www.thyssenkrupp-materials.co.uk/stainless-steel-304-14301.html (accessed Nov. 29, 2022).

[122] H. TAN NGUYEN, 'Thermal Characterization of In-Sb-Te thin films for Phase Change Memory Application', UNIVERSITÉ DE BORDEAUX, 2015.

[123] X. Bourrat, A. Fillion, R. Naslain, G. Chollon, and M. Brendlé, 'Regenerative laminar pyrocarbon', *Carbon*, vol. 40, no. 15, pp. 2931–2945, 2002, doi: 10.1016/S0008-6223(02)00230-0.

[124] 'Principles of Lock-in Detection | Zurich Instruments', Dec. 20, 2019. https://www.zhinst.com/en/resources/principles-of-lock-in-detection (accessed Sep. 22, 2022).

[125] Stanford Research Systems, *MODEL SR830: DSP Lock-In Amplifier*. 2011. [Online]. Available: https://www.thinksrs.com/downloads/pdfs/manuals/SR830m.pdf

[126] P. Y. Sulima, J. L. Battaglia, T. Zimmer, and J. C. Batsale, 'Self heating modeling of SiGe heterojunction bipolar transistor', *Int. Commun. Heat Mass Transf.*, vol. 34, no. 5, pp. 553–563, May 2007, doi: 10.1016/J.ICHEATMASSTRANSFER.2006.11.010.

[127] J. Pailhes *et al.*, 'Thermal quadrupole method with internal heat sources', *Int. J. Therm. Sci.*, vol. 53, pp. 49–55, Mar. 2012, doi: 10.1016/J.IJTHERMALSCI.2011.10.005.